

Copyright is owned by the Author of the thesis. Permission is given for a copy to be downloaded by an individual for the purpose of research and private study only. The thesis may not be reproduced elsewhere without the permission of the Author.

# **Micro Implantable Pressure Sensors**

**For Lifetime Monitoring of Intracranial Pressure**



**Nireekshan Kumar Sodavaram**

School of Engineering and Advanced Technology

Massey University

This dissertation is submitted for the degree of

*Doctor of Philosophy*



I would like to dedicate this thesis to my loving Mom . . .



## **Declaration**

I hereby declare that except where specific reference is made to the work of others, the contents of this dissertation are original and have not been submitted in whole or in part for consideration for any other degree or qualification in this, or any other university. This dissertation is my own work and contains nothing which is the outcome of work done in collaboration with others, except as specified in the text and Acknowledgments. This dissertation contains around 36,000 words including appendices, bibliography, footnotes, tables and equations and has fewer than 221 figures.

Nireekshan Kumar Sodavaram

March 2019



## **Acknowledgements**

Firstly, I would like to express my unreserved gratitude to my supervisor Dr. Khalid Mahmood Arif, and co-supervisor(s) Dr. Fakhru Alam, and Prof. Johan Potgieter for their constant support and guidance throughout this project.

Secondly, I am very grateful for the generous advice and assistance of my industry mentors Associate Professor David Budgett and Dr. Daniel McCormick throughout this research.

To the members of Implantable Devices Group at Auckland Bioengineering Institute including Dixon Leung, Ian Glass, Robert Gallichan, Beverly Chen, and Utkarsh Anand Saxena for your advice and support.

I am incredibly grateful to Callaghan Innovation, the government agency supporting high-tech business in New Zealand for funding my Ph.D. research, without which this research would not have been possible.

Thank you, Massey University, and Millar Limited for the necessary financial assistance whenever required. Thank you, my fellow Ph.D. students, the technical and administrative staff at Massey University for creating such an outstanding environment.

Finally, a huge thank you to Ananiah Durai Sundararajan, Julia Jing Ma, and Muhammad Harris for your unwavering support from day one of my Ph.D. studies.

- Mum, Dad, and David; thank you all for your relentless support and providing financial assistance whenever needed. Especially my Mum who passed away suddenly and couldn't see my success.

## **Abstract**

The elevation of intracranial pressure (ICP) associated with traumatic brain injury (TBI), hydrocephalus and other neurological conditions is a serious concern. If left untreated, increased pressure in the brain will reduce cerebral blood flow (CBF) and can lead to brain damage or early death. Currently, ICP is monitored through invasive catheters inserted into the brain along with a shunt. However, insertion of catheters or shunts is an invasive procedure that introduces vulnerability to infection. In principle, the risk of infection would be overcome by a fully implantable pressure monitoring system. This would be particularly valuable for hydrocephalus patients if lifetime monitoring was available. An implantable pressure monitoring system relies on a thin flexible membrane as part of the pressure sensor. The thin film membrane displaces under load and correspondingly induces a change in a relevant electrical quantity (resistance, or capacitance). Micro-electro-mechanical system (MEMS) is the technology that helps in creating micro/nano-mechanical structures integrated with signal conditioning electronics. These micro structures can be inserted into the brain, where the thin film is exposed to a corrosive fluid (saline/blood) at a temperature of approximately 37 °C. The miniaturization in MEMS permits examination, sensing and monitoring from inside the patient for longer durations. However, the accuracy, particularly in terms of sensor drift over long durations, is a key concern. In general, the issue of drift is attributed to the aging and mechanical fatigue of thin film structures, particularly the thin flexible membrane. Therefore, it is essential to analyze the thin film deflection and fatigue behaviour of MEMS pressure sensors for achieving long-term reliability and accuracy. Thus, the high-level goal

of this research is to identify a viable approach to producing a flexible membrane suitable for deployment as a lifetime implantable pressure measuring system.

In this context, finite-element modelling (FEM) and finite-element analysis (FEA) of thin film deflection and fatigue behaviour have been conducted. The FEM was implemented in COMSOL Multiphysics with geometries resembling a capacitive type pressure sensor with titanium (Ti) thin film membrane deposited onto the silicon substrate. The mechanical behavior of thin film structures including stresses, strains, elastic strain energy density, and thin film displacements of several thicknesses (50  $\mu\text{m}$ , 25  $\mu\text{m}$ , 4  $\mu\text{m}$ , 1  $\mu\text{m}$ , 500 nm, 200 nm) have been studied. In addition, fatigue physics module has been added to the FEM to analyze the fatigue life of thin film structures. The FEA results in the form of fatigue usage factors have been plotted. Finally, to analyze the effect of fluid pressure transmission of the thin film membrane inside the closed skull, fluid-structure interaction has been modelled. The model represents a 2D fluid medium with the thin film membrane. The velocity magnitude, displacement, shear rate (1/s) and kinetic energy density ( $\text{J}/\text{m}^3$ ) of 4  $\mu\text{m}$  and 25  $\mu\text{m}$  thick Ti films has been plotted. From this analysis, 4  $\mu\text{m}$  thin film membrane showed good tradeoff for thickness, pressure transmission, and mechanical behaviour.

To validate the FEM, a custom designed acoustic-based thin film deflection and fatigue life experiments have been set up. The experimental design comprised of: (1) A voice coil-based multimedia speaker and subwoofer system to assist in displacing the thin film membranes, (2) A laser displacement sensor to capture the displacements, (3) A spectrum analyzer palette for generating random vibrations, (4) Dataloggers to record the input vibrations and thin film displacements, and (5) Scanning electron microscopy (SEM) to visualize the surface topography of thin film structures. Thin film titanium (Ti) foils of 4  $\mu\text{m}$  and 25  $\mu\text{m}$  thick were obtained from William Gregor Ltd, Ti-shop, London. The thin-film specimens were clamped to 3 mm acrylic substrates and bonded to the subwoofer system. The Gaussian random vibrations generated from the spectrum analyzer loaded the voice coil of the multi-media

speaker system, which assists in displacing the thin films. The SEM surface observations are divided into two regions: (1) Pre-cycle observation, where the thin film surfaces are observed before the application of any load, and (2) Post-cycle observation, where the thin films surfaces are observed after application of cyclic loadings.

Based on the understanding of the FEM and experimental studies, a conceptual framework of MEMS pressure sensor has been developed. In this part of the work, initially, underlying concepts of complementary-metal-oxide silicon (CMOS) circuit simulation, MEMS modelling, and CMOS layout design have been discussed. Next the MEMS fabrication process involving deposition (sputtering), etching, and final packaging have been discussed. Finally, an optimized design process of the membrane-based sealed cavity MEMS pressure sensors has been outlined.



# Contents

<b>List of Figures</b>	<b>xvii</b>
<b>List of Tables</b>	<b>xxv</b>
<b>Nomenclature</b>	<b>xxvii</b>
<b>1 Introduction</b>	<b>1</b>
1.1 Background . . . . .	5
1.1.1 Hydrocephalus . . . . .	10
1.1.2 Hydrocephalus Treatment . . . . .	11
1.1.3 The Underlying Issues of a CSF Shunt . . . . .	13
1.1.4 Intracranial Pressure (ICP) . . . . .	14
1.1.5 Problem Statement . . . . .	25
1.1.6 Overview of the Proposed Research . . . . .	27
1.1.7 Thesis Outline . . . . .	30
<b>2 Literature Review</b>	<b>33</b>
2.1 Introduction . . . . .	33
2.2 The Nature and Dynamics of ICP . . . . .	34
2.3 The External Factors Affecting ICP . . . . .	39
2.3.1 Types of Pressure Measurements . . . . .	40

2.3.2	The Effect of Weather on Atmospheric Pressure . . . . .	42
2.3.3	The Effect of Altitude on Atmospheric Pressure . . . . .	43
2.4	Atmospheric Pressure Measurements in Auckland . . . . .	44
2.5	Material and Specimens . . . . .	45
2.6	Finite-Element Model and Analysis . . . . .	51
2.7	Experimental Testing . . . . .	59
2.8	Summary . . . . .	60
<b>3</b>	<b>Finite-Element Modelling and Simulations</b>	<b>61</b>
3.1	Introduction . . . . .	61
3.2	Theory of Thin Film Deflection . . . . .	63
3.2.1	The Effect of Thin Film Stresses . . . . .	64
3.2.2	Thin Film Deflection Model . . . . .	66
3.2.3	Finite-Element Simulations . . . . .	72
3.3	Fatigue Behaviour Modelling . . . . .	88
3.3.1	Fatigue Design Variables . . . . .	92
3.4	Summary . . . . .	103
<b>4</b>	<b>Experimental Testing</b>	<b>111</b>
4.1	Introduction . . . . .	111
4.2	Materials and Specimens . . . . .	111
4.3	Measurement Technique . . . . .	115
4.4	SEM Visualization . . . . .	118
4.5	Extended FEM of Crack Growth . . . . .	119
4.6	Summary . . . . .	122
<b>5</b>	<b>Implantable Pressure Sensor: MEMS Fabrication Framework</b>	<b>123</b>
5.1	Introduction . . . . .	123

---

5.2	Types of MEMS pressure sensors . . . . .	125
5.2.1	Piezoresistive Sensing . . . . .	125
5.2.2	Capacitive Sensing . . . . .	126
5.2.3	Transduction Stages . . . . .	127
5.3	CMOS-MEMS Fabrication . . . . .	127
5.3.1	CMOS Circuit Simulations . . . . .	128
5.3.2	CMOS Layout Design . . . . .	131
5.3.3	MEMS Fabrication . . . . .	133
5.3.4	Commercial MEMS Fabrication process . . . . .	137
5.3.5	CMOS-MEMS Packaging . . . . .	138
5.4	An Optimized Wafer-Level MEMS Fabrication . . . . .	139
5.5	Summary . . . . .	142
<b>6</b>	<b>Conclusions and Future Work</b>	<b>145</b>
6.1	Conclusions . . . . .	145
6.2	Future Work . . . . .	148
	<b>Bibliography</b>	<b>151</b>
	<b>Appendix A</b>	<b>165</b>
A.1	Thin Film Shape: FEA . . . . .	165
	<b>Appendix B FEM of MEMS Capacitive Sensor</b>	<b>169</b>
B.1	Introduction . . . . .	169
B.1.1	Capacitance Modelling . . . . .	170
	<b>Appendix C List of Publications</b>	<b>177</b>



# List of Figures

1.1	The conceptual diagram of ventriculoperitoneal (VP) shunt along with ICP monitor . . . . .	3
1.2	The Coronal section of the brain at the level of the thalamus showing the Ventricles, Cerebellum, Spinal cord, etc. . . . .	6
1.3	A conceptual diagram depicting CSF flow inside fluid-filled ventricles of the brain [20] . . . . .	7
1.4	The conceptual diagram of Monro-Kellie hypothesis . . . . .	8
1.5	The effect of MAP and ICP on CBF . . . . .	9
1.6	The conceptual diagram showing the (a) normal ventricle and (b) enlarged ventricle . . . . .	11
1.7	The ICP waveform showing the nature of peaks (P1-Systolic pressure; P2-Elastance; P3-Aortic Valve) (a) Normal ICP; (b) Abnormal ICP; (c) Critically ICP . . . . .	16
1.8	Lundberg ICP wave - Plateau wave (A), High amplitude B waves, and Low amplitude C waves [46] . . . . .	17
1.9	The anatomic sites for ICP monitoring: Epidural, subdural, intraparenchymal, intraventricular, lumbar subarachnoid . . . . .	19
1.10	The conceptual diagram of fibre-optic catheter tip pressure transducer . . . . .	20

1.11	ICP monitoring using Neurovent-P telemetric ICP monitor from Raumedic systems [60] . . . . .	24
1.12	A 3D MEMS membrane based capacitive pressure sensor . . . . .	25
1.13	A cross-section of capacitive pressure sensor . . . . .	26
1.14	The flowchart of the proposed research . . . . .	28
2.1	The conceptual diagram showing the intracranial volume changes . . . . .	36
2.2	An ICP frequency spectrum of Kaolin-introduced Male Wistar Rats: Normal Wistar rat (green colour) and hydrocephalus (kaolin)-introduced Wistar rat (red colour) . . . . .	37
2.3	A - Low and stable ICP wave, B – High and stable ICP, C – Vasogenic B waves: they are saw tooth type rhythmic oscillations caused by changes in cerebral blood volume (CBV) due to depressed consciousness and reduced internal compliance, D – plateau (A) waves: momentary rises in the baseline pressure to amplitude of 60 mm Hg for about 5 – 10 minutes before falling back to baseline or below, E – G – cause due to the influence of respiratory and cardiac wave components, H – Refractory intracranial hypertension which can cause death [46] . . . . .	38
2.4	The types of pressure measurements . . . . .	40
2.5	Types of pressure measurement including absolute, gauge and atmospheric pressures . . . . .	45
2.6	The plot of the capture of atmospheric pressure oscillations in Auckland using Mensor CPT6100 barometric sensor . . . . .	46
2.7	Types of pressure measurement including absolute, gauge and atmospheric pressures . . . . .	52
2.8	(a) The deformed plate, (b) The moments and forces acting on a plate . . . . .	54
2.9	The S-N curve of Ti-6Al-4V Ti alloy . . . . .	57

---

3.1	The pictorial representation showing the (a) the stress due to straining, (b) Residual stresses, (c) the stress due to deflection . . . . .	65
3.2	The conceptual diagram depicting the effect of (a) tensile, (b) compressive residual stresses on a thin film membrane deposited on a silicon substrate .	67
3.3	The force components of a membrane-based pressure sensor under deflection	68
3.4	The shape of thin film deflection . . . . .	71
3.5	The input pressure load (a) Atmospheric pressure (b) ICP . . . . .	74
3.6	The 2D CAD model of MEMS pressure sensor . . . . .	76
3.7	The FEA plots showing (a) von Mises stresses, (b) Total displacement, (c) Total volumetric strain, (d) Elastic strain energy density of 50 $\mu\text{m}$ thin film Ti sheet . . . . .	78
3.8	The FEA plots showing (a) von Mises stresses, (b) Total displacement, (c) Total volumetric strain, (d) Elastic strain energy density of 25 $\mu\text{m}$ thin film Ti sheet . . . . .	79
3.9	The FEA plots showing (a) von Mises stresses, (b) Total displacement, (c) Total volumetric strain, (d) Elastic strain energy density of 4 $\mu\text{m}$ thin film Ti sheet . . . . .	80
3.10	The FEA plots showing (a) von Mises stresses, (b) Total displacement, (c) Total volumetric strain, (d) Elastic strain energy density of 1 $\mu\text{m}$ thin film Ti sheet . . . . .	81
3.11	he FEA plots showing (a) von Mises stresses, (b) Total displacement, (c) Total volumetric strain, (d) Elastic strain energy density of 500 nm thin film Ti sheet . . . . .	82
3.12	The FEA plots showing (a) von Mises stresses, (b) Total displacement, (c) Total volumetric strain, (d) Elastic strain energy density of 200 nm thin film Ti sheet . . . . .	83

---

3.13	The FEA plots showing (a) von Mises stresses, (b) Total displacement of 50 $\mu\text{m}$ thin film Ti sheet due to mismatches in thermal expansion . . . . .	84
3.14	The FEA plots showing (a) von Mises stresses, (b) Total displacement of 25 $\mu\text{m}$ thin film Ti sheet due to mismatches in thermal expansion . . . . .	84
3.15	The FEA plots showing (a) von Mises stresses, (b) Total displacement of 4 $\mu\text{m}$ thin film Ti sheet due to mismatches in thermal expansion . . . . .	85
3.16	The FEA plots showing (a) von Mises stresses, (b) Total displacement of 1 $\mu\text{m}$ thin film Ti sheet due to mismatches in thermal expansion . . . . .	85
3.17	The FEA plots showing (a) von Mises stresses, (b) Total displacement of 500 nm thin film Ti sheet due to mismatches in thermal expansion . . . . .	86
3.18	The FEA plots showing (a) von Mises stresses, (b) Total displacement of 200 nm thin film Ti sheet due to mismatches in thermal expansion . . . . .	86
3.19	The 2D CAD model for FSI analysis . . . . .	87
3.20	The FEA plots of 25 $\mu\text{m}$ thin film showing (a) velocity magnitude, (b) displacement of thin film in fluid, (c) shear rate of the thin film membrane, (d) kinetic energy density . . . . .	88
3.21	The FEA plots of 4 $\mu\text{m}$ thin film showing (a) velocity magnitude, (b) displacement of thin film in fluid, (c) shear rate of the thin film membrane, (d) kinetic energy density . . . . .	89
3.22	The 3D CAD model of MEMS capacitive pressure sensor . . . . .	90
3.23	The 3D FEA plots showing (a) von Mises stresses, (b) Total displacement, (c) Total volumetric strain, (d) Elastic strain energy density of 50 $\mu\text{m}$ thin film Ti sheet . . . . .	91
3.24	The 3D FEA plots showing (a) von Mises stresses, (b) Total displacement, (c) Total volumetric strain, (d) Elastic strain energy density of 25 nm thin film Ti sheet . . . . .	92

---

3.25	The 3D FEA plots showing (a) von Mises stresses, (b) Total displacement, (c) Total volumetric strain, (d) Elastic strain energy density of 4 nm thin film Ti sheet . . . . .	93
3.26	The 3D FEA plots showing (a) von Mises stresses, (b) Total displacement, (c) Total volumetric strain, (d) Elastic strain energy density of 1 nm thin film Ti sheet . . . . .	94
3.27	The 3D FEA plots showing (a) von Mises stresses, (b) Total displacement, (c) Total volumetric strain, (d) Elastic strain energy density of 500 nm thin film Ti sheet . . . . .	95
3.28	The intrusion and extrusion model of crack growth . . . . .	96
3.29	The fatigue process flow . . . . .	96
3.30	A model of S-N curve . . . . .	97
3.31	A fatigue load cycle . . . . .	97
3.32	A Goodman fatigue curve . . . . .	98
3.33	A model of notch created on a thin film and stress concentration factor . . . . .	99
3.34	The stress-strain curve showing the good operational region . . . . .	100
3.35	Gauss-point stress tensor showing non proportional loading . . . . .	101
3.36	Fatigue usage factor of 50 $\mu\text{m}$ 2D thin film Ti membrane . . . . .	105
3.37	Fatigue usage factor of 25 $\mu\text{m}$ 2D thin film Ti membrane . . . . .	105
3.38	Fatigue usage factor of 4 $\mu\text{m}$ 2D thin film Ti membrane . . . . .	106
3.39	Fatigue usage factor of 1 $\mu\text{m}$ 2D thin film Ti membrane . . . . .	106
3.40	Fatigue usage factor of 500 nm 2D thin film Ti membrane . . . . .	107
3.41	Fatigue usage factor of 50 $\mu\text{m}$ 3D thin film Ti membrane . . . . .	107
3.42	Fatigue usage factor of 25 $\mu\text{m}$ 3D thin film Ti membrane . . . . .	108
3.43	Fatigue usage factor of 4 $\mu\text{m}$ 3D thin film Ti membrane . . . . .	108
3.44	Fatigue usage factor of 1 $\mu\text{m}$ 3D thin film Ti membrane . . . . .	109

3.45	Fatigue usage factor of 500 nm 3D thin film Ti membrane . . . . .	109
4.1	Thin film Ti specimens (a) 4 $\mu\text{m}$ thick, (b) 25 $\mu\text{m}$ thick . . . . .	112
4.2	The SEM pictographs of (a) 4 $\mu\text{m}$ thick, (b) 25 $\mu\text{m}$ thick . . . . .	112
4.3	The block diagram of acoustic-based fatigue testing system . . . . .	113
4.4	The experimental setup of acoustic-based fatigue testing system . . . . .	113
4.5	Thin film Ti specimens (a) 4 $\mu\text{m}$ thick, (b) 25 $\mu\text{m}$ thick . . . . .	114
4.6	The conceptual diagram showing the surface of clamped Ti thin films . . . . .	115
4.7	The Gaussian random vibration curve from spectrum analyzer . . . . .	116
4.8	The displacement plot of 4 $\mu\text{m}$ thin film Ti membrane . . . . .	117
4.9	The conceptual diagram of acoustic vibration distributions across the 3 mm thick circular acrylic sheet . . . . .	118
4.10	The scatter plot of number of cycles to failure with respect to the thickness of thin film Ti and its clamping positions on the acrylic sheet . . . . .	119
4.11	Thin film Ti specimens (a) 4 $\mu\text{m}$ thick, (b) 25 $\mu\text{m}$ thick . . . . .	120
4.12	The X-FEM based crack growth plot of 4 $\mu\text{m}$ thick, thin film Ti membrane . . . . .	121
5.1	A pictorial representation of various components of a MEMS systems . . . . .	124
5.2	A cross-sectional view of MEMS piezo resistive pressure sensor . . . . .	126
5.3	A conceptual view of pressure transduction scheme . . . . .	127
5.4	The CMOS-MEMS Pressure sensor design flow . . . . .	129
5.5	(a) Circuit of a NMOS current mirror; (b) Small signal equivalent of a NMOS current mirror . . . . .	130
5.6	A typical layout of CMOS current mirror with N-channel MOSFET . . . . .	131
5.7	A typical layout design of a MEMS pressure Sensor with an on-chip tran- simpedance amplifier drawn on global foundries (GF) 130 nm CMRF8SF CMOS design process . . . . .	132

---

5.8	A typical bulk MEMS micromachined pressure sensor (a) Mask Layout view or Top view; (b) 2D Cross Sectional view . . . . .	133
5.9	MEMS microfabrication process flow . . . . .	134
5.10	Cross-section view of a Post-CMOS MEMS fabrication as a Multi-chip Module	138
5.11	MEMS wafer-level processing of silicon substrates - thin film deposition and etching . . . . .	140
5.12	MEMS wafer-level processing of glass substrates - thin film deposition, etching and metalization . . . . .	141
5.13	MEMS wafer-level bonding of silicon and glass substrates . . . . .	141
5.14	MEMS sequential process for final metalization and vacuum sealing . . . . .	142
5.15	Final Packaging of MEMS Pressure Sensors . . . . .	142
6.1	The block diagram of the proposed ultrasonic fatigue testing system . . . . .	149
6.2	The proposed MEMS pressure sensor rig . . . . .	149
A.1	The thin film deflection of various shapes (a) Circular membrane, (b) Square membrane, (c) Rectangular membrane, (d) Elliptical membrane . . . . .	166
B.1	The CAD model of MEMS capacitive pressure sensor with borosilicate sealed cavity . . . . .	171
B.2	The electric potential plot of MEMS capacitive pressure sensor with 4 $\mu\text{m}$ thin film membrane . . . . .	173
B.3	The electric displacement field norm of MEMS capacitive pressure sensor with 4 $\mu\text{m}$ thin film membrane . . . . .	173
B.4	The Maxwell stress tensor plot of MEMS capacitive pressure sensor with 4 $\mu\text{m}$ thin film membrane . . . . .	174
B.5	The graph showing the change in capacitance with the change in pressure . . . . .	175

---

C.1	A technical paper published in <i>Microsystem Technologies</i> , Springer-Verlag GmbH Germany, part of Springer Nature 2018 <a href="https://doi.org/10.1007/s00542-018-4230-6">https://doi.org/10.1007/s00542-018-4230-6</a> . . . . .	178
C.2	A paper presented in IEEE Conference proceedings . . . . .	179
C.3	A technical paper published in <i>Journal of Mechanical Science and Technology</i> , Springer . . . . .	180
C.4	A technical paper published in <i>International Journal of Precision Engineering and Manufacturing</i> , Springer . . . . .	181
C.5	A review paper submitted to the <i>Sensors</i> MDPI . . . . .	182
C.6	A poster presented at manufacturing and design (MaD) conference 2018 . . . . .	183
C.7	Best poster award at MaD conference 2018 . . . . .	184
C.8	A poster presented at the 9th international conference on Advanced materials and nanotechnology (AMN9) . . . . .	185

# List of Tables

1.1	Threshold limits of cerebral auto-regulation [22] . . . . .	8
1.2	The most common types of shunt systems. (Available at: <a href="https://www.hydroassoc.org/shunt-systems/">https://www.hydroassoc.org/shunt-systems/</a> ) . . . . .	12
1.3	The classifications of commercially available ICP shunts/catheters . . . . .	21
1.4	The engineering design specifications . . . . .	29
2.1	The ICP threshold values of a healthy adult [46] . . . . .	35
2.2	The nature and shape of ICP and its components [46] . . . . .	39
2.3	Atmospheric pressure fluctuations captured during cyclones across the globe	44
2.4	The effect of altitude on atmospheric pressure . . . . .	47
2.5	The atmospheric pressure oscillations recorded at ABI, UOA, Auckland using Mensor CPT6100 barometric sensor . . . . .	47
2.6	The various classification of biocompatible materials [85, 86, 70] . . . . .	49
2.7	The mechanical properties of Ti ( <a href="http://matweb.com/search/DataSheet.aspx?MatGUID=b350a789eda946c6b86a3e4d3c577b39&amp;ckck=1">http://matweb.com/search/DataSheet.aspx?MatGUID=b350a789eda946c6b86a3e4d3c577b39&amp;ckck=1</a> ) . . . . .	51
2.8	Classification of biocompatible materials used in the body . . . . .	52
2.9	The elemental composition of Ti-6AL-4V . . . . .	53
3.1	The Design Specification of FEM model . . . . .	73
3.2	The dimensions of 2D MEMS pressure sensor model . . . . .	77

3.3	The comparison of deflection, stress due to deflection, residual stress, transmission . . . . .	90
3.4	The comparison of deflection induced fatigue and residual stress induced fatigue . . . . .	103
6.1	Comparison of FEM and experimental fatigue results for different thicknesses of thin-film Ti membranes . . . . .	147
A.1	The model geometry for thin film shape optimization . . . . .	167

# Nomenclature

## Acronyms / Abbreviations

$w_0$  Deflection at the centre

$\Delta \sigma$  Alternating stress

$\Delta P$  Pressure Change

$\Delta p$  Change in the thickness

$\Delta w$  Change in the width

$\nu_m$  Poisson's Ratio of thin film membrane

$\pi$  A mathematical constant (ratio of a circle's circumference to its diameter) equivalent to 3.14159

$\sigma$  Stress

$\sigma_a$  Stress amplitude

$\sigma_e$  Endurance limit stress

$\sigma_N$  Normal stress

$\sigma_N$  Shear stress

$\sigma_u$  Ultimate stress

$\sigma_{max}$  Maximum stress

$\sigma_{min}$  Minimum stress

$\sigma_{mn}$  Mean stress

$\sigma_m$  Membrane Stress

$\sigma_r$  Radial Stress

$\sigma_t$  Tangential stress

$\sigma_{(N,max)}$  Maximum normal stress

$\sin(\alpha)$  Angle between the thin film membrane and force exerted by the substrate

$\tan(\alpha)$  The small angles of  $\sin$  are equivalent to  $\tan(tangent)$

$\varepsilon_t$  Tangential strain

$\varepsilon_0$  Initial strain

$\varepsilon_{cr}$  Creep strain

$\varepsilon_{hs}$  Hygroscopic strain

$\varepsilon_{pl}$  Plastic strain

$\varepsilon_{th}$  Thermal strain

$\varepsilon_r$  Radial strain

4V Four percent of Vanadium

6Al Six percent of Aluminum

A Amplitude

AAMI Association for Advanced Medical Instrumentation

ABI Auckland Bioengineering Institute

ADE Analog Design Environment

ANSI American National Standards Institute

ASTM American Society of Testing and Materials

ATM Atmospheric Pressure

CAD Computer Aided Design

CAE Computer Aided Engineering

CBV Cerebral blood volume

CMOS Complementary Metal Oxide Silicon

CMRF8SF A Global foundries CMOS Design Process

CPP Cerebral perfusion Pressure

CSF Cerebrospinal fluid

CT Computerized tomography

CVD Chemical Vapour Deposition

CVR	Cardiovascular resistance
$E_{sub}$	Young's modulus of the substrate
EDA	Electronic Design Automation
EDX	Energy dispersive X-ray
FDM	Finite Differential Method
FEA	Finite Element Analysis
FEM	Finite-Element Modeling
FES	Finite-Element Simulations
f	Fatigue limit
FOS	Factor of Safety
GPa	Giga Pascals
HCF	High cycle fatigue
ICP	Intracranial Pressure
kg	Kilo gram
K	Kelvin
k	Normal stress sensitivity coefficient
L-Edit	Layout-Editor of Tanner EDA tools
LCF	Low cycle fatigue

LK–H2 Keyence data-logger

LKG–5001 Keyence Laser displacement Model No.

LP Lumbar Puncture

MAP Mean arterial pressure

MEMS Micro-electro-mechanical-systems

MIM Metal-Insulator-Metal

m metre

mmHg Millimeter of mercury

MPa Mega pascals

MRI Magnetic Resource Imaging

$N_f$  Number of cycles to failure

NASA National Aeronautics and Space Administration

NI National Instruments

NMOS N-Type Metal Oxide Silicon

PMOS P-Type Metal Oxide Silicon

PVD Physical Vapour Deposition

ra Radial coordinate

$r_m$  Radius of the thin film membrane

RCA Radio Corporation of America

$s_m$  Side Length of thin film membrane

SEM Scanning Electron Microscope

$\text{Si}_3\text{N}_4$  Silicon Nitride

$\text{SiO}_2$  Silicon Dioxide

STA Surface treated annealing

STEVAL–MKI180V1 An adapter board for LIS3DHH accelerometer

$T_0$  Initial Temperature

$T_{ref}$  Reference Temperature

$t_{sub}$  Thickness of the substrate

TBI Traumatic Brain Injury

TCD Transcranial doppler

TEM Transmission Electron Microscope

Ti Titanium

$t$  Time period

$u_m$  Membrane displacement

$u_v$  Input velocity

$u$  Prescribed displacement

VA Ventriculoarterial

VPL Ventriculopleural

VP Ventriculoperitoneal

X-FEM Extended Finite Element Modeling

XFEM Extended Finite-Element Method

ZnO Zinc Oxide



# Chapter 1

## Introduction

A traumatic brain injury (TBI) or other neurological conditions can cause an intracranial pressure (ICP) elevation inside the brain. The elevation of ICP is a life-threatening condition that can cause brainstem compression, and poor blood circulation [1]. If left untreated, the chronic ICP elevation can cause brain damage or death. The causes of ICP elevation can be linked to severe disorders in the circulation of cerebrospinal fluid (CSF), meningitis inflammation, obstructive hydrocephalus, intracranial hematoma, intracranial mass lesions, abscess in subdural and extradural empyema, high blood pressure, stroke, aneurysm, venous sinus thromboses, hypervitaminosis, and tumor growth [2]. The clinical suspicion of elevated ICP presents with several signs and symptoms such as a headache, blurred vision, vomiting, altered behavioural changes, weakness with moving or talking, fatigue, sleep apnea, etc. [2]. The diagnosis of ICP elevation involves the knowledge of a patient's history, physical examination and fundoscopic exam that reveals the status of ICP elevation. Imaging the anatomy of the head and the brain using computed tomography (CT) and magnetic resource imaging (MRI) can also reveal the signs of elevated ICP via enlarged ventricles, herniation, abscesses, tumours, etc. [2]. The treatment can include the prescription of drugs for aiding in

the reduction of brain swelling. In the case of TBI, decompressive craniotomy is an operation to remove a part of the bone flap of the skull to access the brain [3].

The initial treatment and management of ICP elevation includes a surgical procedure that introduces a needle into subarachnoid spaces of the brain. An external manometer connected to the needle measures the fluid pressure [2]. A measurement above 15 mmHg is an indication of elevated ICP. This follows lumbar puncture (LP) in the presence of raised ICP, which is also a surgical procedure involving CSF drainage from the spinal cord for diagnostic testing [4]. For continuous monitoring of ICP, a catheter is inserted along with a shunt into the skull to monitor ICP simultaneously and drain excessive CSF. Some of the procedures of CSF shunting include (1) Ventricular catheter, a technique that allows direct drainage of CSF from the lateral ventricles [5], (2) Ventriculoperitoneal (VP) shunt along with an ICP catheter for draining the excess CSF into the peritoneal cavity (Fig. 1.1) [6], (3) Ventriculoarterial (VA) shunt that allows drainage of excessive CSF from the ventricle into right atrium of the heart [7], (4) Ventriculopleural (VPL) shunt that helps in draining excessive CSF from the ventricle into the pleural cavity [8], (5) Lumbo-peritoneal (LP) shunt that allows removing excessive CSF from the lumbar spine into the peritoneal cavity [9].

However, the insertion of a catheter or a shunt is an invasive procedure that introduces vulnerability to infection. Furthermore, shunts frequently fail within the first two years of installation. The mechanical failure of the shunt can obscure the actual values of ICP. For example, the failure rates of VP shunt have been estimated at approximately 11 % to 25 % [10]. Similarly, meningitis inflammation is always associated with continuous ventricular fluid drainage with an incidence rate of 4 % to 10 % [11]. Another complication associated with the insertion of LP shunts is the obstruction of CSF; up to 50 % in the first year [11]. Infections can also spread several months after the insertion of a cerebral shunt. These infections include gram-positive bacteria (e.g., *Streptococcus aureus*, *Enterococcus* spp, etc.) and gram-negative bacteria (e.g., *Pseudomonas aeruginosa*, *Escherichia Coli*, etc.) and

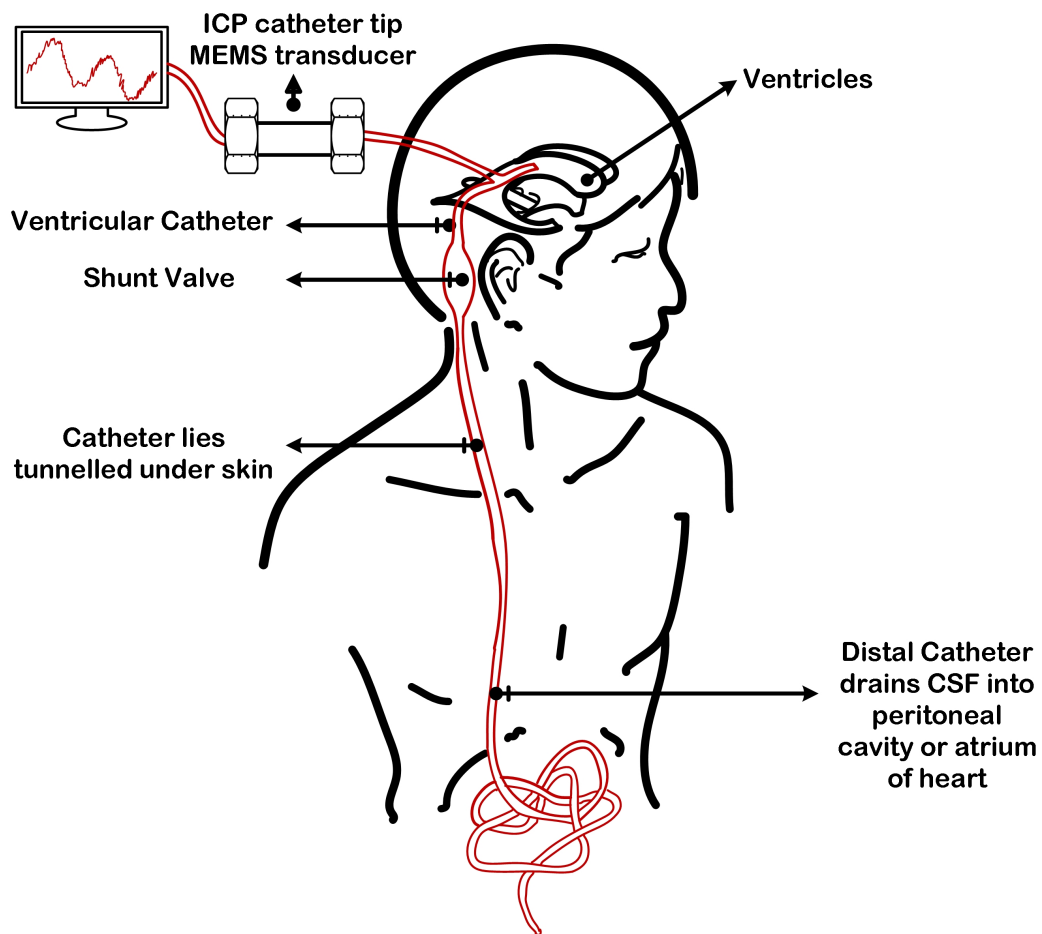


Figure 1.1 The conceptual diagram of ventriculoperitoneal (VP) shunt along with ICP monitor

account for 15 % of shunt-related infections [12]. When the shunt comes in contact with normal skin flora post-surgery, the shunt is contaminated due to wound infection. These infections can spread through the brain and are responsible for 40 % to 60 % of shunt-related infections [13].

In general, the symptoms of shunt-related infections include a headache, nausea, vomiting, inflammation across the shunt implantation site, fever, seizure, etc. Additional infections can depend on the patient's age, type of shunt, and placement site. The outcome of the shunt-related infections is the elevation of ICP. So how do we decide whether there is an actual rise in ICP? Is the elevation of ICP clinically relevant? Or it is because of the shunt-related failures?

In principle, the risk of infection or shunt failures would be overcome by a fully implantable pressure monitoring system [14]. At the very least, a fully implantable pressure sensor can be used as a standby device to measure ICP when the shunt fails to read the correct ICP values. In addition, it can advise the malfunction of the shunt [15]. An implantable pressure monitoring system can be fabricated using micro-electro-mechanical system (MEMS) technology. In general, a MEMS implantable pressure sensor will rely on a flexible thin film membrane and sealed cavity as part of the pressure sensor as shown in Figure 1.13 and will interfere with a corrosive fluid (saline/blood) at a temperature of approximately 37 °C. The advantages of MEMS technology are that it can help in forming flexible membranes into small form factors and create complex structures that can be easily integrated with signal conditioning electronics and implanted within the human body.

The process techniques of MEMS technology are derived from the semiconductor integrated circuit fabrication process. Since the IC manufacturing is a batch fabrication technology, MEMS devices can also be manufactured using a batch fabrication process that reduces the cost of manufacturing and lead time to market [16]. In addition, the feature size of MEMS devices 2 μm to 100 μm are compatible with the sizes of living cells and physiological structures of the human body [17].

In the last few decades, MEMS pressure sensors have been extensively used in non-invasive medical monitoring including respiratory gear, blood pressure cuffs, blood glucose monitoring, and heart rate monitoring. The global market value of MEMS devices in medical applications was valued at USD 1.8 billion in 2012 and is expected to grow at a CAGR of 20.2 % to reach a value of USD 6.5 billion by 2019. MEMS pressure sensors alone were valued at USD 486.0 million in 2012 and are growing at CAGR of 18.7 % between the years 2013 and 2019 (<https://www.transparencymarketresearch.com/mems-medical-applications.html>).

However, the accuracy, particularly in terms of the sensor drift over long durations, is of crucial concern. Drift is often attributed to the underlying physics of the thin film materials

(material aging, mechanical fatigue) used in the MEMS fabrication. Thus, the design of MEMS implantable pressure sensors must carefully consider the following in the initial design phase: (1) The design optimization of the thin film membrane (which is the sensitive part of the sensor); (2) The structural and fatigue behaviour of the micromechanical parts of the sensor [14].

The thin film deflection and fatigue study can be conducted in four different ways: (1) By choosing mechanically stable and biocompatible materials suitable for the application, (2) By optimizing the overall size and shape of the thin-film membrane, (3) Integrating finite-element model (FEM) to thin film study using Multiphysics finite-element analysis (FEA), (4) Experimentally validating the FEM of thin film deflection and fatigue behaviour.

## 1.1 Background

The ventricles of the brain are a set of communicating system cavities within the brain (<https://teachmeanatomy.info/neuro/vessels/ventricles/>). They are series of connected hollow spaces responsible for the production, transportation, and reabsorption of CSF. The ventricular system comprises two lateral ventricles, the third ventricle, the cerebral aqueduct, and a fourth ventricle (Fig. 1.2). The choroid plexuses are a network of capillaries and specialized ependymal cells found in the lateral ventricles. The ependymal cells (that enclose the choroid plexus) filter the water and the other substances from the blood capillaries and transport them to the ependymal layers inside the cerebral ventricles. The filtered fluid (containing sodium, potassium, glucose, and proteins) fills the spaces of the ventricles, the central canal of the spinal cord, and the subarachnoid space of the meninges [18].

The main function of CSF is to provide nutrition to the brain, remove the byproducts of metabolism and protect the brain and spinal cord from traumatic injury. CSF acts as a

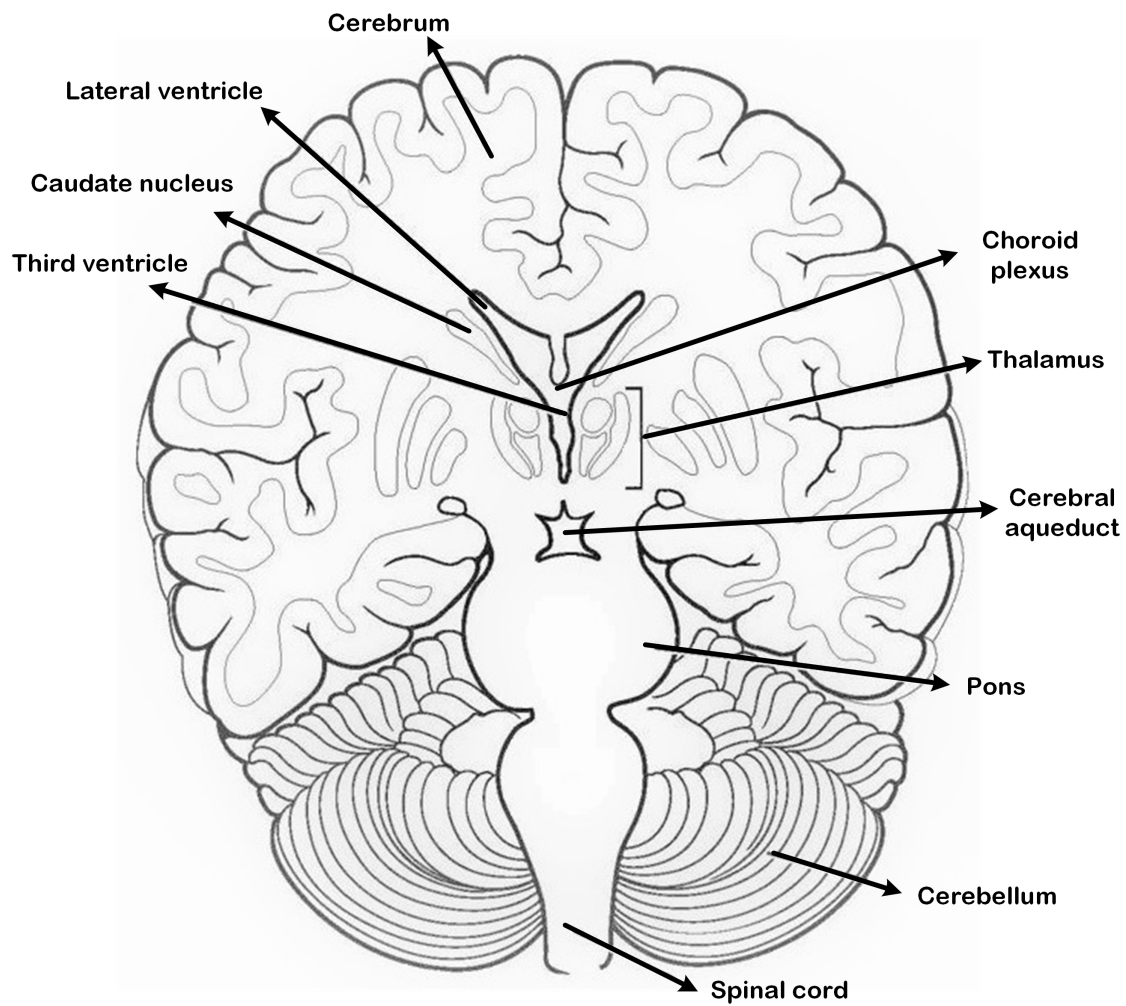


Figure 1.2 The Coronal section of the brain at the level of the thalamus showing the Ventricles, Cerebellum, Spinal cord, etc.

biomarker in the diagnosis of many neurological disorders. The samples of CSF are obtained from the subarachnoid space through a procedure called the lumbar and cisternal puncture.

Fig. 1.3 (Taken from <http://antranik.org/protection-for-the-brain-meninges-csf-blood-brain-barrier/>)

shows the CSF circulation pathway inside the brain (the flow direction is signified with black arrows). The CSF is produced by the choroid plexus in the lateral ventricle and flows into the third ventricle via intraventricular foramen. After that, it passes into the fourth ventricle via the cerebral aqueduct (aqueduct of Sylvius). From the fourth ventricle, it passes into subarachnoid spaces surrounding the brain and spinal cord. It is reabsorbed into the blood-

stream in the superior sagittal sinus (arachnoid villi), which acts as a unidirectional valve. The function of arachnoid villi is to allow the CSF to absorb into the bloodstream only when the CSF pressure becomes greater than the venous pressure (pressure within sinuses). In a healthy adult, around 500 mL of CSF is produced each day, and the reabsorption rate is up to six times the normal rate of CSF formation. Often an injury to the brain obstructs the CSF absorption; examples include the blockage of fluid due to inflammation or thrombosis of sinuses in the subarachnoid spaces. Consequently, CSF pressure increases developing into hydrocephalus [19].

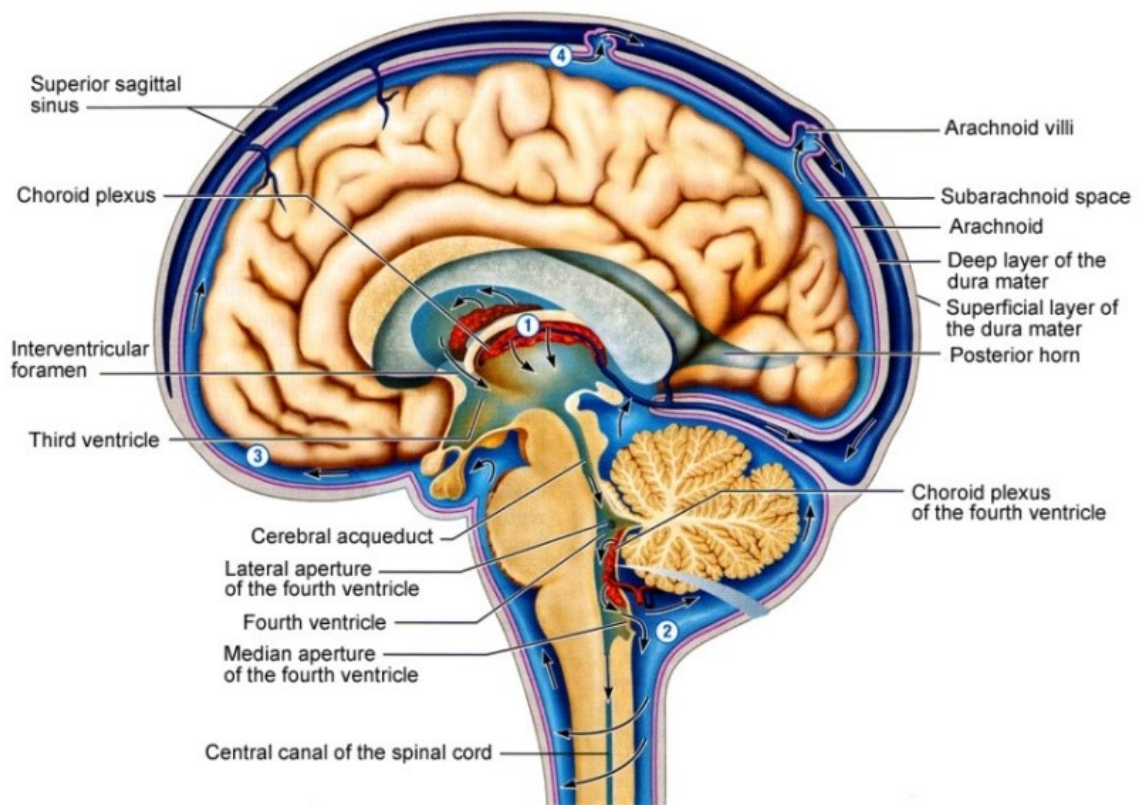


Figure 1.3 A conceptual diagram depicting CSF flow inside fluid-filled ventricles of the brain [20]

According to the Monro-Kellie hypothesis [21], the sum of the intracranial volumes such as the brain, the blood, and the CSF is nearly constant. An increase in one of these volumes must be offset by an equal depreciation of the other (Fig. 1.4a). Cerebral autoregulation is

the brain's hemostatic ability, to maintain constant cerebral blood flow (CBF) over a range of blood pressure despite a change in cerebral perfusion pressure (CPP). The cerebrovascular resistance (CVR) associated with CPP helps in determining CBF. Table 1.1 shows the threshold limits of cerebral auto-regulation in a healthy individual.

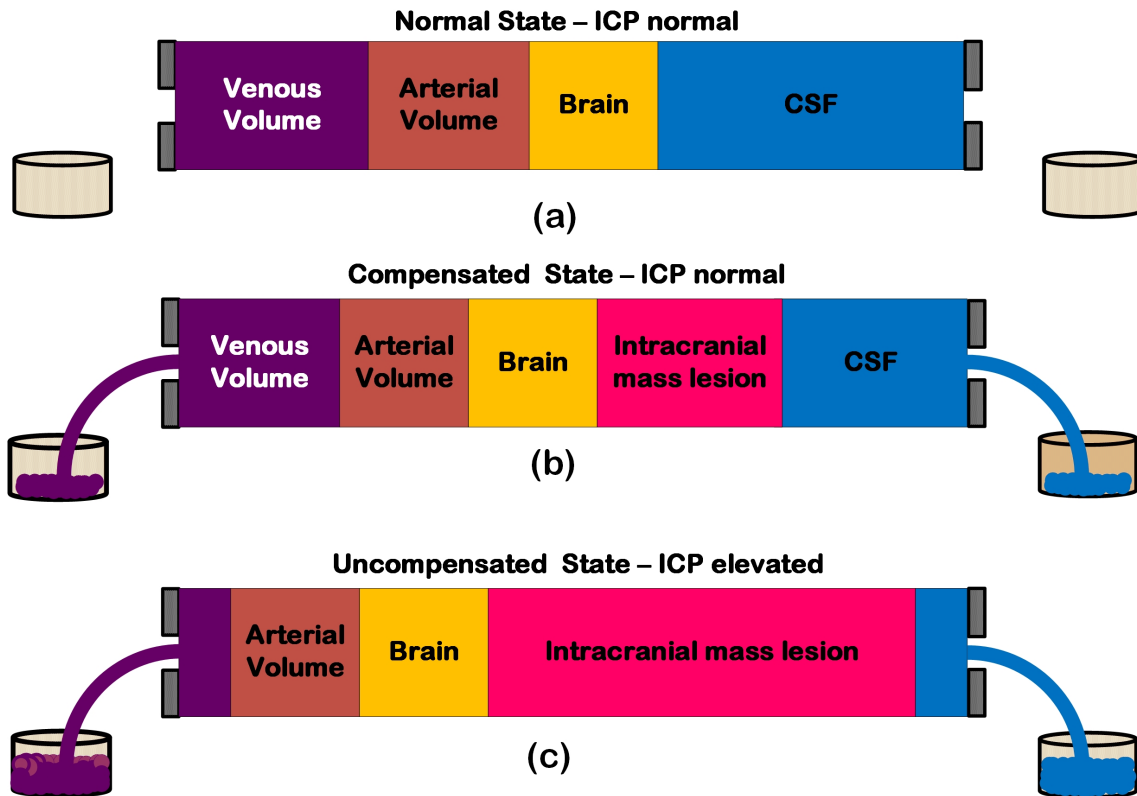


Figure 1.4 The conceptual diagram of Monro-Kellie hypothesis

Table 1.1 Threshold limits of cerebral auto-regulation [22]

Auto-regulation Parameter	Threshold Range
Mean Arterial Pressure (MAP)	80 mmHg to 100 mmHg
Intracranial Pressure (ICP)	5 mmHg to 15 mmHg
Cerebral Perfusion Pressure (CPP)	75 mmHg to 90 mmHg
Cerebral Blood Flow (CBF)	50 mL of blood per 100 g of brain tissue per minute

For example, if a tumour (brain lesion) abnormally grows on a brain tissue due to traumatic injury, brain cell death, or hydrocephalus, vasodilation (a mechanism that helps in dilating the blood vessels) helps in maintaining the cerebral autoregulation [23]. This state is termed as a compensated state of ICP (Fig. 1.4b). However, when CPP drops 60 mmHg, cerebral autoregulation will be compromised making CBF linearly dependent on mean arterial pressure (MAP) and intracranial pressure (ICP) (Fig. 1.4c).

Fig. 1.5 shows the effect of MAP and ICP on CBF in uncompensated cerebral autoregulation of the brain. CPP is defined as the difference between MAP and ICP; while ICP is the pressure inside the rigid skull, MAP forces the blood into the cranial cavity, which in turn perfuses the blood vessels and arteries inside the brain in the intracranial compartment [2]. For example, if MAP is 100 mmHg and ICP is 10 mmHg in a healthy individual, then CPP will be around 90 mmHg.

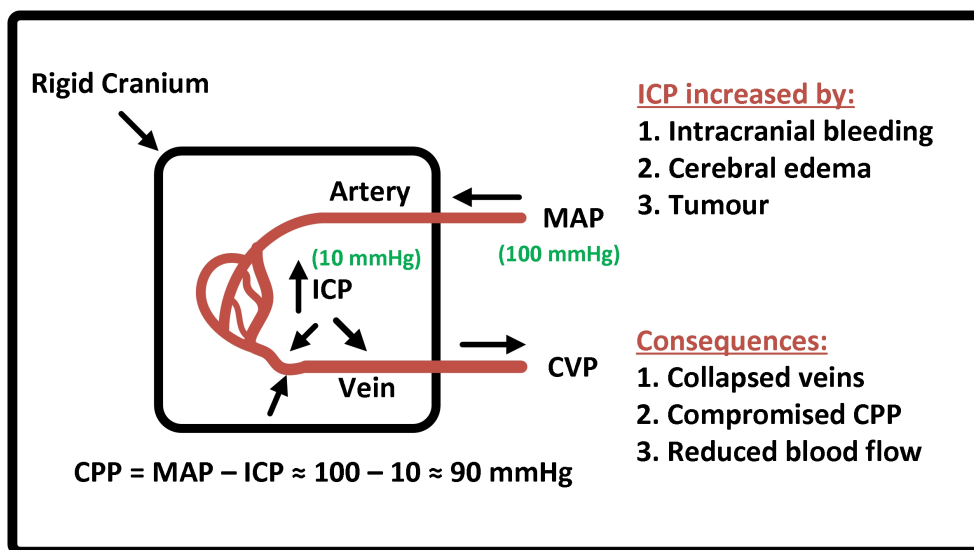


Figure 1.5 The effect of MAP and ICP on CBF

### 1.1.1 Hydrocephalus

Hydrocephalus is a neurological condition that occurs due to the excessive accumulation of CSF inside the brain [24, 25]. This condition can cause abnormal widening of ventricle spaces inside the brain that can subject the tissues to harmful pressure. One in every thousand is born with hydrocephalus, making it very common like down syndrome, spina bifida, and brain tumours (<https://www.hydroassoc.org/about-us/newsroom/facts-and-stats-2/>). It is estimated that around 700,000 Americans are fighting with normal hydrocephalus in the United States (US) alone (<https://www.hydroassoc.org/hydrocephalus/>).

The major classifications of hydrocephalus include (1) congenital, which forms at the birth potentially due to infection during the fetal development [26], (2) acquired, which develops from various infections such as meningitis, intracranial bleeding, traumatic brain injury (TBI), or tumour growth [27], (3) normal-pressure (NPH) which arises from aging-related dementia in elderly patients [28], (4) Ex-vacuo, which ensues after a stroke [29]. In addition, the other classifications include (1) communicating and (2) non-communicating hydrocephalus. While communicating hydrocephalus occurs due to the blockage of CSF just outside the ventricle, non-communicating arises due to the obstruction of CSF in narrow passages connecting the ventricles [30].

The symptoms of hydrocephalus that affect infants and young adults include headaches, muscle spasms, loss of coordination, nausea, seizures, lack of concentration, personality changes, and high-pitched cries. Similarly, the symptoms in middle-aged adults include chronic headaches, loss of coordination, difficulty walking, bladder problems, poor memory, blurred vision, and lack of concentration. In the case of NPH, the symptoms begin slowly and worsen after the age of 60 by impairing the mental ability, visual senses, uncontrollable passage of urine and stools, etc. (<https://www.ninds.nih.gov/Disorders/Patient-Caregiver-Education/Fact-Sheets/Hydrocephalus-Fact-Sheet>)

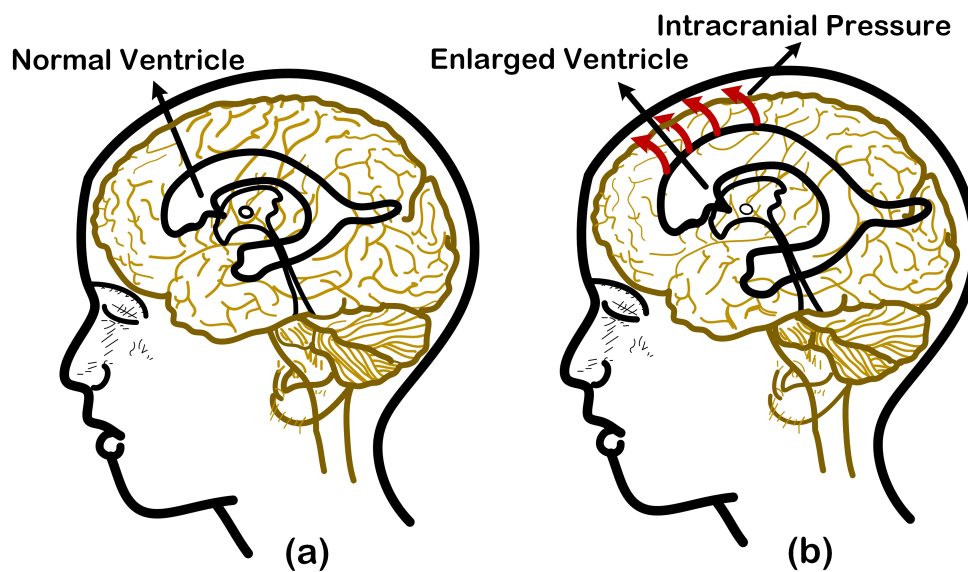


Figure 1.6 The conceptual diagram showing the (a) normal ventricle and (b) enlarged ventricle

Hydrocephalus is diagnosed using an ultrasound test, which involves high-frequency sound waves to create the structural images of the brain, magnetic resource imaging (MRI), which uses magnetic field and radio waves to make cross-sectional representation of the brain, computerized tomography (CT) scan that uses several X-rays to form a cross-sectional image of the brain [31].

### 1.1.2 Hydrocephalus Treatment

Hippocrates first described hydrocephalus between the year 466 BC to 377 BC, which was later elaborated by Vesalius in the year 1555. The term 'enlarged ventricle' was first described after Vesalius encountered a particular case, where a 2-year-old died with an enlarged head. Le Cat performed the first ventricular puncture for continued CSF drainage in the year 1744. Even though the initial attempts were futile, the following approaches involving CSF drainage from the ventricles into subcutaneous tissues, subdural spaces, temporal sinus, sagittal sinus, and peritoneal cavity were successful. In 1905, the first attempt was made to drain CSF from

the lateral ventricle into the peritoneal cavity. However, this resulted in a casualty due to over-drainage. This approach has been improved to form the basis of current CSF drainage [11]

Some of the examples of this approach include the insertion of VP, VA, VPL, and intraventricular catheter shunts into the ventricles to drain CSF. In the US alone, the annual incidence of VP shunt placement is 5.5 per 100,000 with approximately 30,000 procedures performed each year amounting to US\$ 95 million. However, they frequently fail or block (e.g., in children they block about 50 % of the time within the first two years of installation), requiring multiple shunt revisions.

The most common shunt systems and their functions are show in the Table 1.2.

Table 1.2 The most common types of shunt systems. (Available at: <https://www.hydroassoc.org/shunt-systems/>)

Shunt type	CSF source location	CSF drainage location
VP	Ventricle	Peritoneal cavity
VA	Ventricle	Right atrium of the heart
VPL	Ventricle	Pleural cavity
LP	Lumbar spine	Peritoneal cavity

In general, a shunt comprises of three main components [32].

1. **A proximal catheter:** A catheter or tube that drains the excessive CSF from the ventricular or the spinal lumbar sac.
2. **A valve:** A device that controls the CSF flow rate.
3. **A distal catheter:** A catheter or tube at the end that is placed inside the peritoneal (abdominal), heart or pleural cavity for draining the CSF.

4. **Additional add-ons:** Antechambers, anti-siphon devices, flow compensating devices, programmable valves

The primary function of a ventricular shunt is to control the elevation of ICP by draining the CSF from ventricles into the peritoneal cavity. Alternatively, CSF can be drained into an external bag connected to the end of distal catheters [33]. With the process of ventricular CSF drainage, ICP is monitored using catheter-based pressure transducers inserted into the patient's line. During ICP measurements, the CSF drainage must be temporarily stopped. These transducers allow temporal measurement of ICP with a precondition to stop the CSF drainage temporarily. ICP can be recorded while the patient is awake, asleep, lying down, sitting, or standing [34].

The insertion of the shunt is a surgical procedure involving drilling a burr hole placing the catheter into the ventricles. During the process, the patient is made to lie down with head elevated at 45 °C in a supine position. In general, a burr hole is drilled at Kocher's point to avoid superior sagittal sinus and frontal cortex motor strip [35].

### 1.1.3 The Underlying Issues of a CSF Shunt

The potential for infection due to the insertion of the shunt and ICP catheter is one of the major complications in neurological interventions. Inadequacies in the sterile technique and improper handling of the shunt system can contaminate the shunts with skin flora. Moreover, the infection can worsen due to the bacterial adhesion and colonization arising from the silicone elastomer. Most infections emanate immediately after the shunt is exposed to the environment and the symptoms present after 2 months to 3 months. In some instances, shunt infections are manifested with the formation of overt meningitis syndrome and, in others, the presentations are subtle and worsen gradually. While intravenous (IV) antibiotics can

be used to sterilize the inner surfaces of the shunt to promote the surface resistance to the bacterial growth, re-infection occurs after antibiotics are discontinued [11].

Besides, CSF shunts frequently fail in the first two years of installation. Failures are mostly linked to mechanical faults in the distal end of the shunt catheters; shunt disconnections; abdominal complications, etc. The debris of the mechanical parts tends to stay inside the human body and can obstruct the normal functioning of various organs such as bowel, stomach, and liver. The failure rates include infections and occlusion, and blockage [36]. The overall incidence of the shunt failure in the first year of insertion is 40 % and 50 % in the second year. Shunt blockage can occur at any time and usually presents an elevation in ICP. The presentation is age dependent, and infants suffer from nausea, vomiting, irritability, and enlargement of fontanel. The most common sites for shunt blockage are the ventricular catheter tip (obstructed by the growth of choroid plexus) and shunt valve (lumen blocked by blood and tissue debris). In a retrospective study involving 1015 patients treated with a VP shunt, most of the revisions were in the first six months of the shunt placement [37]. Similarly, in another study investigating the risk of VP shunts for an eight-year period, a total of 143 shunt revisions were necessary for 95 patients comprising 43 males and 52 females) [38].

Some of the signs of the shunt malfunction are headaches, vomiting, lethargy, irritability, seizures, confusion, blurred vision, swelling across the shunt tract, and raised ICP [39]. So how do we decide whether there is an actual rise in the ICP? Has the shunt failed? Or has an infection due to the shunt insertion altered the value?

#### **1.1.4 Intracranial Pressure (ICP)**

ICP is the total pressure inside the skull, which is exerted by intracranial volumes such as the brain, the blood, and the CSF. In other words, ICP is a resultant of the interaction between

the brain, CSF and blood flow inside the brain [40]. The value of ICP varies with the age, position and nature of the neurological condition [41]. In a healthy individual ICP typically ranges between 5 mmHg to 15 mmHg and changes with the cardiac and respiratory cycles. In children, the normal values of ICP range between 3 mmHg to 7 mmHg and in infants, it varies between 1.5 mmHg to 6 mmHg. An individual with ICP values greater than 20 mmHg needs treatment; values greater than 40 mmHg indicate life-threatening intracranial hypertension [42].

ICP varies with position and oscillates with the cardiac and respiration cycles. For example, when expiring against a closed glottis (Valsalva manoeuvre), particularly during coughing and defecating, intrathoracic pressure vacillates, which will affect jugular veins, epidural venous plexus, cardiac output, arterial pressure, and heart rate. The elevated venous pressure is spread to the intracranial vault space, culminating in a corresponding elevation in ICP (Figure 1.7c). [43].

The underlying dynamics of ICP are complex; several patterns of ICP waveform have been depicted. ICP has three components: (1) percussion wave formed from the systolic pressure transmitted to the choroid plexus, where CSF is produced, (2) elastance wave developed due to the rigid cranium and its effect on the ventricular expansion, (3) dicrotic wave generated by the closure of the aortic valve. Figure 1.7 shows various components of the ICP waveform including P1 representing percussion wave, P2 signifying brain's compliance or elastance, and P3 signifying closure of aortic wave. Under normal conditions, P1 is always greater than P2 indicating the normal compliant brain. In the case of brain injury, the compliance of the brain starts degrading resulting in P2 becoming greater than P1. This phenomenon, where  $P2 > P1$ , is termed 'disturbed intracranial elastance'. This means that a small increase in the intracranial volume would significantly increase the ICP [44].

Therefore, ICP monitoring provides accurate information on the intracranial dynamics and brain elastance from the waveform assessment. The information that can be derived from

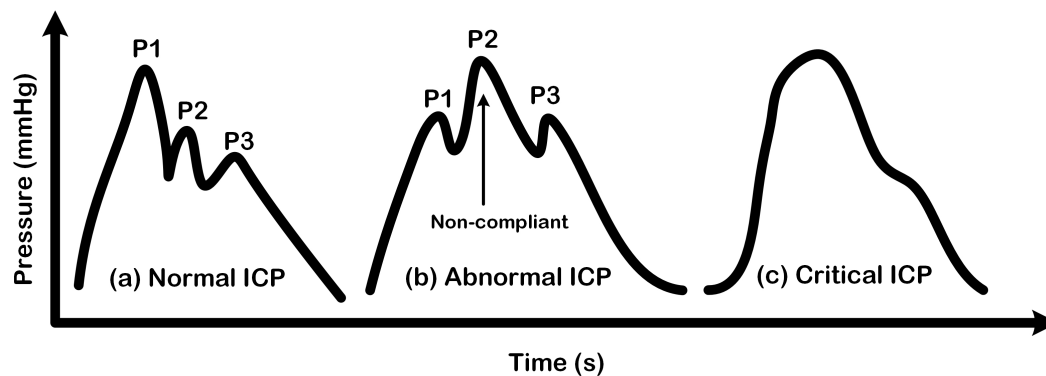


Figure 1.7 The ICP waveform showing the nature of peaks (P1-Systolic pressure; P2-Elastance; P3-Aortic Valve) (a) Normal ICP; (b) Abnormal ICP; (c) Critically ICP

ICP waveform includes cerebral perfusion pressure (CPP), regulation of CBF, and cerebral blood volume (CBV) and vasogenic events [45].

With the elevation of ICP, the compliance of the brain is compromised, leading to vasodilation cascade, increased CBV and swollen brain. The low compensatory intracranial volume causes several vasogenic events that will show up like waves in the ICP waveform. Lundberg classified these pathological waves into plateau (A), B, and C waves as shown in Figure 1.8. Plateau waves signify the standard conditions of a non-compliant brain or reduced elastance and occur for a period of 5 min to 10 min with an amplitude of 50 mmHg to 100 mmHg. B waves are sharply peaked fluctuations that happen for a brief period of 1 min to 2 min and represents rhythmic oscillations. These waves tend to increase in a crescendo manner from a variable baseline to an amplitude of about 20 mmHg to 30 mmHg and reflect vasomotor changes inside the brain. C waves represent fluctuations of baroreceptor and chemoreceptor reflexes and may have no clinical significance as they are found in both healthy individuals and patients.

ICP monitoring is useful in various neurosurgical and neurological conditions such as stroke, brain injury, intracranial hematoma, meningitis, acute liver failure, hydrocephalus, craniosynostosis, benign intracranial hypertension, etc. In hydrocephalus, accurate monitoring of ICP

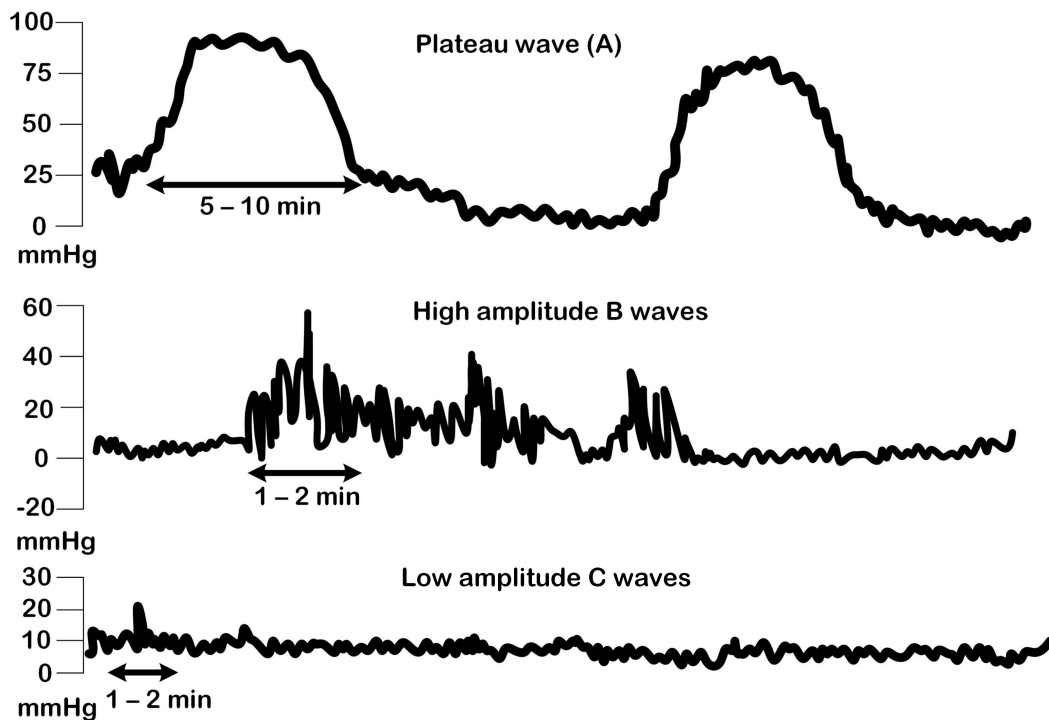


Figure 1.8 Lundberg ICP wave - Plateau wave (A), High amplitude B waves, and Low amplitude C waves [46]

is necessary for a CSF drainage-based diagnosis and subsequent monitoring of the shunt malfunction.

### *Acute ICP Monitoring*

ICP elevation has been closely linked with poor clinical outcomes after brain injury, neurotrauma, intracerebral hemorrhage, and intracranial hematoma. Acute ICP monitoring of patients, particularly after neurosurgery involving tumour removal, repair of blood vessels, etc., can be made, in general, either directly from the brain's parenchyma or ventricles or indirectly through secondary markers of the brain's pressure. Some of the indirect (non-invasive) ICP monitoring approaches include the transcranial doppler (TCD), which assists in measuring the velocity of CBF in the tissues by calculating the associated changes in the ultrasound frequencies. ICP can be deduced from the TCD velocities and mean arterial

pressure (MAP). However, the ICP measurement using an indirect approach is cumbersome. Direct measurements of ICP from the brain's parenchyma, epidural, subdural or subarachnoid spaces using a catheter tip transducer is valuable neurological armamentarium.

The direct measurements of ICP can be made from several intracranial sites as shown in Figure 1.9. Currently, ventricular catheters are the gold standard for ICP monitoring and are placed into the right sided lateral ventricles (non-dominant hemisphere). In general, a ventricular catheter allows fluid-based ICP monitoring by creating an equilibrium between the pressure in the catheter and intraventricular pressure. The pressure measurement is made through strain-gauges. However, ventricular catheters are associated with higher risk of infection, intracranial hemorrhage and seizures. Besides, insertion of catheters into ventricles can cause discomfort to the patients and may be subject to the risk of intracranial haemorrhage [47]. While using ventricular catheters, the rule of thumb is to temporarily stop CSF drainage during ICP measurement. The CSF drainage is stopped every 30 min to 60 min for a brief period of 5 min to 10 min to allow ICP transduction using the MEMS solid-state sensor. CSF must be assessed everyday for white blood count, protein, glucose and bacterial cultures. To mitigate the problem of infection, antimicrobial-impregnated catheters like VentriClear™ II [48], can be used in the ventricular ICP monitoring. VentriClear™ II includes a clear silicon tubing with impregnated antimicrobial agents such as minocycline and rifampin that reduces bacterial colonization. Even though they showed a significant reduction in the amount of viable infection [49], larger group studies may be needed to validate their clinical relevance. Alternatively, ICP can be measured using MEMS micro-transducer tipped catheters using strain gauges, pneumatic or fibre-optic sensing techniques. These micro-transducer tips can be placed directly into the brain's parenchyma by twist drilling a burr hole. Even though these transducers offer a lower infection rate, they are associated with a significant amount of zero drift and require an ideal replacement within five days of installation. Alternative placement sites to the parenchyma include subdural, epidural or subarachnoid spaces fitted

with screws and bolts. However, these placement sites are not as accurate as compared to the brain parenchyma. The primary locations for the placement of ICP monitors are shown in Figure 1.9. The placement of the ICP catheter sensor depends on the specific type of the pressure transduction technique.

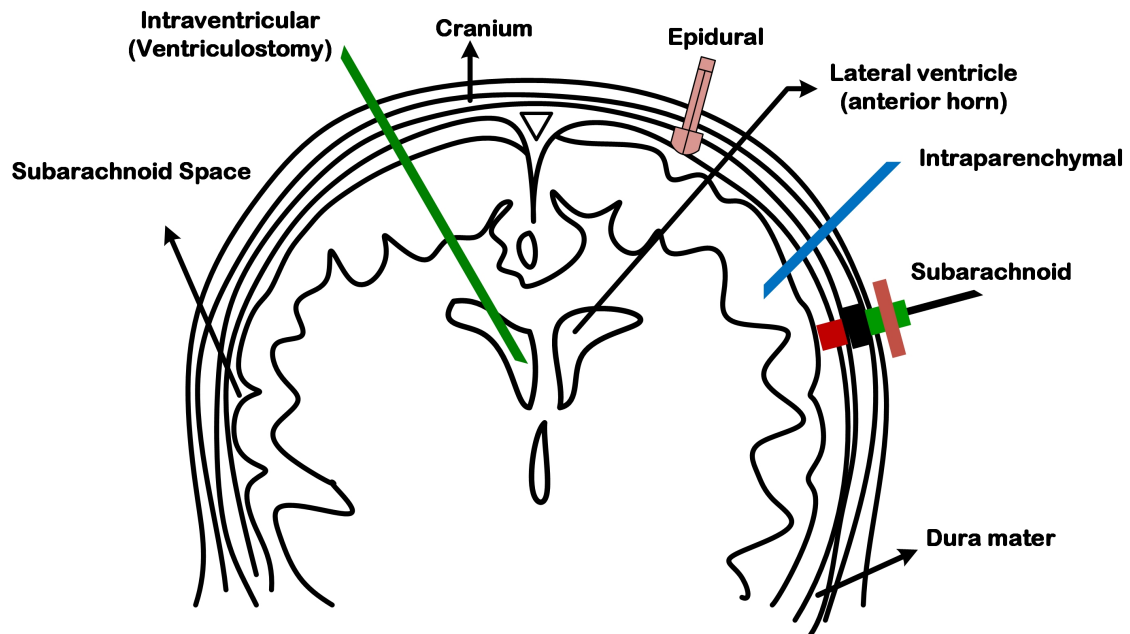


Figure 1.9 The anatomic sites for ICP monitoring: Epidural, subdural, intraparenchymal, intraventricular, lumbar subarachnoid

The pressure transduction techniques include the (1) Pneumatic method, which comprises an air filled balloon attached at the distal end of the catheter tube, (2) Starin-gauge based micro-transducers, which comprise a flexible thin film diaphragm (membrane) that will induce resistance changes relative to the pressure load, (3) Fibre-optic sensors, which include differences in the light intensity due to a flexible mirror [47]. Examples of pneumatic sensors include a Spiegelberg KG pneumatic ICP catheter sensor from Aesculap, GmbH & Co. This sensor comprises an air-filled bag mounted at the tip of the catheter, which enables the ICP to diffuse through the airbag to the pressure transducer [50]. It is one of the most inexpensive options in the group of ICP monitors, but it is not suitable for baseline ICP pressure > 25 mmHg [51]. Similarly, examples of piezoelectric or piezoresistive strain gauge-based

ICP catheters include Codman Microsensor®(manufactured by Johnson & Johnson), and Neurovent-P ICP monitor (from Raumedic®systems). Fibre-optic ICP catheters (Figure 1.10) have many advantages, which include the miniaturization, negligible electromagnetic interference, and better remote monitoring and multiplexing. Several studies demonstrated that that fibre-optic catheters have no vulnerability to infections [52]. Some of the examples of fibre-optic pressure transducers include Camino ICP monitor, 420LP, and Samba sensors [53]. The Samba sensors drift at a rate of 0.45 mmHg per hour.

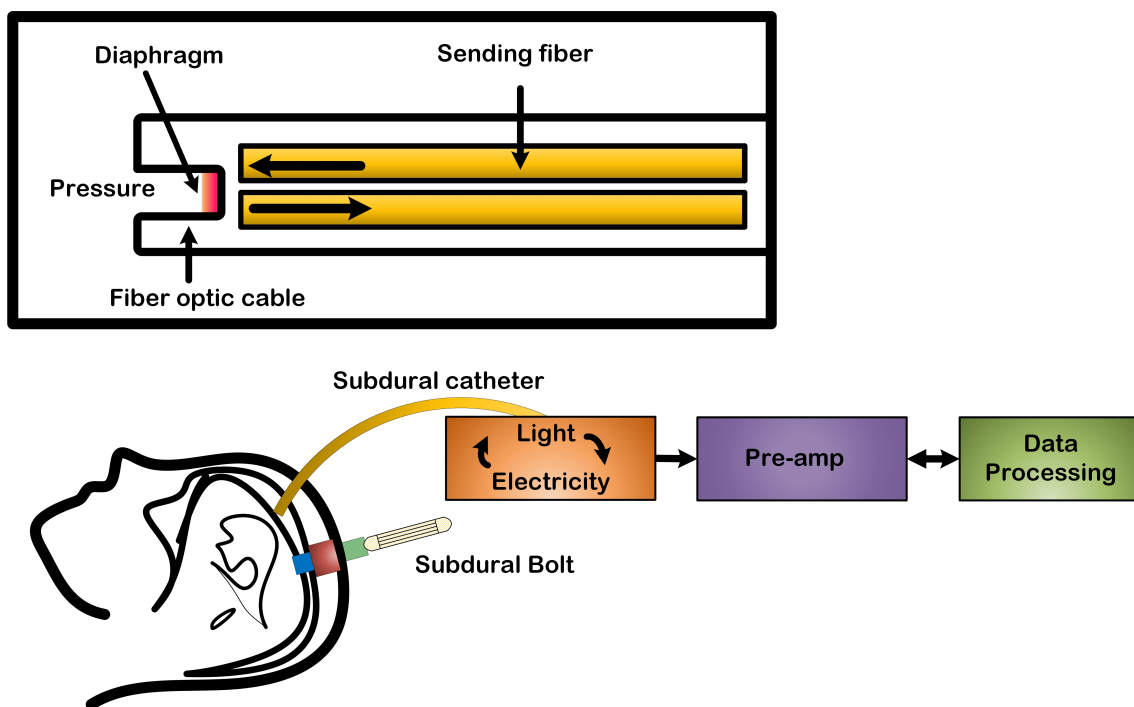


Figure 1.10 The conceptual diagram of fibre-optic catheter tip pressure transducer

Some of the commercially available catheter-based ICP monitors along with their placement positions and zero drift are listed in Table 1.3. They include, Camino®ICP monitoring kits, Codman Microsensor®, Neurovent-P and Neurodur ICP catheters from Raumedic systems®, Gaeltec®epidural sensor, fluid-filled catheters, silverline ventricular drainage catheter, and 420LP Samba ICP sensors.

Table 1.3 The classifications of commercially available ICP shunts/catheters

<b>Type of monitor</b>	<b>Placement site</b>	<b>Zero drift</b>
Camino bolt with transducer tipped catheter (Integra Life-sciences) [54]	Parenchymal or Subarachnoid space	First 24 hours: $\pm 2$ mmHg, next 4 days: $< \pm 1$ mmHg per day
Camino ICP monitoring catheter with Licox Bolt fitting. Available <a href="http://occ.integralife.com/">http://occ.integralife.com/</a>	Parenchyma with manual screw;	First 24 hours (maximum): $0 \pm 2$ mmHg, next 5 days: $< \pm 1$ mmHg per day [55]
Codman Microsensor®ICP transducer (Johnson & Johnson);	Parenchyma or Subdural space with manual button	$< \pm 5$ mmHg per 7 days
Neurovent-P ICP catheter (Raumedic Systems)	Parenchymal	3 mmHg per 3 days
Neurodur-P epidural ICP sensor (Raumedic Systems)	Epidural	0 mmHg
Ventrix®(Integra Life-sciences)	Ventricles	First 24 hours: $\pm 2$ mmHg, next 4 days: $< \pm 2$ mmHg per 2 days
Gaeltec®epidural ICP sensor (Gaeltec Devices ltd)	Epidural	1.5 mmHg per day
Fluid-filled transducers	Parenchyma	$< \pm 2$ mmHg for 8 hours
Silverline®Ventricular drainage catheter with cranial bolt (silver impregnated polyurethane) (Spiegelberg GmbH & Co.)	Lateral ventricles	Maximum drift after a period of 28 days is $\pm 3$ mmHg
420LP Samba ICP sensors (Harvard Apparatus)	Epidural	$\pm 0.45$ mmHg per hour

An alternative neurosurgery procedure is endoscopic third ventriculostomy (ETV) that helps in creating a bypass of the CSF inside the cranium without using a shunt or catheter. The fluid is bypassed using an endoscope through the thin membrane at the bottom of the third ventricle. Through this surgery, CSF flows over the surface of the brain and reabsorbs into the bloodstream. Even though ETV eliminates the shunt dependency with a success rate of 65 % to 75 %, it can aggravate ICP elevation and enlargement of ventricles in the case of the surgery failure.

### ***Chronic ICP Monitoring***

Neurological conditions such as hydrocephalus, post-traumatic hydrocephalus (PTH), and normal hydrocephalus (NPH) which are treated by ventricular shunts or ETV may require lifetime monitoring of ICP. The existing methods of ICP monitoring use invasive procedures of inserting a pressure transducer with external connections. Repeated use of percutaneous ICP sensors introduces vulnerability to infection and limits the measurement durations. Besides, ICP catheter tip transducers drift after five days demanding replacement of the catheter.

A fully implantable ICP sensor system would overcome the risk of infection and drift in a catheter tip transducer. Also, these fully implantable sensors can help in detecting the shunt failures that can display elevated ICP. However, the accuracy, particularly in terms of sensor drift over long durations, is a key concern. An implantable pressure monitoring system will rely on a flexible membrane as part of the pressure sensor and will interfere with a corrosive fluid (saline/blood) at a temperature of approximately 37 °C. The choice and success of a fully implantable pressure sensor depends on the ICP placement site and pressure measurement technique.

In the year 1967, a first fully implantable ICP sensor with radio telemetry was developed by Atkinson et al. that enabled absolute pressure measurements. This sensor was sensitive to fluctuations in the atmospheric (barometer) pressure and altitude. This laid a path for the future of biomedical implantation [56]. In contrast to absolute pressure measurement, Cosman et al. developed a differential pressure measurement ICP monitor with passive telemetry, for subdural ICP measurements. This device has a failure rate of 24 but can provide continuous ICP measurements for 14 months[57]. However, in general, subdural ICP measurements are less sensitive than ventricular ICP. Alternatively, ICP can also be measured from epidural spaces. For example, a capacitive sensor with a flexible thin film membrane has been designed for epidural ICP measurements. However, long-term accuracy studies involving 127 patients showed that the device could only survive in 13 patients for longer durations with a presented drift of 0.5 mmHg per week. Besides, the drawbacks of this device were drift due to the mechanical fatigue of the thin film membrane, leakage in the encapsulation, and packaging stress [58].

In contrast, telemetric ICP measurements can be made by implanting the sensor in the right frontal lobe via a surgical hole and be used as an inline pressure sensor along with a CSF shunt. As an example, a telemetric ICP sensor was developed by Nagano Keiki Seisakusyo Co. Ltd., Tokyo, [59]. The telesensor comprises passive wireless telemetry. Measurements made in 94 patients showed a typical zero drift of  $\pm 5$  mmHg to  $\pm 25$  mmHg per year [59].

A commercially successful fully implantable telemetric ICP sensor is Neurovent-P-tel, manufactured by Raumedic systems. This device can be implanted below the scalp of the cranial bone and ICP measurements can be made from the brain's parenchyma. The device is comprised of a catheter 1.76 mm thick and 25 mm long with a thin film membrane-based pressure sensor, radio-frequency transmission coil (TDT 1 readP), and battery-driven data-logger. ICP measurements can be switched between short and long play modes; An inbuilt acoustic alarm rings when ICP exceeds critical values [60]. A significant drift of  $\pm 1.6$  mmHg

over 24 months has been recorded by the manufacturers. However, when the device was actually implanted, it was subjected to a drift of  $\pm 2$  mmHg per 29 days [61].

Recently, there has been a significant rise in the usage of microwave and RF techniques in the biomedical industry. Prototypes of analogue wireless implantable monitoring devices operating at the industrial-scientific-medical (ISM) band of 2.4 GHz and digital ICP devices have been discussed by Xu Meng et al. In long term studies the AICP device provided data over a period of 45 days without any drift. For implementing a digital device, a commercially available MEMS capacitive sensor board (eZ430-RF2500T) was packaged with a MSP430 microcontroller and CC2500 low power wireless radio [62]. This sets a new precedent in manufacturing low-cost digital ICP sensors for long-term wireless monitoring.

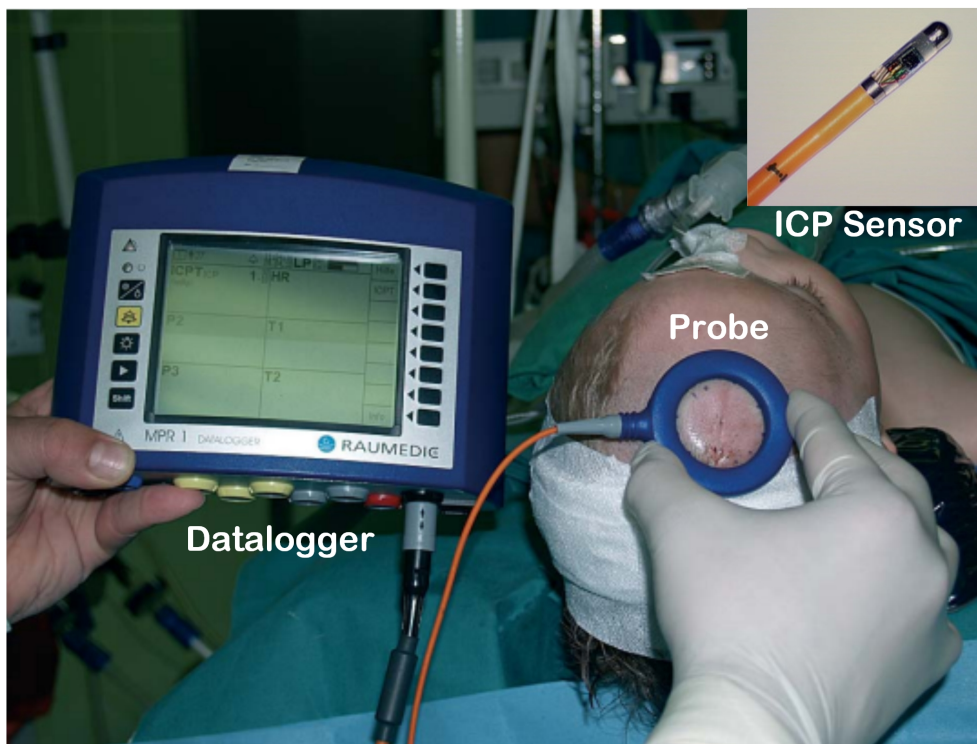


Figure 1.11 ICP monitoring using Neurovent-P telemetric ICP monitor from Raumedic systems [60]

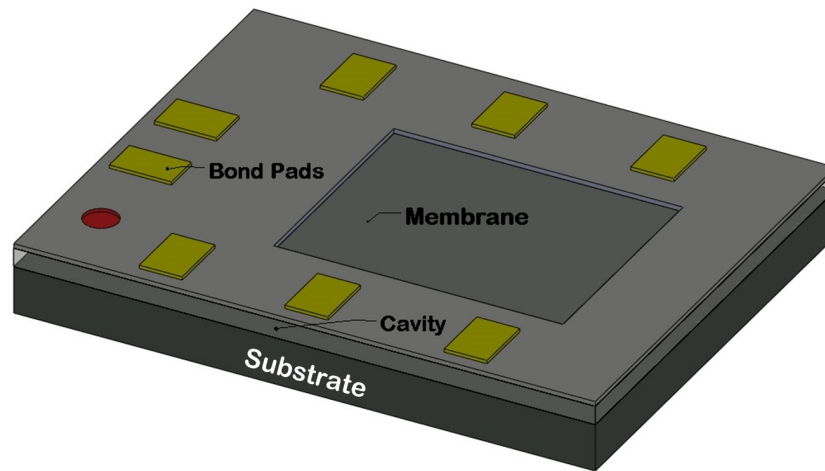


Figure 1.12 A 3D MEMS membrane based capacitive pressure sensor

### 1.1.5 Problem Statement

Even though, there has been significant progress in the design of fully implantable pressure sensors, the accuracy, particularly in terms of the sensor drift over longer durations, is a serious concern. An overwhelming majority of implantable pressure sensor systems rely on a simple design of flexible membrane and a sealed cavity as part of the pressure sensor, a wireless telemetry for transmission of the data and powering the device simultaneously, and other signal conditioning circuits for processing the data. A thin film membrane is normally exposed to the biological medium and interferes with corrosive fluid at 37 °C. When the membrane is subjected to a randomly varying fluid pressure load, it deflects and induces corresponding change in the capacitance. A MEMS membrane-based sealed cavity capacitive pressure sensor is shown in Figure 1.12 and a cross-sectional view of a MEMS membrane-based pressure sensor is shown in Figure 1.13.

The thin film membrane (pressure sensitive element) must be durable over longer durations as it can be subjected to randomly varying loads in its operational period. However, material aging and mechanical fatigue of thin film material can make the sensor vulnerable to drift. In long-term monitoring, the mechanical stiffness of thin film membrane deteriorates due

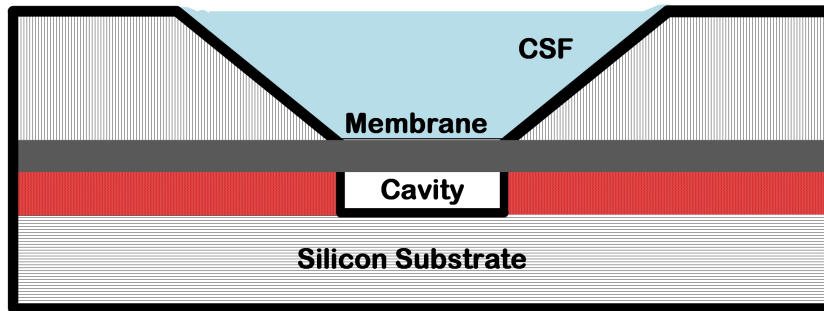


Figure 1.13 A cross-section of capacitive pressure sensor

to the attachment of cells or tissues. These attached debris can cause permanent fatigue of thin films. Besides, other interfering factors such as inelastic deformations, oxide growth on thin films, and sealed cavity effusions can cause more damage to thin film in long-term monitoring. Similarly, packaging the pressure sensor along with signal conditioning and telemetry is challenging, including interactions of biological mediums with implanted micro systems, biocompatibility, surgical placement location, etc.

The primary requisite of a fully implantable pressure sensor is to provide a stable and consistent response during its operational period. The signal disparities must be only due to ICP and not the other interfering factors. In general, long-term drift experienced by the sensor is classified as a signal or sensitivity drift. While signal drift occurs when a pressure measurement drifts to an undesirable value, a sensitivity drift is attributed to gradual reductions in the sensitivity of the sensor over a period. The primary source of drift is the material aging and mechanical fatigue of the materials used in the fabrication, particularly the thin films. Fatigue is a localized and permanent structural damage to the thin-film membranes subjected to varying loads. The stresses resulting from the varying loads can result in microcracks or fracture of the entire component [63]. Microcracks initiate because of plastic strain produced by the varying stresses. Even though the average stresses in biomedical applications are often low, the local stress concentrations contribute to mechanical fatigue failure. If thin film metal membranes are subjected to randomly varying pressure loads,

high-stress regions or stress risers can promote the crack formation and propagation until the final fracture [64]. Hence, it is important to introduce finite-element models (FEM) to study the thin film deflection and fatigue behaviour of thin membranes in the initial design phase.

### 1.1.6 Overview of the Proposed Research

The objective of this Ph.D. research is to (1) Develop FEM models and study the effect of thin-film deflection and fatigue behaviour on the long-term performance of MEMS membrane-based pressure sensors in the lifetime monitoring of ICP, (2) Experimentally validate the thin film deflection and fatigue behavior of thin film membrane based pressure sensors, and (3) Develop a conceptual framework for designing and fabricating MEMS capacitive pressure sensor for lifetime ICP monitoring.

Figure 1.14 depicts the flow of this Ph.D. research. The work starts with a data collection, which is related to ICP. It is necessary to study the nature and dynamics of ICP because of its complex physiology. In general, the fluctuations in the systolic blood pressure of the cardiac cycle and oscillations in respiration can cause corresponding changes in the blood flow. The changes can interfere with the behavior of ICP, particularly with intracranial haemorrhage, brain infection and injuries. On the other hand, gravitational forces and barometric pressure fluctuations mostly are the physiological interferences with physiological pressure. Therefore, a thorough literature study was involved in the initial design phase.

In the second phase, Multiphysics based FEM has been used to study the thin film deflection and fatigue behaviour. The study has been conducted in five different ways: (1) By choosing a mechanically stable and biocompatible material suitable for the brain; (2) By optimizing the overall dimensions of the thin film membrane and the pressure sensor; (3) By using solid mechanics Multiphysics models to study the thin film deflections, the behaviour of stresses and strains; (4) By using FEM multiaxial fatigue models to study the mechanical fatigue

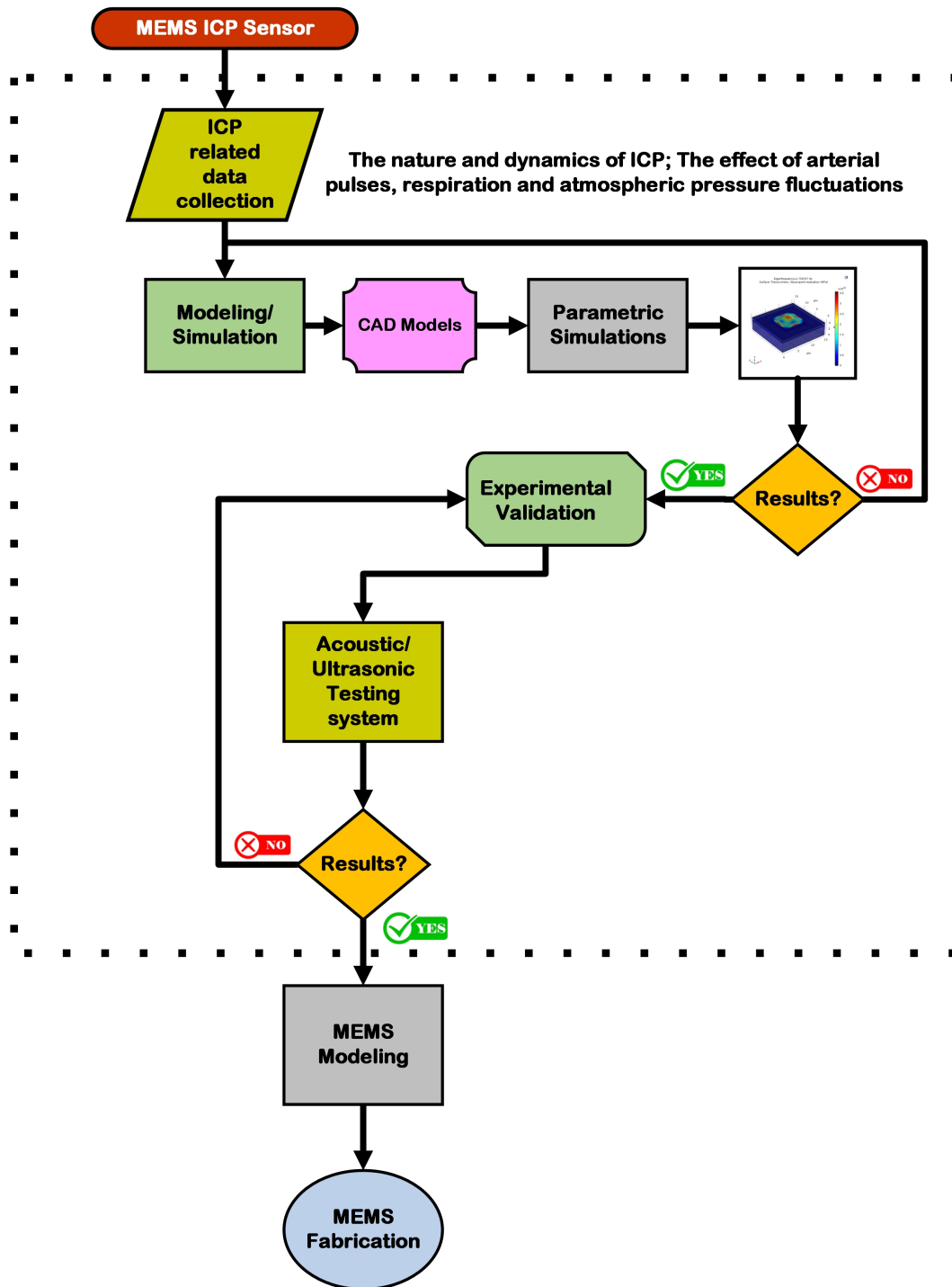


Figure 1.14 The flowchart of the proposed research

behaviour of thin film membranes; (5) By using fluid-structure FEM models to study the pressure transmission of the thin film membrane.

Table 1.4 The engineering design specifications

<b>Specification</b>	<b>Value</b>
Fatigue life	A minimum of 4 years to 10 years
Cycles	A minimum of 150 million cycles
Pressure transmission capability	$4\ \mu\text{m} \leq t \leq 500\ \text{nm}$
Load constraints	0 mmHg to 103 mmHg 0 mmHg to 980 mmHg
Material constraint	Titanium (Ti), Stainless steel Alumina, Zirconia
Thickness constraint	$4\ \mu\text{m} \leq t \leq 500\ \text{nm}$
Device dimensions	Around $400\ \mu\text{m} \times 400\ \mu\text{m}$

In the third phase, experiments were set up to validate the results of the FEM models. The tests were custom setup from a multimedia speaker-based acoustic system (Figure 2.2). The system comprises a subwoofer speaker system (Logitech Z313), laser displacement sensor (LK-HG 5001, Keyence, USA), Accelerometer (LIS3DHH, ST Microelectronics), Spectrum analyzer (NI LabVIEW), Data loggers (LK-Navigator - LK-H2, Unico 6.0). In the fourth stage, the effect of residual stresses introduced during MEMS fabrication and hygroscopic swelling due to multi-module packaging is studied.

The engineering design specifications of FEM and experimental validations are listed in Table 1.4

### 1.1.7 Thesis Outline

The thesis is organized into six chapters.

Chapter 2 presents a comprehensive literature review of this research work. The study starts with the collection of data related to intracranial pressure (ICP). The nature and dynamics of ICP are essential in the initial design phase of MEMS micro-system, particularly in the optimization of thin film membrane for lifetime monitoring. The nature of ICP is complicated as it depends on mean arterial and respiratory (intrathoracic) pressures. Thus, a basic understanding of arterial and respiratory fluctuations is essential for achieving long-term reliability and accuracy of MEMS sensors. In the second section, the effect of atmospheric pressure and gravitation forces has been discussed. The human body is subjected to uniform atmospheric pressure and gravitational force and the effect of atmospheric fluctuations is studied to help build absolute pressure sensors that are the popular choice in biomedical applications.

Chapter 3 outlines the finite-element modelling (FEM) and simulations of the MEMS micro-sensors system. The model starts with the theory of selection of mechanically stable and biocompatible materials suitable for designing a MEMS sensor for ICP monitoring. Next, various mechanical properties including tensile yield strength, compressive yield strength, Poisson's ratio, fatigue strength, stress concentration factors, etc. are considered for developing a good Multiphysics-based FEM model. A parametric study involving the size and thickness optimizations is essential for understanding the pressure transmission of thin film membrane, which is thickness dependent. Therefore, details of the parametric study have been included in the third section of this chapter. In the fourth section, the underlying physics of thin film deflection and fatigue behaviour is included for better finite-element simulations (FES), thereby improving the long-term reliability and accuracy of MEMS pressure sensors for lifetime ICP monitoring. In the last section, an extended-finite-element model (XFEM) is

included to study the topography of the fatigued surface of thin film membranes and the effect of micro-cavities and discontinuities on the underlying stress intensity factors that promote fatigue crack growth.

Chapter 4 describes the experimental setup of thin film deflection and fatigue behaviour. In the first section, the materials and specimen required for building an experimental setup are discussed. In the second section, the measurement technique is outlined. The brief literature on sonic-based fatigue techniques and accelerated random vibrations-based fatigue testing is also included. The displacement study using laser displacement sensors is also discussed here. In the final section, the SEM visualization of the fatigued thin surface is added to see the fractographical surface of thin film membrane.

Chapter 5 presents the MEMS micro-sensor system overview and proposed solution for the fabrication of MEMS thin film membrane-based pressure sensors. In the first section, the concept of MEMS fabrication is discussed. The MEMS system level design and simulations, the issues with deposition, etching and packaging is also delineated.

Chapter 6 discusses the conclusion and future work.



# Chapter 2

## Literature Review

### 2.1 Introduction

The literature review is broadly classified into the following sections:

1. The nature and dynamics of ICP, which is required as an input to the MEMS pressure sensor.
2. The external factors affecting ICP.
3. Material and Specimens.
4. Finite-element modelling (FEM) and analysis (FEA).
5. Experimental testing.

The chapter starts with a literature review on the nature and dynamics of ICP, which is potentially a major input to the MEMS pressure sensor for long-term ICP monitoring. In this section, the complex nature of ICP and its wave components are presented. The components from the human body include a MAP, respiratory pulses, and Intrathoracic fluctuations. The external components include the effect of gravitational force and the oscillations in

atmospheric pressure. Here, the information gathered on various forms of ICP waveforms, baseline ICP values, the impact of weather and altitude on atmospheric pressure are also outlined. In the second section, the required materials and specimens for the design of MEMS pressure sensors are discussed. In the third and final section, the FEM and experimental testing of MEMS pressure sensors are illustrated.

## 2.2 The Nature and Dynamics of ICP

In a healthy adult, the baseline ICP typically ranges between 5 mmHg to 15 mmHg, which is governed by the principles of the Monro-Kellie hypothesis. The normal value ICP depends on the age, body position, and the underlying neurological condition. Table 2.1 shows the normal ICP values based on the age, body posture and clinical condition.

The basic principles governing ICP were first formed by Harvey Cushing based on Monro-Kellie hypothesis. Principally, the hypothesis states that the intracranial contents such as the brain, the cerebral blood, and CSF are constant and an increase in one of the volumes must be offset with an equal decrease of the other components (Figure 1.4a). Under normal conditions, the brain maintains a balance between the arterial blood inflow and venous blood outflow and similarly between CSF production and drainage [47]. In case of intracranial haemorrhage or cerebral edema, it occupies additional space in the form of extrinsic mass lesion (Figure 1.4b,c) or causes an increase in CSF volume (hydrocephalus) (Figure 2.1a), or an increase in the cerebral blood (Figure 2.1b), or swelling in the brain tissue (Figure 2.1c), restricting the actual contents of the brain causing pressure build up inside the brain. [47]

ICP is pulsatile and varies with fluctuations in the blood pressure over the cardiac cycle, oscillations induced by respiration and changes in the vasomotor centre, the part of the brain that manages the blood pressure. However, mean arterial pressure will have more impact on

Table 2.1 The ICP threshold values of a healthy adult [46]

<b>Age</b>	<b>ICP</b>
Adult and older children	7 mmHg to 15 mmHg
Young children	3 mmHg to 7 mmHg
Infants	1.5 mmHg to 6 mmHg
<b>Body posture</b>	<b>ICP</b>
Supine	7 mmHg to 15 mmHg
Vertical	10 mmHg
<b>Condition</b>	<b>ICP</b>
Hydrocephalus	Above 15 mmHg
Traumatic Brain Injury	Above 20 mmHg
Refractory hypertension	40 mmHg to 70 mmHg

the ICP waveform than the other pressure fluctuations. Figure 2.2 shows an ICP spectrum recorded from kaolin-introduced live male Wistar rats at the Auckland Bioengineering Institute (ABI), University of Auckland. The spectrum shows various components which include slow wave, respiratory and cardiac regions

The arterial blood pressure causes vascular pulsations in large blood vessels triggering oscillations in the ventricular system. The oscillations induced by respiration generally coexist with variations in central venous pressure. Venous pressure, in turn, causes oscillations in intrathoracic pressure [65]. Besides the arterial and respiratory pulsations, slowly varying low-frequency pressure oscillations are found inside the skull. These slow waves signify the variations in CBV associated with the regulation of the CBF, particularly during injury to the brain (cerebral vasodilation and vasoconstriction).

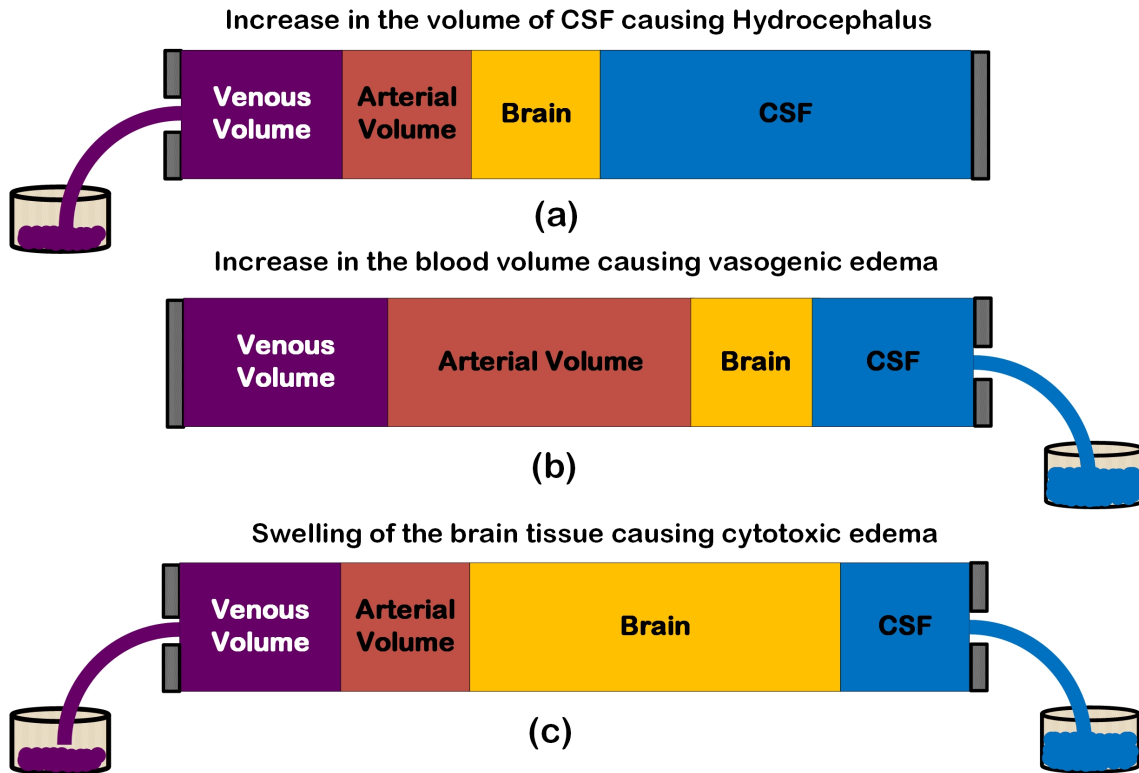


Figure 2.1 The conceptual diagram showing the intracranial volume changes

Figure 2.3 shows ICP patterns recorded continuously in various acute states during subarachnoid haemorrhage, intracranial haematoma, etc.

The waves are classified into the following: (1) A low and stable ICP wave ranging below 20 mmHg and as shown in Figure 2.3A. This is often seen in patients suffering from hydrocephalus, cough and minor headaches. (2) A slightly elevated ICP above 20 mmHg as shown in Figure 2.3B and is commonly associated with traumatic brain injuries or edema or intracranial haemorrhage. (3) Low frequency vasogenic 'B' waves ranging between 5 mmHg to 7 mmHg as shown in Figure 2.3C. These waves occur at a rate of 0.3 cycles/min to 0.4 cycles/min and represent cerebral vasodilation or vasoconstriction [66]. (4) Momentary sporadic plateau or 'A' waves ranging between 40 mmHg to 70 mmHg as shown in Figure 2.5D. These waves signify the status of cerebral autoregulation. Sudden ICP spikes up to 50 mmHg as shown in Figure 2.3E occurs due to a sudden rise in arterial blood pressure

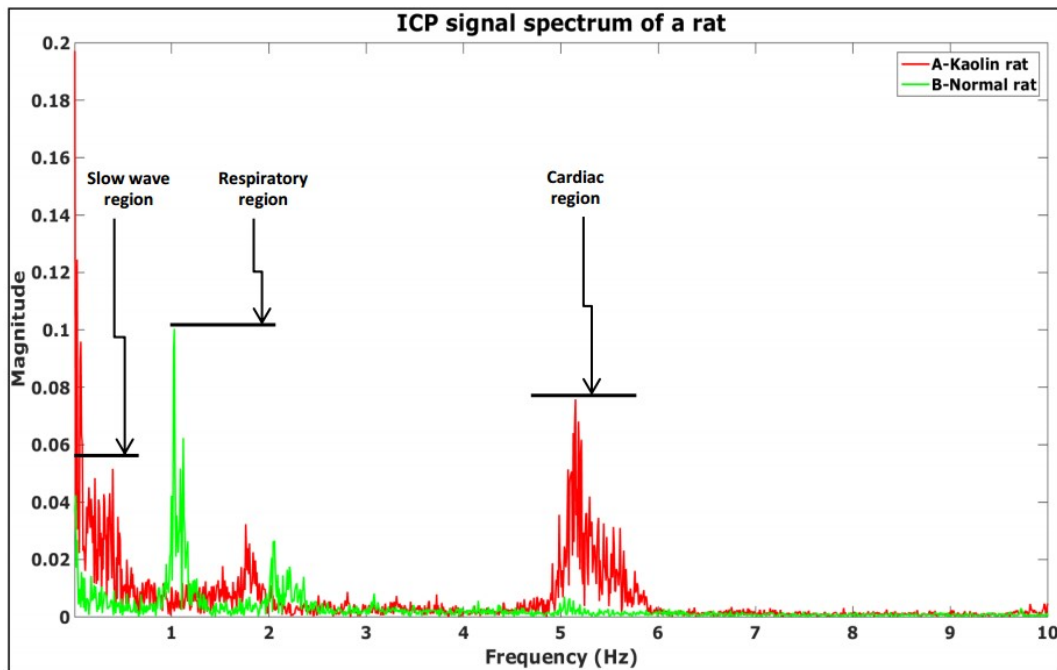


Figure 2.2 An ICP frequency spectrum of Kaolin-introduced Male Wistar Rats: Normal Wistar rat (green colour) and hydrocephalus (kaolin)-introduced Wistar rat (red colour)

(ABP). A plateau rises in ICP up to 60 mmHg (as shown in Figure 2.3F) due to a sudden drop in ABP. An ICP spike associated with the condition of hyperemia as shown in Figure 2.3G signifying the compromised cerebral autoregulation and CPP becomes linearly dependent of the MAP, ICP. It shows that ICP varies with flow velocity and venous oxygen saturation. An ICP pattern associated with refractory hypertension ranging above 100 mmHg is shown in Figure 2.3H. The vertical line represents the condition of ischemia, where an abrupt rise in the heart rate and decline in ABP can be seen.

In summary, the various components of ICP waveform are listed in Table 2.2 with their magnitude and frequencies.

However, ANSI/AAMI NS28/Ed.1 1998/(R)2006 standards (<http://www.aami.org/standards/index.html>) defines a standard ICP value to be in the range of 0 mmHg to 103 mmHg for the safety and performance requirements of implantable pressure sensors.

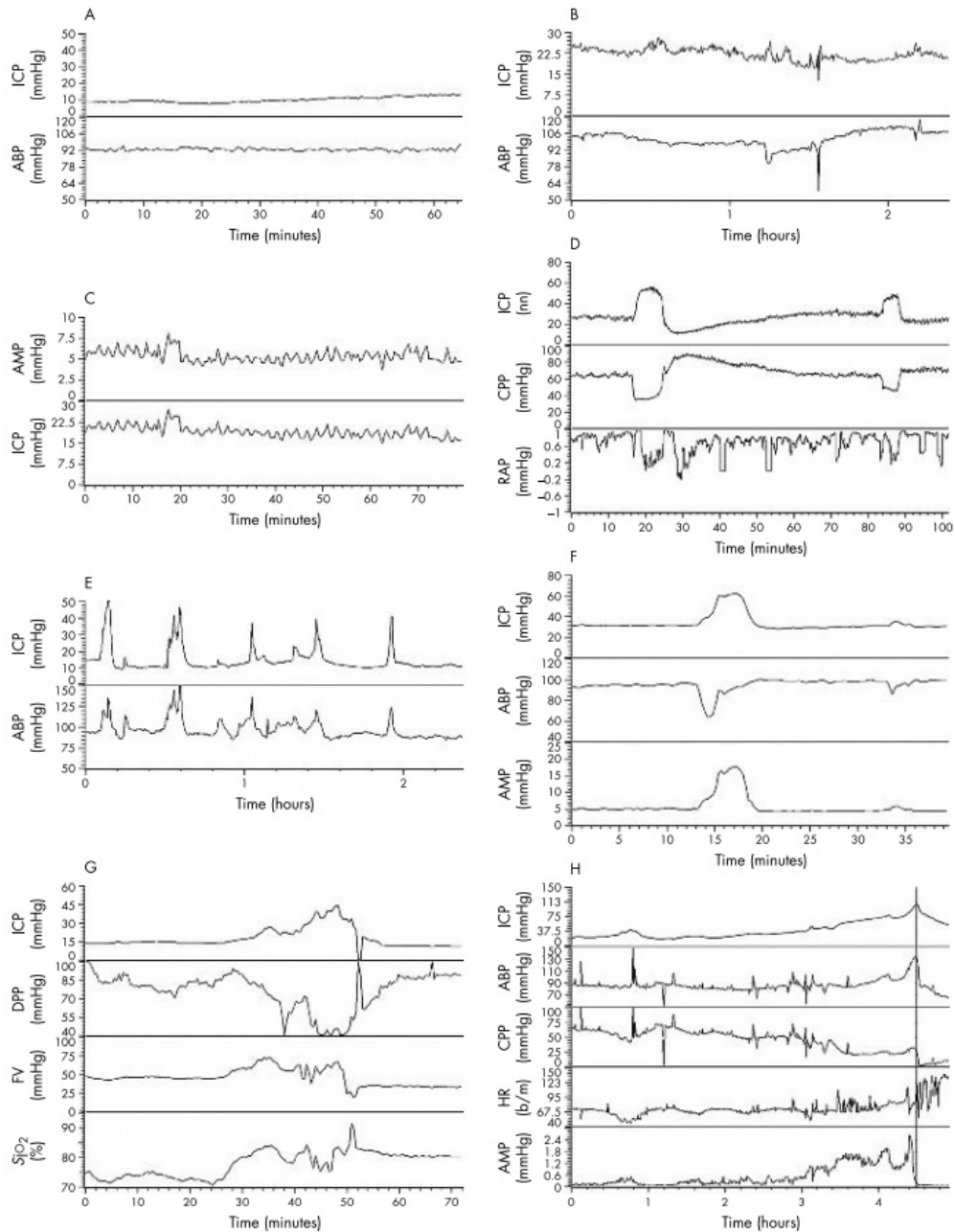


Figure 2.3 A - Low and stable ICP wave, B – High and stable ICP, C – Vasogenic B waves: they are saw tooth type rhythmic oscillations caused by changes in cerebral blood volume (CBV) due to depressed consciousness and reduced internal compliance, D – plateau (A) waves: momentary rises in the baseline pressure to amplitude of 60 mm Hg for about 5 – 10 minutes before falling back to baseline or below, E – G – cause due to the influence of respiratory and cardiac wave components, H – Refractory intracranial hypertension which can cause death [46]

Table 2.2 The nature and shape of ICP and its components [46]

Type of components	Shape of the wave	Magnitude	Frequency
<b>Plateau A</b>	Sudden momentary rises	40 mmHg to 70 mmHg	5 min to 10 min
<b>Vasogenic B</b>	Saw tooth rhythmic	5 mmHg to 7 mmHg	1 min to 2 min
<b>Arterial Pulses</b>	Oscillations induced by CBV	3 mmHg	50 beats/min to 180 beats/min
<b>Respiratory Pulses</b>	Coexists with Venous pressure and signifies oscillations in intrathoracic pressure	8 mmHg to 10 mmHg	8 cycles/min to 20 cycles/min

### 2.3 The External Factors Affecting ICP

The physiological pressures not only comprise of pressure associated with arterial, respiration or other organs but also are influenced by external forces such as the gravitational pull and oscillations in the atmospheric pressure. Therefore, it is essential to differentiate the physiological pressure component from these external forces. In general, a human body is subjected to uniform atmospheric pressure and sensor devices that measure pressure with reference to the atmospheric pressure are essential, so that the in vivo measurement is not affected by the atmospheric pressure variations. However, it is difficult to fabricate a sensor maintaining a sea-level atmospheric pressure of 760 mmHg [67]. In contrast, most implantable sensors are made in reference to a vacuum (0 mmHg) sealed with glass on one side of a thin film membrane known as absolute pressure sensors as it is easier to maintain a vacuum than a predefined pressure. Thus, variations in the atmospheric pressure must

be considered. Figure 2.4 shows the conceptual diagram of different types of pressure measurement techniques.

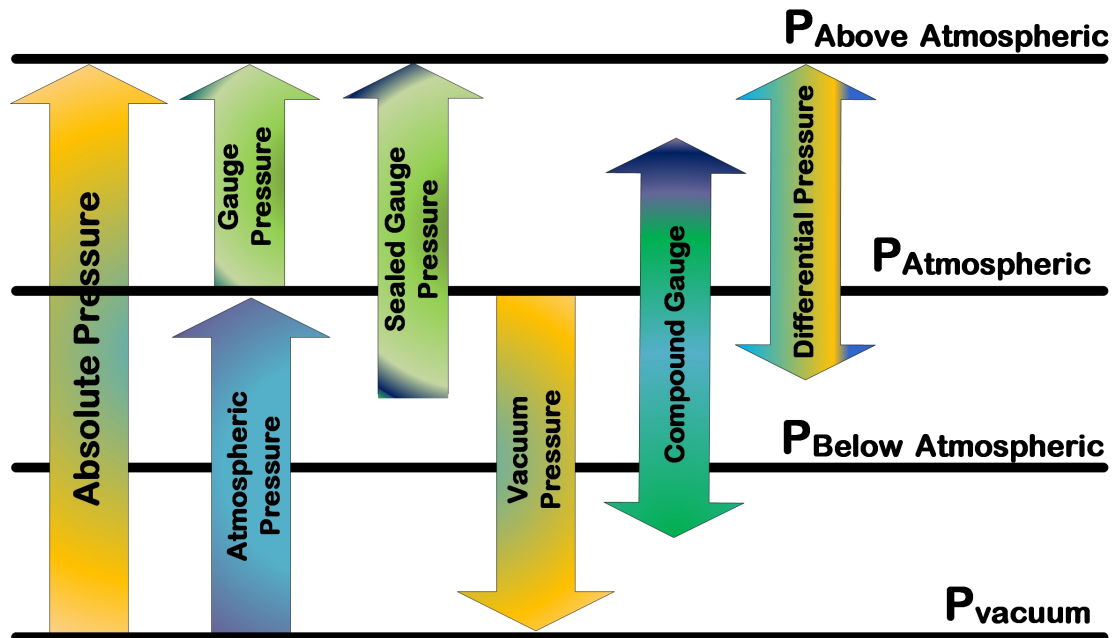


Figure 2.4 The types of pressure measurements

### 2.3.1 Types of Pressure Measurements

In MEMS, all the pressure measurements are made in reference to a predefined pressure or perfect vacuum (Zero pressure). Thus, the pressure measurements can be broadly classified as (<http://www.ni.com/white-paper/13034/en/>):

1. Gauge Pressure
2. Sealed Pressure
3. Absolute Pressure
4. Differential Pressure

### **Gauge Pressure Measurement**

A Gauge pressure sensor measures the subjected input pressure load in reference to ambient atmospheric pressure. Applications require pressure measurement with respect to ambient conditions can utilize gauge pressure sensors. The best example is car tire pressure measurement. However, Gauge pressure sensors are susceptible to humidity in dry weather.

### **Sealed Gauge Pressure Measurement**

A sealed Gauge pressure sensor is similar to the standard gauge pressure sensors, but measures pressure with reference to a cavity pressure sealed to ambient atmospheric pressure (760 mmHg). The Sealed cavity would protect the internal electronics from humidity and improves the long-term accuracy of the sensor.

### **Absolute Pressure Measurement**

An absolute pressure sensor measures the subjected pressure with respect to a cavity pressure perfectly sealed to a vacuum (0 mmHg). The best examples include barometric pressure measurement or measurements that require removal of air pressure influence. Absolute measurement is expressed mathematically as

$$P_{absolute} = P_{gauge} + P_{atmosphere} \quad (2.1)$$

### **Differential Pressure Measurement**

A differential pressure sensor measures the pressure difference between the subjected input pressure and predefined reference pressure (e.g., 400 mmHg).

In biomedical applications, the measurement of physiological pressure is within the cavities of a human body, and pressure sensors that measure pressure with respect to a cavity sealed to a perfect vacuum are preferred. Therefore, the effect of weather and altitude on atmospheric pressure fluctuations must be considered [68].

### **2.3.2 The Effect of Weather on Atmospheric Pressure**

The atmosphere encompassing the earth is made up of air and various gaseous substances. Air is an element that has mass and weight and comprises of molecules that are in constant motion. Therefore, air exerts large amounts of pressure on the earth causing weather changes. When the particles of the sky get warmer, expansion occurs making the atmosphere less dense, and when the particles get cooler, contraction occurs making the atmosphere thicker. In general, the force exerted by the air above the earth is termed as 'air pressure'. However, the pressure exerted is not uniform, and the earth's surface is covered with regions of low and high air pressure ([https://www.cengage.com/resource\\_uploads/downloads/0495555061\\_137182.pdf](https://www.cengage.com/resource_uploads/downloads/0495555061_137182.pdf)).

High pressure occurs when the atmosphere over an area becomes heavier. Thus, the heavy air creates space for itself on the earth's surface. In summer, the weather is always dry and stable, and the sky is mostly clear.

In contrast, the air above the low-pressure area is less dense than the air below. When the wind starts to cool down, it forms clouds in the sky which pour down to the earth. Sometimes, snow is also formed depending on the temperature of the surrounding areas. Thus, the

low-pressure areas are the reasons behind unstable weather conditions like snow, ice, rain, storm, etc.

The weather data reported on television is always at mean sea level. Therefore, the formula to convert sea level pressure to atmospheric pressure is given as (<https://keisan.casio.com/exec/system/1224575267>):

$$P_0 = P \left( 1 - \frac{0.0065h}{T + 0.0065h + 273.15} \right)^{-5.257} \quad (2.2)$$

Where,  $P_0$  is the sea level standard atmospheric pressure;  $P$  is the atmospheric pressure;  $T$  is the temperature;  $h$  is the altitude.

Table 2.3 enumerates some of the atmospheric pressures changes recorded during many cyclones across the globe.

### 2.3.3 The Effect of Altitude on Atmospheric Pressure

As discussed earlier, the denser air is held closer to the surface of the earth by the gravitational force. As the air travels upwards, the density of the air decreases making it thinner at higher levels (<https://www.scientificamerican.com/article/if-heat-rises-why-does-th/>) (Figure 2.5).

The relationship between the atmospheric pressure fluctuations and the altitude affects the design of absolute pressure sensors as they measure pressure with reference to sealed cavity vacuum pressure. Ideally, a perfect vacuum cannot be achieved for medical requirements which require approximately 736.6 mmHg of the sea level pressure. Orbitec technologies (<https://www.scribd.com/document/379565757/Orbitec-Vacuum-Reference-pdf>) provide a reference vacuum chart for designing vacuum-based pressures sensors (Table 2.4).

Table 2.3 Atmospheric pressure fluctuations captured during cyclones across the globe

<b>Cyclone</b>	<b>Region</b>	<b>Year</b>	<b>Speed</b>	<b>Atm. Pressure</b>
Cuba	Western Caribbean	1932	175 mph	686.306 mmHg
Allen	Northern Mexico	1980	190 mph	674.305 mmHg
Katrina	USA	2005	175 mph	676.555 mmHg
Rick	Pacific	2009	180 mph	679.555 mmHg
Megi	Philippines	2010	145 mph	663.804 mmHg
Haiyan	Philippines	2013	130 mph	671.305 mmHg
Hudhud	India	2014	115 mph	712.558 mmHg
Winston	South Pacific	2015	145 mph	686.308 mmHg

## 2.4 Atmospheric Pressure Measurements in Auckland

In general, the atmosphere consists of natural noises including infrasonic, sonic, and ultrasonic components that emanate from the chaotic turbulence present in the air. These interferences can trigger the atmospheric pressure to vary at extra-low-frequencies ranging between 0.0001 Hz to 1 Hz. While the upper frequency (1 Hz) is closer to the infrasonic spectrum, lower frequencies represent vast variations in barometric pressure with a rate exceeding the critical value of 1.5 mmHg to 3 mmHg. However, in general, the critical value of  $\frac{dp}{dt}$  is stated to be in the range of 3.7 mmHg to 7.5 mmHg per day (366 cycles per year) and 1.5 mmHg to 3 mmHg every three hours (2,920 cycles per year) in stormy weather.

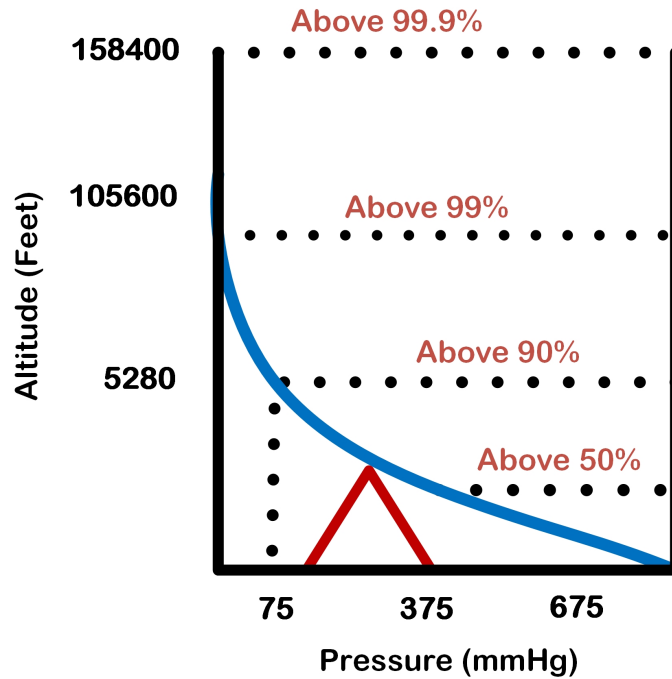


Figure 2.5 Types of pressure measurement including absolute, gauge and atmospheric pressures

Barometric pressure was recorded continuously for two years at Auckland Bioengineering Institute, University of Auckland, Auckland, using a Mensor CPT6100 barometric sensor. Table

## 2.5 Material and Specimens

The essential requirements of material required in biomedical applications are mechanical stability and biocompatibility. The mechanical stability of a biomaterial is its ability to withstand the mechanical fatigue during its operational period. On the other hand, biocompatibility is the ability of a human body to continue to function normally even with the interferences of a foreign body [69]. In biomedical applications, the feature of biocompatibility can help in in-vivo performance with minimum possible biological reaction inside

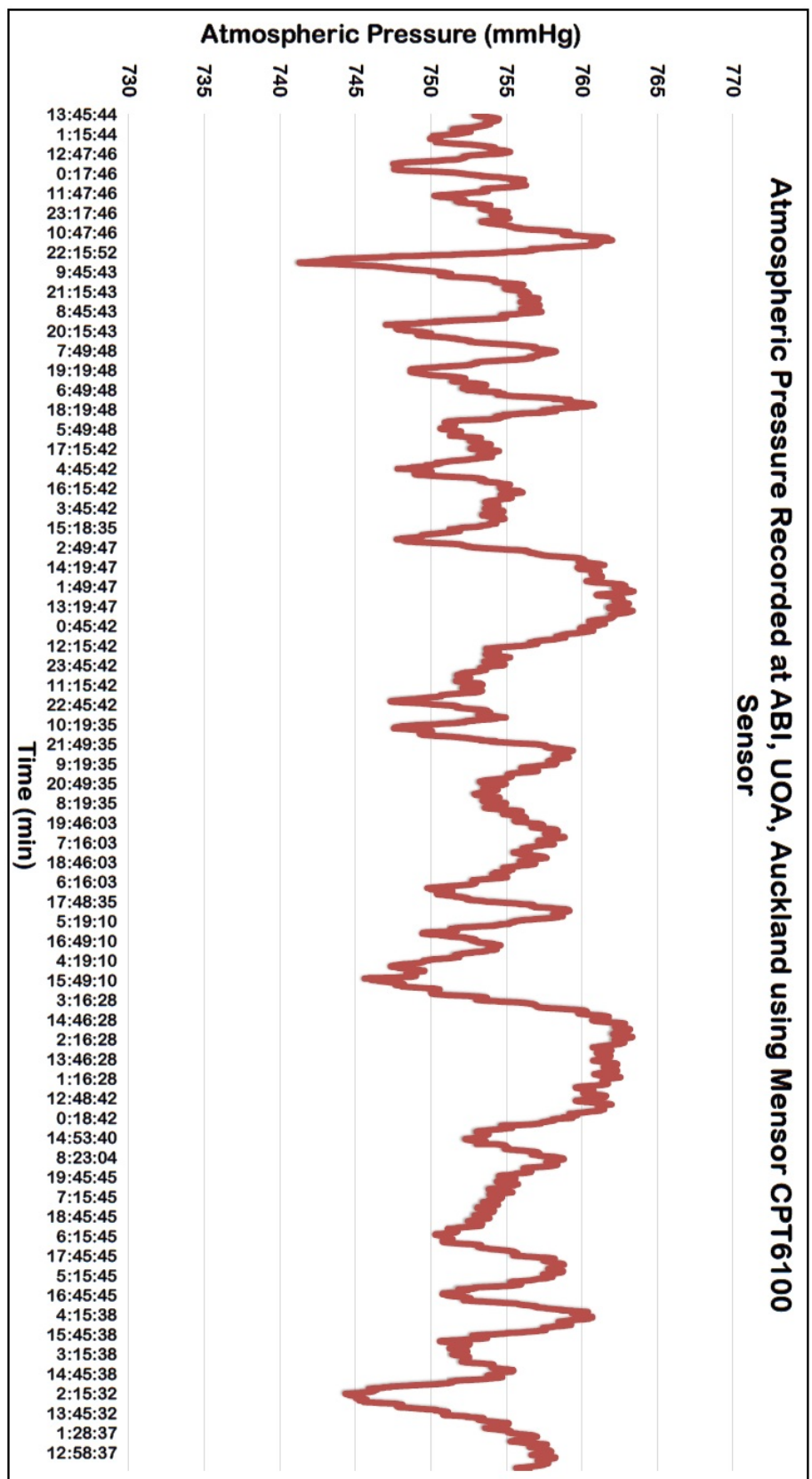


Figure 2.6 The plot of the capture of atmospheric pressure oscillations in Auckland using Mensor CPT6100 barometric sensor

Table 2.4 The effect of altitude on atmospheric pressure

<b>Altitude</b>	<b>Temperature</b>	<b>Atm. Pressure</b>	<b>Sea Level Pressure</b>
40000 Feet	-57 °C	141.2 mmHg	729.389 mmHg
20000 Feet	-24 °C	349.5 mmHg	759.069 mmHg
10000 Feet	-5 °C	522.7 mmHg	760.314 mmHg
5000 Feet	5 °C	632.5 mmHg	760.247 mmHg
2500 Feet	10 °C	693.9 mmHg	760.127 mmHg
500 Feet	14 °C	746.3 mmHg	759.932 mmHg
Sea level	15 °C	760.0 mmHg	759.999 mmHg
-500 Feet	16 °C	773.9 mmHg	760.059 mmHg
-2500 Feet	20 °C	830.6 mmHg	759.429 mmHg

Table 2.5 The atmospheric pressure oscillations recorded at ABI, UOA, Auckland using Mensor CPT6100 barometric sensor

<b>Alt</b>	<b>Temp</b>	<b>Min. Pressure</b>	<b>Av. Pressure</b>	<b>Max. Pressure</b>	<b>Variance</b>
165.5 m	15 °C	731.53 mmHg	756.54 mmHg	769.61 mmHg	34.5 mmHg

the brain. However, the human body will not entirely ignore the influence of a foreign body. Once the pressure sensors are implanted, a series of chemical reactions will follow. Besides, the thin film membrane, which is the pressure sensitive element is continuously in contact with the biological medium. This allows the cells, tissues, and other debris to adhere to the thin film membrane, which makes it vulnerable to fretting fatigue, corrosion, and biofouling. Therefore, the biocompatibility studies are essential before the fabrication of a MEMS pressure sensor [70].

A wide range of biomaterials are available for a myriad of applications including orthopaedics, cardiovascular, ophthalmic, and dental restorations. For example, these biomaterials can be used for treating heart valves, and arteries in cardiovascular applications [71]. The design and selection of biomaterials depends on the requirements of an application. In general, biomaterials are broadly grouped into (1) Ceramics [72], which comprises of materials including carbon nanotubes [73], graphene [74], alumina and zirconia [75]; (2) Metals and its alloys [76], which comprises of stainless steel [77], cobalt [78], nitinol [79] titanium [80], and platinum [81], and (3) Polymers [82] which comprises of liquid crystal polymers (LCP) [83] and silicone [84]. Table 2.6 lists the classification and characteristic specifications of biomaterials.

Most of these biomaterials are used in dental restorative or orthopaedic applications. However, for the fabrication of MEMS pressure sensors that are useful in the long-term monitoring of physiological pressure, the choice of material should be based on mechanical stability and biocompatibility. Can new biomaterials be integrated into the standard microfabrication which is adapted to silicon-based materials? A silicon-based pressure sensor uses silicon-based thin-film pressure sensors deposited on rigid substrates [87]. These thin-films act as flexible membranes that deflect under the stimulus of intracranial pressure and induce a corresponding change in the original capacitance [88]. Silicon-based capacitive MEMS pressure sensors are widely used in automotive, aerospace and military applications due to their inherent small size, and low-cost batch fabrication techniques. However, in biomedical applications, silicon-based materials can be toxic and have issues with water intrusion when inserted in biological media. Therefore, biocompatible materials such as metals would be an appropriate choice. Metallic biomaterials have substantial economic and clinical impact in the biomedical field, and they would be more suitable in the fabrication of thin-film membranes as they can offer excellent mechanical strength to survive stresses and strains in long-term ICP pressure monitoring [89, 90].

Table 2.6 The various classification of biocompatible materials [85, 86, 70]

<b>Materials</b>	<b>Advantages</b>	<b>Disadvantages</b>	<b>Examples</b>
Polymers	<ol style="list-style-type: none"> <li>1. Resilient,</li> <li>2. Easy to fabricate</li> </ol>	<ol style="list-style-type: none"> <li>1. Not strong</li> <li>2. Deforms easily</li> <li>3. May degrade</li> </ol>	<ol style="list-style-type: none"> <li>1. Nylon</li> <li>2. Silicone</li> <li>3. Polyester</li> <li>4. PDMS</li> <li>5. Parylene C</li> </ol>
Metals	<ol style="list-style-type: none"> <li>1. Strong</li> <li>2. Ductile</li> <li>3. Mechanical Stability</li> </ol>	<ol style="list-style-type: none"> <li>1. May corrode</li> <li>2. Dense</li> <li>3. Difficult to make</li> </ol>	<ol style="list-style-type: none"> <li>1. Titanium alloys</li> <li>2. Co-Cr alloys</li> <li>3. Au</li> <li>4. Ag</li> <li>5. Stainless steel</li> </ol>
Ceramics	<ol style="list-style-type: none"> <li>1. Biocompatible</li> </ol>	<ol style="list-style-type: none"> <li>1. Brittle</li> <li>2. Not resilient</li> <li>3. Weak in Tension</li> </ol>	<ol style="list-style-type: none"> <li>1. Alumina</li> <li>2. Zirconia</li> <li>3. Calcium phosphates</li> </ol>
Composites	<ol style="list-style-type: none"> <li>1.Strong</li> <li>2. Custom made</li> </ol>	<ol style="list-style-type: none"> <li>1 Difficult to make</li> </ol>	<ol style="list-style-type: none"> <li>1. carbon-carbon,</li> <li>2. wire,</li> <li>3. fibre-reinforced,</li> <li>4. bone cement</li> </ol>

Currently, biocompatible metals such as stainless steel, titanium (Ti) and platinum (Pt), are integrated into the fabrication of thin film membranes based on MEMS pressure sensors. Over the last few decades, stainless steel-based metallic biomaterials have been widely used because of their good resistance to chloride solutions. However, these biomaterials are bulky

and exhibit poor sensitization (loss of alloy integrity). Some examples of stainless steel based MEMS pressure sensors are (1) A capacitive pressure sensor developed by Sung-Phil Chang et al. [91]. The sensitivity of this sensor measured as 9.03 ppm/kPa with a net capacitance change of 0.14 pFF over a pressure range of 0 kPa to 179 kPa; (2) A pressure sensor with medical grade stainless steel thin film membrane developed by Xing Chen et al. [92]. The sensitivity of this sensor 110 ppm/mmHg over a pressure range of 0 mmHg to 250 mmHg.

In contrast, Ti alloys are low-density biomaterials (approximately 60 % of the density of iron and nearly half of the density of 301 stainless steel), high specific strength and excellent corrosion resistance [93]. Table 2.7 shows the mechanical properties of Ti-6Al-4V titanium alloy compared with other metallic biomaterials. When compared to other biomaterials, Ti-6Al-4V have the following advantages, (1) Good corrosion resistance to a saline environment, (2) Low density and high strength-to-weight ratio, (3) Low modulus of elasticity, and (5) Excellent fatigue resistance. In addition to low modulus, Ti-6Al-4V has high tensile yield strength and an ability to form an oxide layer that can protect the thin film membrane from debris from the tissues that form biofouling in long-term monitoring.

The crystal structure of pure Ti at ambient temperature and pressure is a hexagonal close-packed (HCP)  $\alpha$  phase as shown in the Figure 2.7a. At about 881.85 °C HCP  $\alpha$  phase titanium undergoes an allotropic transformation to a body-centred cubic (BCC)  $\beta$  phase that remains stable to the melting point (Figure 2.7b) [94, 95]. The metallurgy of Ti microstructure greatly depends on the crystallographic transformations of these two phases [27].

Table 2.8 shows the properties of  $\alpha$  phase and  $\beta$  phase alloys. The potential advantage of adding alloys to pure titanium is the modification of the transformation temperature and the production of a two-phase field, where both the  $\alpha$  and  $\beta$  phase can be exploited. These alloys are termed as ( $\alpha+\beta$ ) alloys. Elements that promote the  $\alpha$  phase properties at high temperatures are known as  $\beta$  stabilizers, and those that help in stabilizing  $\beta$  phase properties at low temperatures are known as  $\alpha$  stabilizers. For example, Aluminum (Al) is a popular  $\alpha$

Table 2.7 The mechanical properties of Ti (<http://matweb.com/search/DataSheet.aspx?MatGUID=b350a789eda946c6b86a3e4d3c577b39&ckck=1>)

Property	Ti-6Al-4V	Pure Titanium	Stainless Steel
Density	4430 kg m <sup>3</sup>	4150 kg m <sup>3</sup>	7800 kg m <sup>3</sup>
Young's Modulus	114 GPa	103 GPa	200 GPa
Poisson's Ratio	0.33	0.37	0.34
Elongation at break	10 %	20 %	40 %
Tensile Yield Strength	1100 MPa	448 MPa	1500 MPa
Tensile Ultimate Strength	1170 MPa	344 MPa	2000 MPa
Creep Strength at temp 455 °C	300 MPa	162 MPa	300 MPa
Fatigue Strength at 1.00e <sup>7</sup>	160 MPa		

stabilizer, which assists in promoting the stability of titanium's  $\alpha$  phase beyond 882 °C, can aid in improving their strength and resistance to corrosion.

ASTM standards B265 classifies Ti into several grades and Ti-6Al-4V falls into medical grade 5. Ti-6Al-4V–grade 5 is available commercially in the form of solution treated annealed (STA) titanium alloy. The fatigue strength of STA Ti alloy is 160 MPa measured with the notch stress concentration factor ( $k_f$ ) of 3.3. The composition of Ti-6Al-4V is shown in Table 2.9.

## 2.6 Finite-Element Model and Analysis

A thin film deflection is defined as a vertical displacement of a point at a location on the thin film membrane. In general, deflection is produced when a thin film membrane is subjected to

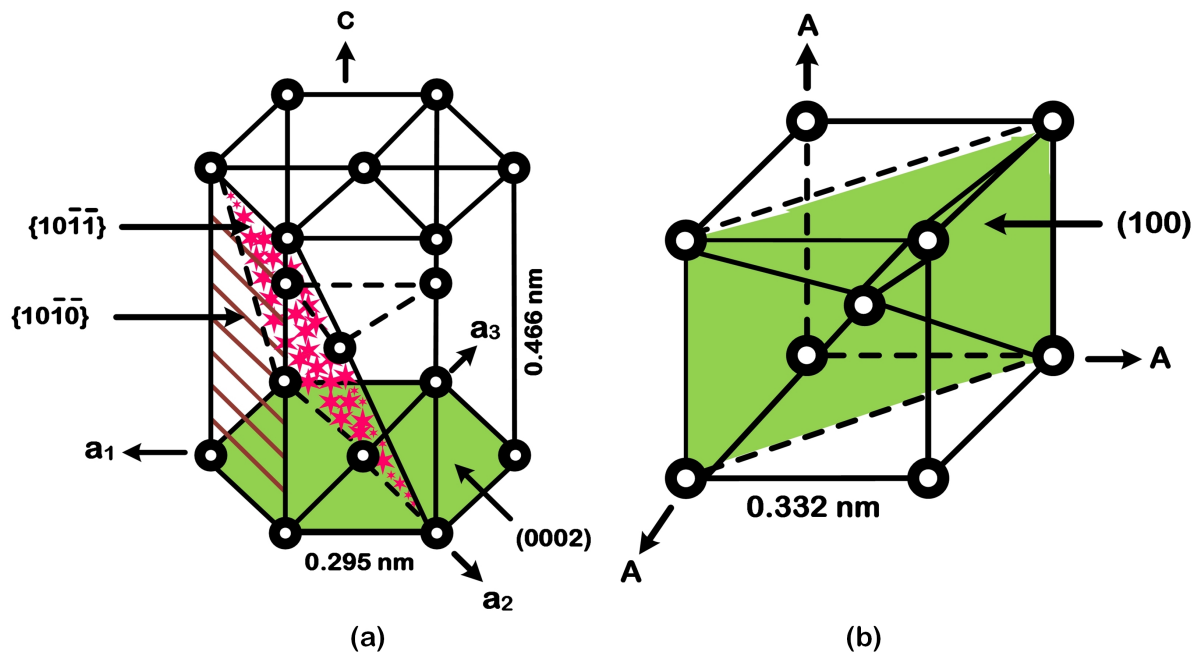


Figure 2.7 Types of pressure measurement including absolute, gauge and atmospheric pressures

Table 2.8 Classification of biocompatible materials used in the body

Alloy types	Advantages	Disadvantages	Element
$\alpha$ Alloys	<ol style="list-style-type: none"> <li>1. Easy weldable,</li> <li>2. Good ductility,</li> <li>3. High temperature creep strength,</li> <li>4. Good oxidation resistance,</li> <li>5. Relatively tough at cryogenic temperatures.</li> </ol>	<ol style="list-style-type: none"> <li>1. Non-heat treatable</li> </ol>	<ol style="list-style-type: none"> <li>1. Al,</li> <li>2. Oxygen</li> </ol>
$\beta$ Alloys	<ol style="list-style-type: none"> <li>1. Readily heat treatable</li> <li>2. Weldable</li> <li>3. High Strength at intermediate temperatures,</li> <li>4. Excellent cold formability</li> </ol>	<ol style="list-style-type: none"> <li>1. Brittle</li> </ol>	<ol style="list-style-type: none"> <li>1. Md,</li> <li>2. Silicon,</li> <li>3. Vanadium</li> </ol>

Table 2.9 The elemental composition of Ti-6AL-4V

Element	Composition	Remarks
Aluminium	5.5 % to 6.75 %	$\alpha$ Stabilizer
Vanadium	3.5 % to 4.5 %	$\beta$ Stabilizer
Iron	0.4 %	
Oxygen	0.2 %	
Nitrogen	0.08 %	
Hydrogen	0.015 %	
Residuals	0.4 %	

a cyclic load (e.g., pressure or temperature), which is measured from the original position to the neutral surface of the deformed thin film membrane. Several internal and external factors affect the nature of deflection. While the internal factors include the straining due to residual stresses, which are a residue of the MEMS fabrication process defects, the external factors include straining due to externally applied forces [96]. Besides, the thin film deflection is also affected by the cross-section of the thin film membrane and other structural layers in the MEMS pressure sensor. Thus, it is essential to analyze the effect of the internal and external factors on the structural behaviour of the thin film membrane.

### Plate Theory

Lagrange formulated the first general equation of plate behaviour in the year 1828. Then in 1829, Poisson expanded the general plate equation under static loading. However, the flexural rigidity of the plate was set to constant. The theory of thin plates, small deflection theory was proposed by Kirchoff in 1850. The assumptions of the thin plate theory are [97]

1. The thin film material is elastic, homogeneous, and isotropic
2. The plate is initially flat
3. The thin plate comprises of a neutral axis in the centre that separates the plate into two sections (above and below neutral axis).
4. When the plate is subjected to a cyclic load, the thin plate deforms.
5. The deformation of neutral axis is negligible to the thickness of the plate.
6. The lines normal to the neutral axis remain normal after deformation. Therefore, the vertical shear is neglected in the modelling.
7. The normal stress ( $\sigma_z$ ) can be neglected as it is very small.
8. The neutral axis of the thin plate remains unaffected as the deflections are very small compared to the thickness of the plate.

Figure 2.8a and 2.8b shows the deformed plate and resultant moments and forces on a unit cell of thin film membrane material respectively.

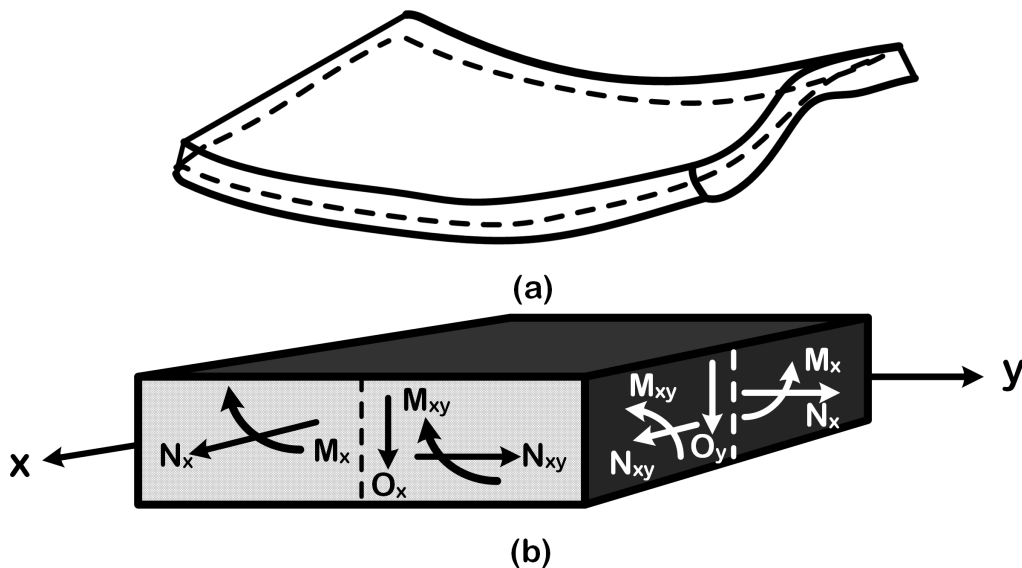


Figure 2.8 (a) The deformed plate, (b) The moments and forces acting on a plate

The equations 2.3 and 2.4 describes the normal forces and moments

$$\begin{aligned} N_x &= \int_{\frac{-h}{2}}^{\frac{+h}{2}} \sigma_{xx} dz \\ N_y &= \int_{\frac{-h}{2}}^{\frac{+h}{2}} \sigma_{yy} dz \end{aligned} \quad (2.3)$$

Where,  $N_x$  and  $N_y$  are the in-plane normal forces in x and y directions respectively,  $\sigma_{xx}$  and  $\sigma_{yy}$  are the stresses due to x and y components respectively.

$$\begin{aligned} M_x &= \int_{\frac{-h}{2}}^{\frac{+h}{2}} z \sigma_{xx} dz \\ M_y &= \int_{\frac{-h}{2}}^{\frac{+h}{2}} z \sigma_{yy} dz \end{aligned} \quad (2.4)$$

Where,  $M_x$  and  $M_y$  are the in-plane bending moments

The equation 2.5 describes the in-plane shear force and twisting moments.

$$\begin{aligned} N_{xy} &= \int_{\frac{-h}{2}}^{\frac{+h}{2}} \sigma_{xy} dz \\ M_{xy} &= \int_{\frac{-h}{2}}^{\frac{+h}{2}} z \sigma_{xy} dz \end{aligned} \quad (2.5)$$

Where,  $N_{xy}$  is the in-plane shear force,  $M_{xy}$  is the in-plane twisting moment

The equation 2.6 describes the out-of-plane shearing forces.

$$\begin{aligned}
 O_x &= \int_{\frac{-h}{2}}^{\frac{+h}{2}} \sigma_{zx} dz \\
 O_y &= \int_{\frac{-h}{2}}^{\frac{+h}{2}} \sigma_{yz} dz
 \end{aligned}
 \tag{2.6}$$

Where,  $O_x$  and  $O_y$  are the out-of-plane shear forces.

When a thin film is subjected to externally applied cyclic loads, the moments, normal and shear forces aid in the deflection. In addition to the development of stresses due to deflection, thin film structures will have residual stresses from the MEMS fabrication process defects. The stress due to deflection residual stresses of a thin plate can be calculated by solving a set of differential equations. These calculations would eventually aid in the determination of fatigue failure of thin films subjected to cyclic stresses.

FEM and FEA are the powerful computational tools used in studying the underlying physics of complex thin film structures. The foundations of FEA of thin film structures is based on the fundamental laws of mechanics that are expressed in mathematical models (partial differential equations). In turn, these mathematical models are discretized by FEM for easy computation. William P. Eaton et al. [98] proposed a small deflection membrane theory that analyses stress due to large deflection and built-in residual stresses of a thin film membrane. The analytical FEM of thin film deflection of the circular diaphragm is validated with experimental results. Y B Tian et al. [99] developed a two dimensional axisymmetric FEM to predict the stresses due to deflection and residual stresses. In this model, residual stress distributions are analyzed in a machined ultra-thin wafer. C.E. Imrak et al. [100] analyzed the deflection of rectangular thin plates fixed at the corners under a uniformly distributed load. The model was based on classical cosine series expansion. Vanam B.C.L. et al. [101] analyzed the deflection of isotropic rectangular plates parametrized over various boundary conditions. The FEA was carried using MATLAB and ANSYS . Wang Yun et al.

[102] investigated the axisymmetric bending of isotropic circular plates that are subjected to transverse loads using direct displacement method . P.S. Gujar et al. [103] studied bending of an isotropic circular plate using classical plate theory in ANSYS.

The result of stresses due to deflection and residual stresses is fatigue failure at cyclic loads below the yield strength, A fatigue module is broadly classified into classical stress and multiaxial stress models. The classical stress models use S–N curve to relate the stress amplitude to the fatigue life of a thin film structure. The classical stress-life methods for studying the fatigue life of all metals have their origins in the work of Wohler (S-N curve). The S-N curves describes the number of cycles to failure for a specific stress amplitude. Figure 2.9 shows the S-N curve of Ti thin film material generated from COMSOL. However, the classical S-N-based fatigue analysis is suitable for equal Uniaxial loading.

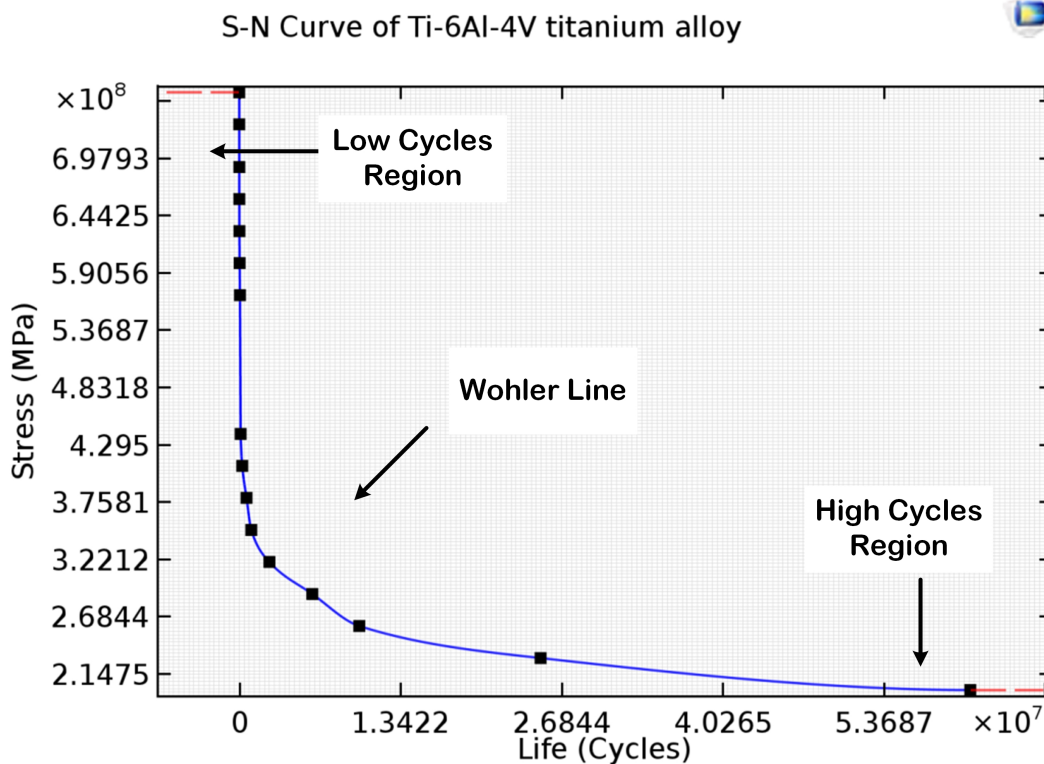


Figure 2.9 The S-N curve of Ti-6Al-4V Ti alloy

Uniaxial stress loading is a simplified theoretical concept which may not work in real time applications as the thin film membranes are subjected to randomly varying loads. Multiaxial fatigue models are essential in the prediction of multiaxial stress states of thin film membrane. Some of the multiaxial critical plane fatigue-based models include Findley, Matake, McDiarmid, Gough, and Normal stress. Denis Benasciutti et al. [104] discussed the random stress induced multiaxial fatigue using spectral methods. The model is based on the Matake critical plane multiaxial model that is described in frequency-domain. Brown et al. [105] presented a fatigue failure theory using multiaxial stress-strain conditions in the low-cycles region. Xavier Pitoiset et al. [106] proposed a frequency domain implementation of Crossland's failure criterion for metallic structures under cyclic stresses and strains. Chu et al. [107] investigated multiaxial neuber equivalencing technique for studying the fatigue behavior of plastically deformed notch areas. Del Liano et al. [108] conducted multiaxial fatigue and failure analysis of helical compression springs to determine fatigue crack imitation. The fatigue analysis is carried out using nCode ANSYS (<https://www.ansys.com/products/structures/ansys-ncode-designlife>). Nima et al. [109] investigated low cycle multiaxial fatigue behaviour of Ti alloys. In this analysis, the von Mises criterion and linear damage rule based critical plane model was used to predict the fatigue life under various block loadings. McDiarmid et al. [110] proposed a simple general multiaxial fatigue criterion. In this model, the fatigue strength is a function of shear stress amplitude and maximum normal stress on a critical plane. Luca Susmel [111] reformulated the maximum variance method for multiaxial fatigue assessment of real damaged mechanical components. Jing et al. [112] devised a simple method suitable for assessing fatigue behaviour of metallic materials subjected to proportional and non-proportional loadings. Andrea et al. [113] presented a critical plane multiaxial fatigue criterion, which is based on the Carpinteri-Spagnoli criterion. Maitoumam et al. [114] presented a general overview of a multiaxial fatigue life model for complex cyclic loading. Andrea et al. [115] reformulated a frequency domain critical plane

fatigue criterion for life estimation of smooth metallic structures under multiaxial random loading. Nima Shamsaei et al. [116] studied the fatigue life of steel and superalloys under multiaxial loading using the bulk material properties. Wang et al. [117] compares several multiaxial fatigue criteria. The criteria are broadly classified into stress, strain, and energy based multiaxial models.

## 2.7 Experimental Testing

Servo hydraulic-based fatigue testing systems are used for testing the fatigue life of structures up to  $10^7$  cycles. These systems operate at frequencies ranging between 20 Hz and 50 Hz. In general, a servo-hydraulic system comprises of a hydraulic cylinder which is driven by the servo-valve-feedback controller. When the thin film specimens are loaded with the hydraulic cylinder, they generate oil pressure driven displacements for each cycle. However, heat produced during the testing must be dissipated by using appropriate cooling [118]. For testing fatigue life of structural membranes beyond  $10^5$  cycles, the fatigue system must operate at frequencies higher than 1 kHz. For example, fatigue testing for  $10^9$  cycles takes about 7 months to 8 months using a conventional servo-hydraulic system. Therefore, voice coil-based servo-hydraulic fatigue systems operating on the principle of electrostatics have been developed. These systems use audio speakers to regulate pressure changes in hydraulic fluid and generate higher frequencies. Jill et al. [119] presented fatigue testing at higher frequencies using a 1 kHz servo-hydraulic fatigue testing system. Most of the servo-hydraulic fatigue systems are expensive and setting a custom-made hydraulic system is tedious.

Patrick et al. [120] designed a custom-made pressure chamber to test the performance characteristics of a next-generation fibre-optic pressure sensor for physiological applications. The pressure sensor was calibrated for a pressure range of 0 mmHg to 250 mmHg using

a hydraulic pressure regulation system (Ruska 7250, GE sensing, Houston, Texas). The custom-designed pressure rig was mounted on an Electro Force 3200 Test device (Bose Corporation, Eden Prairie, MN) to test the sensor device. The pressure sensor was subjected to a 0.02 Hz sawtooth signal of varying amplitude. The fatigue response of the thin film diaphragm was observed for 10000 cycles. However, the fatigue tests were conducted for low cycles. Most catastrophic failures occur at operating cycles beyond  $10^8$  cycles. Wanger et al. [121] studied gigacycle ( $10^9$  cycles) fatigue behaviour of austenitic steel at temperatures between  $600\text{ }^\circ\text{C}$  to  $700\text{ }^\circ\text{C}$  under fully reverse loading ( $R=-1$ ). Testing was performed on standard dog bone models. White [122] presented a review on the acoustic fatigue analysis of composite metallic aircraft structures. Chow et al. [123] discussed the acoustic fatigue failures in aircraft caused when the aircraft structures are subjected to randomly varying acoustic sounds from the engine. Some of the unclassified documents of armed services divulge that a sonic fatigue system has been an essential part of aircraft maintenance in the flight dynamics laboratory at Wright-Patterson air force base, Ohio, since March 1962 [124]. A sonic fatigue system has also been an integral part from 1982 in NASA for onboard aileron testing of L-101 aircraft [125]. The fatigue testing system comprises of a progressive wave horn with a siren to test the large mechanical structures.

## 2.8 Summary

The brief literature on the factors that impact the design of micro implantable pressure sensors for lifetime ICP monitoring has been reviewed. In the first section, the research on the nature and dynamics of ICP has been presented. Next, the literature on the external factors that affect ICP has been discussed. After that, the literature review on the design optimization of micro implantable pressure sensors including the selection of materials and specimens, FEM of thin film deflection and fatigue behavior, experimental validations have been delineated.

# Chapter 3

## Finite-Element Modelling and Simulations

### 3.1 Introduction

As discussed in the first chapter, the design of long-term reliable MEMS pressure sensors depends on the knowledge and insights into the mechanical behaviour of various materials. The internal material properties, grain size, and surface reactions of thin film materials may differ from bulk materials' properties. Besides, the MEMS manufacturing process, including deposition, etching, and metallization, can introduce additional stresses in the final product. Even though these stresses are relieved using thermal, cryogenic, and laser peening methods, the MEMS structures are still prone to fatigue and bulking in long-term usage. Thus, it is essential to study the mechanical behaviour of the MEMS structures.

In MEMS pressure sensors, the thin film membrane is a pressure sensitive element which is deposited onto a thick silicon substrate. The typical thicknesses of thin film membrane range between 4  $\mu\text{m}$  and 100 nm. These thin layers can be simulated with an appropriate

finite-element mesh via FEM. A FEM tool usually comprises of a solid mechanics physics module that can be utilized for analyzing the behaviour of thin film deflection and mechanical fracture. Linear elastic boundary conditions can be integrated into the structural model to simulate the thin film structures using stationary, time-dependent, frequency domain, and eigenfrequency. The FEM results would include von Mises stresses, Gauss-point evaluation principal stresses, total volumetric strains, elastic strain energy density, deviatoric stress tensors, thin film displacements, etc.

Besides, a fatigue multiphysics module can be added to the solid mechanics model to study the fatigue behaviour of thin film MEMS structures. In general, FEM based fatigue models are broadly classified into classical and multiaxial critical plane methods. Conventional fatigue models depend on S-N curve and include, S-N curve, Basquin model, approximate S-N curve, Coffin-Manson. These models are suitable for proportional loading that oscillates between two values. In contrast, multiaxial critical plane models search for the most critical stress raiser that promotes the crack initiation and propagation and solve fatigue life. These models are suitable for non-proportional and randomly varying loads. The critical plane fatigue module calculates fatigue usage factors which are seen as inversely proportional to a factor of safety. In this research work, COMSOL Multiphysics has been used to numerically simulate the mechanical behaviour of thin film membrane-based MEMS pressure sensor. The simulations include a finite-element-based parametric analysis, which includes the geometrical entries drawn both in two- and three-dimensional layers. The mechanical behaviour in the form of von Mises stresses volumetric strain, elastic strain energy density, thin film deflection, and fatigue usage factors are discussed.

This chapter presents the FEM of thin film deflection and fatigue behavior of thin film Ti membranes. In the first section, the theory of thin film deflection is discussed, which comprises of the underlying physics of thin film deflection, finite-element simulations and

parametric analysis of 2D and 3D thin film structures. In the last section, the fatigue behavior modeling is presented.

## 3.2 Theory of Thin Film Deflection

Modulus of Elasticity and residual stresses are the two mechanical properties that govern the mechanical compliance, sensitivity, and long-term reliability of the membrane-based MEMS pressure sensors [126, 127]. Since these properties are dependent on the deposition and etching processes during the MEMS fabrication, the stability of the thin-film material is difficult to predict at the initial design stages [128]. Therefore, it is essential to include FEM to study the structural behaviour of thin-film deflection and mechanical fatigue. In general, a thin film membrane experiences strain and bending due to external forces acting on the surface. A force acting on the surface of a thin-film membrane of an area ( $A_m = wt$ ), introduces stress and strains on the thin film. Hooke's law defines the relationship of the induced stress ( $\sigma$ ) and strain ( $\epsilon$ ) on the surface of thin film membrane. Equation 3.1 describes the relationship mathematically.

$$\frac{F}{A_m} \approx \sigma_m = E_m \epsilon_m \quad (3.1)$$

Where  $E_m$  is Young's modulus of thin film membrane and  $\epsilon_m$  is the strain the membrane experiences.

### 3.2.1 The Effect of Thin Film Stresses

The main parameters that govern the membrane displacement or deflection include (1) Stress due to straining, (2) Residual stresses, and (3) Bending due to applied pressure load. When a thin film membrane is subjected to an externally applied force, it experiences stress ( $\sigma_m$ ) and strain ( $\epsilon_m$ ) in the cross-section. If the resultant stresses and strains are not huge enough, the thin membrane goes back to its original position (Figure 3.1a)

In MEMS pressure sensors, the thin film membrane is deposited on a silicon substrate and should be considered as a rigid body. Thus, the membrane stretches and compresses to be able to remain fixed between the clamped position (Figure 2.9b). The residual stresses that often result from the MEMS microfabrication process also affect the thin film membrane deflection. For example, if the subjected pressure load is acting at the centre of the membrane, compressive residual stresses play an essential role in the deflection. As the residual stresses vary, the thickness of the thin film membrane also changes. The change in the width ( $\Delta w$ ) and thickness ( $\Delta t$ ) of a thin film membrane due to the straining is expressed mathematically in equation 3.2.

$$\Delta w \approx \nu \frac{\Delta l}{l} w; \Delta t \approx -\nu \frac{\Delta l}{l} t \quad (3.2)$$

The applied pressure load also generates bending due to the gradient of stresses over the entire thickness of the thin film membrane as shown in Figure 2.9c. This bending causes tensile stresses on one side and compressive stresses on the other side of the thin film membrane.

In general, the yield of a MEMS pressure sensor depends on the quantum of residual stresses remaining in the thin film membrane after the MEMS fabrication due to mismatches in the coefficient of thermal expansion between different material layers [129]. These stresses are

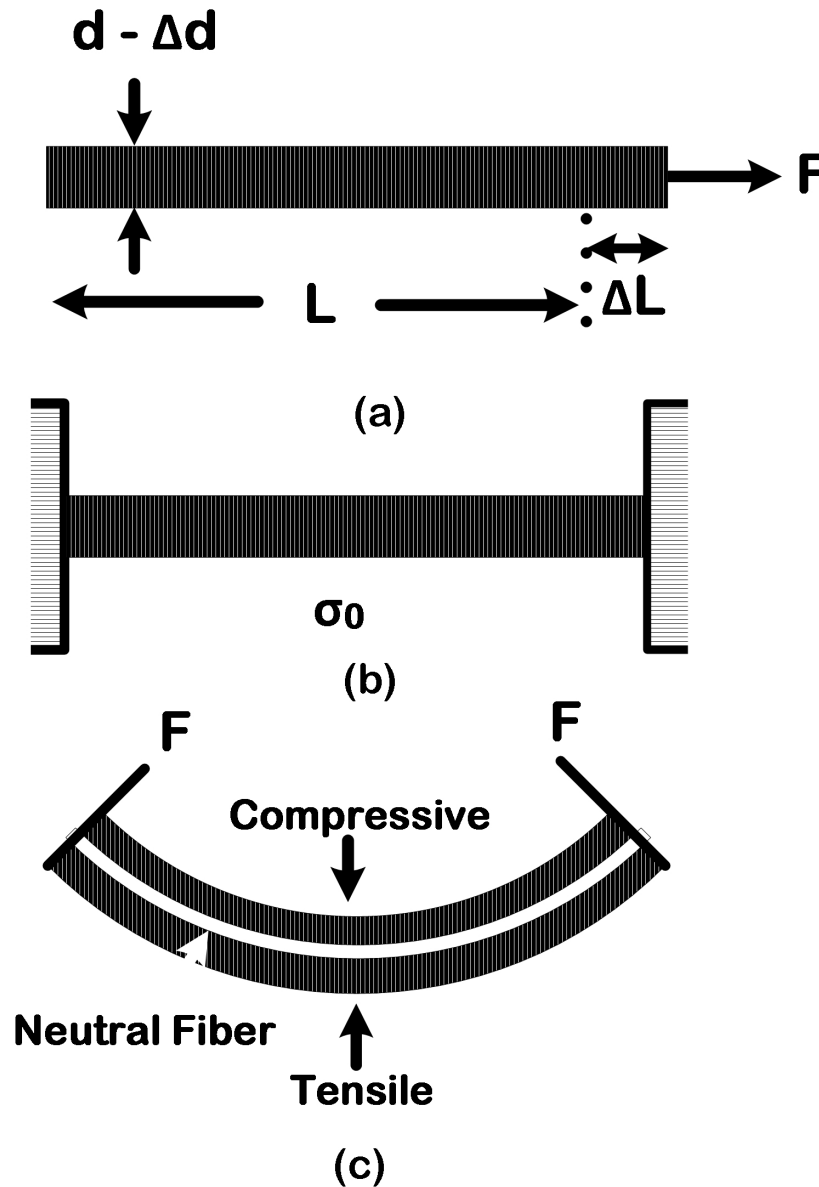


Figure 3.1 The pictorial representation showing the (a) the stress due to straining, (b) Residual stresses, (c) the stress due to deflection

intrinsic to the material and can lead to undesirable tension or compression forces, leading to buckling or cracking of the micro-structures. The effect is noticed after the release of structures at the final release etching process [130]. If the residual stresses are significantly small, the thin film may continue to behave normally. However, changes in the thin film are observed when subjected to externally applied forces. The residual stress in a thin film

membrane can be measured using Stoney's equation 3.3.

$$\sigma_0 = \frac{E_{sub} \cdot t_{sub}^2}{6 \cdot R(1 - \nu_s)t_f} \approx \frac{E_{sub} \cdot t_{sub}^2 \cdot \delta}{3L^2(1 - \nu_s) \cdot t_f} \quad (3.3)$$

Where,  $E_{sub}$  is the Young's Modulus,  $t_{sub}$  is the thickness,  $L$  is the length,  $\delta$  is the end deflection of a long thin film membrane,  $\nu_s$  is the Poisson ratio of the substrate material, Substituting  $R = \frac{L^2}{2\delta}$  results in the equation on the right-hand side.

The thin film membrane with residual tensile stress due to the externally applied pressure tends to peel off from the substrate and vice versa with the thin films with compressive residual stresses. Figure 3.2 shows the effect of the tensile and compressive residual stresses on a thin film membrane deposited on a silicon substrate.

### 3.2.2 Thin Film Deflection Model

Figure 3.3 shows the cross-section of thin film membrane deposited onto a silicon substrate.

The shape of the thin film after experiencing deflection ( $w$ ) due to externally applied pressure ( $\Delta P$ ) is a parabola, which is described by the equation 3.4.

$$w(r) = w_0 \left[ 1 - \left( \frac{r_a^2}{r_m^2} \right)^2 \right] \approx w(r) = \frac{\Delta P^2}{4\sigma_m h} \left[ 1 - \left( \frac{r_a^2}{r_m^2} \right)^2 \right] \quad (3.4)$$

Where,  $w_0$  is the displacement at the centre of the thin film membrane,  $r_m$  is the radius,  $r_a$  is the radial coordinate, and  $h$  is the thin film thickness

The forces of equilibrium at the periphery of the thin film membrane can help in determining the behaviour of deflection. Figure 3.2 shows the vertical force components, which include

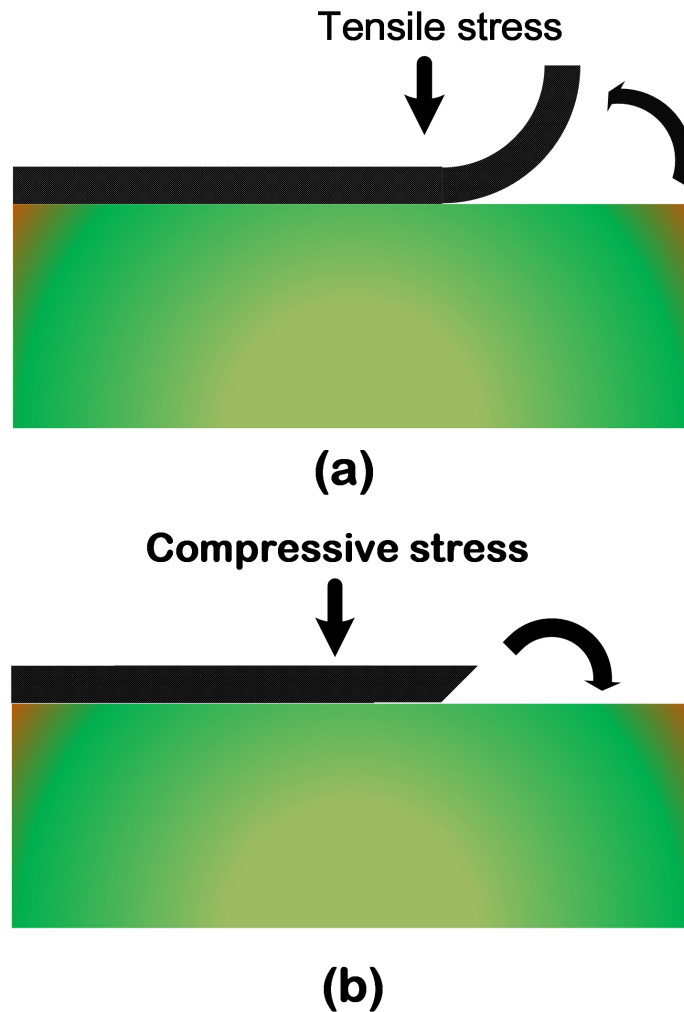


Figure 3.2 The conceptual diagram depicting the effect of (a) tensile, (b) compressive residual stresses on a thin film membrane deposited on a silicon substrate

the resultant force of the pressure drop and the balancing force from the silicon substrate. Both these vertical force components balance each other. Since there are no lateral movements of the thin membrane as it is fixed on all the sides, the total force ( $F_T$ ) acting on the circular thin film membrane will be the pressure exerting on the thin film times the area of the thin film. The pressure inside the intracranial volumes will be ICP ( $P_{ICP}$ ) and the external influence of atmospheric pressure fluctuations ( $P_{ATM}$ ). Equation 3.5 describes the total forces of equilibrium.

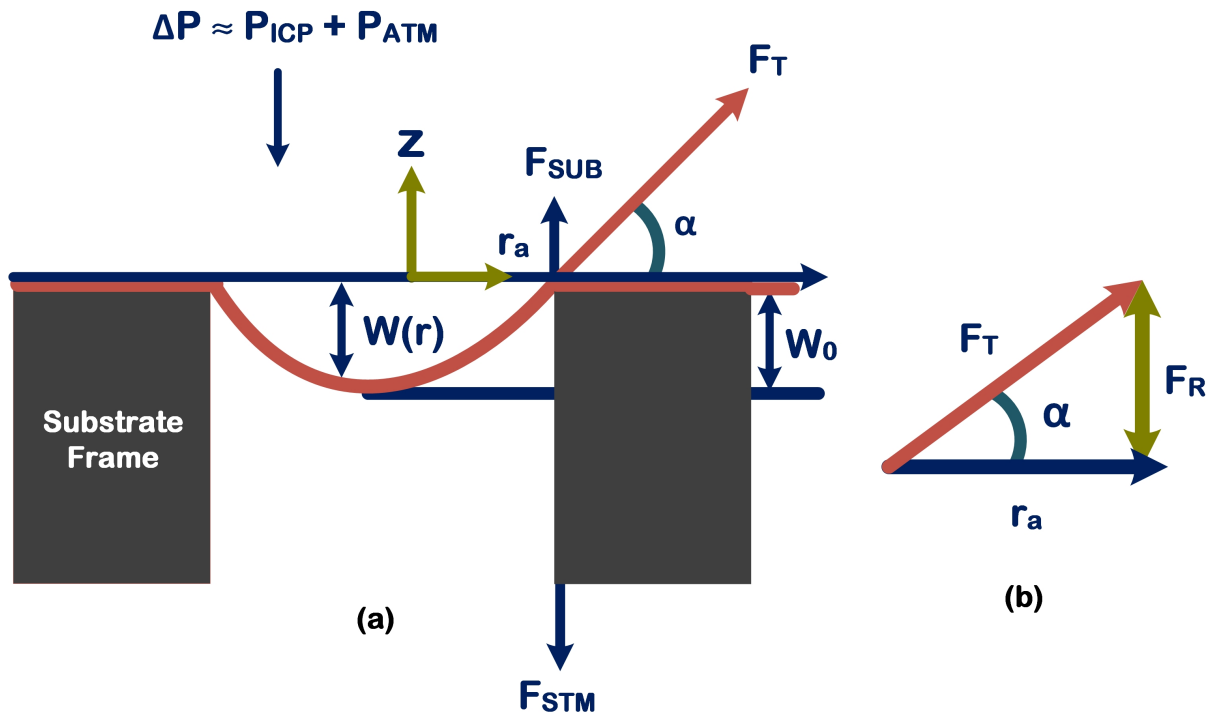


Figure 3.3 The force components of a membrane-based pressure sensor under deflection

$$F_T = \Delta P * \pi r_m^2 \approx P_{ICP} + P_{ATM} * \pi r_m^2 \quad (3.5)$$

The calculation of the total force ( $T_F$ ) depends on the thickness ( $t_m$ ) of the thin film membrane, the subjected stress ( $\sigma_m$ ) on the thin film and the circumference ( $2\pi r_m$ ), if the thin film is circular (Equation 3.6).

$$F_T = \Delta P * \pi r_m^2 \approx -\sigma_m * t_m * 2\pi r_m \sin(\alpha) \quad (3.6)$$

In the case of pressure monitoring inside the brain, the low-pressure loads would cause small deflections in the thin film membrane. Thus, the angle created would be tiny and for such small angles of  $\alpha$  in equation 3.6, the sine would be approximately equivalent to the tangent, which is the slope of the thin film membrane as shown in equation 3.7.

$$F_T = \Delta P * \pi r_m^2 \approx -\sigma_m * t_m * 2\pi r_m \tan(\alpha) \quad (3.7)$$

Thus, the applied pressure drop can be solved by taking the derivative of equation 3.8

$$\Delta P = \frac{4 * w_0 * t_m}{r_m^2} \sigma_m \quad (3.8)$$

It is essential to study the effect of stresses on the thin film membrane to improve the long-term reliability of MEMS pressure sensors for lifetime ICP monitoring. As discussed earlier, the stress due to straining, residual stresses, and bending stresses influence the long-term performances. Residual stresses result from the thermal expansion mismatches in the MEMS microfabrication process and are already present in the thin film before the application of the external pressure load. The stresses due to straining and bending stresses can be calculated from the resultant radial ( $\epsilon_r$ ) and tangential ( $\epsilon_t$ ) strains. Both these strains are described by Hooke's law (Equation 3.9)

$$\epsilon_r = \frac{\sigma_r}{E_m} + \nu_m \frac{\sigma_t}{E_m}; \epsilon_t = \frac{\sigma_t}{E_m} + \nu_m \frac{\sigma_r}{E_m} \quad (3.9)$$

In the finite-element simulations (FEA), to simulate the behaviour of stresses and strains in a thin film membrane, correct boundary conditions are necessary, which include the following in the case of radial and tangential strains.

1. Both the radial and tangential strains are equal at the centre of the thin film membrane because of symmetry (Equation 3.10).

$$\sigma_r = \varepsilon_r \frac{E}{1 - \nu_m} \quad (3.10)$$

2. Tangential strain is negligible at the periphery of the thin film membrane because there are no lateral movements (Equation 3.11).

$$\sigma_r = \varepsilon_r \frac{E}{1 - \nu_m^2} \quad (3.11)$$

The radial strain of the thin film membrane is the extension of neutral fibre (Figure 3.4) during the deflection. The radial strain necessary to bend the thin film membrane from the original position to the shape of a parabola (Figure 3.12) is given as

$$\varepsilon_r = \frac{2 w_0^2}{3 r_m^2} \quad (3.12)$$

The total stress of the thin film membrane ( $\sigma_m$ ) is the sum of residual stress ( $\sigma_0$ ), the stresses due to deflection (radial strain) and is described as equation 3.13

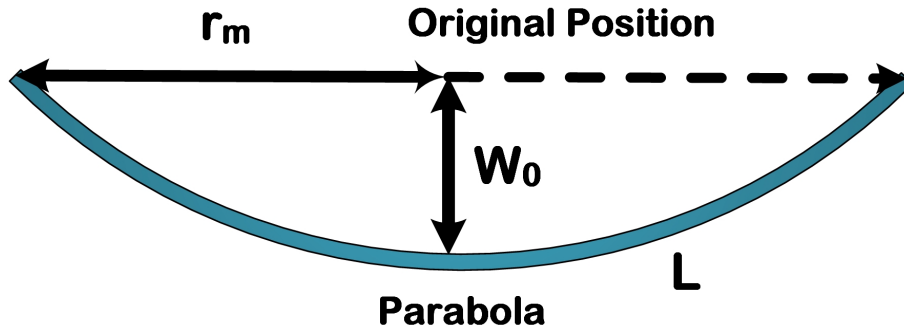


Figure 3.4 The shape of thin film deflection

$$\sigma_m = \sigma_0 + \frac{2 w_0^2}{3 r_m^2} \frac{E}{1 - \nu_m} \quad (3.13)$$

Substituting Equation 3.13 into Equation 3.8 gives Cabrera's equation, which is often used in the calculation of thin film membrane deflection.

$$\Delta P = \frac{4 * w_0 * t_m}{r_m^2} \sigma_m \approx 4 \frac{w_0 * t_m}{r_m^2} \left( \sigma_0 + \frac{2 w_0^2}{3 r_m^2} \frac{E}{1 - \nu^2} \right) \quad (3.14)$$

(or) for a square thin film membrane, Cabrera's equation would be 3.15

$$\Delta P \approx 13.6 \frac{w_0 * t_m}{s_m^2} \left( \sigma_0 + 1.61 \frac{w_0^2}{s_m^2} \frac{(1.446 - 0.427 \nu_m) E_m}{1 - \nu_m} \right) \quad (3.15)$$

If an entire sealed cavity MEMS circular membrane-based pressure sensor is considered, the thin deflection will be due to the pressure difference between the applied pressure and the vacuum (equation 3.16).

$$\Delta P \approx (P_{ICP} + P_{ATM}) = \frac{4t_m w_0}{r_m^2} \left( \frac{4}{3} \frac{t_m^2}{r_m^2} \frac{E_m}{1 - \nu_m^2} + \sigma_0 + \frac{64}{105} \frac{w_0^2}{r_m^2} \frac{E_m}{1 - \nu_m^2} \right) \quad (3.16)$$

(or) for a square membrane, the equation is described as 3.17

$$\Delta P \approx (P_{ICP} + P_{ATM}) = \frac{3t_m w_0}{s_m^2} \left( 20.9 \frac{E_m}{1 - \nu_m^2} \frac{t_m^2}{s_m^2} + 2.32(\sigma_x + \sigma_y) + 12.3 \frac{E_m}{1 - \nu_m^2} \frac{w_0^2}{s_m^2} \right) \quad (3.17)$$

The first term on the right side, in parenthesis, of equation 3.17 defines the bending moments, the second term describes the residual stress and the third term the stresses due to straining. The first term (bending moments) can be neglected in MEMS structures as they only dominate in macroscopic scale (when the mechanical structure is thick). The second term, the residual stress is a significant concern in the design and fabrication of MEMS pressure sensors. This would potentially hamper the long-term stability of the pressure sensor as it can combine with the cyclic stresses due to straining and cause mechanical fatigue and make the device vulnerable to drift.

### 3.2.3 Finite-Element Simulations

FEM of thin-film deflection was implemented using COMSOL Multiphysics [131]; geometrical entries were drawn in both 2D and 3D dimensions to study the thin-film membrane deflection and stress profiles. The geometries resemble a capacitive type MEMS pressure sensor with a thin-film membrane deposited onto the silicon substrate. Two layers were integrated into the geometry, which comprised of silicon as the substrate and titanium as a

thin-film membrane. A cavity has been created between the two layers to form a vacuum reference pressure measurement. A structural mechanics physics model was used to simulate the thin film deflection, stress and strain levels. The model design specifications are listed in Table 3.1. Figure 3.4a shows the atmospheric pressure oscillations plot as a Gaussian distribution. A Gaussian atmospheric oscillation with a mean of 100086.719 Pa and standard deviation of 724.233 87 Pa is plotted against pseudo-random numbers on time intervals between (0,1). Similarly, Figure 3.5b shows the ICP Plateau (A) plot by interpolating a discrete set of known plateau A values.

Table 3.1 The Design Specification of FEM model

<b>Input Load Parameters</b>	
ICP load	0 mmHg to 103 mmHg
Atmospheric load	756.54 mmHg to 769.61 mmHg
Total pressure load	0 mmHg to 827.61 mmHg
<b>Material Properties - Titanium alloy</b>	
Density	4430 kg m <sup>3</sup>
Young's Modulus	114 GPa
Poisson's Ratio	0.33
<b>Material Properties - Silicon substrate</b>	
Density	2329 kg m <sup>3</sup>
Young's Modulus	170 GPa
Poisson's Ratio	0.28

Initially, the FEM model assumes the linear elastic material properties with the isotropic solid model. The important material properties that govern the finite-element simulations

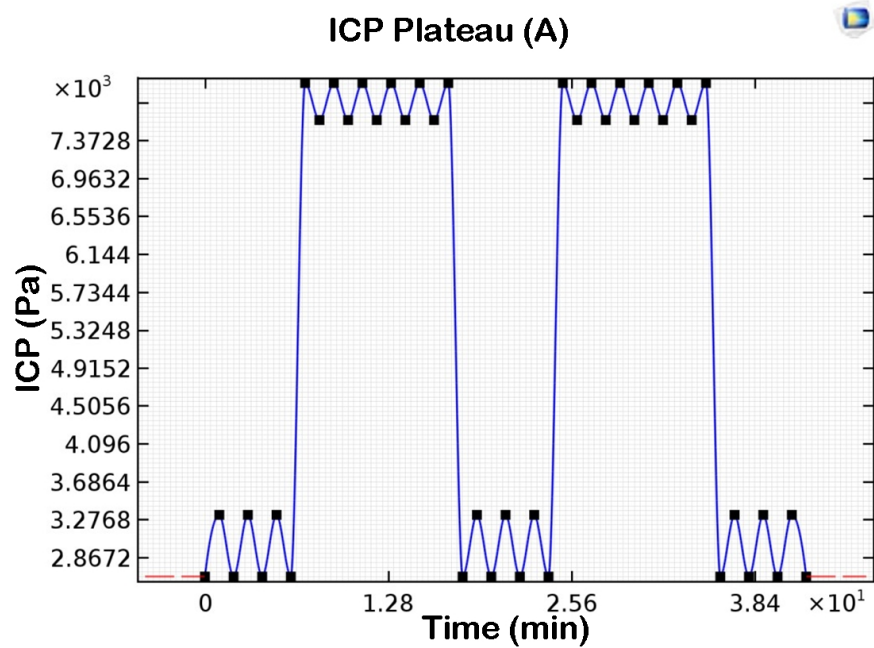
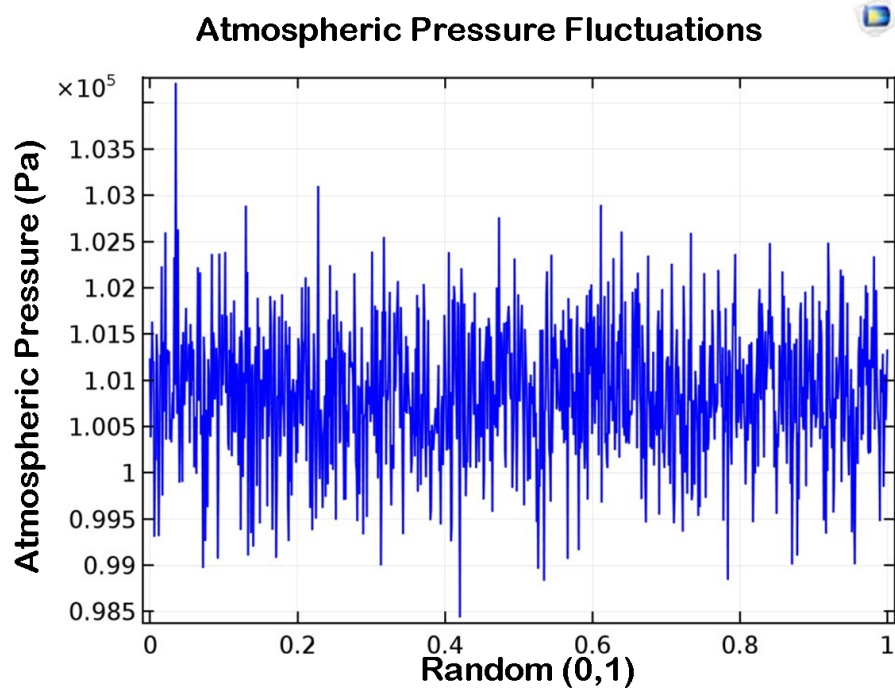


Figure 3.5 The input pressure load (a) Atmospheric pressure (b) ICP

(FEA) include Young's modulus and Poisson's ratio. The boundary conditions for the FEA of thin film deflection include:

1. When  $x=0$ , the membrane is fixed and movement is constrained.
2. The faces adjacent to the zero points are free to deform.
3. Prescribed displacement is added to the faces opposite to the zero point when  $u_z$  is 0.

The linear elastic deflections are described by the 4th order elasticity tensor  $C = C(E, \nu)$ ; and a set of stationary governing equations shown from 3.18a – 3.18e

$$0 = \nabla \cdot S + Fv \quad (3.18a)$$

Where  $S$  is the second Piola-Kirchoff stress in MPa and  $Fv$  is the volume force in  $N.m^{-3}$ . The linear elasticity of the thin film membrane is defined by the equations 3.18b and 3.18c.

$$S = S_{ad} + C : \epsilon_{el}; \epsilon = \epsilon - \epsilon_{inel} \quad (3.18b)$$

$$S_{ad} = S_0 + S_{ext} + S_q \quad (3.18c)$$

Where  $S_{ad}$  is the sum of the additional second Piola-Kirchoff stresses,  $S_0$  is the initial stress in the thin film membrane,  $S_{ext}$  is the external stress,  $S_q$  is the viscous damping stress, and  $C$  is the fourth order stiffness tensor.

$$\epsilon_{inel} = \epsilon_0 + \epsilon_{th} + \epsilon_{hs} + \epsilon_{pl} + \epsilon_{cr} \quad (3.18d)$$

Where  $\epsilon_0$  is the initial strain,  $\epsilon_{th}$  is the thermal strain tensor,  $\epsilon_{hs}$  is the hygroscopic strain tensor,  $\epsilon_{pl}$  is the plastic strain tensor and  $\epsilon_{cr}$  is the creep strain tensor.

$$\epsilon = \frac{1}{2}[(\nabla u)^2 + \nabla u] \quad (3.18e)$$

## Parametric Analysis

The thickness of a thin film membrane would significantly influence the nature of thin film deflection and in turn the fatigue behaviour. In other words, the thicker the diaphragm, the lesser the pressure transmission. In the FEA, the choice of the thickness of the Ti thin film membrane depended on (1) Availability of the material thickness in the market. For example, the commercially available Ti foils are in usually the range of 300  $\mu\text{m}$ , 250  $\mu\text{m}$ , 200  $\mu\text{m}$ , 150  $\mu\text{m}$ , 100  $\mu\text{m}$ , 50  $\mu\text{m}$ , 25  $\mu\text{m}$ , etc., and (2) The capability of deposition technique in MEMS microfabrication. For example, the thicknesses possible with physical vapour deposition such as evaporation and sputtering are in the range of 4  $\mu\text{m}$  and under. Thus, the thickness of 50  $\mu\text{m}$ , 25  $\mu\text{m}$ , 4  $\mu\text{m}$ , 1  $\mu\text{m}$ , 500 nm, and 200 nm were chosen for the parametric simulations of thin film deflection.

## 2D FEA Analysis

Figure 3.6 shows the 2D model of a MEMS capacitive pressure sensor comprising of a silicon substrate, cavity, and thin film membrane. The dimensions of the model are listed in the Table 3.2

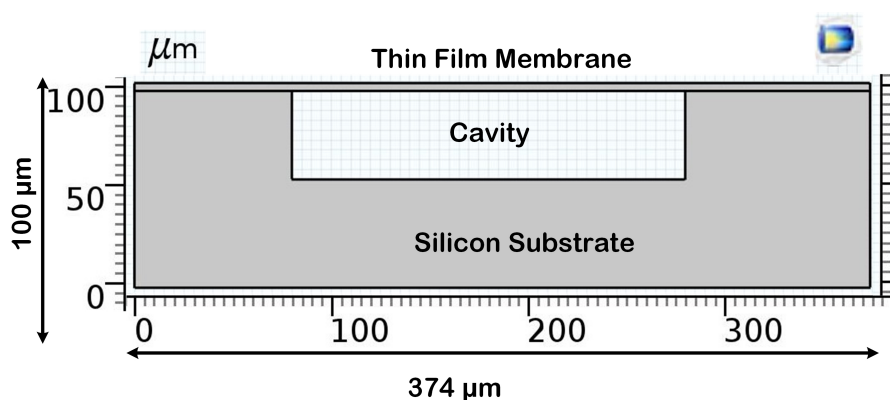


Figure 3.6 The 2D CAD model of MEMS pressure sensor

Table 3.2 The dimensions of 2D MEMS pressure sensor model

<b>Silicon Substrate</b>	
<b>Dimension</b>	<b>Value</b>
Width	374 mmHg
Height	100 mmHg
<b>Cavity</b>	
Width	200 $\mu\text{m}$
Height	45 $\mu\text{m}$
<b>Titanium Alloy</b>	
Width	374 $\mu\text{m}$
Height	50 $\mu\text{m}$ to 0.1 $\mu\text{m}$

The analysis started with the study of stresses, strains, elastic strain energy density, and thin film deflection of Ti membranes of seven different thicknesses (50  $\mu\text{m}$ , 25  $\mu\text{m}$ , 4  $\mu\text{m}$ , 1  $\mu\text{m}$ , 500 nm, and 200 nm). Figures 3.7a - 3.7d show the FEA plots of von Mises stress, thin film deflection, total volumetric strain, and elastic strain energy of 50  $\mu\text{m}$  thin film Ti sheets.

Figures 3.8a - 3.8d show the FEA plots of von Mises stress, thin film deflection, total volumetric strain and elastic strain energy density of 25  $\mu\text{m}$  thin film Ti sheets.

The thicknesses of Ti membrane (50  $\mu\text{m}$  and 25  $\mu\text{m}$ ) are very thick. The strain induced in such a thick membrane (due to cyclic stress loads), is transferred onto the silicon. The effect can be observed in Figure 3.7c and 3.8c. In MEMS fabrication, the deposition equipment cannot process such thicknesses. Even if these thicknesses are possible with MEMS deposition processes, they tend to peel off due to repeatedly applied cyclic stresses (Figure 3.2). Elastic strain energy signifies the relationship between the material's strain

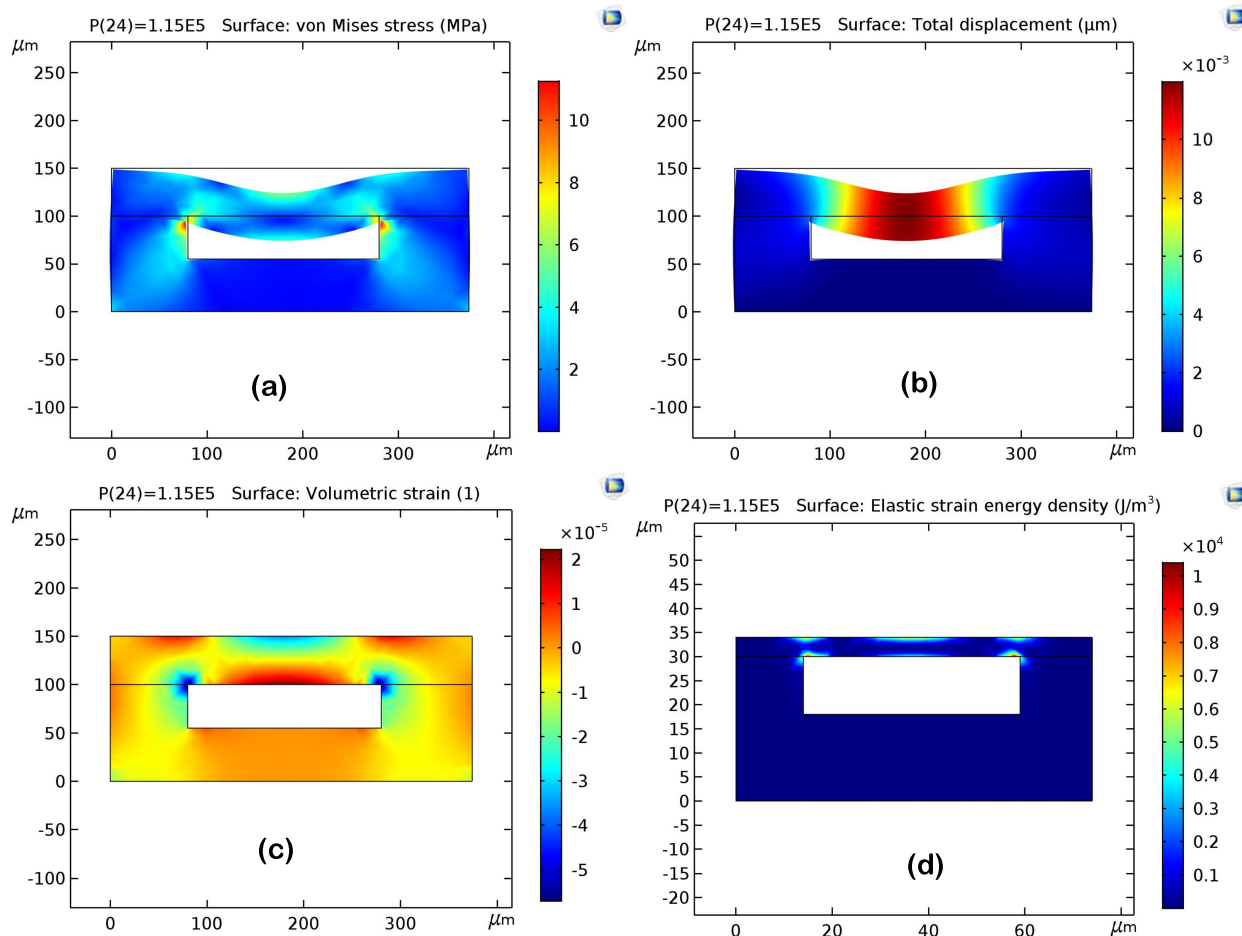


Figure 3.7 The FEA plots showing (a) von Mises stresses, (b) Total displacement, (c) Total volumetric strain, (d) Elastic strain energy density of 50  $\mu\text{m}$  thin film Ti sheet

energy and the deformation gradient (which is a function of stored energy). Equation 3.19 shows the relation between the deformation gradient and stored energy. Figures 3.8c and 3.8d show the elastic strain energy density plot of 25  $\mu\text{m}$  and 4  $\mu\text{m}$  respectively.

$$W = \rho_0 u \quad (3.19)$$

Figures 3.9a - 3.9d shows the FEA plots of von Mises stress, thin film deflection, total volumetric strain and elastic strain energy density of 4  $\mu\text{m}$  thin film Ti sheets.

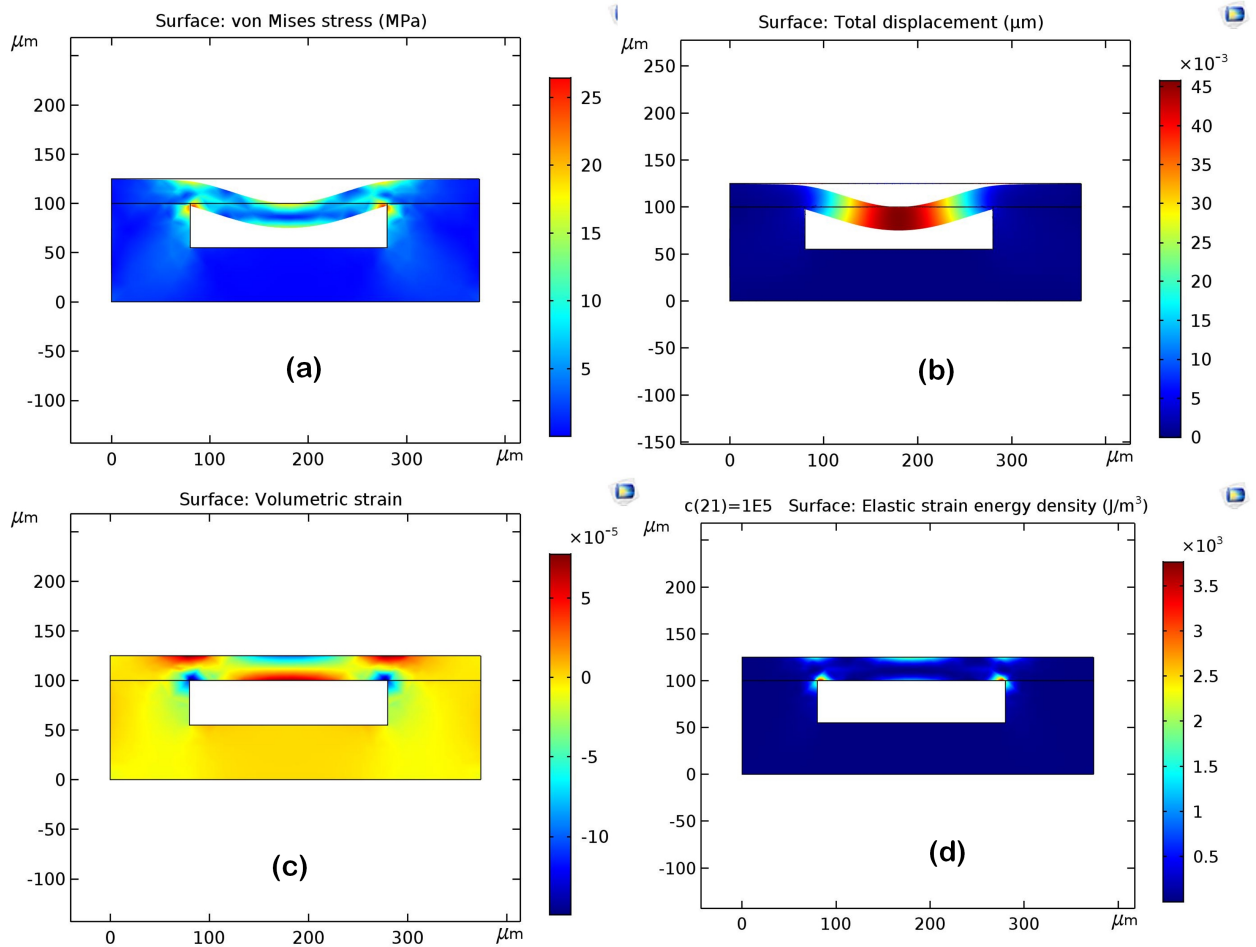


Figure 3.8 The FEA plots showing (a) von Mises stresses, (b) Total displacement, (c) Total volumetric strain, (d) Elastic strain energy density of 25  $\mu\text{m}$  thin film Ti sheet

Figures 3.10a - 3.10d shows the FEA plots of von Mises stress, thin film deflection, total volumetric strain and elastic strain energy density of 1  $\mu\text{m}$  thin film Ti sheets.

Figures 3.11a - 3.11d shows the FEA plots of von Mises stress, thin film deflection, total volumetric strain and elastic strain energy density of 500 nm thin film Ti sheets.

Figures 3.12a - 3.12d shows the FEA plots of von Mises stress, thin film deflection, total volumetric strain and elastic strain energy density of 200 nm thin film Ti sheets.

In addition to the stresses due to deflection (stresses due to straining and bending), residual stresses also play an important role in MEMS pressure sensors. The residual stresses are a

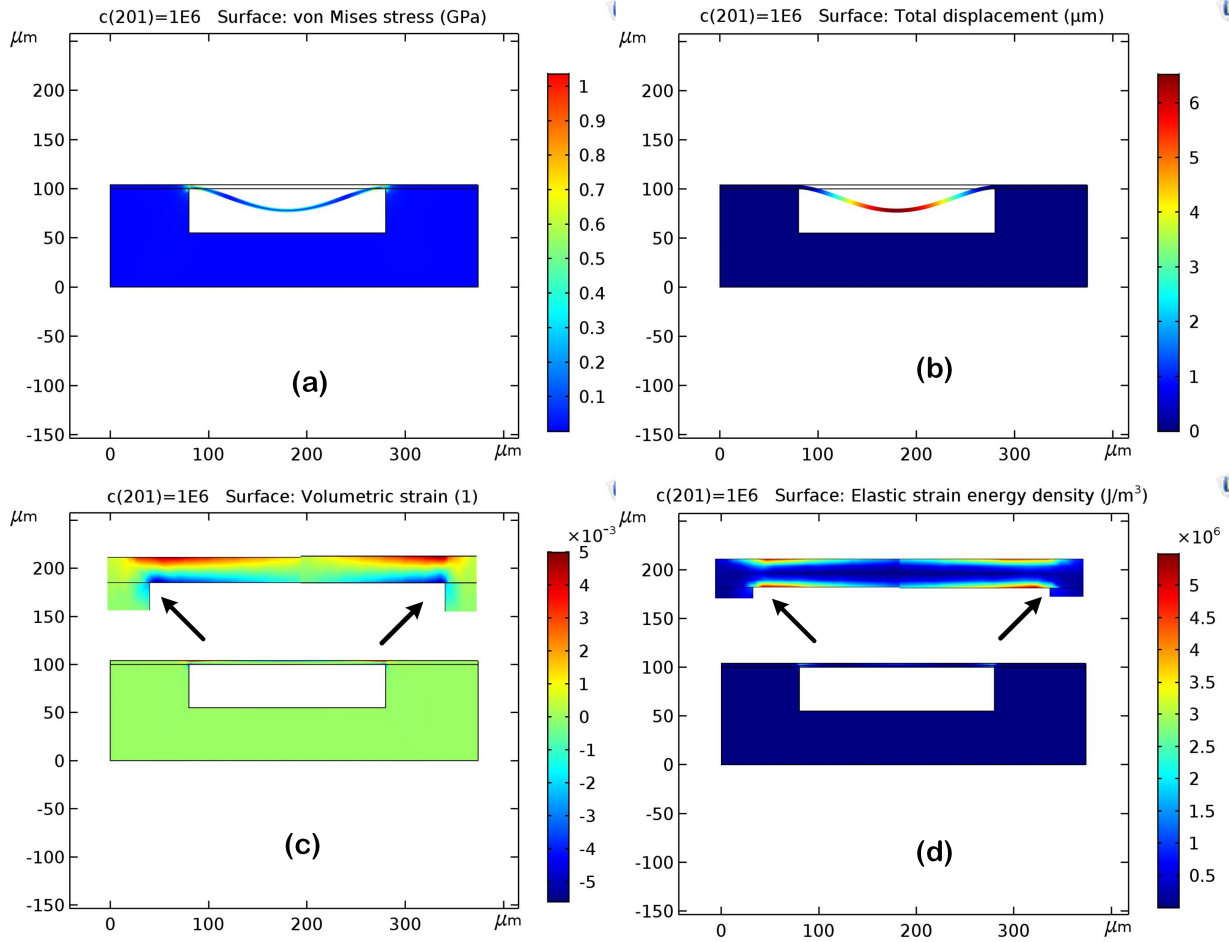


Figure 3.9 The FEA plots showing (a) von Mises stresses, (b) Total displacement, (c) Total volumetric strain, (d) Elastic strain energy density of 4 μm thin film Ti sheet

result of the mismatches in the thermal expansion between the substrate and the thin film membrane. The coefficients of thermal expansion of Silicon and titanium are  $8.60 \times 10^6 \frac{1}{K}$  and  $2.60 \times 10^6 \frac{1}{K}$  respectively. The effect of thermal expansion was added to the 2D model of a MEMS capacitive pressure sensor. The equation 3.20 represents the strain due to the coefficient of thermal expansion.

$$\varepsilon_{th} = \alpha(T_0)(T_0 - T_{ref}) \quad (3.20)$$

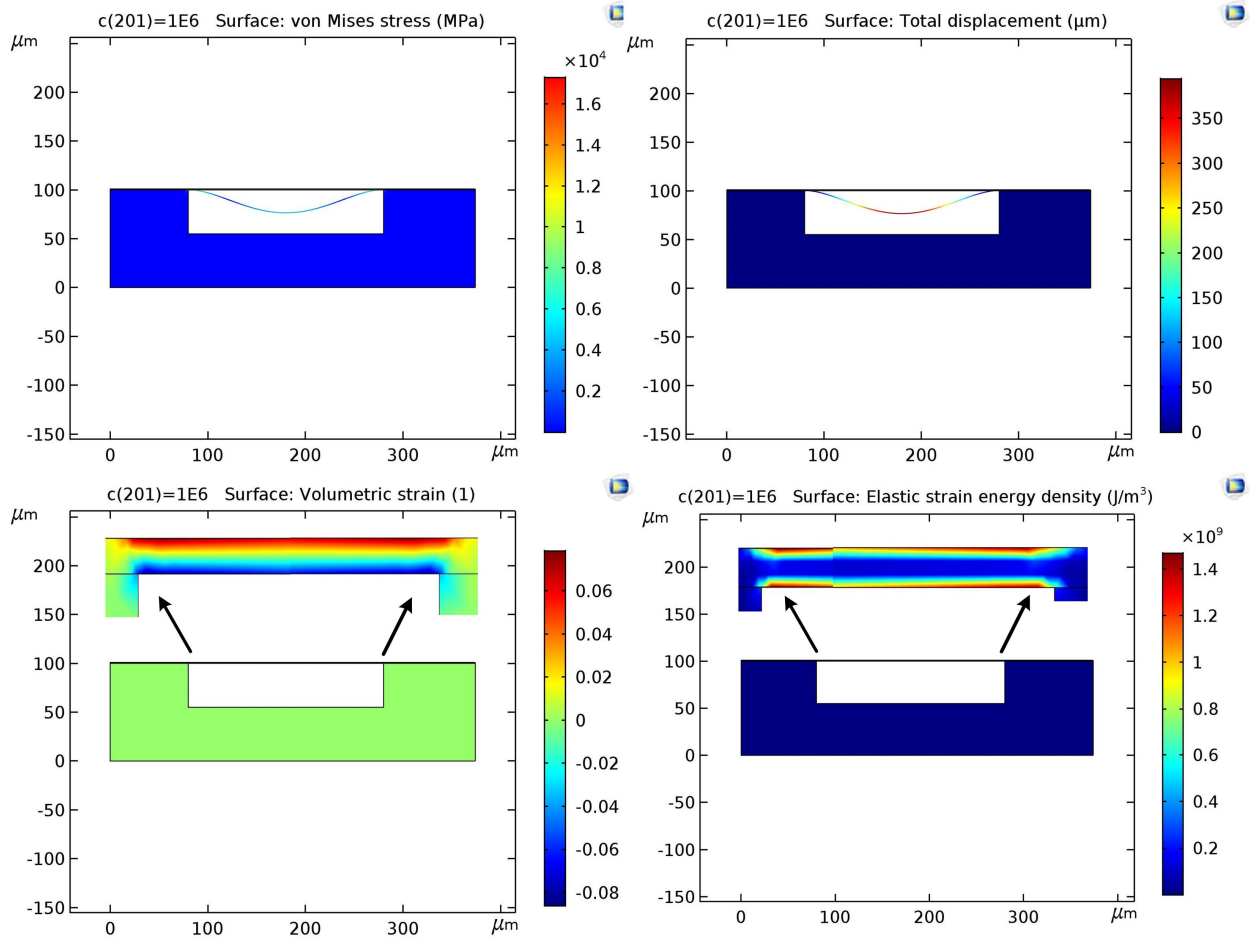


Figure 3.10 The FEA plots showing (a) von Mises stresses, (b) Total displacement, (c) Total volumetric strain, (d) Elastic strain energy density of 1 μm thin film Ti sheet

Where  $\alpha$  is the coefficient of thermal expansion of materials,  $T_0 = 45^\circ\text{C}$  and  $T_{ref} = 374^\circ\text{C}$ .

Figure 3.13 shows the residual stress behaviour and thin film deflection of 50 μm thin film Ti membrane.

Figure 3.14 shows the residual stress behaviour and thin film deflection of 25 μm thin film Ti membrane.

Figure 3.15 shows the residual stress behaviour and thin film deflection of 4 μm thin film Ti membrane.

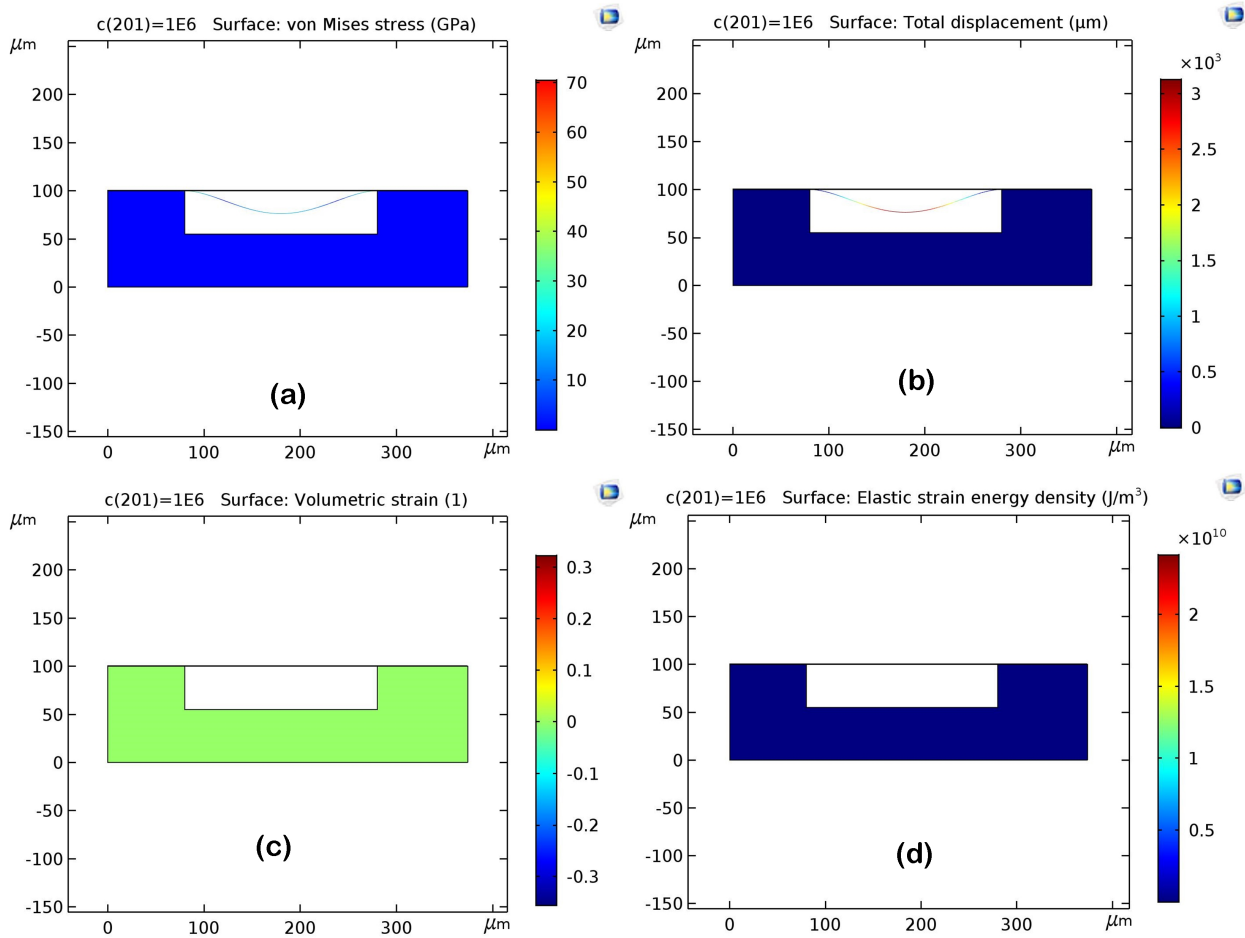


Figure 3.11 he FEA plots showing (a) von Mises stresses, (b) Total displacement, (c) Total volumetric strain, (d) Elastic strain energy density of 500 nm thin film Ti sheet

Figure 3.16 shows the residual stress behaviour and thin film deflection of 1  $\mu\text{m}$  thin film Ti membrane.

Figure 3.17 shows the residual stress behaviour and thin film deflection of 500 nm thin film Ti membrane.

Figure 3.18 shows the residual stress behaviour and thin film deflection of 200 nm thin film Ti membrane.

As discussed earlier, the fully implantable pressure sensors would be potentially implanted inside the brain and interact with corrosive fluid at 37 °C. Thus, it is essential to analyze

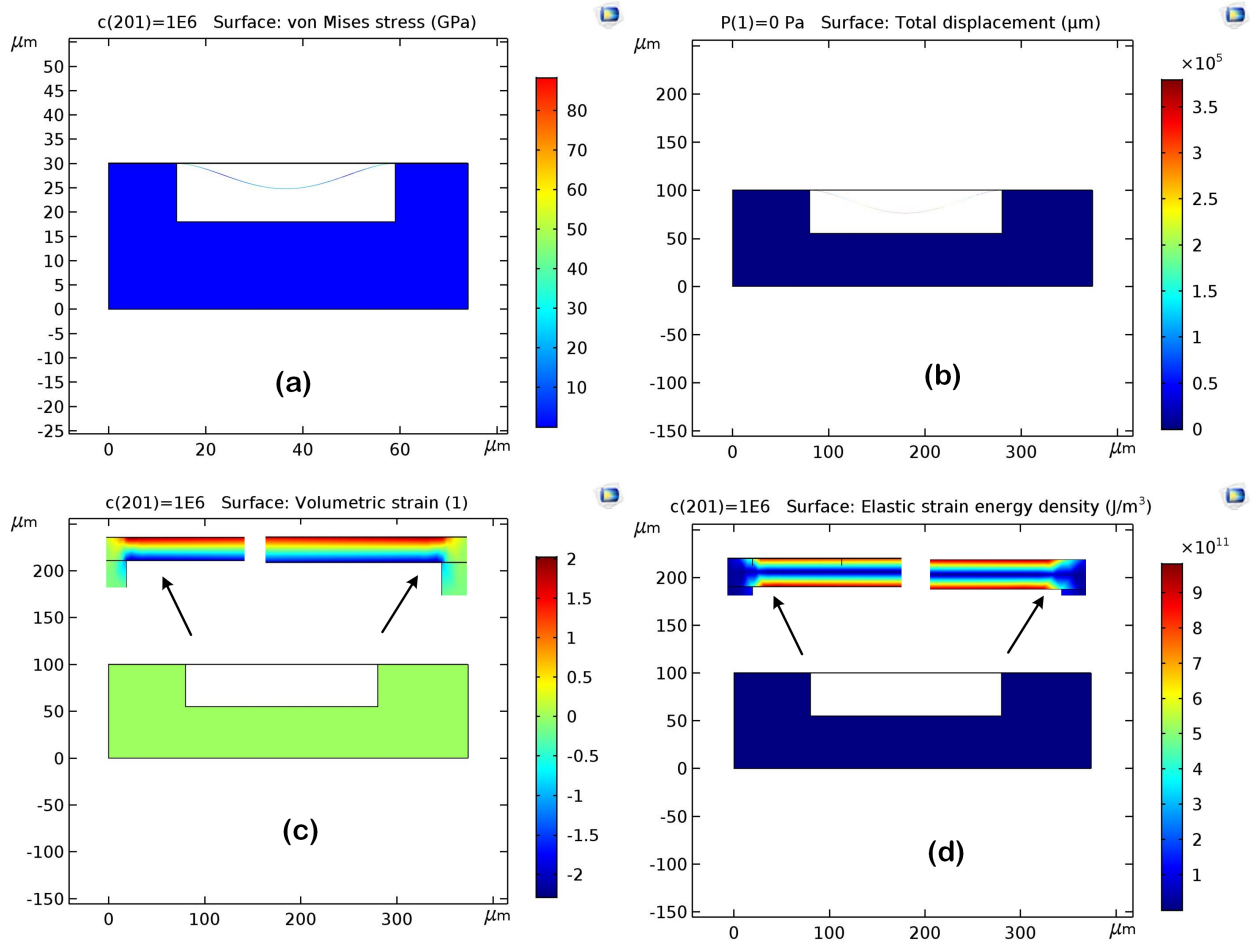


Figure 3.12 The FEA plots showing (a) von Mises stresses, (b) Total displacement, (c) Total volumetric strain, (d) Elastic strain energy density of 200 nm thin film Ti sheet

the transmission of fluid pressure, which is the pressure change occurring inside the closed cranium. Pascal's law states that the pressure change inside a confined incompressible fluid is almost the same everywhere. Fluid-structure associated with the thin film Ti membrane has been simulated for the above-considered thicknesses to study their pressure transmission capability.

Figure 3.19 shows the CAD model of the fluid-structure interaction. It comprises of a fluid medium with the direction of the fluid flow and thin membrane fixed at vertically to study the effect of fluid pressure transmission on the thickness of thin film membrane.

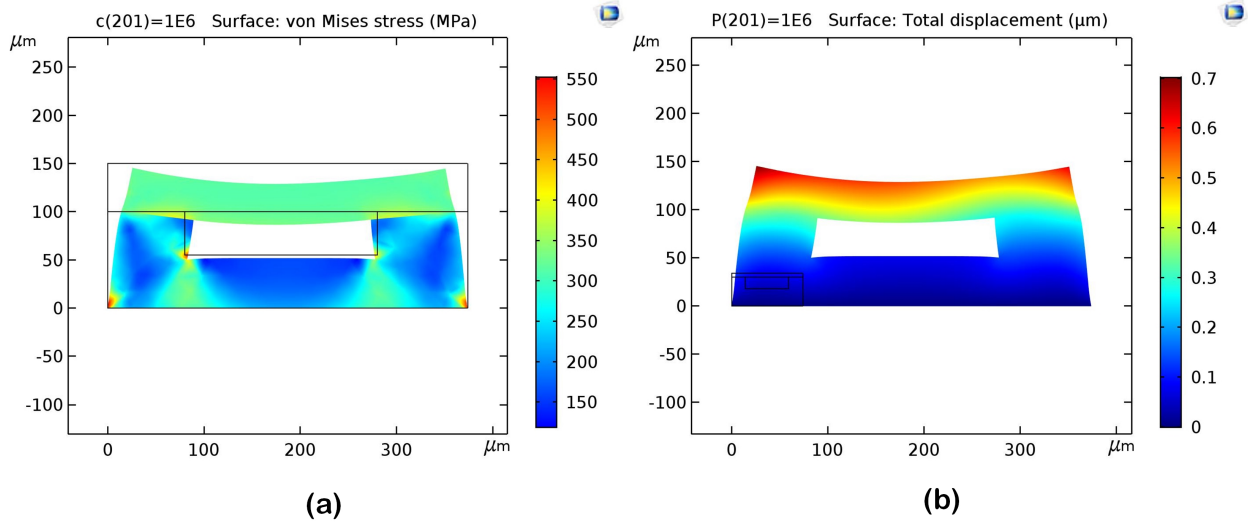


Figure 3.13 The FEA plots showing (a) von Mises stresses, (b) Total displacement of 50  $\mu\text{m}$  thin film Ti sheet due to mismatches in thermal expansion

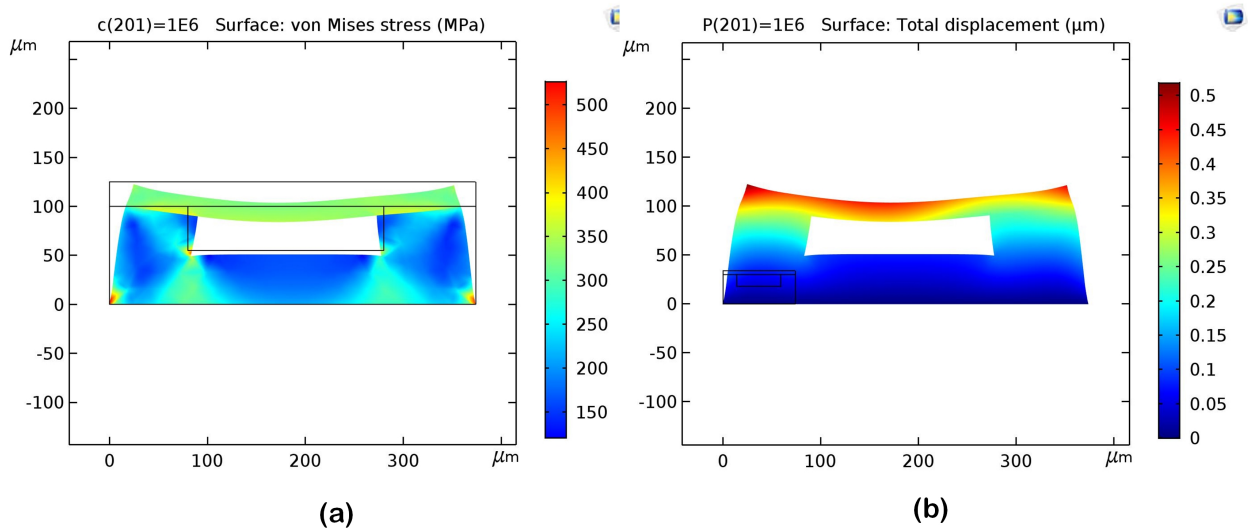


Figure 3.14 The FEA plots showing (a) von Mises stresses, (b) Total displacement of 25  $\mu\text{m}$  thin film Ti sheet due to mismatches in thermal expansion

Incompressible Navier-Stokes equation shown in the Equation 3.21 describes the fluid flow in the fluid medium.

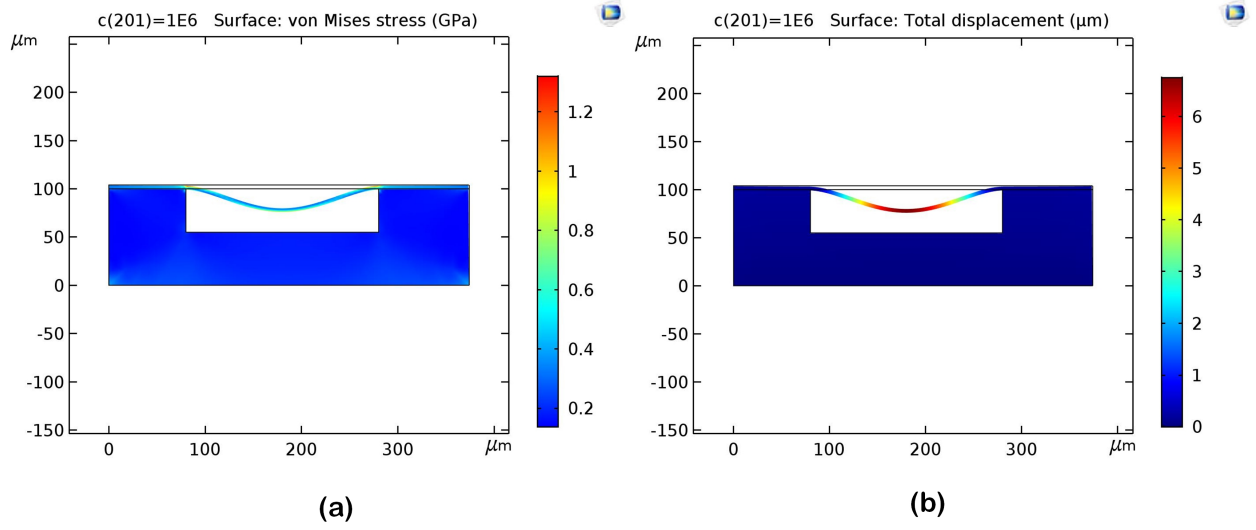


Figure 3.15 The FEA plots showing (a) von Mises stresses, (b) Total displacement of 4  $\mu\text{m}$  thin film Ti sheet due to mismatches in thermal expansion

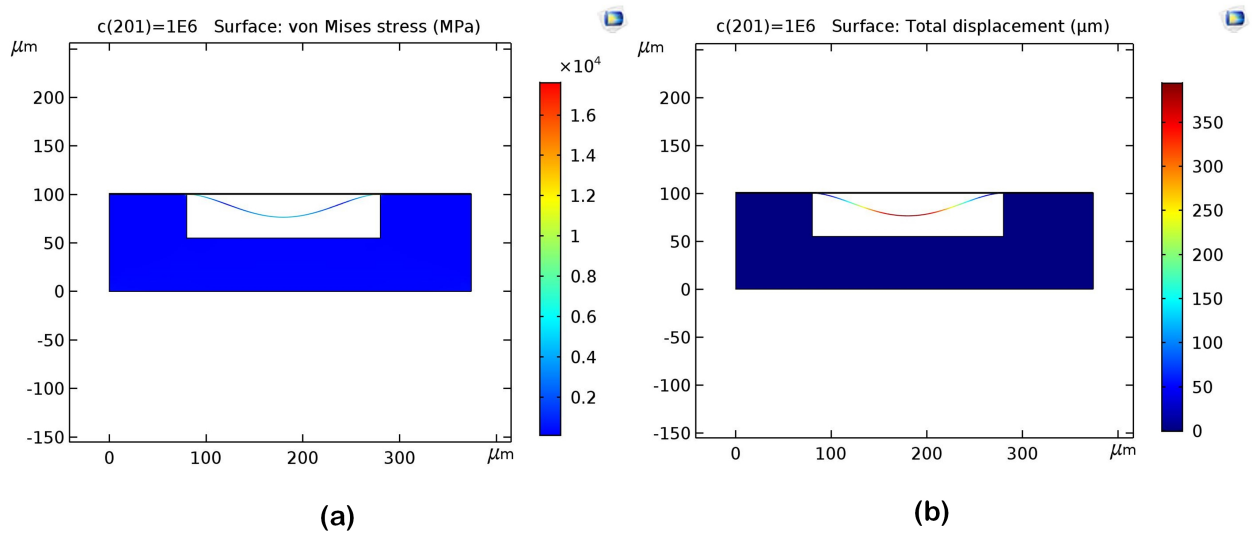


Figure 3.16 The FEA plots showing (a) von Mises stresses, (b) Total displacement of 1  $\mu\text{m}$  thin film Ti sheet due to mismatches in thermal expansion

$$\rho \frac{\partial u}{\partial t} - \nabla \cdot [-pI + \eta(\nabla u + (\nabla u)^T)] + \rho((u - u_m) \cdot \nabla)u = F - \nabla \cdot u = 0 \quad (3.21)$$

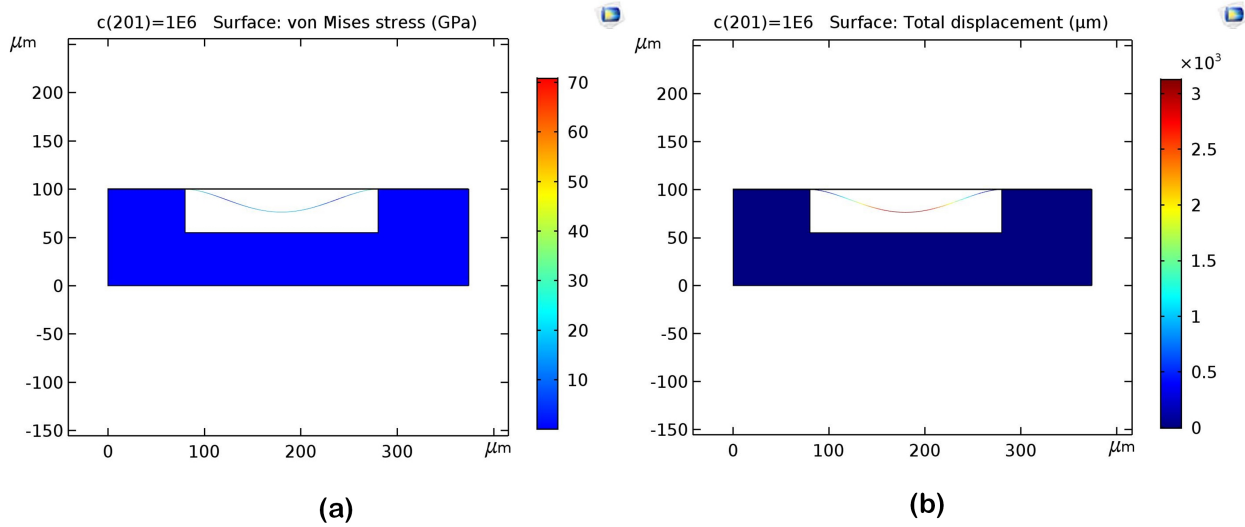


Figure 3.17 The FEA plots showing (a) von Mises stresses, (b) Total displacement of 500 nm thin film Ti sheet due to mismatches in thermal expansion

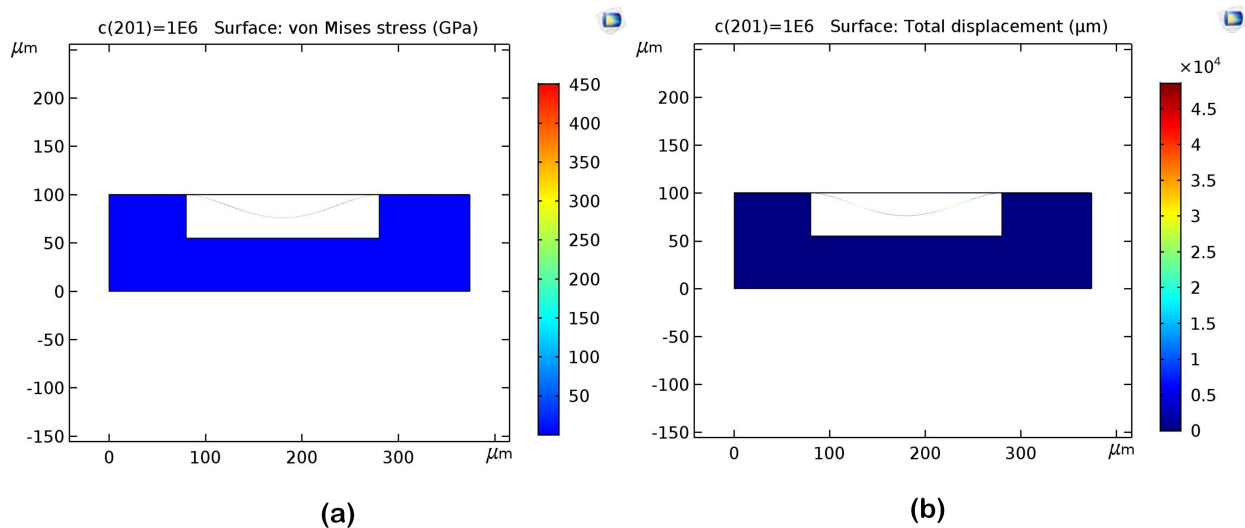


Figure 3.18 The FEA plots showing (a) von Mises stresses, (b) Total displacement of 200 nm thin film Ti sheet due to mismatches in thermal expansion

Where  $\mathbf{u} = (u,v)$  is the velocity field,  $p$  is the pressure,  $\mathbf{I}$  is the unit diagonal matrix,  $\mathbf{F}$  is the volume force affecting the fluid.

The input velocity is characterized by laminar flow, and the inflow boundary conditions are described as shown in the equation 3.22

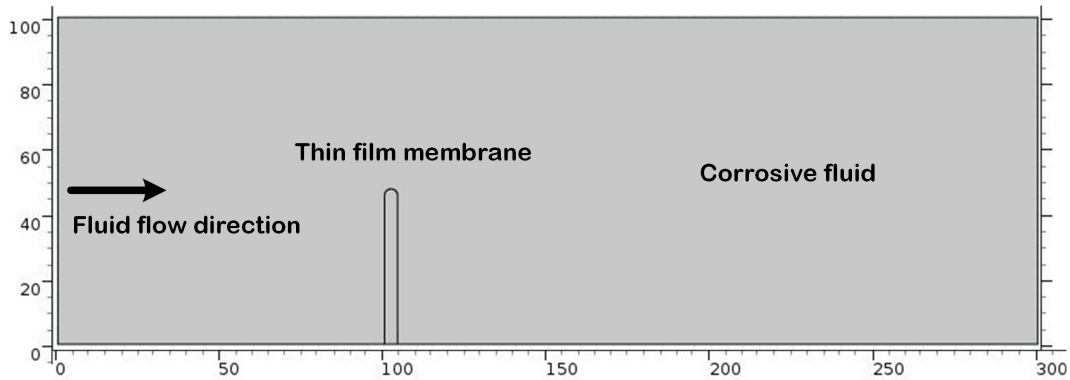


Figure 3.19 The 2D CAD model for FSI analysis

$$u_v = \frac{A \cdot t^2}{\sqrt{(0.04 - t^2)^2 + (0.1t)^2}} \quad (3.22)$$

Where  $u_v$  is the input velocity of the fluid flow,  $A$  is the amplitude, and  $t$  is the time period in seconds.

The boundary conditions at the outflow are set such a way that the pressure is zero and there are no slip conditions. Figure 3.20 and 3.21 shows the FSI of 25  $\mu\text{m}$  and 4  $\mu\text{m}$  thin film Ti membranes.

Table 3.3 compares the thin film deflection, stress behaviour, and pressure transmission of thin film Ti membranes of various thickness and dimensions.

To study the thin film deflection and fatigue behaviour, a 3D analysis of a MEMS Pressure sensor may provide a more realistic view of the underlying physics of the device. Figure 3.22 shows the 3D model of a MEMS capacitive pressure sensor.

Figures 3.23 – 3.27 shows the plot of mechanical behaviour of 50  $\mu\text{m}$ , 25  $\mu\text{m}$ , 4  $\mu\text{m}$ , 1  $\mu\text{m}$ , 500 nm, and 200 nm thin films in 3D

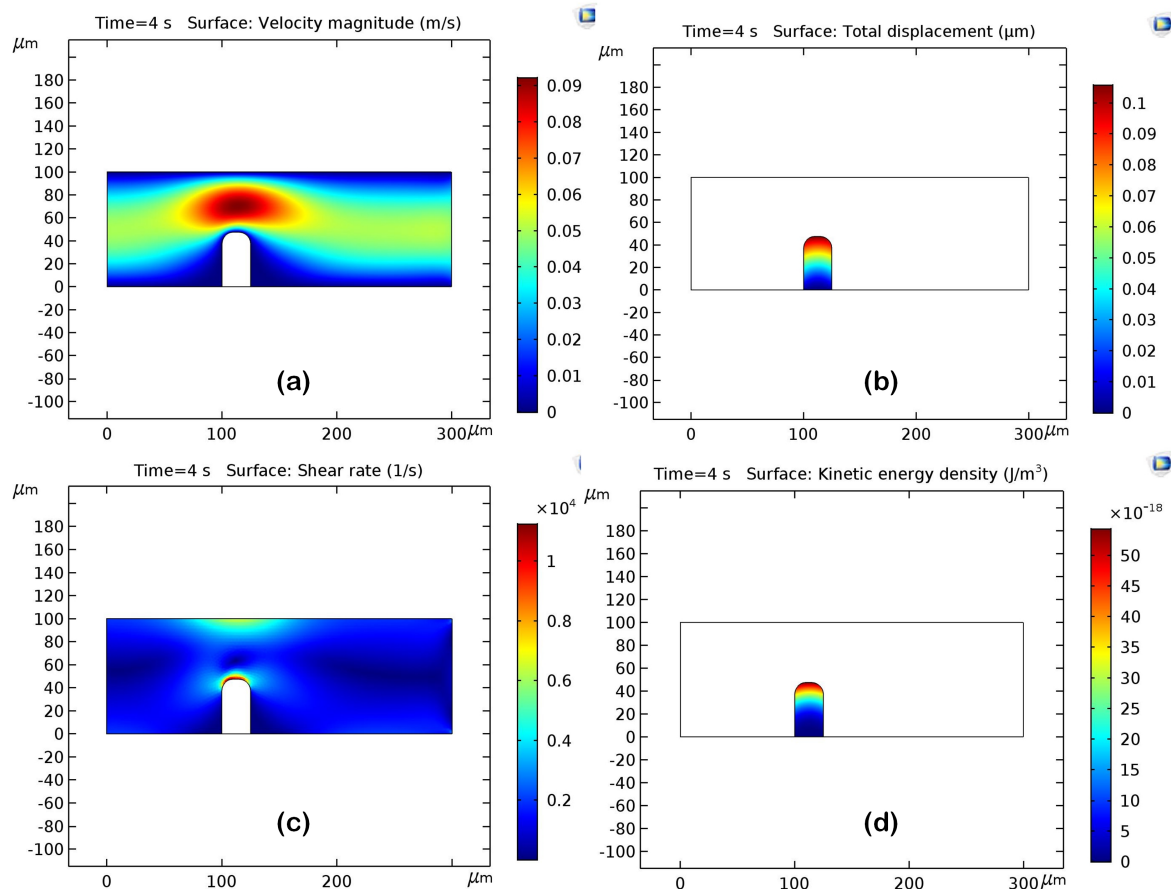


Figure 3.20 The FEA plots of 25  $\mu\text{m}$  thin film showing (a) velocity magnitude, (b) displacement of thin film in fluid, (c) shear rate of the thin film membrane, (d) kinetic energy density

### 3.3 Fatigue Behaviour Modelling

The concept of fatigue emanated after the disaster of de Havilland's Comet airliner - BOAC Flight 781 - in the year 1954. Fracture mechanics was introduced for the first time (based on the Griffith criterion) into the investigation and the initial crack size that caused the catastrophe was estimated to be around 100  $\mu\text{m}$ . Fatigue is understood to be a localized and permanent structural damage to the thin-film membranes subjected to constant cyclic loads [132].

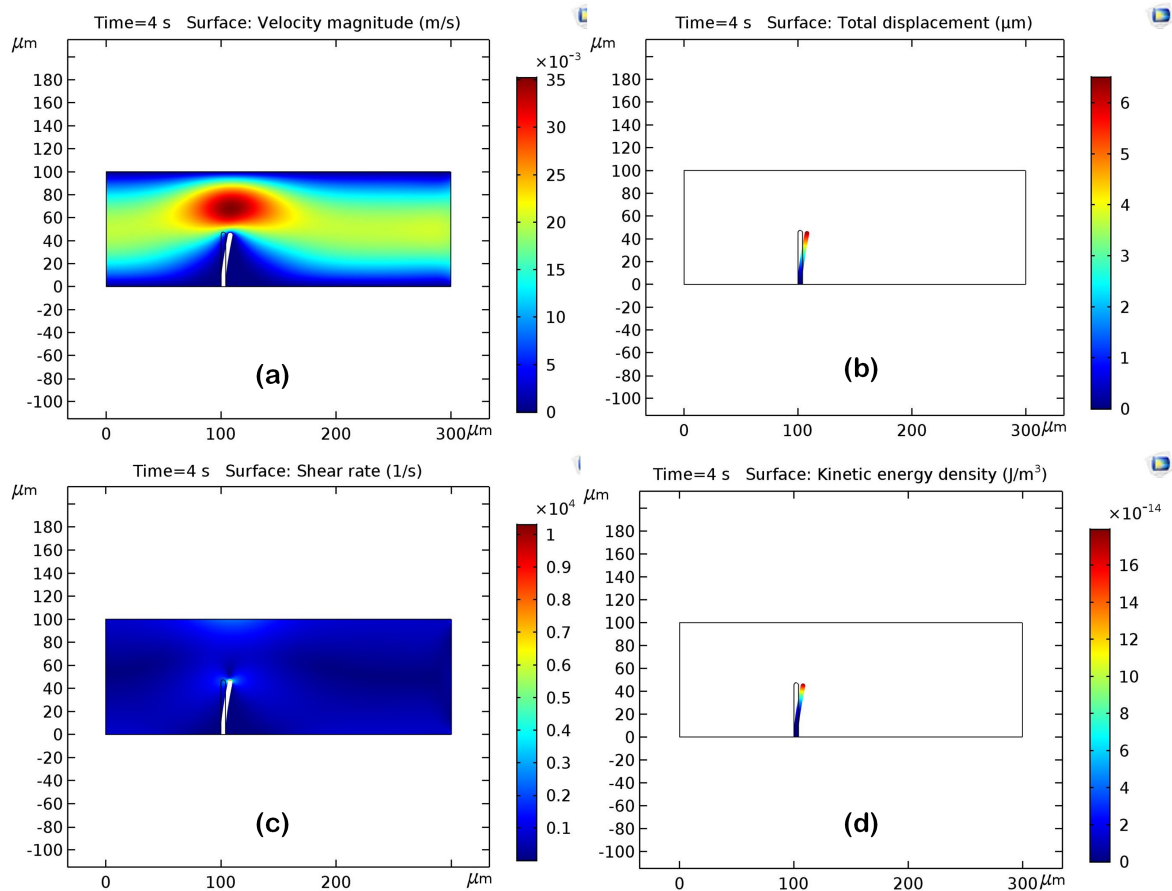


Figure 3.21 The FEA plots of  $4\ \mu\text{m}$  thin film showing (a) velocity magnitude, (b) displacement of thin film in fluid, (c) shear rate of the thin film membrane, (d) kinetic energy density

A fatigue process is assumed to begin microscopically from slip bands inside the material that is subjected to cyclic plastic deformation [133]. After the crack is initiated, it is driven by tensile and shear strains along the slip bands. Over several cycles, the slip bands generate intrusions and extrusions that begin to form a macroscopic crack. Initially, the macroscopic cracks propagate along the slip planes, but eventually grows transversely in the direction of normal stress [134]. Figure 3.28 shows the intrusion and extrusion model of crack growth.

In biomedical applications, the average stress is often low, however, the local stress risers can aggravate the crack growth process. When the thin film membrane is subjected to randomly varying external loads in the presence of intrusions and extrusions, the crack propagates over several cycles culminating in catastrophic failure []. Figure 3.29 shows the fatigue process

Table 3.3 The comparison of deflection, stress due to deflection, residual stress, transmission

Thickness	Deflection	Stress due to deflection	Residual Stress	Transmission
50 $\mu\text{m}$	0.01 $\mu\text{m}$	10 MPa	550 $\mu\text{m}$	Low
25 $\mu\text{m}$	0.45 $\mu\text{m}$	10 MPa	550 $\mu\text{m}$	Low
4 $\mu\text{m}$	6 $\mu\text{m}$	1 GPa	1.2 GPa	Good
1 $\mu\text{m}$	350 $\mu\text{m}$	16 GPa	16 GPa	Good
500 nm	3000 $\mu\text{m}$	70 GPa	370 GPa	High
200 nm	3500 $\mu\text{m}$	80 GPa	450 GPa	High

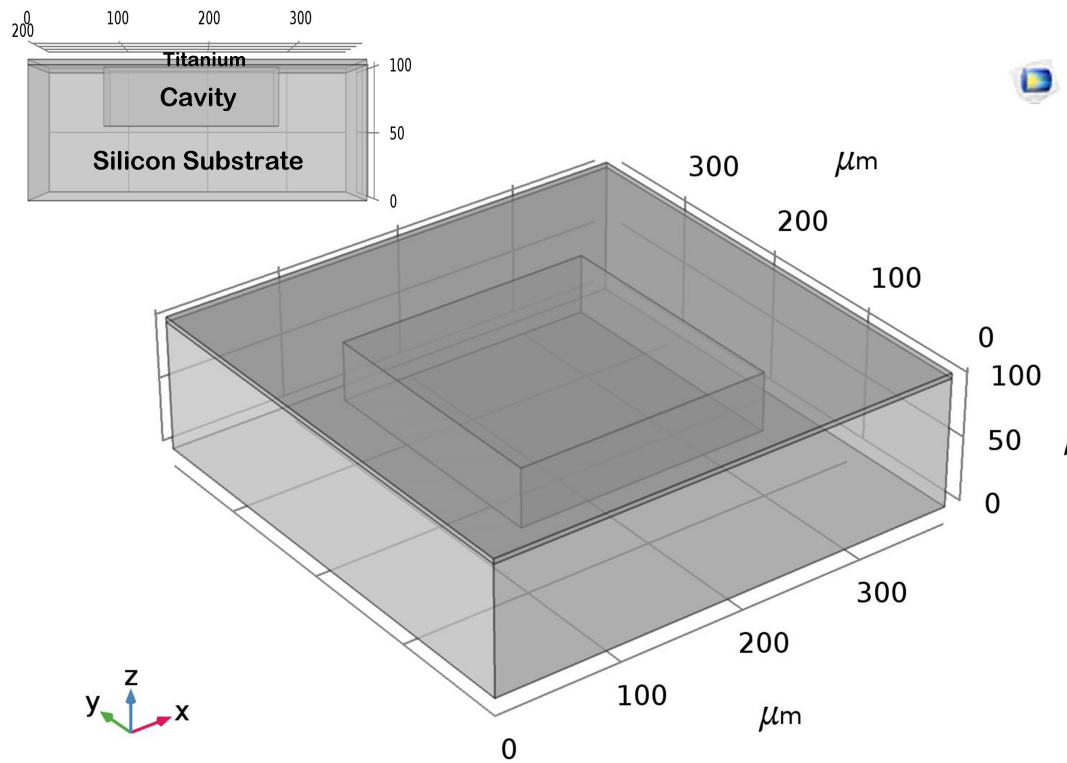


Figure 3.22 The 3D CAD model of MEMS capacitive pressure sensor

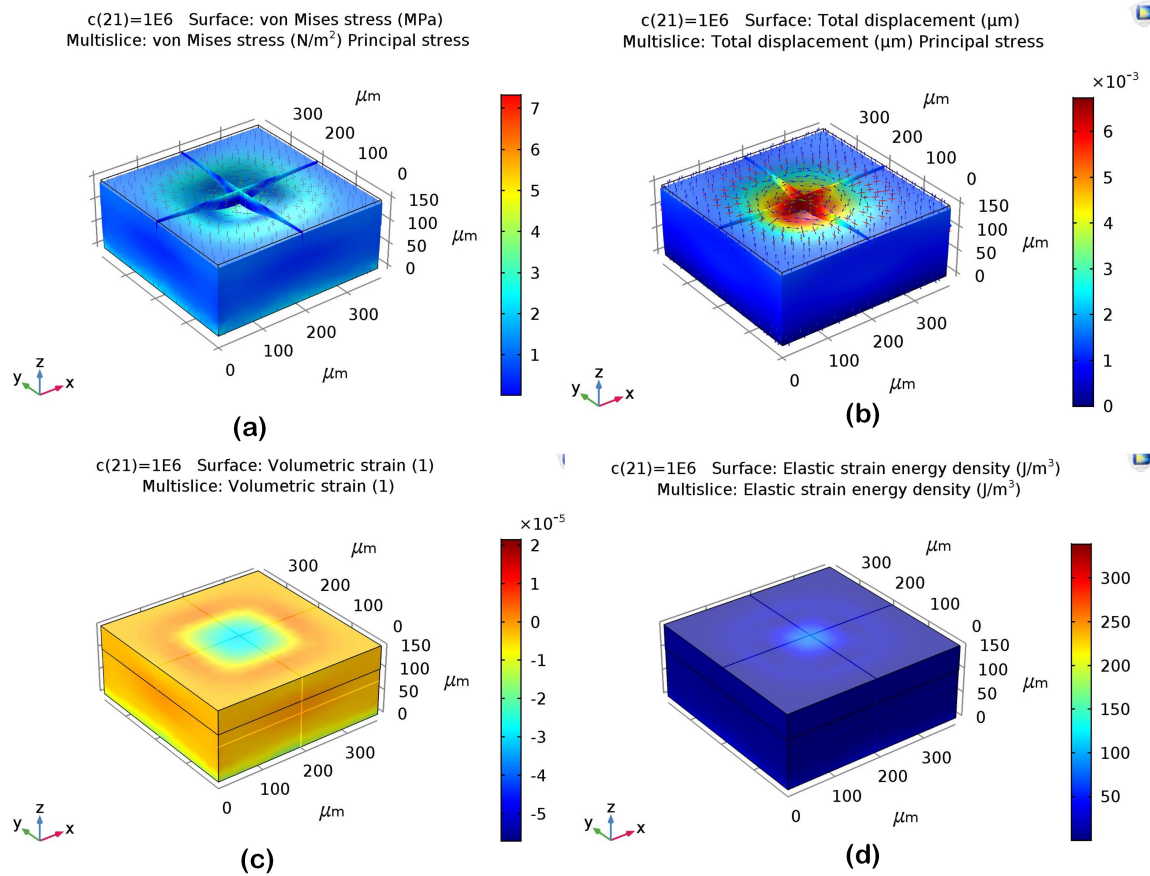


Figure 3.23 The 3D FEA plots showing (a) von Mises stresses, (b) Total displacement, (c) Total volumetric strain, (d) Elastic strain energy density of 50  $\mu\text{m}$  thin film Ti sheet

that begins with the crack initiation, propagation, and crack nucleation. The fatigue failure is identified with the crack initiation as the thin film membrane spends the largest part of its service life before the formation of visible cracks. The other events of the fatigue cycle, signify the final fracture of the thin film structure. Hence, the FEM of fatigue behavior in the initial design phase is essential for improving the long-term reliability of MEMS pressure sensors.

Fatigue failure is broadly classified into (1) Low cycle fatigue (LCF), and (2) High cycle fatigue (HCF) regions. In LCF, the stress amplitudes exceed the elastic limit of the thin film structure, and the structure suffers plastic deformations. On the other hand, the stress amplitudes experienced in HCF are lower than the yield strength of the material. In HCF,

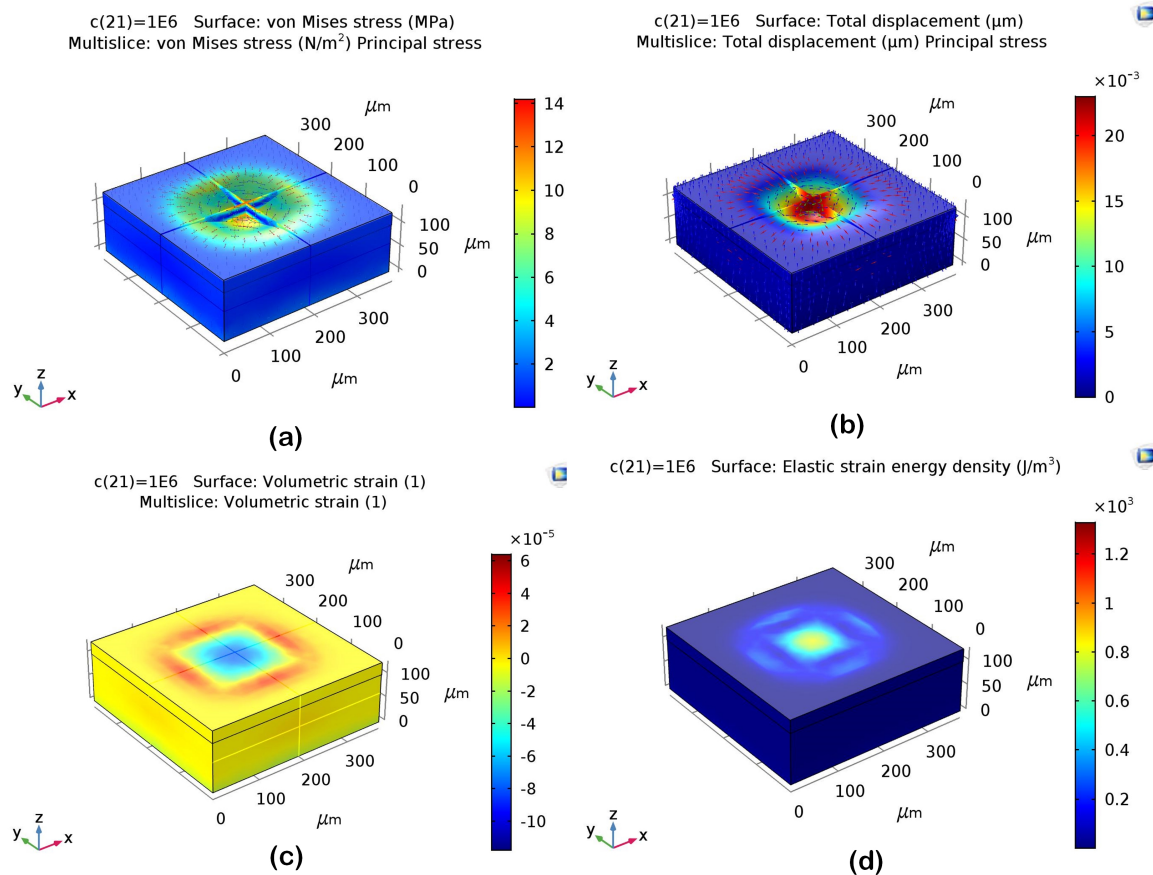


Figure 3.24 The 3D FEA plots showing (a) von Mises stresses, (b) Total displacement, (c) Total volumetric strain, (d) Elastic strain energy density of 25 nm thin film Ti sheet

shear stresses activate localized micro internal stresses above yield stress, with microplastic strain energy dissipation. Here, the entire structure is not involved, but a few high-stress concentration areas, internal to the material causes fatigue failure.

### 3.3.1 Fatigue Design Variables

Fatigue properties are often described using fatigue limit in most materials and fatigue strength in nonferrous metals. Wohler introduced a graphical representation of these fatigue properties, which represents the relationship between cyclic stress amplitude and the number of cycles. Figure 3.30 shows the S-N curve, which is expressed as a bi-logarithmic system

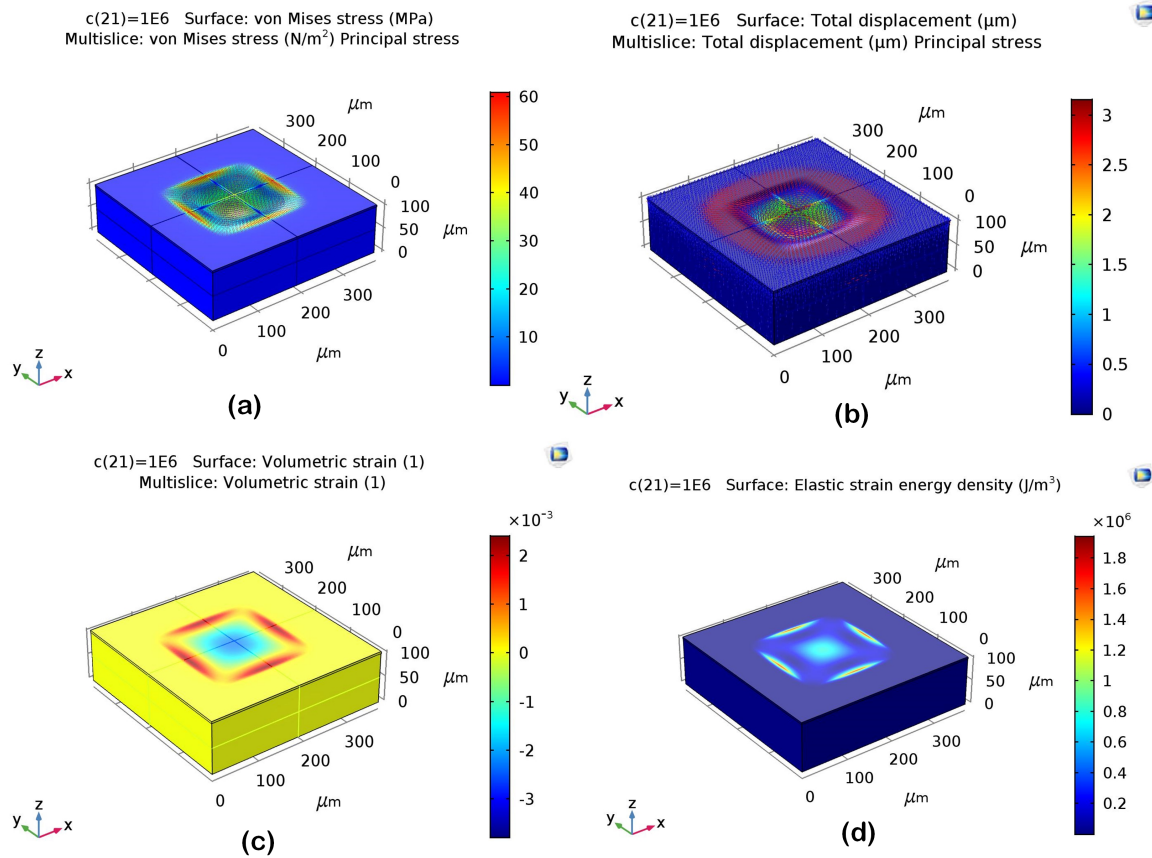


Figure 3.25 The 3D FEA plots showing (a) von Mises stresses, (b) Total displacement, (c) Total volumetric strain, (d) Elastic strain energy density of 4 nm thin film Ti sheet

$\log N_f = A \tilde{m} \log \sigma_a$ ; where  $A$  and  $m$  are taken from ASTM standard E 739 – 91. Alternatively, it is also expressed as an exponential notation  $\sigma_a = \sigma'_f (2N_f)^b$  [135]. In general, an S-N curve depicts a decrease in the number of load cycles as the stress amplitudes increase ( $k$ ). By considering the load cycles for a corresponding stress amplitude, fatigue failure can be evaluated. The equation 3.30 evaluates a fatigue crack from a given stress amplitude and corresponding load cycles.

The characteristic parameters in the S-N curve are the stress amplitude ( $\sigma_a$ ), and the number of load cycles ( $N$ ). A load cycle is defined as the one complete repetition of the load that a membrane is subjected to randomly varying amplitudes (Figure 3.31). Some of the important stress relationships that govern a fatigue analysis include:

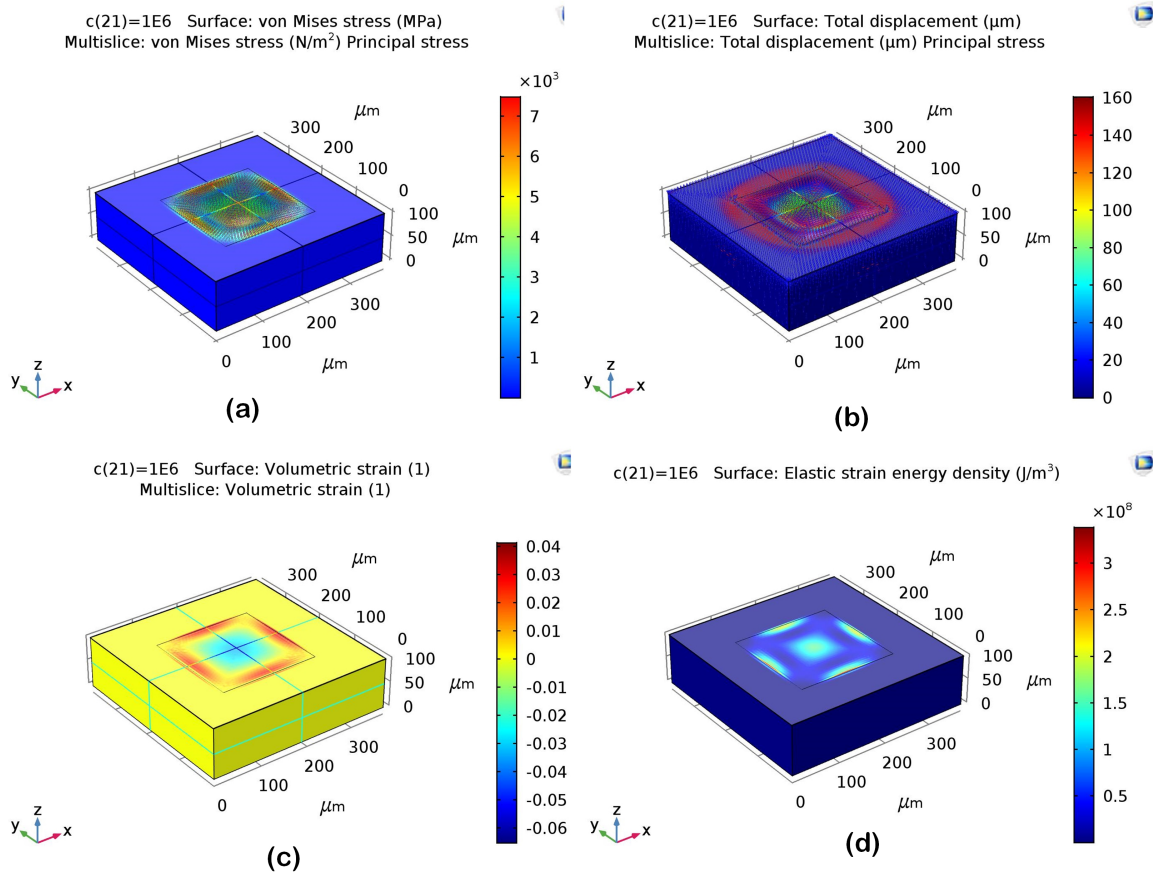


Figure 3.26 The 3D FEA plots showing (a) von Mises stresses, (b) Total displacement, (c) Total volumetric strain, (d) Elastic strain energy density of 1 nm thin film Ti sheet

1. **Mean Stress:** The mean stress ( $\sigma_{mn}$ ) is defined as the arithmetic mean of the maximum and minimum stress (Equation 3.23).

$$\sigma_{mn} \approx \frac{\sigma_{max} + \sigma_{min}}{2} \quad (3.23)$$

Where,  $\sigma_{max}$  is the maximum stress and  $\sigma_{min}$  is the minimum stress.

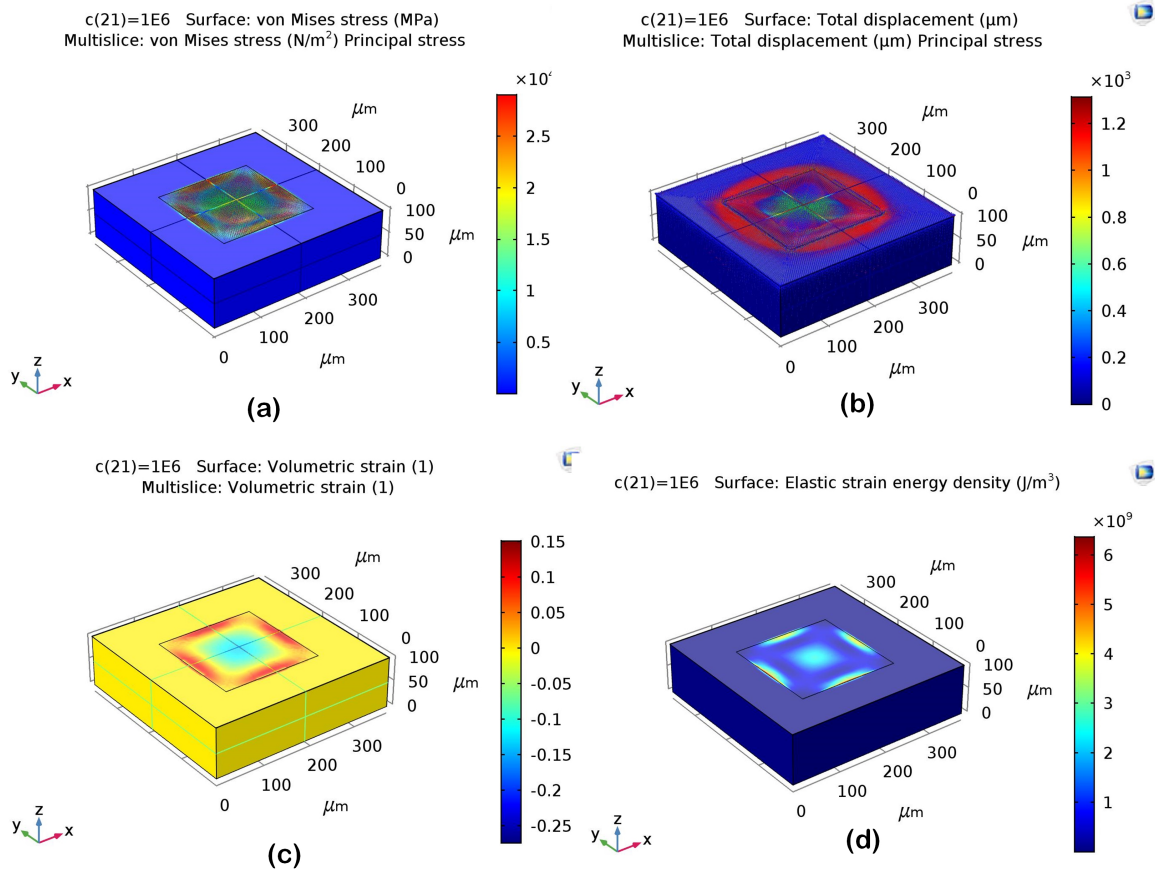


Figure 3.27 The 3D FEA plots showing (a) von Mises stresses, (b) Total displacement, (c) Total volumetric strain, (d) Elastic strain energy density of 500 nm thin film Ti sheet

2. **Alternating Stress (Stress Amplitude):** The alternating stress ( $\sigma_a$ ) is defined as the amount of stress that is deviating from the mean (Equation 3.24).

$$\sigma_a \approx \frac{\sigma_{max} - \sigma_{min}}{2} \quad (3.24)$$

3. **Stress Range:** Stress range (R) is defined as the difference between the maximum stress ( $\sigma_{max}$ ) and the minimum stress ( $\sigma_{min}$ ) (Equation 3.25).

$$\Delta\sigma \approx \sigma_{max} - \sigma_{min} \quad (3.25)$$

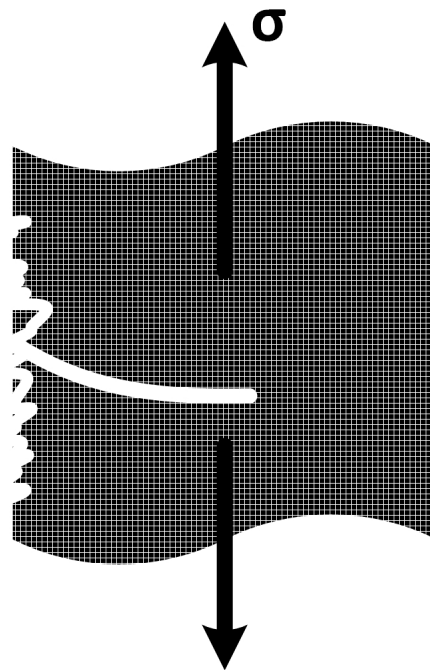


Figure 3.28 The intrusion and extrusion model of crack growth

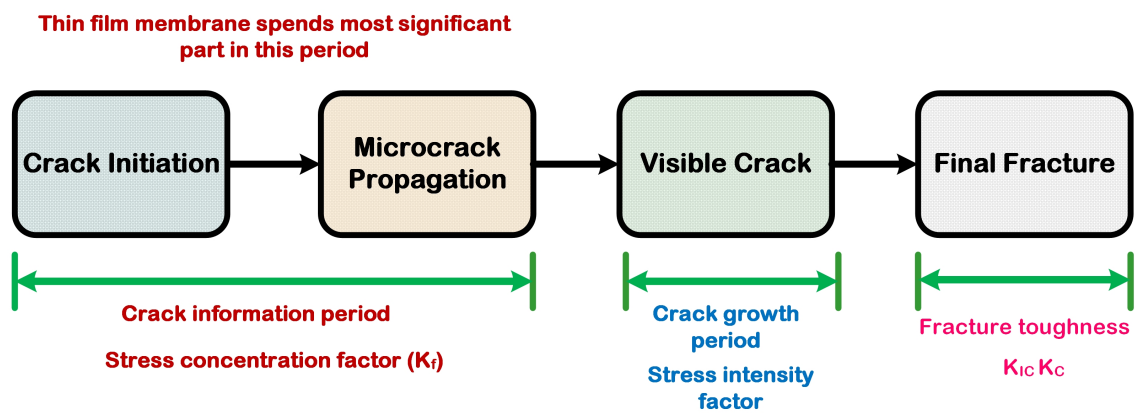


Figure 3.29 The fatigue process flow

4. **Stress Ratio:** Stress ratio is defined as the ratio of maximum stress ( $\sigma_{max}$ ) and minimum stress ( $\sigma_{min}$ ) (Equation 3.11).

$$R = \frac{\sigma_{min}}{\sigma_{max}} \quad (3.26)$$

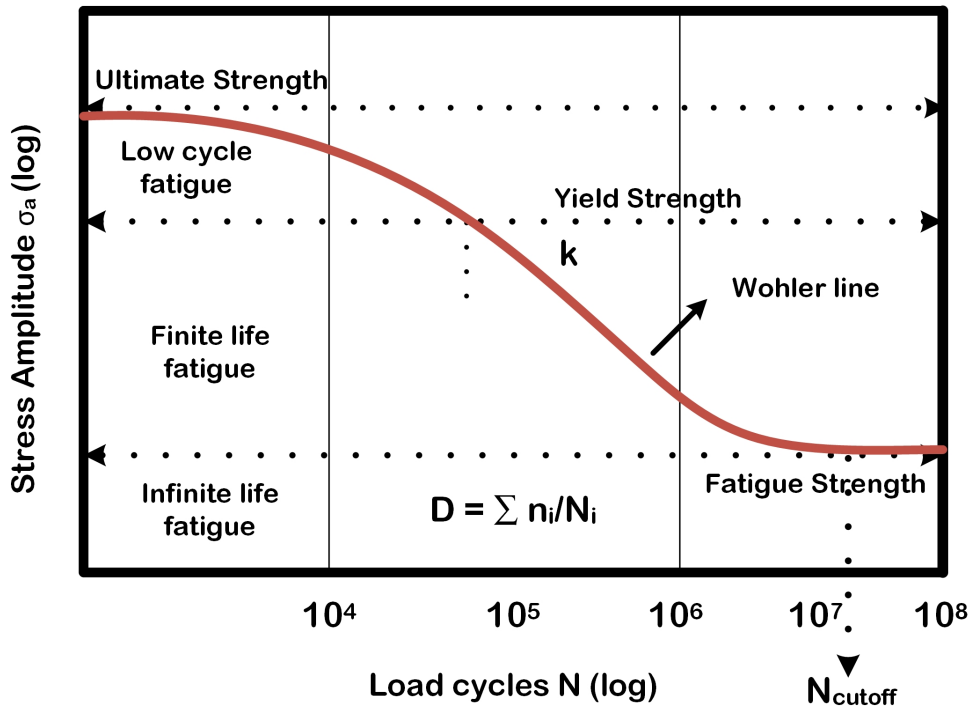


Figure 3.30 A model of S-N curve

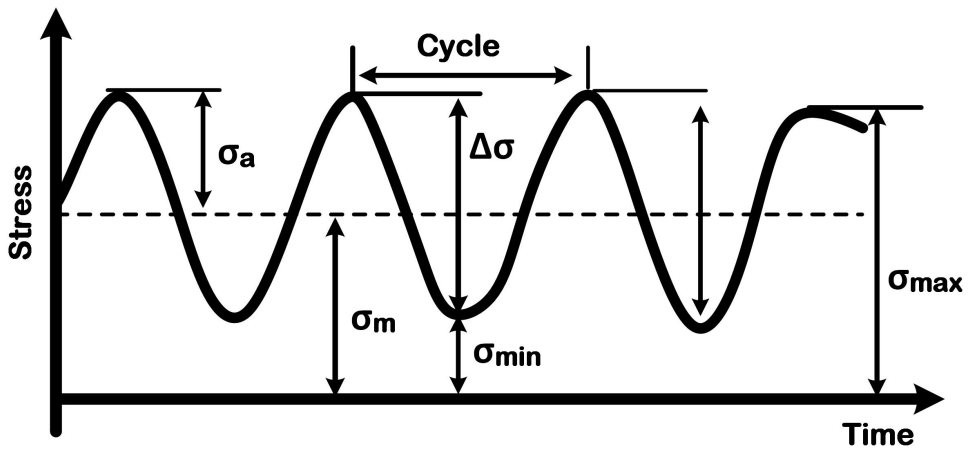


Figure 3.31 A fatigue load cycle

5. **Amplitude Ratio:** Stress amplitude ratio is defined as the ratio of alternating stress ( $\sigma_a$ ) and mean stress ( $\sigma_{mn}$ ) (Equation 3.12).

$$A = \frac{\sigma_a}{\sigma_m} \tag{3.27}$$

6. **Alternating Component:** Alternating component is defined as half of the stress range ( $\Delta \sigma$ ) (Equation 3.13).

$$\sigma_a = \frac{\Delta \sigma}{2} \quad (3.28)$$

7. **Factor of Safety (FOS):** The factor of safety is defined as the estimation of maximum strength of thin film materials to ascertain the safety design specification. It is shown in the Goodman diagram (Figure 3.32) (Equation 3.29).

$$\frac{\sigma_a}{\sigma_e} + \frac{\sigma_m}{\sigma_u} = \frac{1}{n_f} \quad (3.29)$$

Where,  $\sigma_e$  is the endurance limit stress,  $\sigma_u$  is the ultimate stress.

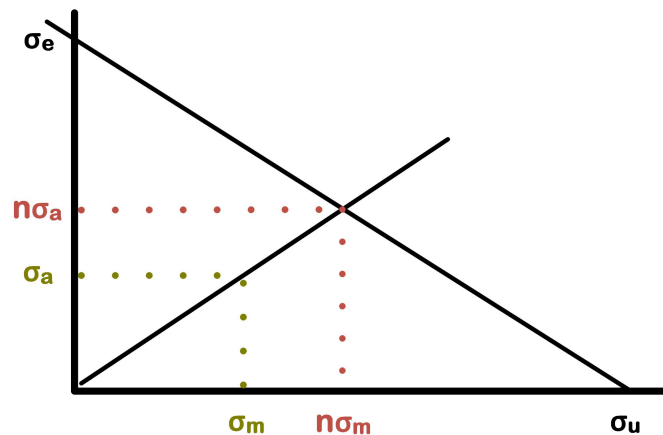


Figure 3.32 A Goodman fatigue curve

8. **Stress concentration factor:** Stress concentrations are the stress raisers that are promoted by the notches formed due to the defects in MEMS microfabrication process. For example, a thin film as shown in Figure 3.33 is subjected to randomly varying pressure loads in the presence of a notch or a hole; the uniform normal stress is

completely disturbed. The point of maximum stress ( $\sigma_{max}$ ) is  $3\sigma$  and occurs at the edge of the hole. The factor of 3 is termed as stress concentration factor ( $K_t$ ).

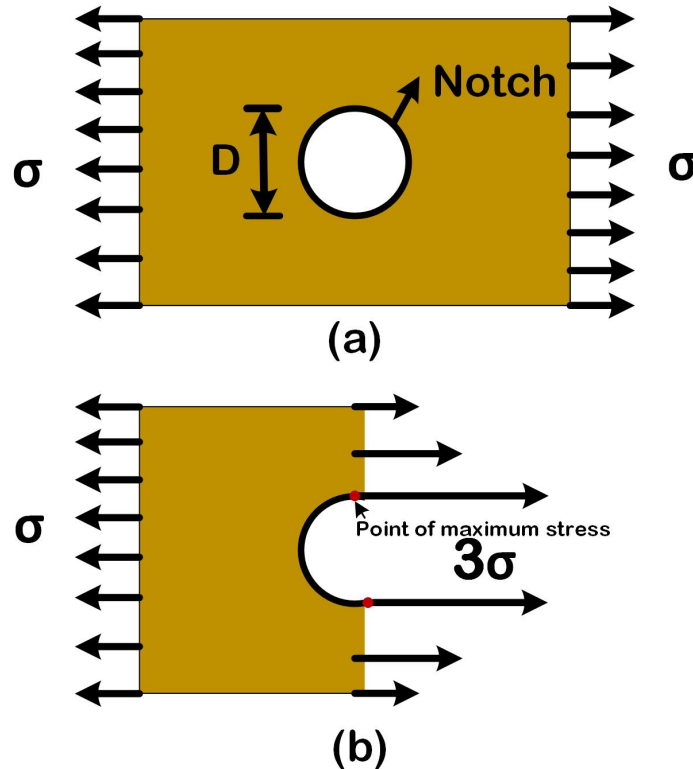


Figure 3.33 A model of notch created on a thin film and stress concentration factor

9. **Ultimate Stress:** The ultimate stress ( $\sigma_u$ ) or tensile strength is the maximum stress that a thin film structure can survive is shown in Figure 3.34

Uniaxial stress loading is a simplified theoretical concept which may not work in the real-time applications as the thin film membranes are repeatedly subjected to randomly varying loads. In many situations, thin film structures experience multiaxial loadings, where at least two principal stresses are always present at a region on the thin film surface. When the thin film is subjected to randomly varying external loads with different time histories, the principal stresses are generally non-proportional and out of phase [34]. In FEM, principal stress orientations or stress tensors provide useful information on the nature of loading the thin film subject to multiaxial stresses. If the Gauss-point stress tensor plot at two different locations

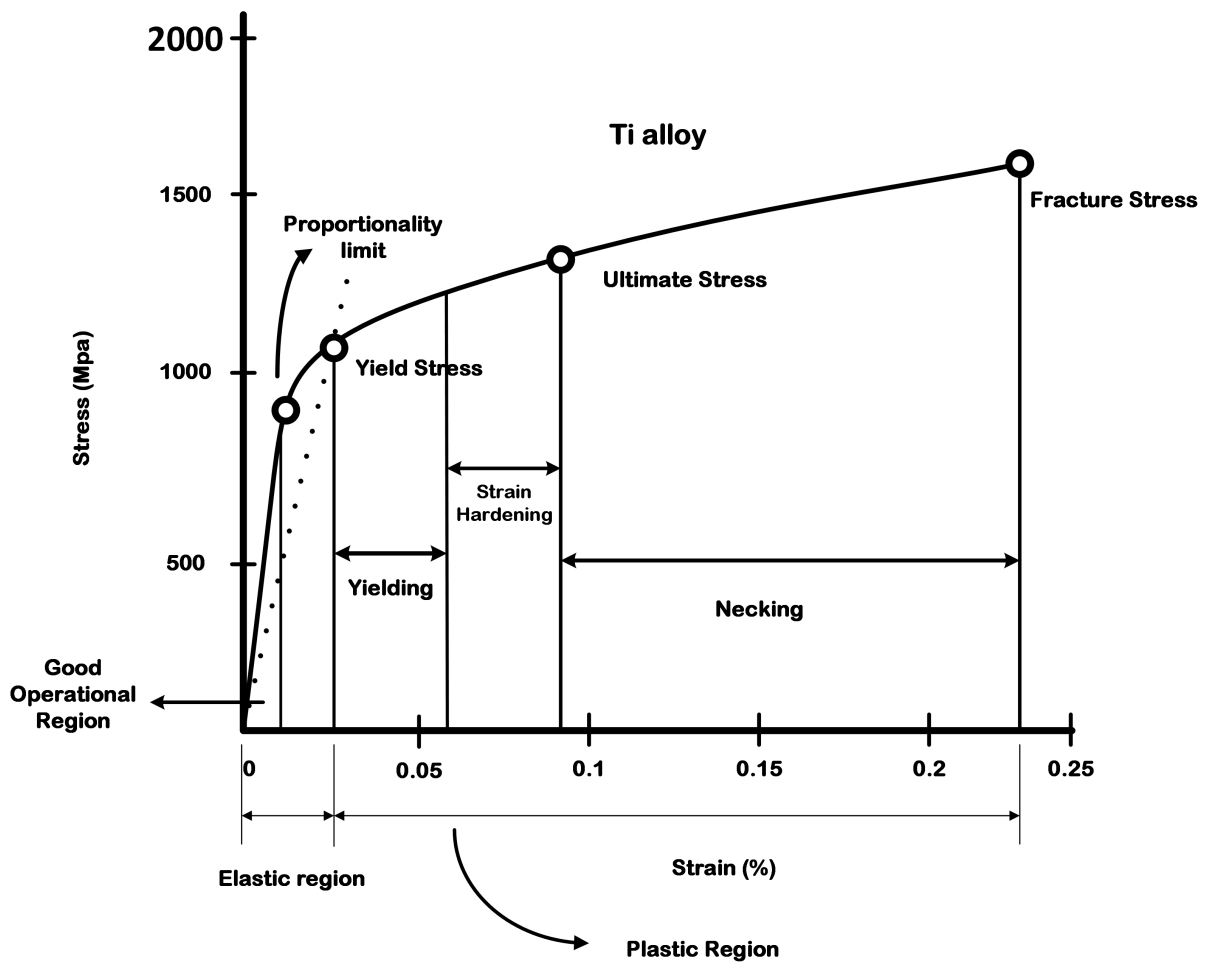


Figure 3.34 The stress-strain curve showing the good operational region

on a thin film membrane is out of phase, the structure is said to be in a multiaxial stress state. As an example, the deviatoric stress tensor plot of a FEM for thin film deflection is shown in Figure 3.35.

The multiaxial fatigue models available for the prediction of multiaxial stress states of thin film membrane include (1) Findley; (2) Matake; (3) McDiarmid; (4) Gough; and (4) Normal stress [117]. In this work, the Findley multiaxial fatigue model has been chosen for its simplicity and accuracy. The assumptions of this model are

1. The surface of the thin film membrane is a critical plane.

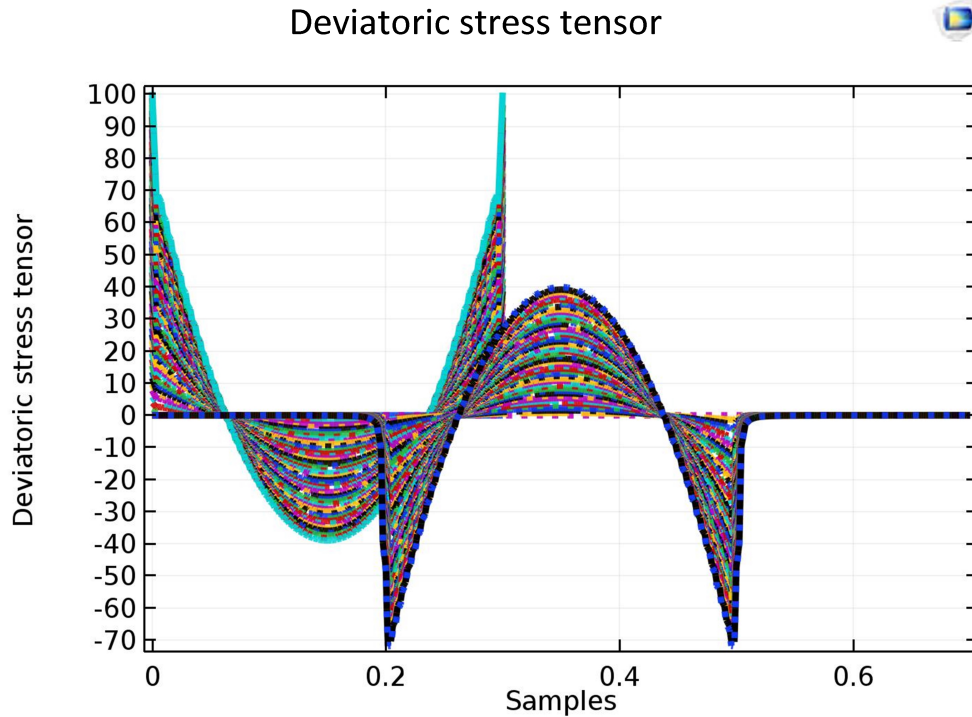


Figure 3.35 Gauss-point stress tensor showing non proportional loading

2. Both the normal stress ( $\sigma_N$ ) and shear stress ( $\sigma_{NS}$ ) are in linear combination for a specified number of cycles to failure. This is described by Equation 3.30.

$$\sigma_{NS} + k\sigma_{(N,max)} = f \quad (3.30)$$

Where  $k$  is the normal stress sensitivity coefficient, and  $f$  is the fatigue limit of a material which is equivalent to the tensile yield strength.

There is a wealth of information that suggested that the Findley multiaxial fatigue model has been applied to titanium alloys. For example, Nima Shamsaei et al. [109] studied the effect of multiaxial fatigue on titanium alloys using fully reversed cyclic loading. The effect of shear stresses has been investigated and details on the surface roughness and the

influence of stress rises due to the presence of notches were also observed. dimensions of 2D MEMS pressure sensor model Patrick et al. [120] built a custom-made sensor test rig, where the fatigue behaviour of a Fabry Perot optical membrane was tested for 10.000 cycles. However, a high number of cyclic loads are required to validate the long-term reliability and accuracy of the thin film membrane that is potentially needed for lifetime monitoring. Ti-6Al-4V—medical grade 5 titanium which is solution treated and annealed (STA) has never been used for forging a thin film membrane which acts as the pressure sensitive elements in various pressure sensors.

For this work, the Findley multiaxial fatigue model is selected for its simplicity and accuracy. The normal stress sensitivity is low for ductile and high for brittle materials. The normal stress sensitivity ( $k$ ) of silicon and Ti is 1.4 and 0.7 respectively. The fatigue limit of a material is equivalent to the tensile yield strength. For silicon  $f$  is 180 MPa and 1100 MPa for Ti. Both of these parameters were supplied as input to the fatigue model. As an output, the COMSOL calculates the fatigue usage factors (value  $< 1$  signifying the infinite life of thin films). These factors can be compared to fatigue strength and a number of cycles to failure. Figures 3.36 and 3.37 show the fatigue behaviour of 50  $\mu\text{m}$  and 25  $\mu\text{m}$  2D thin film Ti membrane.

Figures 3.38 and 3.39 show the fatigue behaviour of 4  $\mu\text{m}$  and 1  $\mu\text{m}$  2D thin film Ti membrane.

Figures 3.40 and 3.41 show the fatigue behaviour of 500 nm 2D and 50  $\mu\text{m}$  3D thin film Ti membrane.

Figures 3.42 and 3.43 show the fatigue behaviour of 25 nm 2D and 4  $\mu\text{m}$  3D thin film Ti membrane.

Figures 3.44 and 3.45 show the fatigue behaviour of 1 nm 2D and 500 nm 3D thin film Ti membrane.

Table 3.4 shows the deflection induced stresses and residual stresses of thin film Ti membrane at various thickness levels.

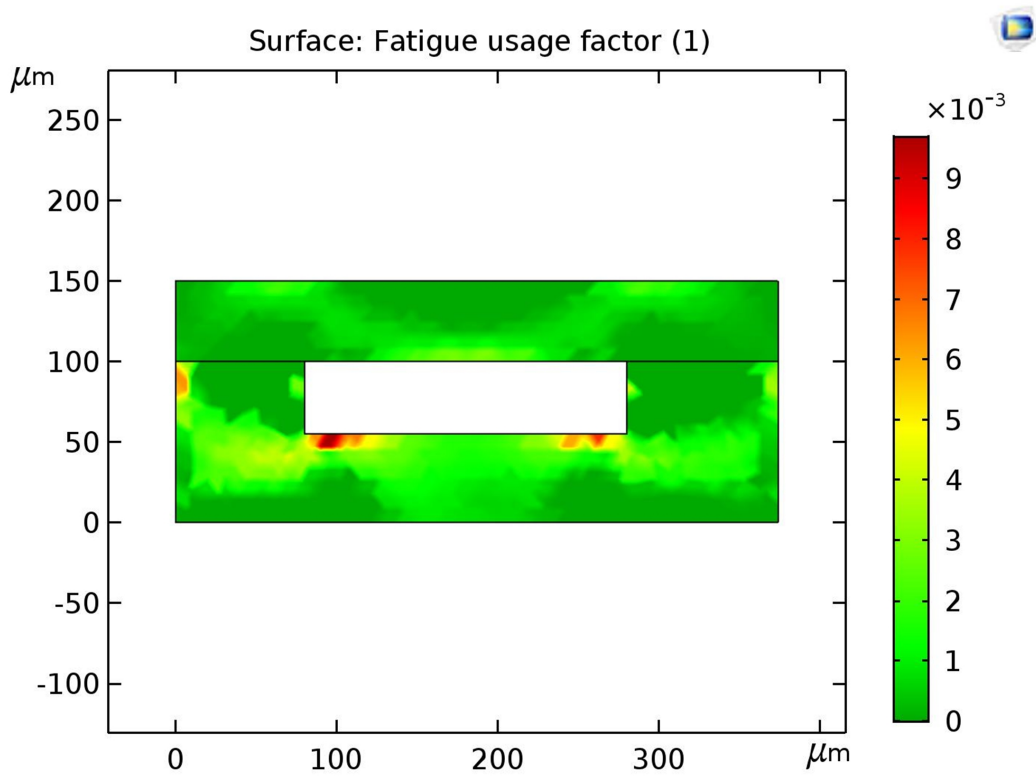
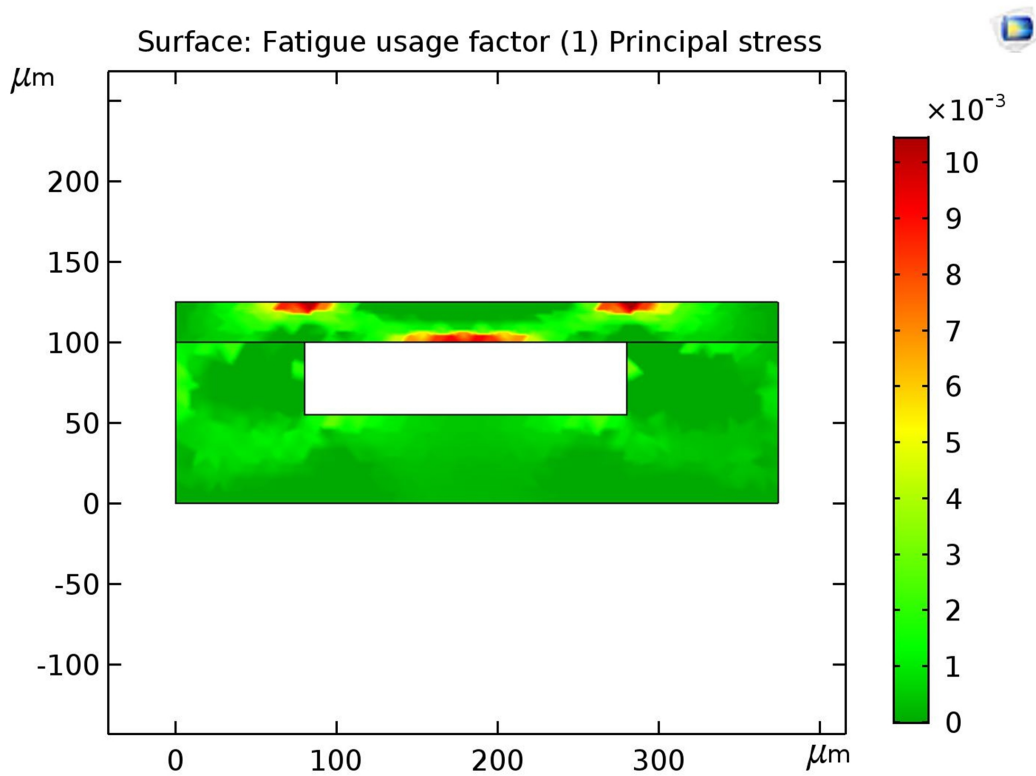
Table 3.4 The comparison of deflection induced fatigue and residual stress induced fatigue

<b>Thickness</b>	<b>Deflection induced fatigue usage</b>	<b>Residual stress induced fatigue usage</b>
50 $\mu\text{m}$	0.003 to 0.009	1.5 to 5
25 $\mu\text{m}$	0.004 to 0.01	0.002 to 0.0045
4 $\mu\text{m}$	0.4 to 0.9	1.5 to 3
1 $\mu\text{m}$	6 to 16	8 to 16

### 3.4 Summary

FEM of thin film deflection and fatigue behaviour has been performed on various thicknesses including 50  $\mu\text{m}$ , 25  $\mu\text{m}$ , 4  $\mu\text{m}$ , 1  $\mu\text{m}$ , 500 nm, 200 nm. The simulation results of thin film deflection and stresses have been plotted and compared (Table 3.3). Similarly, the fatigue behaviour of thin film membrane also has been studied using multiaxial critical plane fatigue models. Fatigue behaviour in the form of fatigue usage factors has been plotted and compared (Table 3.4). The pressure transmission capability of the thin film membrane is also studied using the fluid-structure module in COMSOL and the capability is listed in the Table 3.3 as low, good and high. It can be inferred that the ideal thickness of thin film membrane for long-term reliability and small deflections is between 4  $\mu\text{m}$  and 1  $\mu\text{m}$ . However, the achievable thicknesses in MEMS fabrication is between 1  $\mu\text{m}$  and down to 200 nm. Hence there is a trade-off in achieving optimal dimensions for long-term reliable MEMS pressure sensors. Besides, small deflection theory fails in the case of thin film membranes of thickness

under  $1\ \mu\text{m}$  and requires a large deflection theory to analyze the thin film deflection and fatigue behaviour.

Figure 3.36 Fatigue usage factor of 50  $\mu\text{m}$  2D thin film Ti membraneFigure 3.37 Fatigue usage factor of 25  $\mu\text{m}$  2D thin film Ti membrane

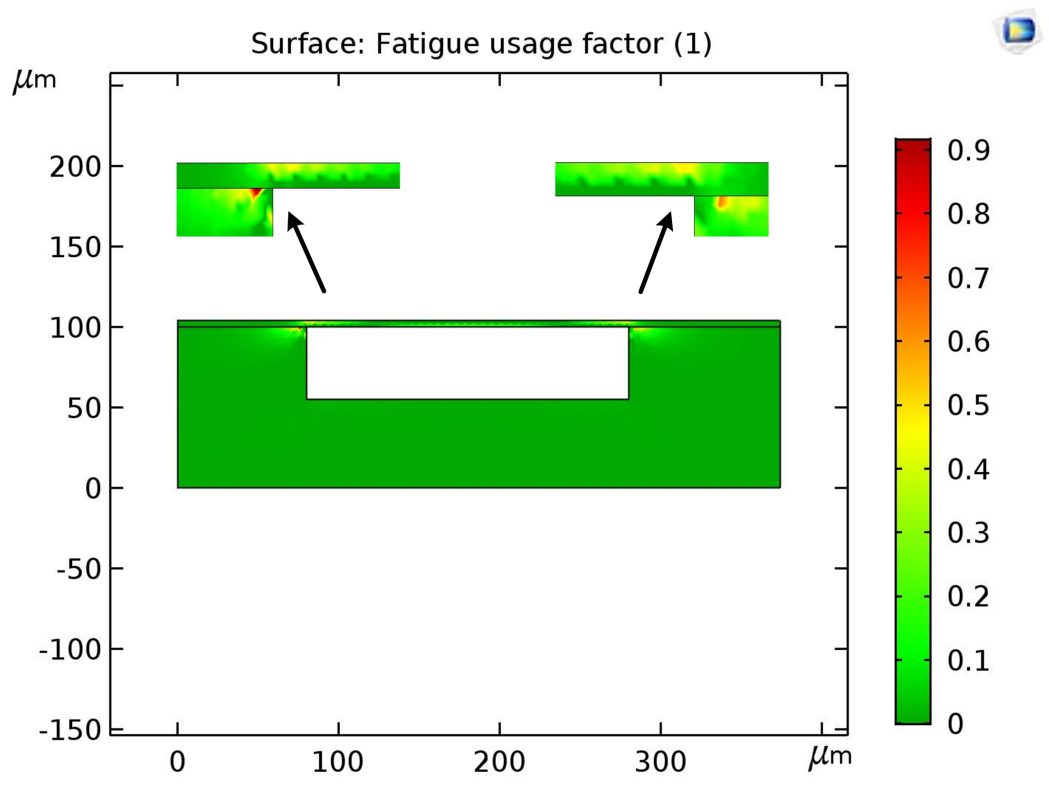


Figure 3.38 Fatigue usage factor of 4  $\mu\text{m}$  2D thin film Ti membrane

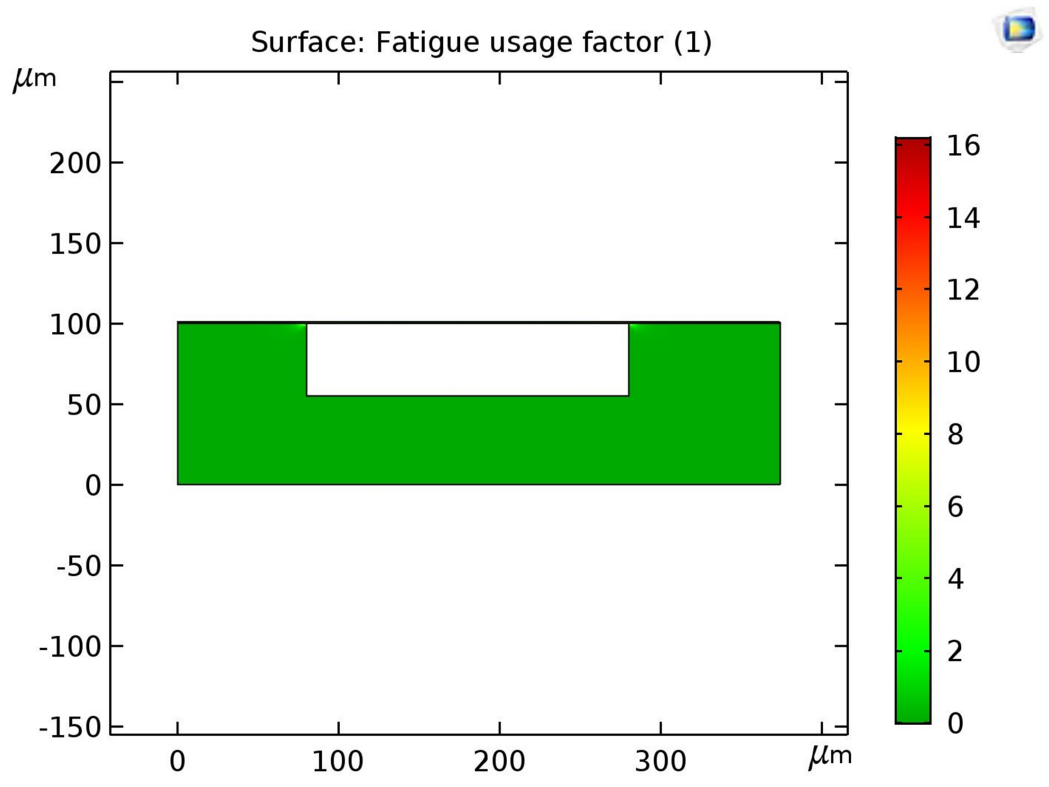


Figure 3.39 Fatigue usage factor of 1  $\mu\text{m}$  2D thin film Ti membrane

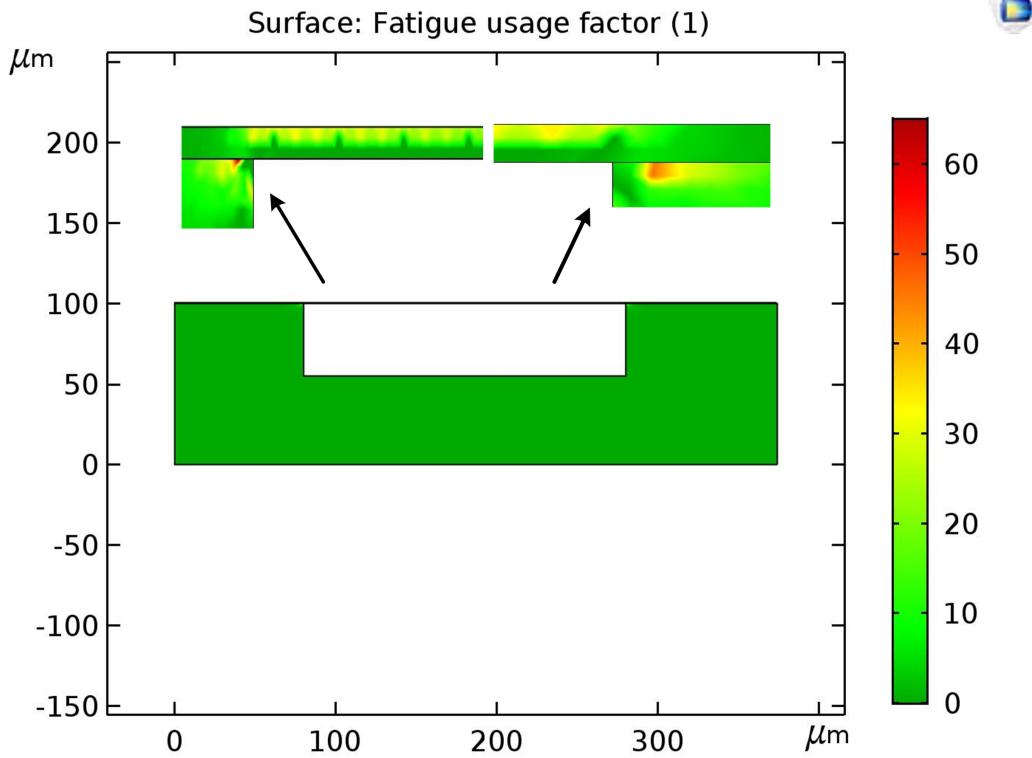


Figure 3.40 Fatigue usage factor of 500 nm 2D thin film Ti membrane

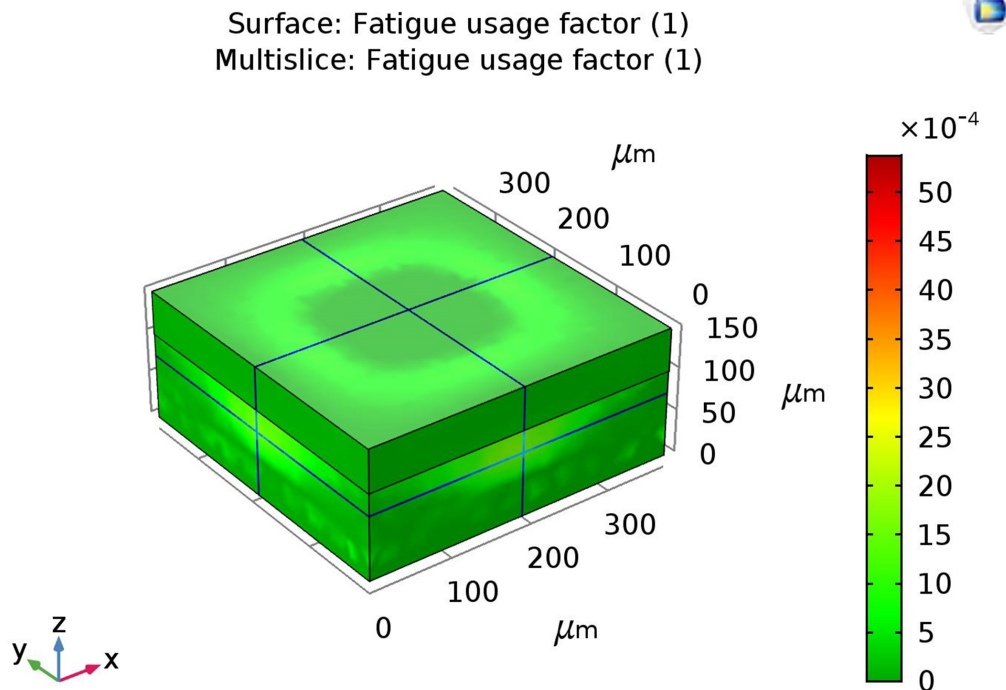


Figure 3.41 Fatigue usage factor of 50  $\mu\text{m}$  3D thin film Ti membrane

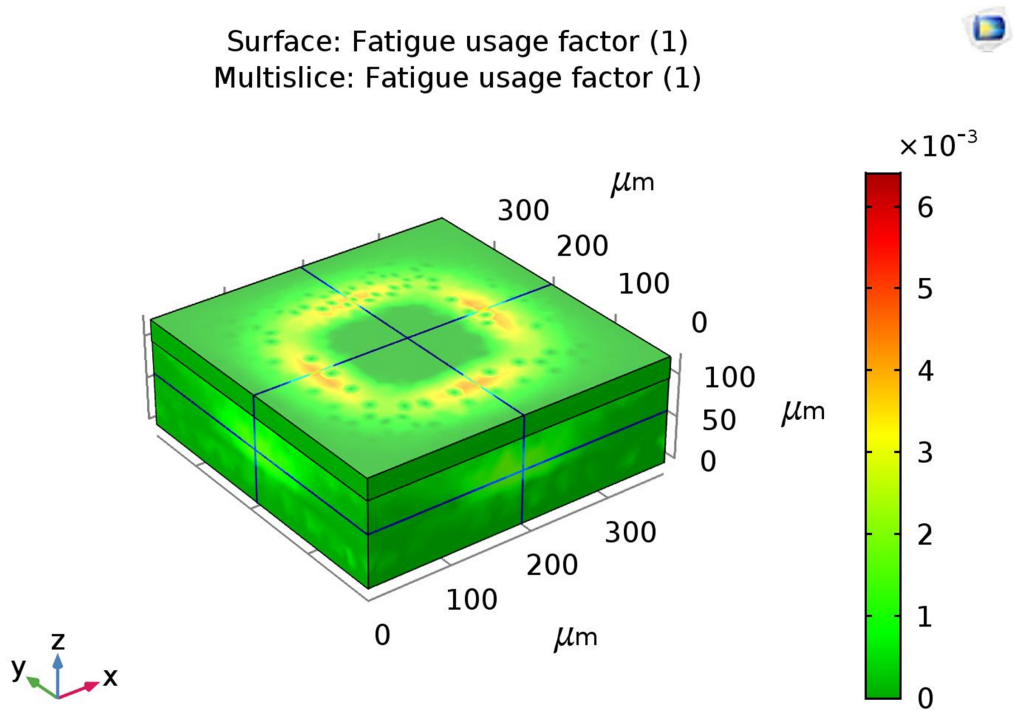


Figure 3.42 Fatigue usage factor of 25 μm 3D thin film Ti membrane

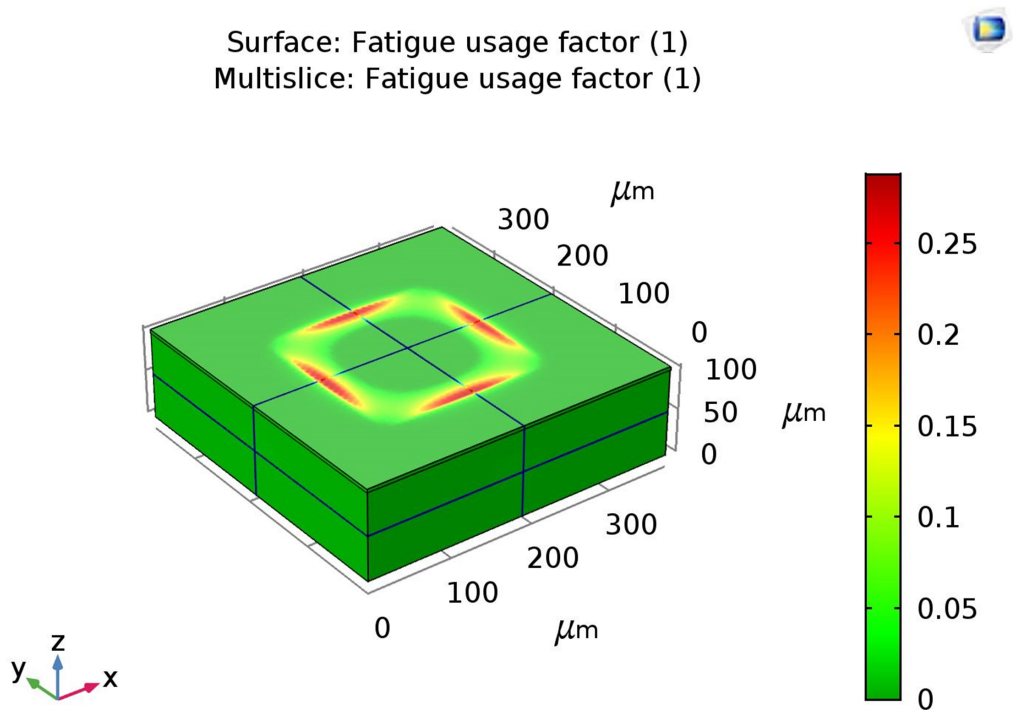


Figure 3.43 Fatigue usage factor of 4 μm 3D thin film Ti membrane

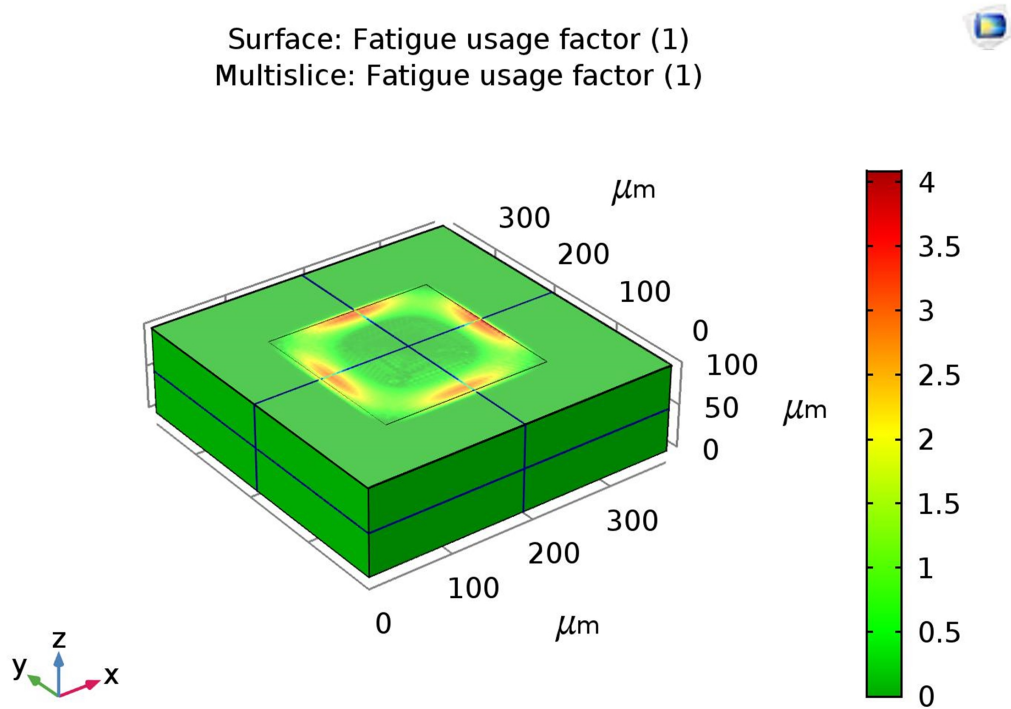


Figure 3.44 Fatigue usage factor of 1 μm 3D thin film Ti membrane

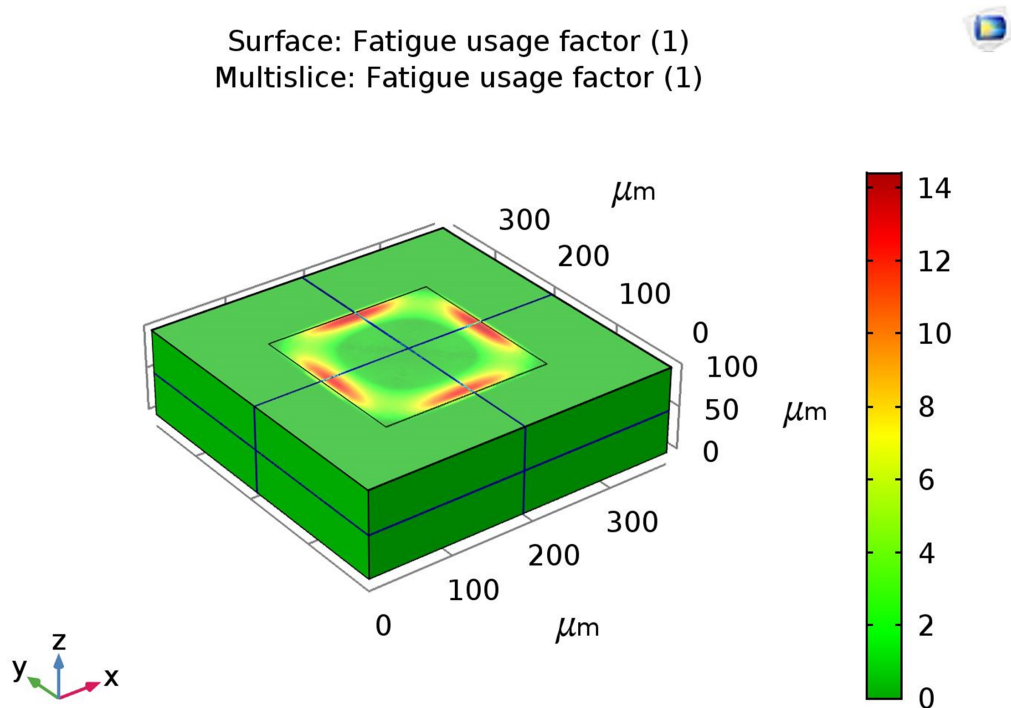


Figure 3.45 Fatigue usage factor of 500 nm 3D thin film Ti membrane



# Chapter 4

## Experimental Testing

### 4.1 Introduction

This chapter deals with the experimental system and results of thin film fatigue life testing.

### 4.2 Materials and Specimens

The thin film Ti alloy (Ti-6Al-4V) was purchased from William Gregor Ltd, Ti-shop, London. The specimen thicknesses are 4  $\mu\text{m}$  and 25  $\mu\text{m}$  as shown in the Figure 4.1. The SEM images of 4  $\mu\text{m}$  and 25  $\mu\text{m}$  were captured as obtained (Figure 4.2). Both the specimens are solution treated at 900 °C to 955 °C and aged at 540 °C. Table 3.1 enumerates the material properties of Ti-6Al-4V-based Ti alloy. It has excellent biocompatibility, particularly in direct contact with cells and tissues. Besides, it has exceptional creep and rupture strength of 575 MPa and 800 MPa at a temperature of 400 °C and 1 % strain respectively. The tensile yield strength is 1100 MPa; the thin film membrane is subjected to cyclic loads less than this yield stress value. However, poor shear strength and surface wear properties can make it vulnerable to

sliding contact on itself and other metals. Surface treatment processes such as nitriding and oxidizing can help in improving the surface wear properties.

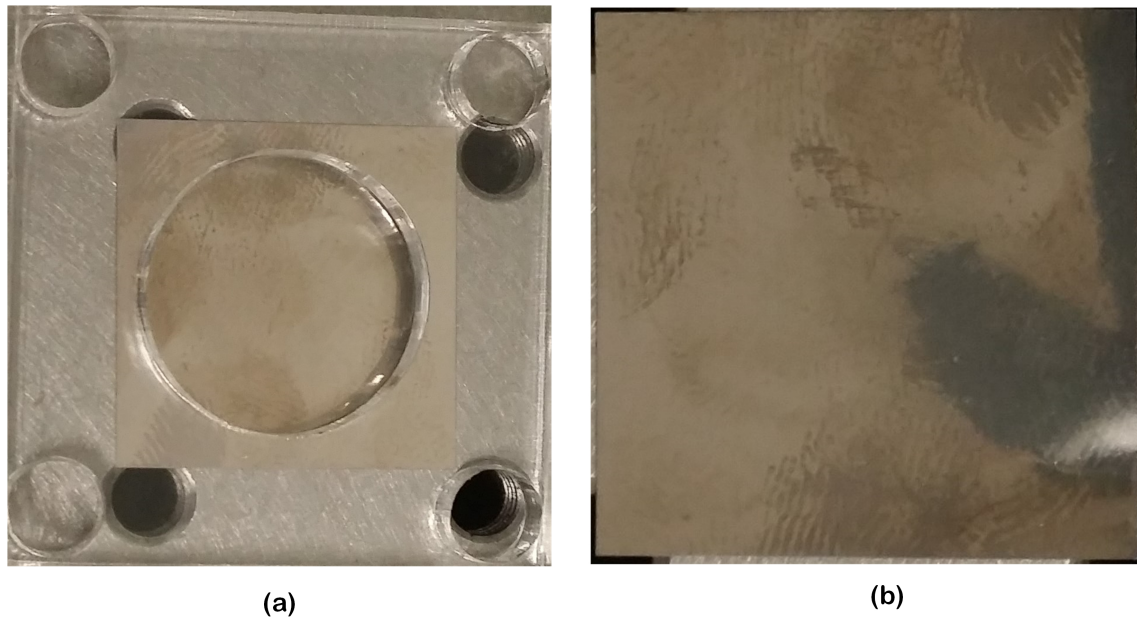


Figure 4.1 Thin film Ti specimens (a) 4  $\mu\text{m}$  thick, (b) 25  $\mu\text{m}$  thick

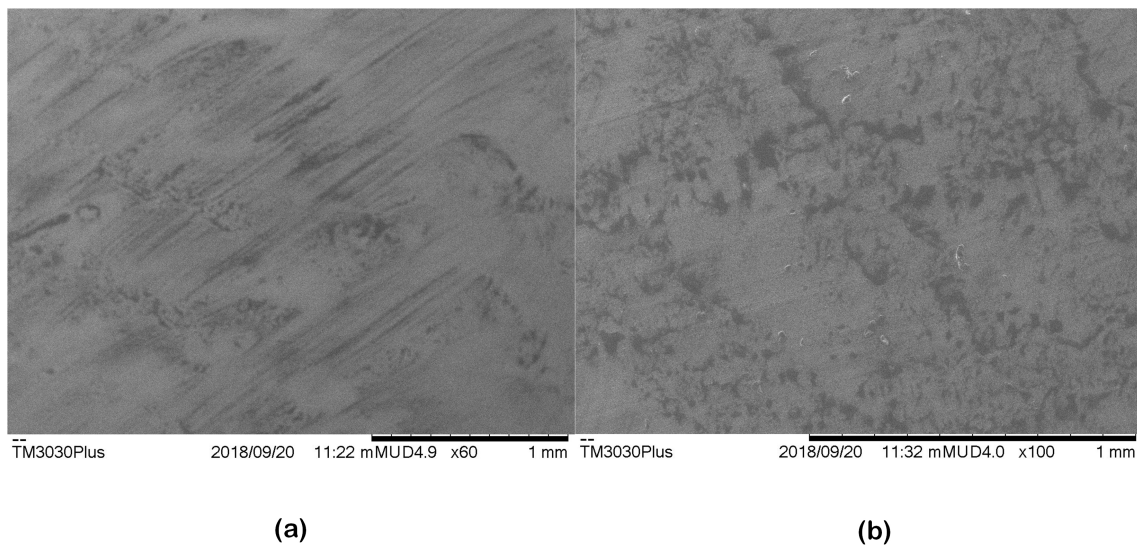


Figure 4.2 The SEM pictographs of (a) 4  $\mu\text{m}$  thick, (b) 25  $\mu\text{m}$  thick

Figures 4.3 and 4.4 shows the conceptual diagram and the actual experimental fatigue set up respectively.

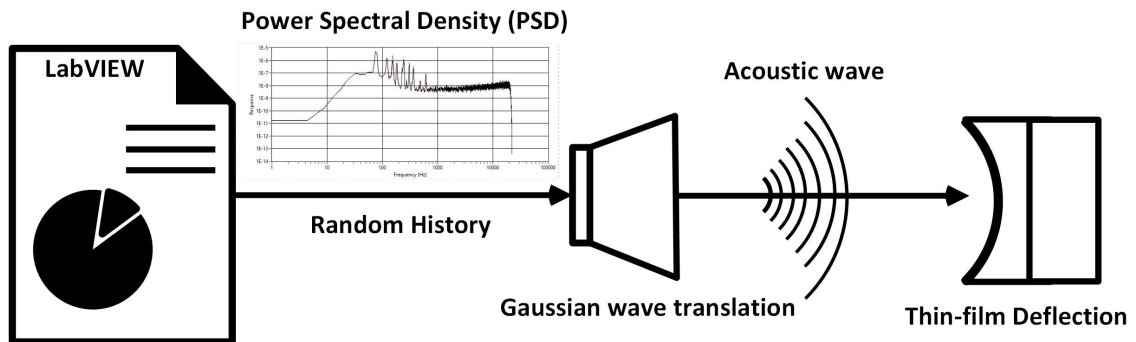


Figure 4.3 The block diagram of acoustic-based fatigue testing system

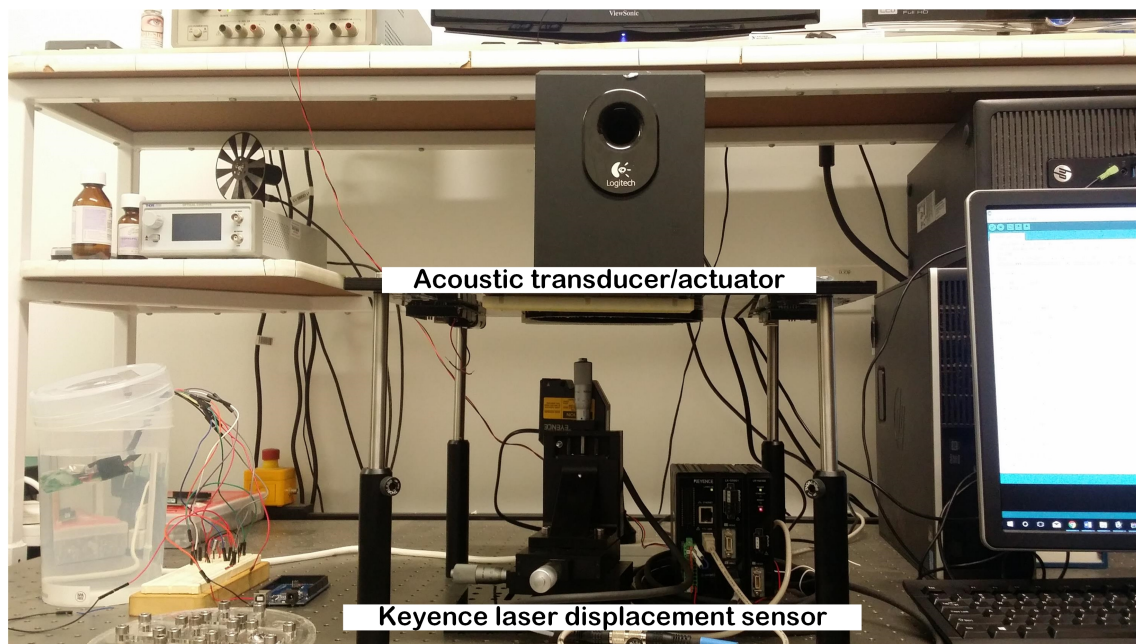
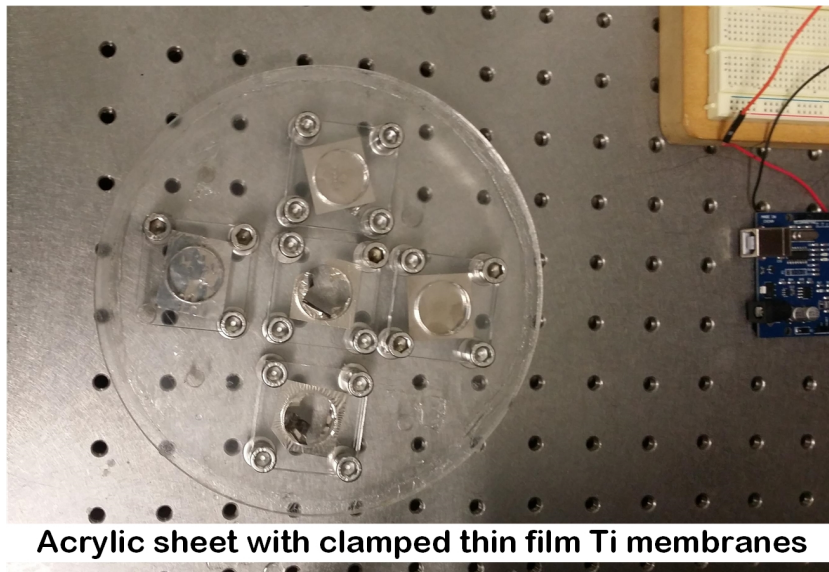


Figure 4.4 The experimental setup of acoustic-based fatigue testing system

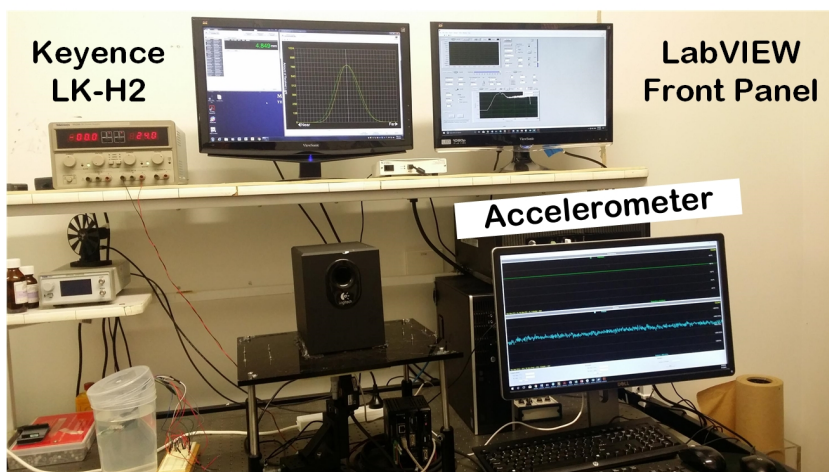
The thin-film specimens ( $4\ \mu\text{m}$  and  $25\ \mu\text{m}$ ) were clamped to 3-millimeter acrylic substrates which were bonded to the circumference of the round subwoofer of the multimedia speaker system (Figures 4.5a and 4.6).

Gaussian random vibrations are generated using a spectrum analyzer (NI LabVIEW). The Gaussian waves are then translated into acoustic vibrations via a voice coil-based acoustic transducer comprising of a subwoofer as an actuator (Height  $\times$  Width  $\times$  Depth :  $146.2\ \text{mm} \times 89.4\ \text{mm} \times 81.0\ \text{mm}$ ). The subwoofer acts as an acoustic booster that can assist in



Acrylic sheet with clamped thin film Ti membranes

(a)



(b)

Figure 4.5 Thin film Ti specimens (a)  $4\ \mu\text{m}$  thick, (b)  $25\ \mu\text{m}$  thick

amplifying the vibrations into large stress amplitudes required in displacing the thin film Ti membranes precisely at the centre. A laser displacement sensor—LKG—5001 series (Keyence, USA) helps in capturing the displacements using Keyence LK-Navigator-2 (LK-H2) software. The Datalogger portals are shown in Figure 4.5b.

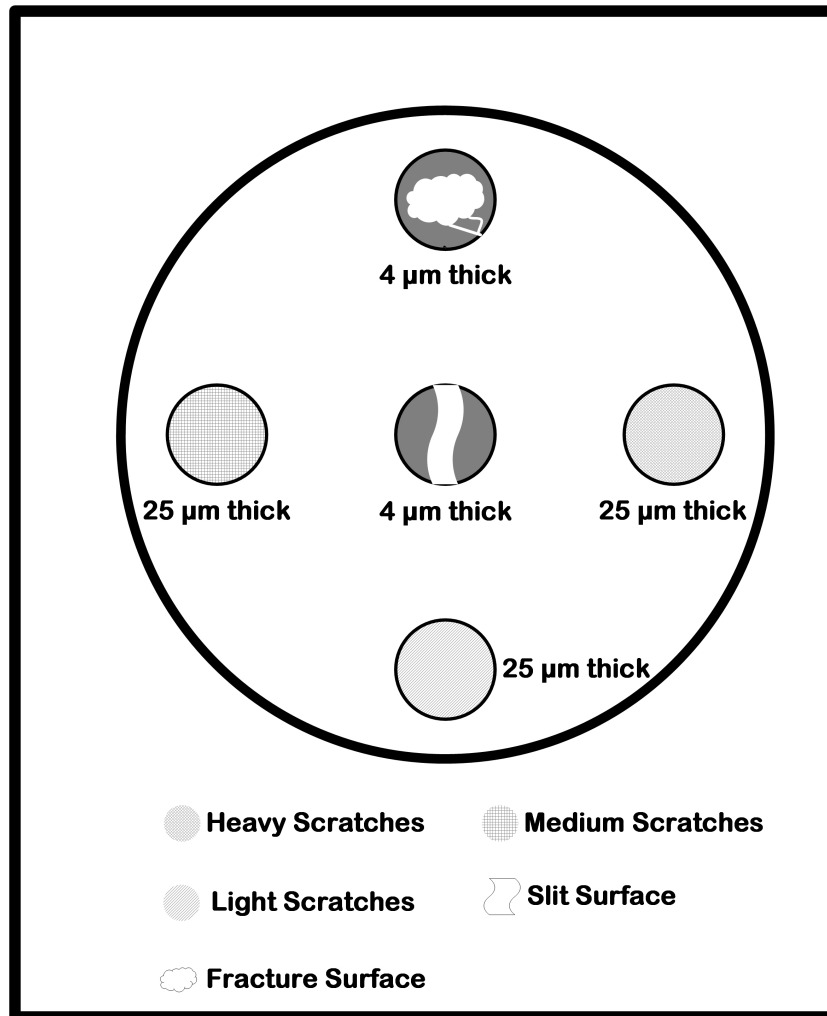


Figure 4.6 The conceptual diagram showing the surface of clamped Ti thin films

### 4.3 Measurement Technique

In the last few years, there has been a significant impetus on the destructive fatigue testing of mechanical structures using dog bone material specimens [136]. The two major types of destructive methods are acoustic- and ultrasonic-based techniques [137, 121]. An acoustic-based fatigue testing system is generally an essential part of aircraft maintenance [137]. Some of the technical reports from NASA divulge that a sonic fatigue test program has been in service from the beginning of 1982 for validating composite onboard ailerons for L-101 aircraft. The old fatigue system consisted of a progressive wave horn with a siren to test

the large mechanical structures [137]. However, the old acoustic systems may not be useful for testing the thin film membranes. In our experiments, acoustic fatigue testing is set up using a modern multimedia speaker and subwoofer system to amplify the sound vibrations to study the thin film deflection and fatigue failure. It is always difficult to load the thin film membranes with the actual brain's cerebrospinal fluid pressure fluctuations.

In the experimental analysis, the thin films are loaded via accelerated Gaussian random vibrations as shown in Figure 4.7 to study the thin film displacement and fatigue behaviour. A random signal is a zero-mean Gaussian process as its mean value centres at zero and is described using standard deviation, for example, the time compression of broadband random vibration tests proposed by Shires [138] or stress power spectral density (PSD) of wide-band Gaussian random loading [139].

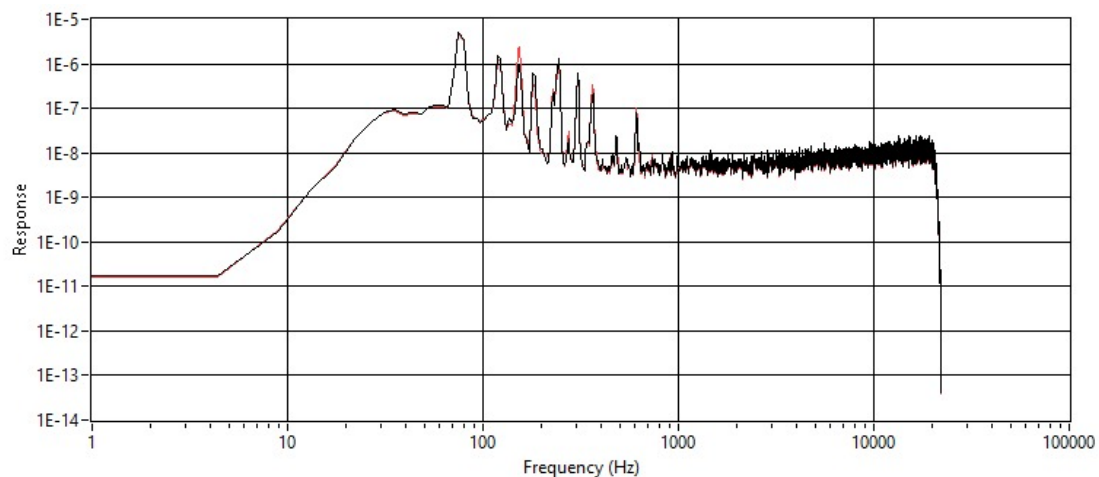


Figure 4.7 The Gaussian random vibration curve from spectrum analyzer

The frequency range used in the experimental analysis is 20 Hz to 10000 Hz. The cyclic vibrations are recorded using an accelerometer (ST Microelectronics STEVAL–MKI180V1). The Gaussian random vibrations were generated using a spectrum analyzer (NI LabVIEW) at a sampling rate of 44 100 Hz with 10000 samples per channel (2 channels). The Gaussian wave frequency was 500 Hz. The voice coil-based in the acoustic transducer translates the Gaussian random vibrations into sound vibrations that are boosted into large amplitudes by a

subwoofer subsystem for displacing the thin film membrane in the centre. The displacements are captured using a laser displacement sensor (LK-HG5001 series, Keyence USA).

The fatigue testing is conducted in two phases, namely pre-cycle and post-cycle, on all the mounted thin film membranes. Displacement response curves for each thin film membrane are obtained from the laser displacement sensor (LK-H2 software). Figure 4.8 shows the displacement plot of 4  $\mu\text{m}$  thin film Ti membrane that was captured by LK-H2 software (Keyence, USA).

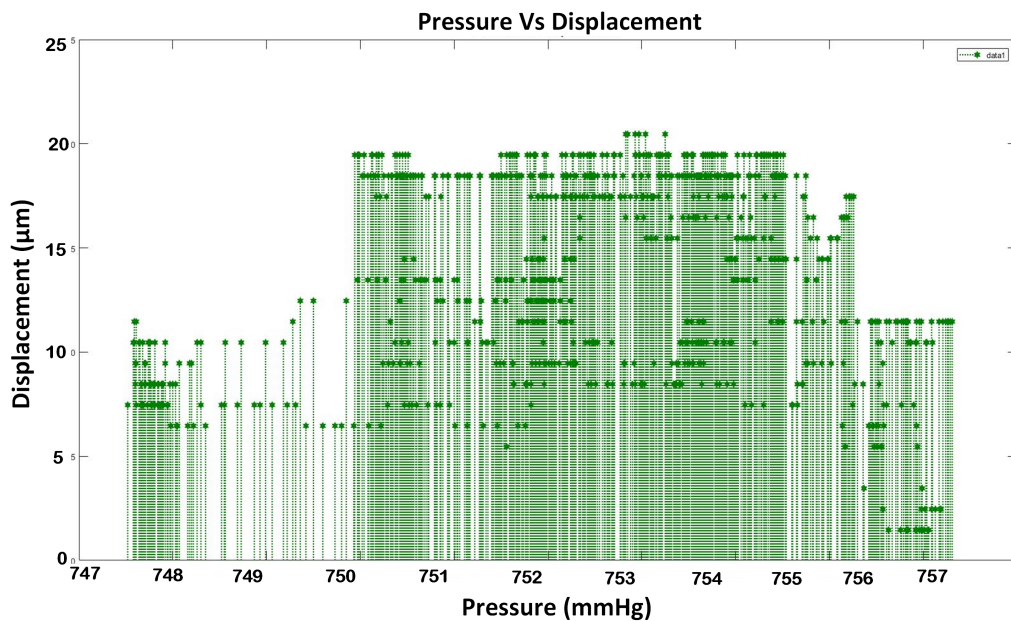


Figure 4.8 The displacement plot of 4  $\mu\text{m}$  thin film Ti membrane

The data from MEMS accelerometer (LIS3DHH, ST Microelectronics) shows that the intensity of the vibration was the highest at the centre and gradually decreased towards the edges. This is pictorially depicted in Figure 4.9, which shows the acoustic vibrations.

The number of cycles to failure was recorded using a timer in seconds (sec). The total number of cycles, the 4  $\mu\text{m}$  thick Ti foil survived, was 160 million (Figure 4.10)

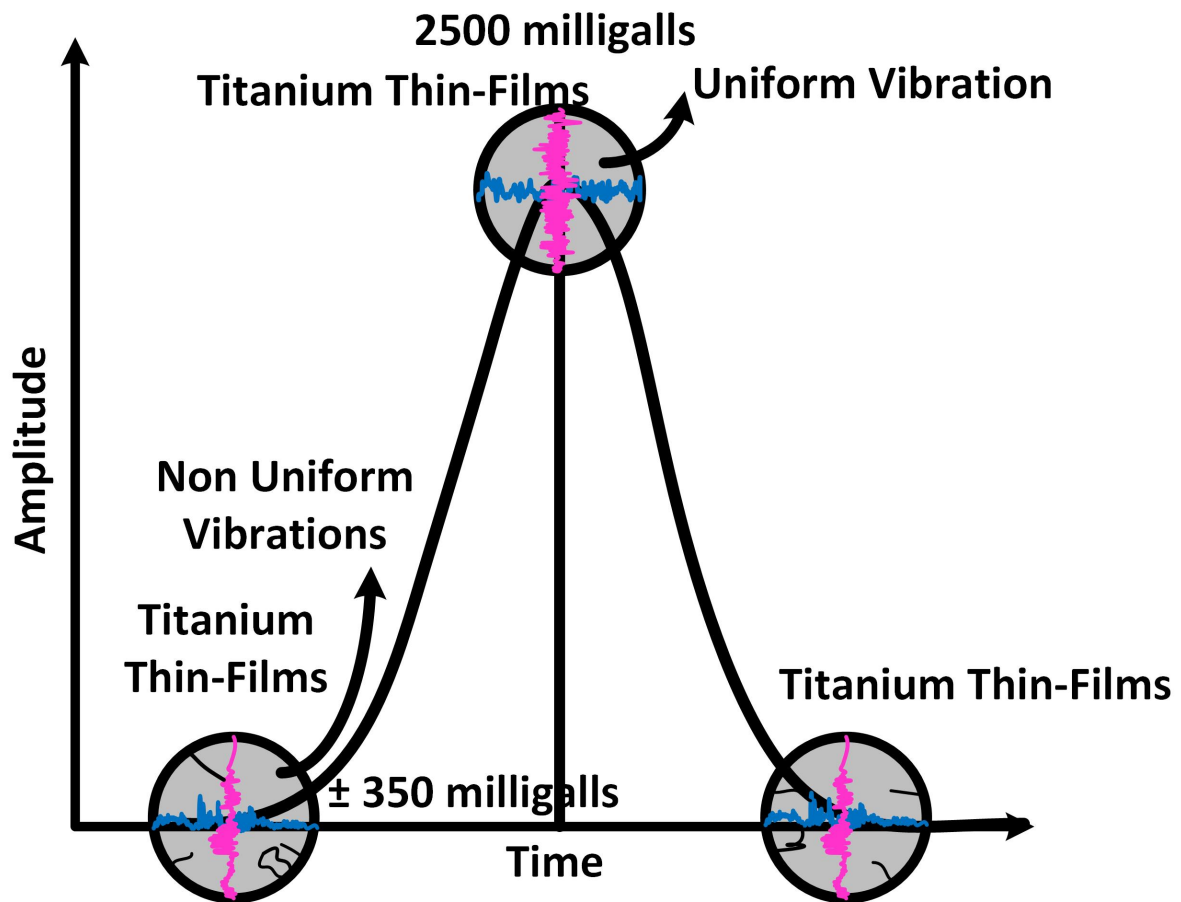


Figure 4.9 The conceptual diagram of acoustic vibration distributions across the 3 mm thick circular acrylic sheet

#### 4.4 SEM Visualization

Fatigued surfaces cannot be identified from the macro fractographical features with the naked eye. Therefore, high definition/ resolution tools such as the optical microscope, transmission electron microscope (TEM) and scanning electron microscope (SEM) are necessary [140]. The presence of a clearly defined flat fracture area with a visible pattern and a sharp transition is often enough for crack identification. Nevertheless, thin structures and flat fracture surfaces with no plastic deformation and visible scratches can be complex and require SEM for verification [140]. Tabletop SEM TM3030Plus has been used to observe the fractographical features of thin film membranes. The secondary electron detector can

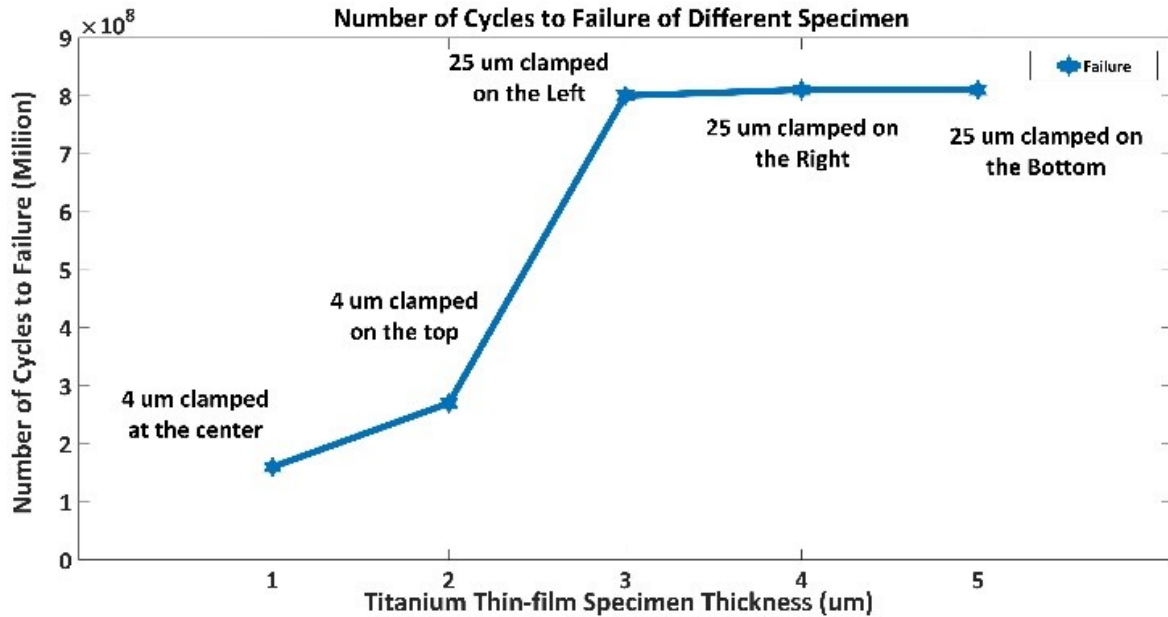


Figure 4.10 The scatter plot of number of cycles to failure with respect to the thickness of thin film Ti and its clamping positions on the acrylic sheet

help in the image observations and the extent of the damage at a low vacuum environment. Besides, the energy dispersive spectrometer (EDX), which is equipped with a silicon drift detector, a large detection area, and a scan generator (Bruker) helps in mapping the surface of the thin film membrane to determine the chemical composition. Figure 4.11 shows both the topography and compositional distribution of 4  $\mu\text{m}$  and 25  $\mu\text{m}$  thin film Ti alloys.

## 4.5 Extended FEM of Crack Growth

After observing the topography of the fatigued surface of thin-film membranes in the presence of micro-cavities and discontinuities; the next stage includes the analysis of the underlying stress intensity factors, which promote the fatigue crack growth. Fracture-based numerical simulations can assist in quantifying and predicting the fatigue life of a specimen [141]. To simulate the fractured samples, techniques such as boundary element; meshfree; finite difference method (FDM), and finite element method (FEM) are available. FEM has been

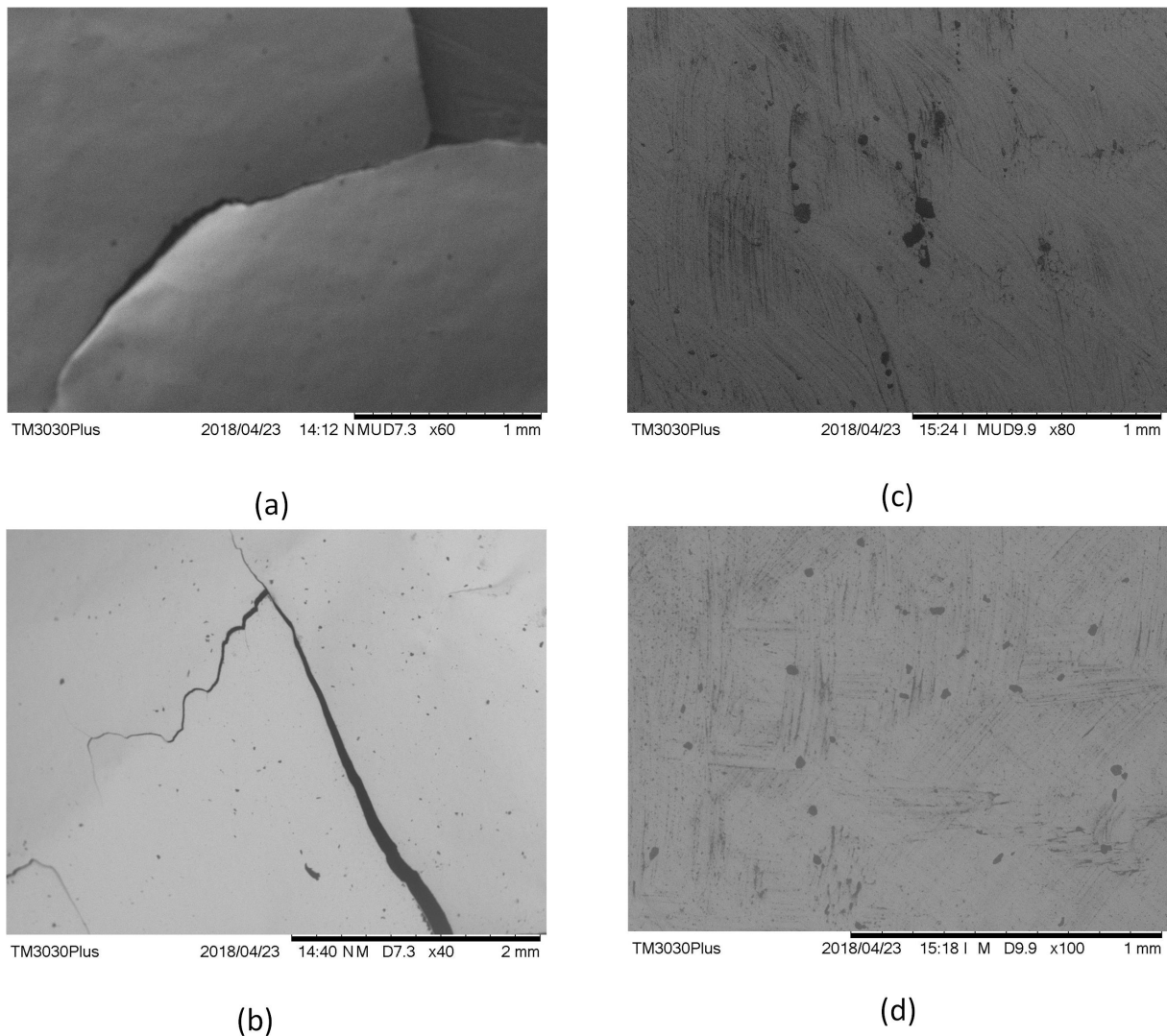


Figure 4.11 Thin film Ti specimens (a) 4 μm thick, (b) 25 μm thick

extensively used in the study of asymptotic stress fields at the tip of the crack. However, the crack surface must be coincident with the edge of the FEM makes the modeling of discontinuities and micro-cavities laborious. Instead, extended finite element method (X-FEM) allows modeling of crack geometry independent of the mesh by enriching the solution space to differential equations with discontinuous functions and is accessible through Abaqus CAE, which offers powerful and complete solutions for numerous intricate problems. In X-FEM, the standard FEM function must be enriched by the enrichment displacement function

which is mathematically expressed as the following equation 4.1).

$$U^h(x) = \sum_{j \in \Omega} \Phi_j(x) u_j + \sum_{k \in \Omega_\psi} \Phi_k(x) \psi(x) a_j \quad (4.1)$$

Where  $(x)$  is a point in the space in the X-FEM,  $\Omega$  is the set of nodes,  $\Phi_j$  is the shape function,  $u_j$  is the classical nodal degree of freedom in the FEM,  $\psi(x)$  is the enrichment function defined over  $\Omega_\psi$  and  $a_j$  is an added set of degree of displacement to the FEM.

The crack propagation is simulated by treating the fatigue crack growth as a linear combination of line segments. Figure 4.12 shows the X-FEM simulation results of the crack propagation of a  $4 \mu\text{m}$  thick, thin film Ti membrane.

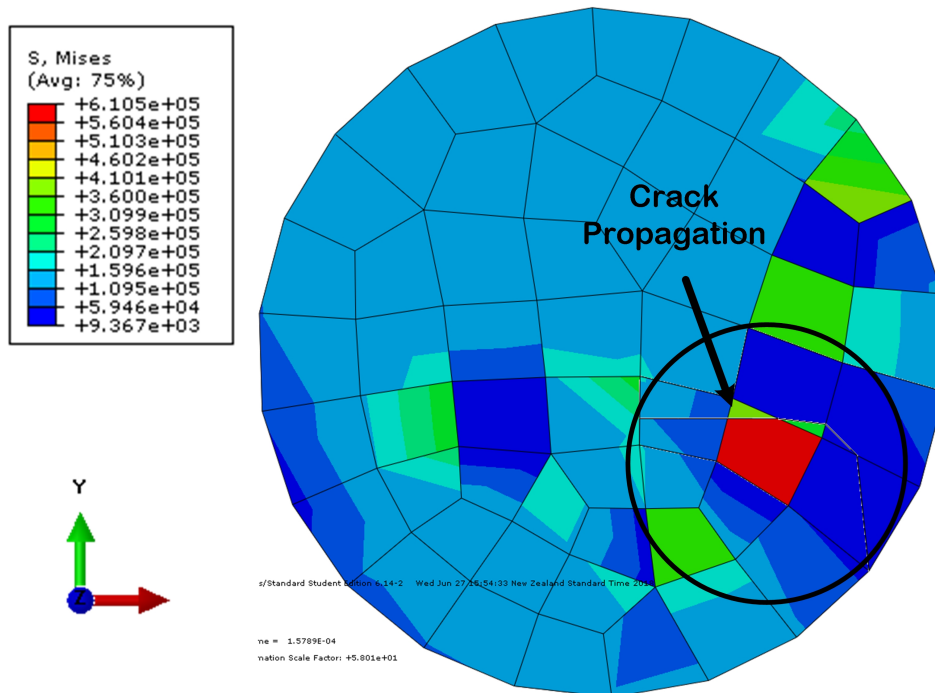


Figure 4.12 The X-FEM based crack growth plot of  $4 \mu\text{m}$  thick, thin film Ti membrane

## 4.6 Summary

The experimental validation of thin film deflection and fatigue behavior has been successfully performed using an acoustic-based fatigue system. The fatigue system was custom set up and comprised of multimedia speaker-subwoofer subsystem, spectrum analyzer (LabVIEW), and laser displacement sensor. The thin film deflection and fatigue results obtained in the experiments had significant correlations. However, the thin film deflections obtained in the experiments were little higher than the deflections obtained in the FEM as the random input load was exaggerated to test the burst pressure of thin film membranes.

# **Chapter 5**

## **Implantable Pressure Sensor: MEMS Fabrication Framework**

### **5.1 Introduction**

The subsequent stage after the modelling, simulation, and testing of the pressure sensor prototype is to fabricate the micro-electro-mechanical (MEMS) micro-pressure sensor. MEMS microfabrication is intricate and demands an optimized framework to build a physical sensor successfully. The following sections discuss the underlying concepts of complementary-metal-oxide-silicon (CMOS)-MEMS-based micro-system design and streamlined design flow of membrane-based MEMS sealed cavity pressure sensors.

In general, a micro-electro-mechanical parts (MEMS) system is a micro-device of characteristic dimensions of less than 1 mm and is composed of micro-mechanical parts integrated with complementary-metal-oxide-silicon (CMOS) based electronics and telemetry (Figure 5.1). While the MEMS micro-mechanical parts could include sensors and actuators that

are capable of measuring physical quantities in the surrounding medium. CMOS electronic circuits include transimpedance, transconductance amplifiers, filters, and wireless telemetry.

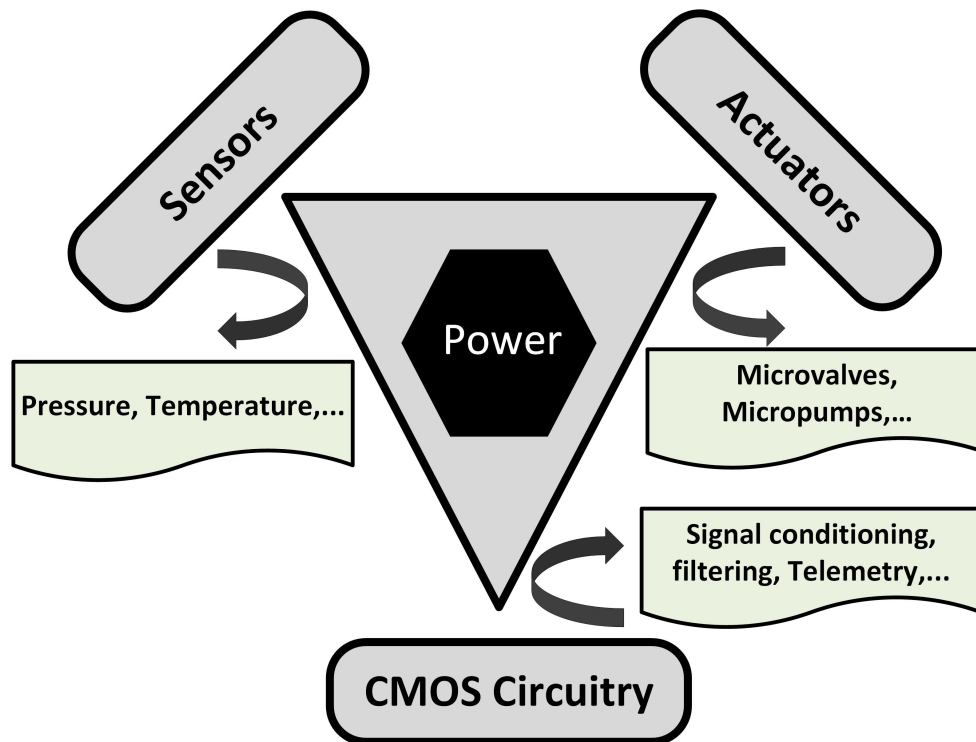


Figure 5.1 A pictorial representation of various components of a MEMS systems

In the last few decades, CMOS-MEMS subsystems have been widely used in diverse applications including automotive, aerospace, biomedical, industrial, and domestic uses. For example, aerospace applications MEMS pressure sensors are used in evaluating velocity, direction, and forces acting on an aircraft. Similarly, MEMS implantable pressure sensors are used in a wide variety of biomedical applications that need pressure sensors for measuring the body's internal pressure. Some of the merits of CMOS-MEMS fabrication include

1. Low-cost manufacturing using batch fabrication.
2. High sensitivity
3. Low noise readout
4. Miniaturized size

5. Low hysteresis
6. Low power consumption
7. Minimized parasitics

## 5.2 Types of MEMS pressure sensors

The basic MEMS sensing mechanisms include (1) Piezoresistive sensing, (2) Capacitive sensing, (3) Inductive sensing.

### 5.2.1 Piezoresistive Sensing

The concept Piezoresistance emanated in 1856 when Lord Kelvin first discovered the change of electrical resistance in metallic devices due to externally applied load. With the advent of integrated circuit fabrication, the piezoresistive effect was discovered in semiconducting materials such as silicon and germanium. The piezoresistive coefficient of a semiconducting material is shown in the equation 5.1

$$\rho_{\sigma} = \frac{(\partial \rho)}{\varepsilon} \quad (5.1)$$

The first piezoresistive semiconducting stress transducers were developed by Pfann et al. in 1961. In this work, MEMS piezoresistive pressure sensors were designed using longitudinal and two transverse diffused resistors in whetstone bridge. In the past decades, micromachined MEMS piezoresistive pressures have undergone a remarkable transformation. Piezoresistors are deposited onto the thin-film membrane, to induce a change in resistance linear to the

deflection [8]. However, due to the dependency of piezoresistive coefficients on temperature and clamping conditions of the thin-films, silicon-based MEMS piezoresistive pressure sensors are prone to considerable thermal drift. A MEMS model of the piezoresistive pressure sensor is shown in Figure 5.2

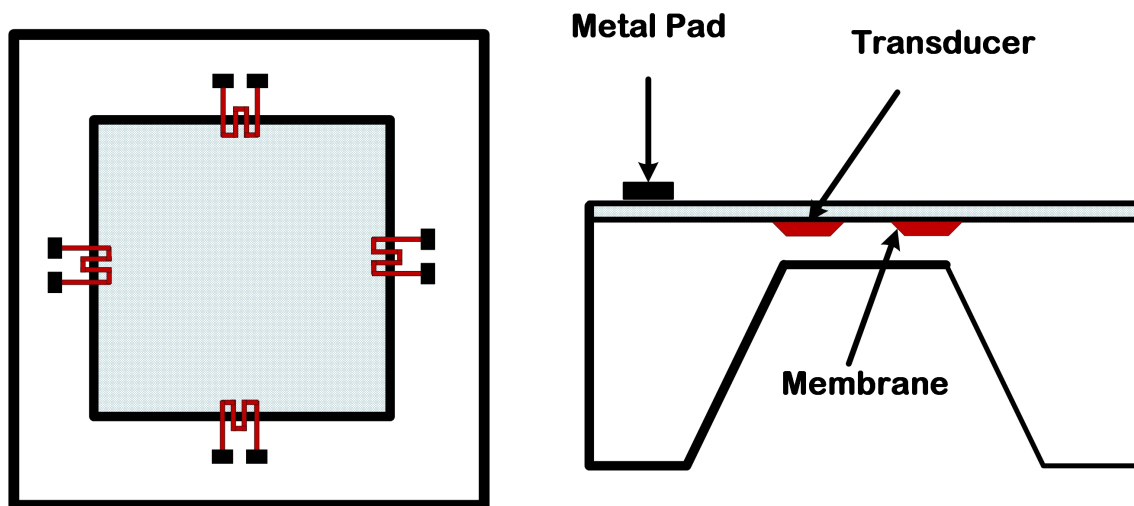


Figure 5.2 A cross-sectional view of MEMS piezo resistive pressure sensor

### 5.2.2 Capacitive Sensing

Alternately, thin-film membranes can be deposited onto a silicon substrate with a small cavity etched between these two layers. In this design, the thin-film acts as one electrode and the substrate as the second electrode forming the function of a capacitor. The deflection of the thin-film electrode can induce a change in the original capacitance under the influence of the applied pressure. A model of a MEMS capacitive pressure sensor is shown in Figure 1.13, and a FEM model is presented in Appendix A.

### 5.2.3 Transduction Stages

Figure 5.3 shows the several transduction process stages. In each stage, the signal is converted from one form of energy to the other, which requires transconductance or transimpedance amplifiers to turn the final output into a more readable form. The combination of a MEMS pressure sensor and amplification circuit is often termed as an integrated Micro-system [142].

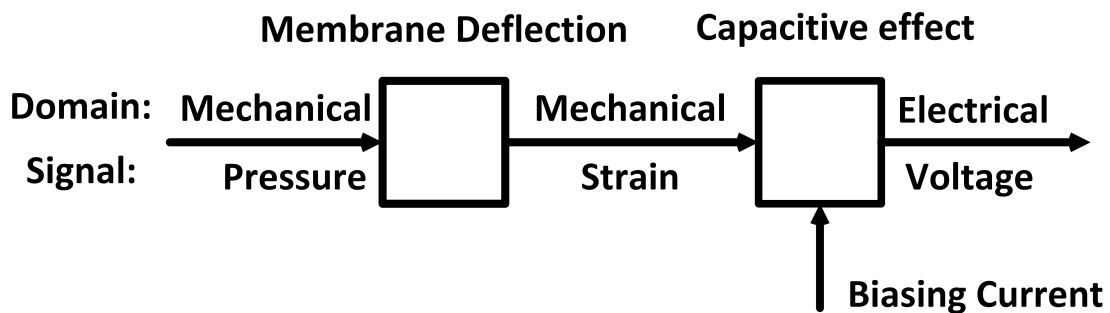


Figure 5.3 A conceptual view of pressure transduction scheme

## 5.3 CMOS-MEMS Fabrication

Figure 5.4 shows the chronological order of the MEMS fabrication process. The process design starts with input data collection (e.g., ICP, blood pressure, bladder pressure, etc.). At this stage, the inherent nature and dynamics of ICP must be reviewed. The review involves the collection of baseline threshold ICP values, the waveform nature of ICP, the dependence of arterial and respiratory pulses, and the external effects of atmospheric pressure fluctuations. Next, the actual MEMS design optimizations will begin. The design optimization stage is broadly classified into modelling, simulation, CMOS-MEMS process selection, MEMS design, CMOS design, and fabrication. In the FEM, the cross-section of the MEMS device plays an important role in the optimization of stresses and strains that influence the behaviour of thin film structures. The MEMS model is drawn using 3D CAD tools such as solid works.

The models should be a replica of the actual MEMS physical device. The design optimization is performed using Multiphysics FEA tools such as COMSOL and ANSYS to simulate the behaviour of the thin film structures that are subjected to cyclic stresses and strains. In MEMS modelling, the effect of mismatches in the thermal expansion of different material layers, and hygroscopic swelling due to the use of epoxy in hybrid packaging is also considered. If the FEA simulations satisfy the necessary design specifications, the CMOS-MEMS fabrication process will be planned in the next stage.

### **5.3.1 CMOS Circuit Simulations**

The CMOS-MEMS integration process is classified into (1) Monolithic integration and (2) Hybrid integration. In monolithic integration, the CMOS and MEMS are designed on the same die. In monolithic integration, the process starts with the selection of the CMOS design process (e.g., CMRF8SF) and CMOS and MEMS are designed on the same die. The etching and release of MEMS structures take place as the post-CMOS-MEMS process. In contrast, MEMS and CMOS are developed separately in the hybrid integration process. In the final step, MEMS and CMOS are integrated using multi-chip module packaging. The CMOS circuit design comprises of defining the circuit inputs/outputs and simulation. The circuits are drawn in the analogue design environment (ADE) that consists of various CMOS circuit elements including PMOS, NMOS, and other fundamental components. The circuit specifications such as the length and width of the transistors are set in the schematic. For example, on-chip signal conditioning circuits such as the transimpedance amplifier (a current to voltage converter) or transconductance amplifier (a differential input voltage to current converter) are usually designed to detect the low signals from the MEMS sensors. The performance characteristics including the bandwidth, gain, noise, and power dissipation of the CMOS transimpedance amplifier must be optimized. An optimized transimpedance amplifier must have a wide bandwidth and high gain to avoid inter-symbol interference (a



form of signal distortion) and also to pick low capacitance values from the sensor output. A current mirror (Figure 5.5) is a basic building block of any cascoding in an amplifier, which will help in producing the exact copy of the input current at the output terminal. The salient feature of the current mirror is high output resistance regardless of the load fluctuations.

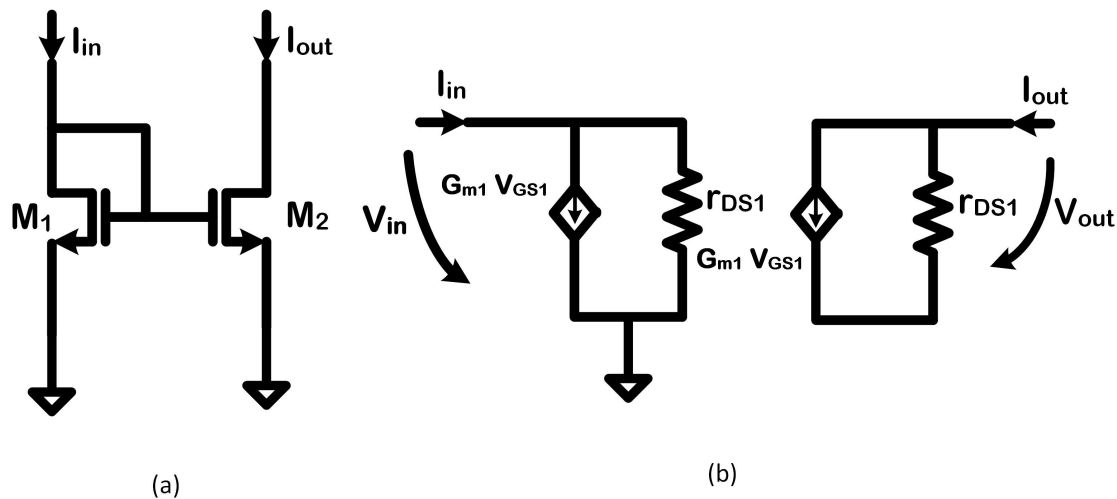


Figure 5.5 (a) Circuit of a NMOS current mirror; (b) Small signal equivalent of a NMOS current mirror

The circuit simulations include the evaluation of the frequency response (small-signal analysis or circuit simulations) of CMOS circuits (e.g., transimpedance amplifier). The small signal analysis plots the output gain and phase margin changes. The simulation tools such as the Cadence spectre can be used to plot the frequency response curves. In the circuit design stage, the necessary space required for MEMS structures are allocated. In most of the CMOS design processes (e.g., CMR8SF), metal-insulator-metal (MIM) capacitors are included as part of the package. These can be used as MEMS spacers. The widths and length of these MIM capacitors can be chosen as per the guidelines of the design process. Once the CMOS circuit meets the design specifications, the design is ready for layout design.

### 5.3.2 CMOS Layout Design

CMOS layout design is a standard means of translating the circuit into a physical device. In the layout design process, a stick diagram is drawn as an intermediate layer to convey the layer information through various colour codes (or monochrome encoding). It shows all the components, vias, placement of components, routing, etc. The layout editors such as the Virtuoso from cadence help in drawing the layout of a CMOS circuit with a custom-made design process (130 nm CMRF8SF from global foundries). The inbuilt design rule check (DRC), parameter extraction, layout vs schematic (LVS) and parasitic extraction will help in checking and preserving the functionality of the design. Figure 5.6 shows the layout of the CMOS current mirror.

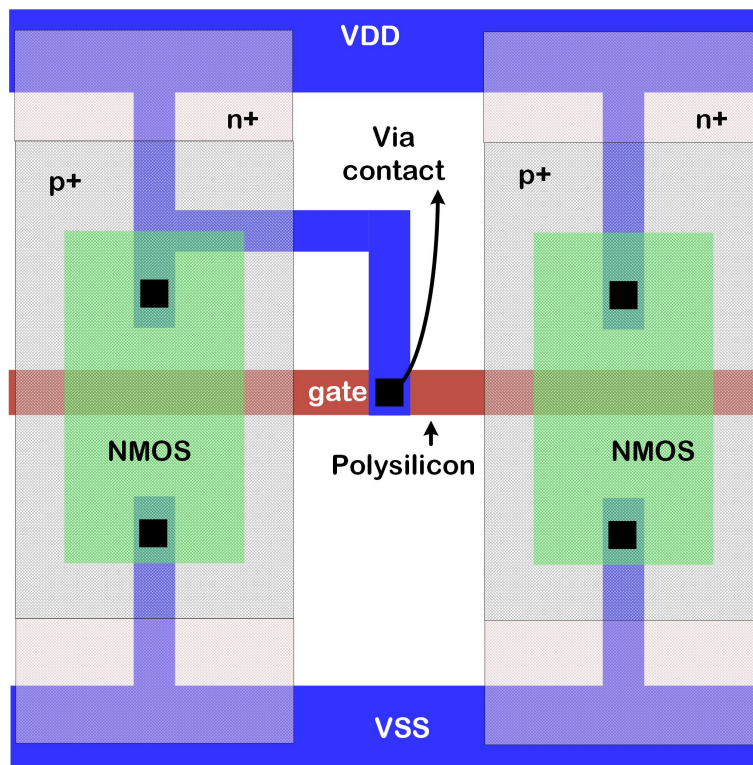


Figure 5.6 A typical layout of CMOS current mirror with N-channel MOSFET

The final layout is submitted to MOSIS in the form of GDSII stream format, which is a database file format and a standard for data exchange in the IC manufacturing industry. Figure

5.7 shows the optimized layout of CMOS transimpedance amplifier and MEMS capacitive pressure sensor on 130 nm global foundries CMOS design process (CMRF8SF).

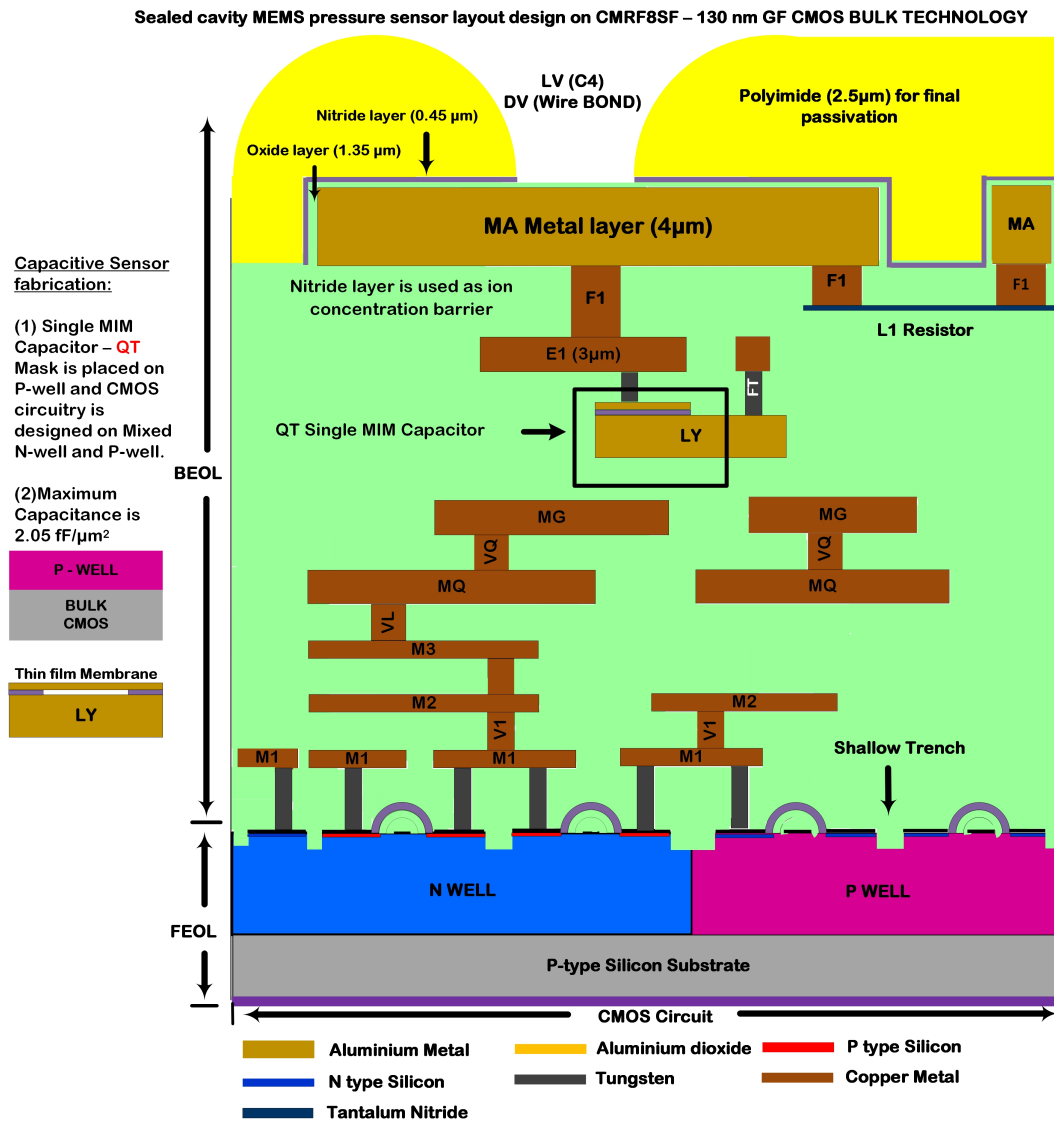


Figure 5.7 A typical layout design of a MEMS pressure Sensor with an on-chip transimpedance amplifier drawn on global foundries (GF) 130 nm CMRF8SF CMOS design process

The final stage in the monolithic integration of a CMOS-MEMS pressure sensor is the design of the fabrication of a MEMS pressure sensor using a post-CMOS-MEMS approach. A mask layout is necessary for patterning the mechanical structure of the pressure sensor. As discussed earlier, thin film membrane-based pressure sensors are popular choices in the ICP

monitoring. Therefore, a thin film membrane patterned on a silicon substrate with necessary etching is drawn using L-Edit software from Tanner EDA. Figure 5.8 shows the mask layout of a membrane-based MEMS pressure sensor.

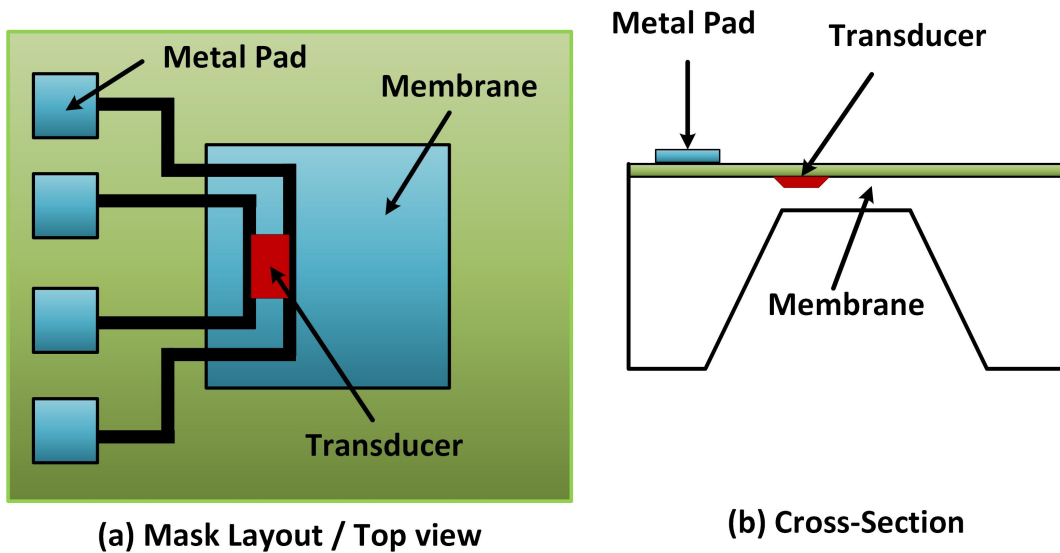


Figure 5.8 A typical bulk MEMS micromachined pressure sensor (a) Mask Layout view or Top view; (b) 2D Cross Sectional view

### 5.3.3 MEMS Fabrication

MEMS fabrication techniques were originally adapted from the semiconductor integrated circuit (IC) industry [16]. Figure 5.9 shows the standard MEMS process sequence, which includes: (1) The preparation of the silicon substrate (RCA Clean), (2) Deposition of thin films; (3) Etching of thin films and Substrates, (3) Release etching of microstructures, sacrificial layers and interim structures [143, 144].

The materials used in the MEMS fabrication are (1) single-crystal silicon substrates used as the substrate in various MEMS manufacturing [145]. Silicon is reliable until a temperature of 700 °C but softens and deforms at temperatures greater than 700 °C; (2) Silicon oxides such as SiO<sub>2</sub> used as sacrificial layers and insulators. SiO<sub>2</sub> is obtained from the thermal oxidation

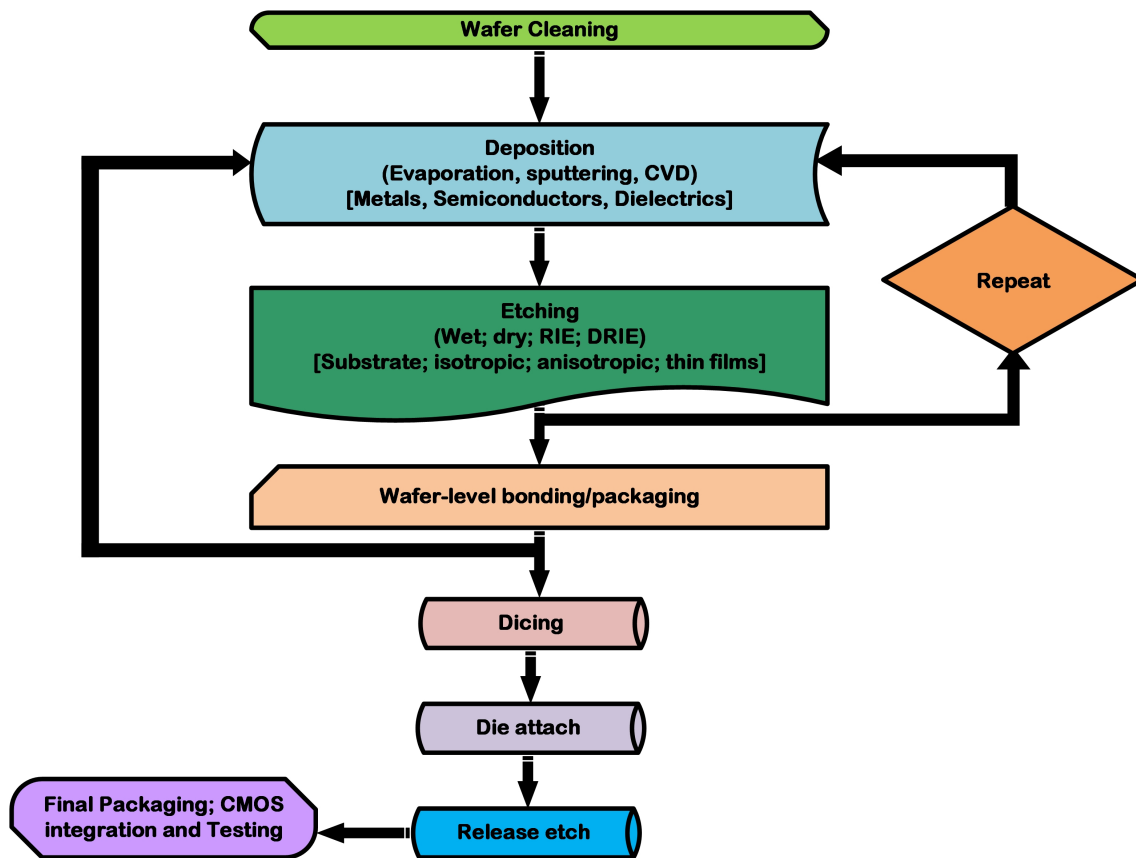


Figure 5.9 MEMS microfabrication process flow

of silicon at temperatures above 800 °C. The other oxides layers such as Aluminum oxide (Sapphire), Zinc oxide (ZnO) can be formed from various deposition processes including chemical vapour deposition (CVD) [146], physical vapour deposition (PVD) [147, 148], and atomic layer deposition (ALD) [149, 150]. SiO<sub>2</sub> has a reputation for inducing large intrinsic stresses that are difficult to control during oxidation process and hampers the long-term reliability of MEMS devices [151]. Alternately, silicon nitride (Si<sub>3</sub>N<sub>4</sub>), can be used as a sacrificial or insulation layer or as a thin film membrane. This is due to their higher moduli and lower intrinsic stresses than SiO<sub>2</sub>. The choice of materials for the deposition process depends on the requirements of a specific application. For example, titanium (Ti) is a biocompatible material, which is highly sought after in the encapsulation of medical devices. This material can be deposited using sputtering deposition, or PVD technique [152]. Other

materials such as gold, nickel, and Permalloy (Ni<sub>81</sub>Fe<sub>19</sub>) use electroplating as a deposition technique [153]. Aluminum (Al), and copper (Cu) interconnections in MEMS fabrication can be deposited via sputtering. However, they are limited to non-corrosive environments and temperatures below 300°C. For higher temperatures interconnections are made using materials like gold, titanium, and tungsten [153, 154]. For bonding poor adhesive films (e.g., platinum to silicon and its oxides), thin metal layers such as chromium, titanium, and alumina (Al<sub>2</sub>O<sub>3</sub>) are frequently used as intermediate layers [155]. Polymers such as polyimides or photo-resists are used as a device protection layer and thin-film membranes in MEMS packaging with varying thickness of few nanometers to hundreds of microns. Special photo-resists such as epoxy-based SU-8 can also be deposited via spin coating up to 100 μm thick for bonding various wafers [156]. Silicon carbide (SiC) and diamond can be used as an alternative substrate material to silicon owing to their advantages including hardness, high modulus of elasticity, resistance to harsh environments, mechanical stability at higher temperatures, wide bandgap, and high thermal conductivity. They can now be deposited on traditional silicon substrates via various micro-machining processes. [157–159].

MEMS etching processes include reactive ion etching (RIE), deep reactive ion etching (DRIE), surface micro-machining, and laser micromachining. Here, the materials are exposed to various etchants such as wet chemicals and gases while the surface of interest is being etched to form precise patterns. In the etching process, mask and lithography play an important role in the definition of accurate and precise patterns [160]. In summary, various MEMS processes include epitaxy growth of crystalline silicon, oxidation process, sputter deposition, evaporation, CVD, atmospheric-pressure CVD (APCVD), low-pressure CVD (LPCVD), plasma-enhanced CVD (PECVD), spin-on methods, lithography process, patterning resist, etching process, release etching process, anodic bonding; grinding, chemical-mechanical polishing, electroplating, molding, epoxies, non-lithographic microfabrication techniques; laser micromachining, screen printing; soft lithography, and nanoimprint

lithography[143, 144]. MEMS packaging or hermetic sealing is to ensure the protection of a micro system from the surrounding environment. Besides, the package provides reliable interconnections between the sensor and the outside world. In general, wafer level packaging is preferred due to its batch fabrication capabilities, hermeticity, and 3D integration. Wafer level packaging includes various bonding methods such as direct bonding (e.g. glass to silicon anodic bonding and silicon to silicon fusion bonding); and bonding using an intermediate metal, glass or polymer layer [161]. The subcategories in the direct bonding include (1) Anodic bonding, which is used to hermetically seal a silicon or glass substrate to metal without using any intermediate layer [162, 163]. As an example, Ti-6Al-4V alloy can be successfully bonded to bioactive glasses (e.g. 45S5 and 52S4.6) at temperatures ranging between 250 °C to 300 °C. Similarly, anodic bonding can be used to seal two gorilla glass at temperatures ranging between 200 °C hermetically to 400 °C hermetically [164]. (2) Direct fusion bonding, which involves hermetic sealing of two silicon wafers at room temperature and subsequently annealing them at a temperature between 700 °C to 1100 °C [165, 166]. As an example, ALD Alumina ( $\text{Al}_2\text{O}_3$ ) can be directly fused to  $\text{Si}_3\text{N}_4$  thin films at 600 °C [164]. Similarly, Copper-Copper fusion bonding can form a vertical interconnection in a microsystem [167]. Alternatively, the subcategories in intermediate layer-assisted bonding include: (1) Eutectic bonding, a low-temperature bonding process that uses intermediate metal layers to bond materials that exhibit poor adhesive strength to silicon. As an example, eutectic bonding can be used to glue gold (Au) to silicon substrates via Ti intermediate layer at a bonding temperature of 400 °C [168]. (2) Glass-frit bonding, another low-temperature bonding process, where a low melting point glass is used to glue two wafers substrates. In case of bonding silicon wafers with aluminum, the active melting glass compound is lead-silicate glass with a wetting temperature of 425 °C to 452 °C [169]. (3) The epoxy seal is a hermetic sealing technology for aiding safe passage of copper wires through electrical bulkheads without any leakage. Today, epoxy seals can be used in various titanium and steel

metal encapsulated devices. Epoxies such as Teflon, PVC, Polyimide and benzo-cyclo-butene (BCB) can be used in bonding and sealing materials for zero level packaging or housing RF MEMS [170, 171].

### 5.3.4 Commercial MEMS Fabrication process

Instead of setting up a custom cleanroom MEMS fabrication process, there are a couple of commercially available MEMS processes which include Multi-User MEMS (MUMPS) and SUMMiT (Sandia Ultra-planar Multi-level MEMS technology). They provide low-cost batch fabrication to industry and universities across the globe. Here, in the first design phase, the mask layout is designed using system level Layout designers such as MEMS pro. The mask is then sent to the foundry in the form a GDSII file for physical fabrication. The commercial designs of MUMPS include, (1) a three-layer polysilicon-based micromachining process – Poly MUMPS, (2) an electroplated nickel process – Metal MUMPS, (3) silicon-on-insulator-based micromachine process – SOI MUMPS. For the fabrication of MEMS sensors for long-term monitoring, Metal MUMPS may be suitable as thin film metal membranes can be formed and can provide lifetime stability. These design rules are restricted to the standards of the commercial foundry [172].

In contrast, the SUMMiT offers various advantages over MUMPS, which include tighter tolerances; Nanoscale structures; and additional releasable structures. However, it doesn't add a metal layer which makes it non-suitable for pressure sensors that need mechanically stable and biocompatible metal thin film membranes. Another disadvantage is that the turnaround time is more than that for MUMPS and customized MEMS setups and can be more expensive as well [173].

### 5.3.5 CMOS-MEMS Packaging

For better sensitivity, one-chip CMOS electronics are normally preferred (Figure 5.10). The two types of CMOS-MEMS integration approaches include a hybrid approach [174] and monolithic integration. In the hybrid approach, the MEMS and CMOS are designed on different substrates and interconnected via flip chip or wire bonding. In contrast, monolithic integration starts with CMOS fabrication and the MEMS device is created on the same chip as a post-CMOS MEMS process. The choice of CMOS-MEMS integration depends on the specific requirements of a conceptual design, cost and possible process yields. Monolithic integration is cost-effective only if the process yield is potentially 100 %, otherwise hybrid integration would be much more efficient [175]. In a post-CMOS MEMS process, enough space for a MEMS structure is pre-designated before the CMOS fabrication. However, the maximum post-processing of a MEMS design is constrained to 450 °C, which hinders the creation of complex shapes. Besides, the CMOS electronics must be protected from potential damage [176]. Thus, the post-processing approach limits the use of materials having low deposition and annealing temperature such as a low crystallization temperature. For better yields, it is better to fabricate CMOS and MEMS and make the interconnection via a hybrid approach or multi-chip module [177]. MEMS can be integrated into CMOS in various

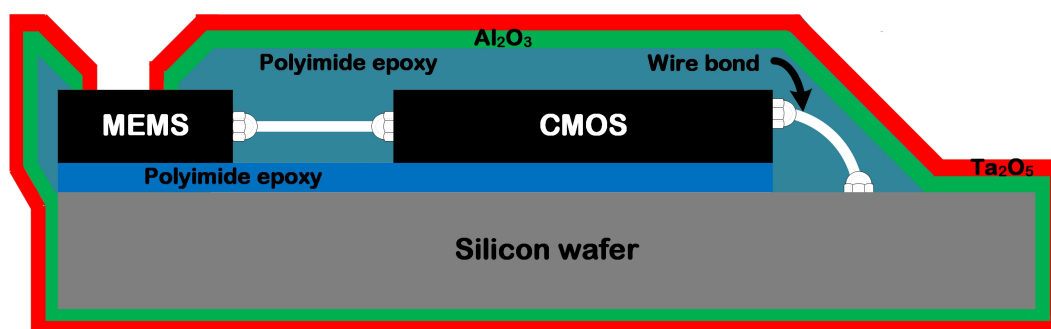


Figure 5.10 Cross-section view of a Post-CMOS MEMS fabrication as a Multi-chip Module

styles including (1) stacking the MEMS structures on top of a finished CMOS die, (2) micromachining the layers after completion of the standard CMOS fabrication process using

various fabrication techniques presented in the previous section. For example, a capacitive pressure sensor fabricated on a 0.18  $\mu\text{m}$  as post-CMOS MEMS process [178], in order to release the structural thin film membrane, deposition, PECVD-based oxide layer patterning, etching the sacrificial layer to release the suspended membrane; and final etching of the passivation oxide layers to open the pads and allow electrical interconnections. Similarly, a CMOS integrated capacitive pressure sensor fabricated on a silicon-germanium MEMS (SiGeMEMS) process and integrated to CMOS signal conditioning circuits as a hybrid approach using direct wafer-level bonding [179]. A wireless capsule microsystem to detect and monitor pH, pressure, and the temperature of the gastrointestinal tract [180]. The device was fabricated as a cylindrically shaped capsule of 28 mm in outer length and 13 mm in outer diameter. Further opportunities in CMOS-MEMS integration via the LSI foundry and other open and closed facilities can be reviewed here [181–184].

## 5.4 An Optimized Wafer-Level MEMS Fabrication

An optimized example of a wafer level packaging of membrane-based pressure sensors is discussed below. Two different wafer materials (silicon and glass) are chosen as the substrates. In the first stage, the silicon wafer is prepared for micromachine process using RCA clean [185]. Next, a stress-relieved  $\text{Si}_3\text{N}_4$  of 200 nm thickness is deposited on the backside of the silicon wafer via low-pressure chemical vapour deposition (LPCVD) process [186]. Similarly, titanium 500 nm thick is deposited on the front side of the silicon wafer using sputter deposition [187]. A photoresist is deposited on top of the 200 nm thick  $\text{Si}_3\text{N}_4$  on the back side of the silicon wafer; Patterns are formed for cavity etching. Inductively coupled plasma–reactive ion etching (ICP-RIE) is used to form the cavity with titanium etch stop (Figure 5.11).

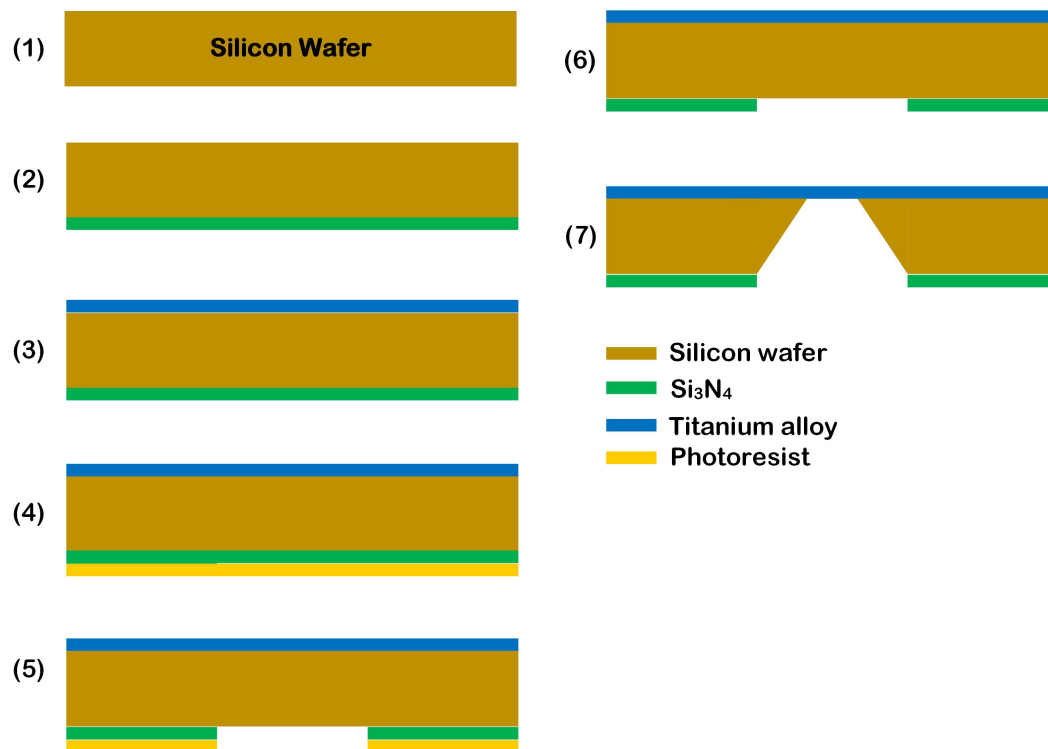


Figure 5.11 MEMS wafer-level processing of silicon substrates - thin film deposition and etching

In the second stage, Corning 7440, a glass wafer substrate is prepared for micromachine processing with a mixture of  $\text{H}_2\text{SO}_4$  and  $\text{H}_2\text{O}_2$ . A  $300\ \mu\text{m}$  thick polysilicon is deposited on the top surface of the glass wafer using LPCVD at  $550\ ^\circ\text{C}$ . Similarly, a  $200\ \mu\text{m}$  thick,  $\text{Si}_3\text{N}_4$  is bonded to the back surface of the glass substrate using plasma activated direct bonding [188]. Polysilicon is etched (isotropic etching) using the same ICP-RIE used in the etching of  $\text{Si}_3\text{N}_4$  in the previous stage. Nickel chromium ( $200\ \mu\text{m}$ ) and Gold ( $500\ \mu\text{m}$ ) are deposited using an E-beam evaporation system for electrode formation. Finally, a small piece of additional glass is bonded to increase the height of the cavity (Figure 5.12).

In the third stage, the silicon wafer is bonded to Corning 7440 glass wafer substrate using anode bonding technique at temperatures  $300\ ^\circ\text{C}$  to  $400\ ^\circ\text{C}$  [189]. Before the bonding process, a small strip of the titanium thin film membrane is etched using Deep reactive ion etching (DRIE) for creating metal contacts for electrical connections (Figure 5.13).

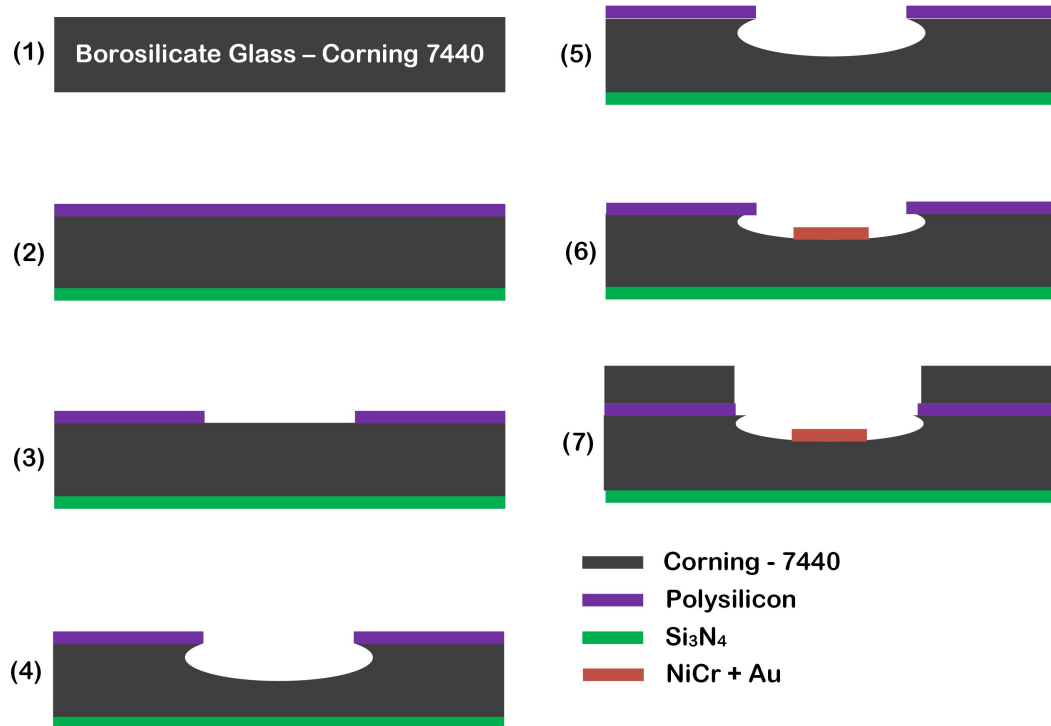


Figure 5.12 MEMS wafer-level processing of glass substrates - thin film deposition, etching and metalization

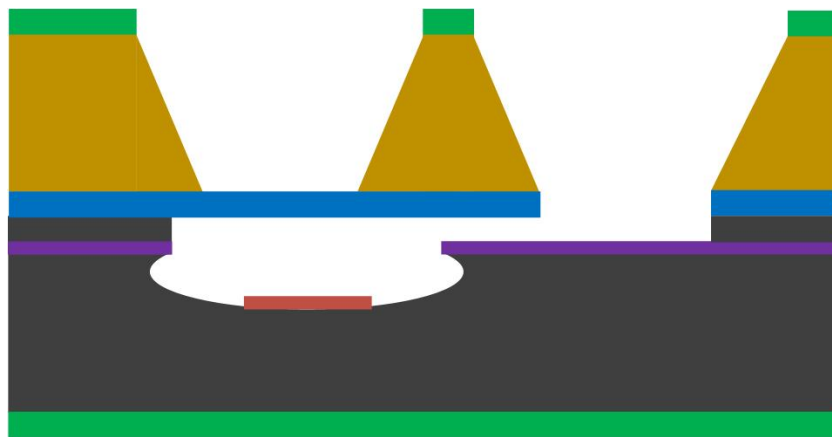


Figure 5.13 MEMS wafer-level bonding of silicon and glass substrates

In the fourth stage, metalization using a vertical feed-through approach and vacuum sealing is accomplished. This is achieved by forming thick hermetically sealed electrical feed-throughs and sealing the cavity in the vacuum (Figure 5.14).

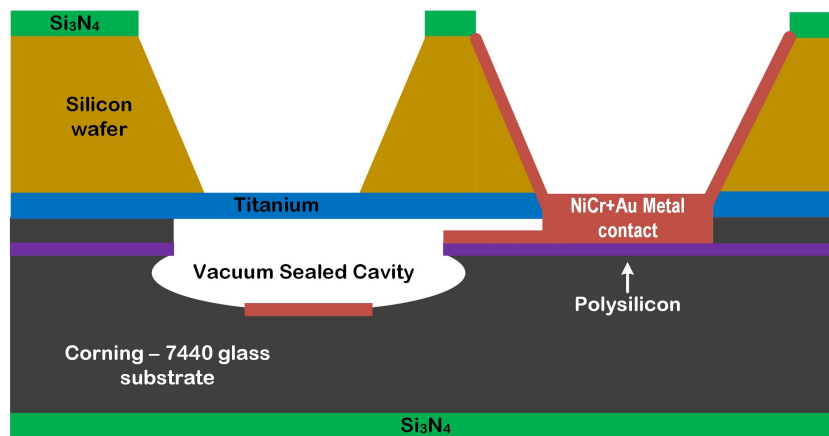


Figure 5.14 MEMS sequential process for final metalization and vacuum sealing

In the fifth stage, the CMOS-MEMS pressure sensor is encapsulated with  $\text{Al}_2\text{O}_3$  and  $\text{Ta}_2\text{O}_5$  dual layer biocompatible materials (Figure 5.15).

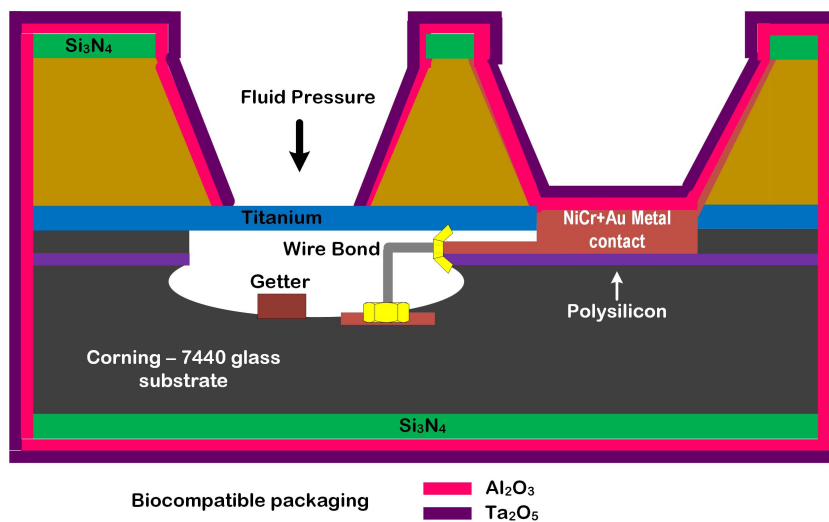


Figure 5.15 Final Packaging of MEMS Pressure Sensors

## 5.5 Summary

A conceptual framework of CMOS-MEMS fabrication has been presented in this chapter. Initially, the underlying concepts of CMOS circuit simulation, MEMS modelling, and CMOS layout design have been discussed. Next, the MEMS fabrication process involving deposition

---

(sputtering), etching and final packaging have also been discussed. Finally, an optimized design process of a membrane-based sealed cavity MEMS pressure sensor has been outlined.



# Chapter 6

## Conclusions and Future Work

### 6.1 Conclusions

Modelling, Simulation, and Testing of mechanical behaviour including the thin film deflection, and the fatigue life of a thin film Ti alloys-based MEMS pressure sensor have been successfully conducted in this research. Initially, a literature study on the nature and dynamics of ICP was conducted. The literature review included, the study of internal and external factors affecting the behaviour of ICP. Various patterns of ICP waveform including the interference of arterial and respiratory pulsations have been collected. The collected patterns were used as input to the MEMS pressure sensors model. Not only that, but the impact of atmospheric pressure fluctuations on the behaviour of ICP has also been studied. A MEMS barometric micro-sensor (Mensor CPT6100) was used to record the atmospheric pressure variations in Auckland. The captured readings were plotted in Excel and used as an input to the MEMS pressure sensor model-like ICP wave patterns. Next, the FEM of thin film deflection and fatigue behaviour has been set up in COMSOL Multiphysics FEA software. A small literature review on the modelling and simulation of thin film membranes

has been conducted. underlying concepts of stress and thin film deflection of membranes has been introduced. It was found that stresses due to deflection (stresses due to straining and bending) and residual stresses are the major components that affect the deflection and fatigue behaviour of thin film membranes. These stresses are dependent on the cross-section and dimensions of thin film membranes. Thus, a parametric analysis involving the simulation of various MEMS sensor models with different thicknesses has been performed.

In the third stage, experiments were set up to validate the FEM of thin film deflection and fatigue behaviour. An acoustic-based fatigue system was custom-made to test the deflection and fatigue life of thin film Ti alloys. Here, the fatigue testing is performed over a frequency range of 20 Hz to 1000 Hz. Five thin-film titanium foils (two 4  $\mu\text{m}$  thick and three 25  $\mu\text{m}$ ) are mounted onto a 3 mm thick clear acrylic sheet which is then mounted to the acoustic transducer. The thin film Ti membranes were loaded with Gaussian random vibrations (generated by a spectrum analyzer from LabVIEW) that were recorded using an accelerometer (ST Microelectronics STEVAL–MKI180V1). The sampling rate of 44 100 Hz with 10000 samples per channel (2 channels) and the Gaussian wave frequency of 500 Hz are used. The voice coil and subwoofer subsystem as part of the acoustic transducer in the acoustic speaker aided in generating high-intensity vibrations required to displace the thin film membranes at the centre. Laser displacement sensor (LK–HG5001, Keyence, USA) was used to capture the displacement of thin film alloys. There were significant correlations observed in the thin film deflection of 25  $\mu\text{m}$  and 4  $\mu\text{m}$  in the FEM and experimental setup. The correlations are shown in the Table 6.1.

Even though, there is no particular data suggesting the threshold operational life of an ICP sensor, the longer the sensor's accurate performance inside the cranium with possible minimum drift, the better. The FEM and experiments validate that the desired engineering specifications have been met with 4  $\mu\text{m}$  thin film Ti membrane. The thickness tolerances of thin film membrane can be around 0.5  $\mu\text{m}$  to 4  $\mu\text{m}$  thick.

Table 6.1 Comparison of FEM and experimental fatigue results for different thicknesses of thin-film Ti membranes

Thickness	No. of Cycles (FEM)	No. of cycles (Exp)	FUS	Pressure transmission
50 $\mu\text{m}$	1 Quadrillion	Nil	0.009	No
25 $\mu\text{m}$	12 Trillion	10 billion	0.01	No
4 $\mu\text{m}$	1 Billion	160 Million	0.9	Yes
1 $\mu\text{m}$	40 Million	Nil	16	Yes
500 nm	$10^4$ cycles	Nil	50	Yes
200 nm	$2.1 \times 10^3$ cycles	Nil	80	Yes
100 nm	563 cycles	Nil	90	Yes

The residual thin-films were observed under scanning electron microscopy (SEM) for damage evaluation and the extension of microcrack formation. Tabletop SEM TM3030Plus has been used to observe the fractographical features of thin-film membranes. After observing the topography of the fatigued surface of thin-film membranes in the presence of micro cavities and discontinuities, the next stage includes the analysis of the underlying stress intensity factors, which promote the fatigue crack growth. The extended finite element method (X-FEM) (Abaqus CAE) aided in the modelling of crack geometry independent of the mesh by enriching the solution space to differential equations with discontinuous functions.

Even though the modelling, simulation, and testing of membrane-based MEMS pressure sensors managed to provide precise results, there are still some drawbacks that must be considered, particularly in the experimental setup. Firstly, it was observed that the thin-film deflection was not purely linear although the clamping was rigid. Secondly, the high-intensity acoustic vibrations were concentrated more at the centre of the circular acrylic sheet. Thirdly, audible frequencies can only be useful to study the top surface of thin-film materials and has a problem of noise. Fatigue testing systems can also be set up using ultrasonic frequencies. The ultrasonic frequencies are above the normal human audible range (20 – 40 kHz) and

the problem of noise at acoustic frequencies can be mitigated. The ultrasonic fatigue testing system may comprise of a piezoelectric generator, ultrasonic booster, and an ultrasonic horn. Ultrasonic horn (sonotrode) is the most important part of the ultrasonic fatigue testing system; it determines the intensity of stress amplitudes displacing the thin films. As part of the future work, a sealed cavity MEMS pressure sensor will potentially be fabricated along with a custom testing rig to hold the microsensor. The custom test rig will contain the fluid and will be directly mounted to the tip of the sonotrode.

## 6.2 Future Work

The future work would potentially include the MEMS modelling and fabrication and testing of membrane-based MEMS capacitive pressure sensors. The fabrication design plan is discussed in Chapter 5. Section 5.4 outlines the wafer-level MEMS fabrication process sequence. The wafer-level fabrication offers several advantages including low-cost batch fabrication, high yield, low time to market, etc. Once a MEMS device is fabricated, the ultrasonic fatigue testing system can be set up to test the device for thin film deflection and fatigue behaviour. Figure 6.1 shows the ultrasonic fatigue testing system.

A custom pressure chamber rig would be made for testing the MEMS pressure sensors for thin film deflections and fatigue behaviour. Figure 6.2 shows the proposed pressure chamber test rig. A large hole for degassed water is filled in the pressure chamber and the MEMS sensor is fixed inside the chamber.

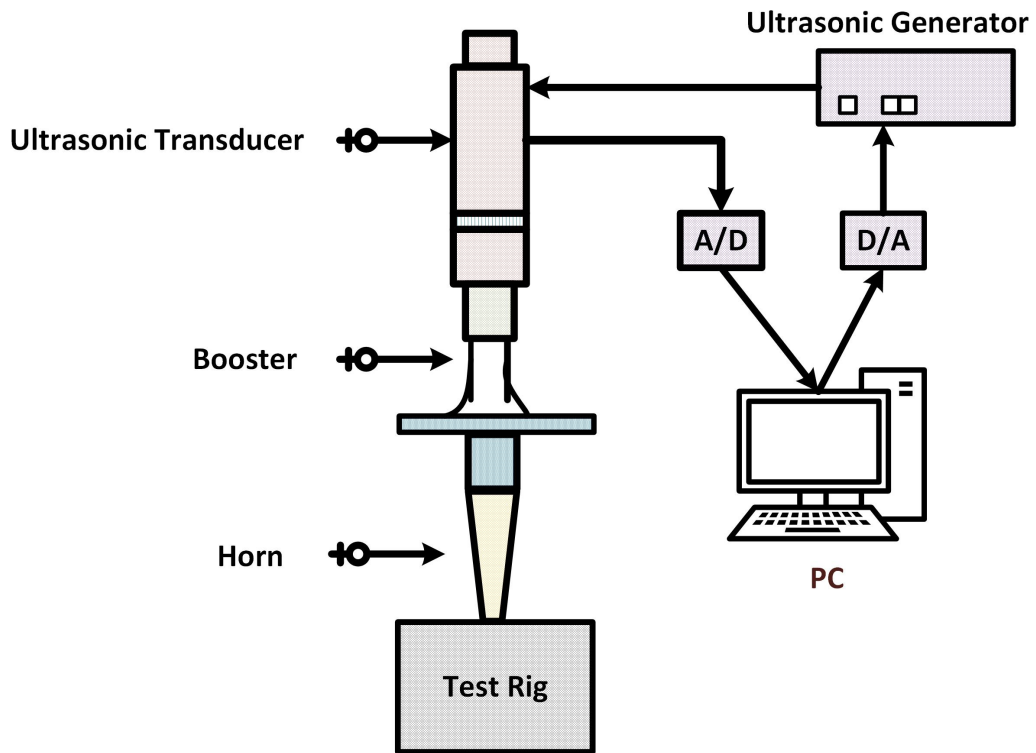


Figure 6.1 The block diagram of the proposed ultrasonic fatigue testing system

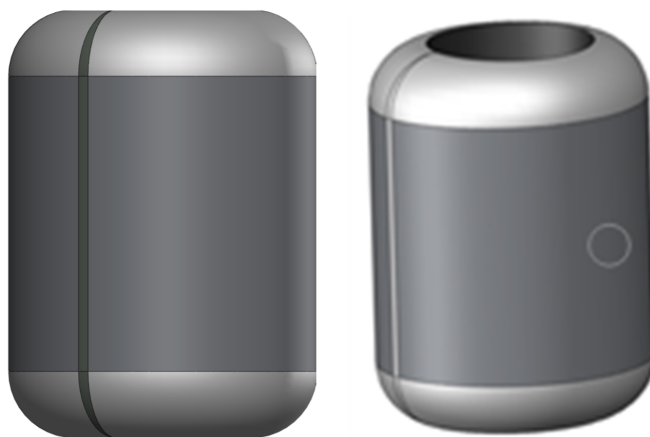


Figure 6.2 The proposed MEMS pressure sensor rig



# Bibliography

- [1] Randall M Chesnut, Gustavo Petroni, and Carlos Rondina. Intracranial-pressure monitoring in traumatic brain injury. *The New England journal of medicine*, 368(18):1751, 2013.
- [2] Venessa L Pinto and Adebayo Adeyinka. Increased intracranial pressure. 2018.
- [3] Ji Won Moon and Dong Keun Hyun. Decompressive craniectomy in traumatic brain injury: A review article. *Korean journal of neurotrauma*, 13(1):1–8, 2017.
- [4] GP Duffy. Lumbar puncture in the presence of raised intracranial pressure. *Br Med J*, 1(5641):407–409, 1969.
- [5] Sofy H Weisenberg, Stephanie C TerMaath, Chad E Seaver, and James A Killeffer. Ventricular catheter development: past, present, and future. *Journal of neurosurgery*, 125(6):1504–1512, 2016.
- [6] Scott C Dulebohn and Fassil B Mesfin. Ventriculoperitoneal shunt. 2017.
- [7] Celal Yavuz, Sinan Demirtas, Ahmet Caliskan, Kaan Kamasak, Oguz Karahan, Orkut Guclu, Suleyman Yazıcı, and Binali Mavitas. Reasons, procedures, and outcomes in ventriculoatrial shunts: A single-center experience. *Surgical neurology international*, 4, 2013.
- [8] Robert Francis Clifford Jones, Bruce George Currie, and Bernard Chi Tack Kwok. Ventriculopleural shunts for hydrocephalus: A useful alternative. In *Annual Review of Hydrocephalus*, pages 75–76. Springer, 1990.
- [9] Yad R Yadav, Vijay Parihar, Mallika Sinha, et al. Lumbar peritoneal shunt. *Neurology India*, 58(2):179, 2010.
- [10] Michelle Paff, Daniela Alexandru-Abrams, Michael Muhonen, and William Loudon. Ventriculoperitoneal shunt complications: A review. *Interdisciplinary Neurosurgery*, 13:66–70, 2018.
- [11] David N Irani. *Cerebrospinal fluid in clinical practice*. Elsevier Health Sciences, 2009.
- [12] Kim W Benner, Simone Spellen, and Abby Jeske. Pharmacology of shunt infections. *US Pharm*, 4:18, 2014.

- [13] Yenis Gutierrez-Murgas and Jessica N Snowden. Ventricular shunt infections: immunopathogenesis and clinical management. *Journal of neuroimmunology*, 276(1-2):1–8, 2014.
- [14] Lawrence Yu, Brian Kim, and Ellis Meng. Chronically implanted pressure sensors: challenges and state of the field. *Sensors*, 14(11):20620–20644, 2014.
- [15] Ellyce Stehlin. *Clinical Compatibility of an Implantable Pressure Sensing Device With Consideration of the Intracranial Pressure Application*. PhD thesis, ResearchSpace@ Auckland, 2015.
- [16] R Jacob Baker. *CMOS: circuit design, layout, and simulation*, volume 1. John Wiley & Sons, 2008.
- [17] Amy C Richards Grayson, Rebecca S Shawgo, Audrey M Johnson, Nolan T Flynn, Yawen Li, Michael J Cima, and Robert Langer. A biomems review: Memes technology for physiologically integrated devices. *Proceedings of the IEEE*, 92(1):6–21, 2004.
- [18] Martin M Mortazavi, N Adeeb, CJ Griessenauer, H Sheikh, Saeed Shahidi, RI Tubbs, and RS Tubbs. The ventricular system of the brain: a comprehensive review of its history, anatomy, histology, embryology, and surgical considerations. *Child's Nervous System*, 30(1):19–35, 2014.
- [19] Reynold Spector, S Robert Snodgrass, and Conrad E Johanson. A balanced view of the cerebrospinal fluid composition and functions: focus on adult humans. *Experimental neurology*, 273:57–68, 2015.
- [20] Shailesh Koirala. *Cerebrospinal fluid, its formation and circulation*, 2018.
- [21] Dong-Joo Kim, Zofia Czosnyka, Magdalena Kasprowicz, Piotr Smielewski, Oliver Baledent, Anne-Marie Guerguerian, John D Pickard, and Marek Czosnyka. Continuous monitoring of the monro-kellie doctrine: is it possible? *Journal of neurotrauma*, 29(7):1354–1363, 2012.
- [22] Michael J Rosner and Sheila D Rosner. Cerebral perfusion pressure management of head injury. In *Recent Advances in Neurotraumatology*, pages 293–296. Springer, 1993.
- [23] Marilyn J Cipolla. *Control of cerebral blood flow*. 2009.
- [24] Satoshi Matsumoto and Norihiko Tamaki. *Hydrocephalus: Pathogenesis and Treatment*. Springer Science & Business Media, 2012.
- [25] Giuseppe Cinalli, Wirginia June Maixner, and Christian Sainte-Rose. *Pediatric hydrocephalus*. Springer Science & Business Media, 2012.
- [26] Adré J du Plessis, Shenandoah Robinson, and Joseph J Volpe. Congenital hydrocephalus. *Volpe's Neurology of the Newborn E-Book*, page 58, 2017.
- [27] Jorg Baldauf and Henry WS Schroeder. 15 acquired hydrocephalus in adults. *Cerebrospinal Fluid Disorders*, page 273, 2016.

- [28] Norman Relkin, Anthony Marmarou, Petra Klinge, Marvin Bergsneider, and Peter McL Black. Diagnosing idiopathic normal-pressure hydrocephalus. *Neurosurgery*, 57(suppl\_3):S2–4, 2005.
- [29] JH Salmon, JY Gonen, and L Brown. Ventriculoatrial shunt for hydrocephalus: ex vacuo psychological and clinical evaluation. *Diseases of the nervous system*, 32(5):299, 1971.
- [30] Harold L Rekate. A contemporary definition and classification of hydrocephalus. In *Seminars in pediatric neurology*, volume 16, pages 9–15. Elsevier, 2009.
- [31] Michael A Williams and Jan Malm. Diagnosis and treatment of idiopathic normal pressure hydrocephalus. *Continuum: Lifelong Learning in Neurology*, 22(2 Dementia):579, 2016.
- [32] JM Drake, JRW Kestle, and S Tuli. Csf shunts 50 years on—past, present and future. *Child's Nervous System*, 16(10-11):800–804, 2000.
- [33] Zhang et al. Ventriculoperitoneal shunting surgery with open distal shunt catheter placement in the treatment of hydrocephalus. *Cell biochemistry and biophysics*, 73(2):533–536, 2015.
- [34] C. Toporek et al. *Hydrocephalus: A guide for patients, families, and friends*. Patient-Centered Guides, 1999.
- [35] Rajanandini Muralidharan. External ventricular drains: management and complications. *Surgical neurology international*, 6(Suppl 6):S271, 2015.
- [36] T. Appelgren et al. Long-term outcome after treatment of hydrocephalus in children. *Pediatric neurosurgery*, 46(3):221–226, 2010.
- [37] Sven Poeggel, Daniele Tosi, Dinesh Babu Duraibabu, Gabriel Leen, Deirdre McGrath, and Elfed Lewis. Optical fibre pressure sensors in medical applications. *Sensors*, 15(7):17115–17148, 2015.
- [38] Morton Lund-Johansen, Frode Svendsen, and Knut Wester. Shunt failures and complications in adults as related to shunt type, diagnosis, and the experience of the surgeon. *Neurosurgery*, 35(5):839–844, 1994.
- [39] Samuel R Browd, Brian T Ragel, Oren N Gottfried, and John RW Kestle. Failure of cerebrospinal fluid shunts: part i: obstruction and mechanical failure. *Pediatric neurology*, 34(2):83–92, 2006.
- [40] Mi Ok Kim, Audrey Adjani, Michael F O'Rourke, Alberto P Avolio, Peter Smielewski, John D Pickard, and Marek Czosnyka. Principles of cerebral hemodynamics when intracranial pressure is raised: lessons from the peripheral circulation. *Journal of hypertension*, 33(6):1233, 2015.
- [41] M Czosnyka, PJ Hutchinson, M Balestreri, M Hiler, P Smielewski, and JD Pickard. Monitoring and interpretation of intracranial pressure after head injury. In *Brain Edema XIII*, pages 114–118. Springer, 2006.

- [42] Naveen Sankhyan, KN Vykunta Raju, Suvasini Sharma, and Sheffali Gulati. Management of raised intracranial pressure. *The Indian Journal of Pediatrics*, 77(12):1409–1416, 2010.
- [43] Mark E Wagshul, Per K Eide, and Joseph R Madsen. The pulsating brain: a review of experimental and clinical studies of intracranial pulsatility. *Fluids and Barriers of the CNS*, 8(1):5, 2011.
- [44] Mary Abraham and Vasudha Singhal. Intracranial pressure monitoring. *Journal of Neuroanaesthesiology and Critical Care*, 2(03):193–203, 2015.
- [45] Christopher Hawthorne and Ian Piper. Monitoring of intracranial pressure in patients with traumatic brain injury. *Frontiers in neurology*, 5:121, 2014.
- [46] M Czosnyka, PJ Hutchinson, M Balestreri, M Hiler, P Smielewski, and JD Pickard. Monitoring and interpretation of intracranial pressure after head injury. In *Brain Edema XIII*, pages 114–118. Springer, 2006.
- [47] Maya Harary, Rianne GF Dolmans, and William B Gormley. Intracranial pressure monitoring—review and avenues for development. *Sensors*, 18(2):465, 2018.
- [48] Brandon K Root, Benjamin G Barrena, Todd A Mackenzie, and David F Bauer. Antibiotic impregnated external ventricular drains: meta and cost analysis. *World neurosurgery*, 86:306–315, 2016.
- [49] Roger Bayston, Waheed Ashraf, and Catherine Ortori. Does release of antimicrobial agents from impregnated external ventricular drainage catheters affect the diagnosis of ventriculitis? *Journal of neurosurgery*, 124(2):375–381, 2016.
- [50] Jun Zhong, Manuel Dujovny, Hun K Park, Eimir Perez, Alfred R Perlin, and Fernando G Diaz. Advances in icp monitoring techniques. *Neurological research*, 25(4):339–350, 2003.
- [51] Josef-Michael Lang, Jürgen Beck, Michael Zimmermann, Volker Seifert, and Andreas Raabe. Clinical evaluation of intraparenchymal spiegelberg pressure sensor. *Neurosurgery*, 52(6):1455–1459, 2003.
- [52] J Stuart Crutchfield, Raj K Narayan, Claudia S Robertson, and Lloyd H Michael. Evaluation of a fiberoptic intracranial pressure monitor. *Journal of neurosurgery*, 72(3):482–487, 1990.
- [53] Lucy Murtha, Damian McLeod, and Neil Spratt. Epidural intracranial pressure measurement in rats using a fiber-optic pressure transducer. *Journal of visualized experiments: JoVE*, (62), 2012.
- [54] Rosa M , David Santamarta, et al. Camino intracranial pressure monitor- prospective study of accuracy and complications. *Journal of Neurology, Neurosurgery & Psychiatry*, 69(1):82–86, 2000.
- [55] Karen L Saban. Aacn-aann protocols for practice: Monitoring technologies in critically ill neuroscience patients. *Journal of Neuroscience Nursing*, 41(5):287–288, 2009.

- [56] James R Atkinson, David B Shurtleff, and Eldon L Foltz. Radio telemetry for the measurement of intracranial pressure. *Journal of neurosurgery*, 27(5):428–432, 1967.
- [57] Nicholas T Zervas, Eric R Cosman, and Bernard J Cosman. A pressure-balanced radio-telemetry system for the measurement of intracranial pressure: A preliminary design report. *Journal of neurosurgery*, 47(6):899–911, 1977.
- [58] Gündüz Güçer, Lawrence Viernstein, Arthur Wang, and Richard Szymanski. Ten-year follow-up on the performance of a telemetric intracranial pressure sensor. *Neurosurgery*, 22(5):892–896, 1988.
- [59] T Ohta, H Miyake, S Nagasawa, Y Nagano, and H Tanabe. Chronologic changes in intraventricular pressure and ventricular size after ventriculo-peritoneal shunt—telemetric measurement using osaka telesensor (ns-20). In *Intracranial Pressure VIII*, pages 889–895. Springer, 1993.
- [60] Stefan Welschehold, Eva Schmalhausen, Philippe Dodier, Sonja Vulcu, Joachim Oertel, Wolfgang Wagner, and Christoph A Tschan. First clinical results with a new telemetric intracranial pressure-monitoring system. *Operative Neurosurgery*, 70(suppl\_1):ons44–ons49, 2011.
- [61] James M Barber, Catherine J Pringle, Helen Raffalli-Ebezant, Omar Pathmanaban, Roberto Ramirez, and Ian D Kamaly-Asl. Telemetric intra-cranial pressure monitoring: Clinical and financial considerations. *British journal of neurosurgery*, 31(3):300–306, 2017.
- [62] Xu Meng, Kevin D Browne, Shi-Min Huang, Constance Mietus, D Kacy Cullen, Mohammad-Reza Tofghi, and Arye Rosen. Dynamic evaluation of a digital wireless intracranial pressure sensor for the assessment of traumatic brain injury in a swine model. *IEEE Transactions on Microwave Theory and Techniques*, 61(1):316–325, 2013.
- [63] Claude Bathias. *Fatigue limit in metals*. John Wiley & Sons, 2013.
- [64] Peter George Forrest. *Fatigue of metals*. Elsevier, 2013.
- [65] John Michael S Chua Chiaco, Nisha I Parikh, and David J Fergusson. The jugular venous pressure revisited. *Cleveland Clinic journal of medicine*, 80(10):638, 2013.
- [66] Despina A Lalou, Marek Czosnyka, Joseph Donnelly, Andrea Lavinio, John D Pickard, Matthew Garnett, and Zofia Czosnyka. Influence of general anaesthesia on slow waves of intracranial pressure. *Neurological research*, 38(7):587–592, 2016.
- [67] Connie L Miller, Suhasini Kotcherlakota, Andrea Evans, and Patrick Rejda. Intracranial pressure monitoring. 2014.
- [68] Tatsuo Tagawa, Toshiyo Tamura, and P Ake Oberg. *Biomedical sensors and instruments*. CRC press, 2011.
- [69] Joon Park and Roderic S Lakes. *Biomaterials: an introduction*. Springer Science & Business Media, 2007.

- [70] Andreas Inmann and Diana Hodgins. *Implantable sensor systems for medical applications*. Elsevier, 2013.
- [71] Paul Ducheyne. *Comprehensive Biomaterials II*. Elsevier, 2017.
- [72] Toshiki Miyazaki, Masakazu Kawashita, and Chikara Ohtsuki. Ceramic-polymer composites for biomedical applications. *Handbook of Bioceramics and Biocomposites*, pages 287–300, 2016.
- [73] Sebastian Kruss, Andrew J Hilmer, Jingqing Zhang, Nigel F Reuel, Bin Mu, and Michael S Strano. Carbon nanotubes as optical biomedical sensors. *Advanced drug delivery reviews*, 65(15):1933–1950, 2013.
- [74] Artur M Pinto, Ines C Goncalves, and Fernao D Magalhaes. Graphene-based materials biocompatibility: a review. *Colloids and Surfaces B: Biointerfaces*, 111:188–202, 2013.
- [75] M Bianchi, A Gambardella, Matteo Berni, S Panseri, M Montesi, N Lopomo, A Tampieri, M Marcacci, and A Russo. Surface morphology, tribological properties and in vitro biocompatibility of nanostructured zirconia thin films. *Journal of Materials Science: Materials in Medicine*, 27(5):96, 2016.
- [76] Mitsuo Niinomi, Masaaki Nakai, and Junko Hieda. Development of new metallic alloys for biomedical applications. *Acta biomaterialia*, 8(11):3888–3903, 2012.
- [77] M Martinesi, M Stio, C Treves, and F Borgioli. Biocompatibility studies of low temperature nitrided and collagen-i coated aisi 316l austenitic stainless steel. *Journal of Materials Science: Materials in Medicine*, 24(6):1501–1513, 2013.
- [78] Dean J Kereiakes, David A Cox, James B Hermiller, Mark G Midei, William B Bachinsky, E Dean Nukta, Martin B Leon, Stanley Fink, Linda Marin, Alexandra J Lansky, et al. Usefulness of a cobalt chromium coronary stent alloy. *The American journal of cardiology*, 92(4):463–466, 2003.
- [79] J Ryhänen. Biocompatibility of nitinol. *Minimally Invasive Therapy & Allied Technologies*, 9(2):99–105, 2000.
- [80] MJ Jackson, J Kopac, M Balazic, D Bombac, M Brojan, and F Kosel. Titanium and titanium alloy applications in medicine. In *Surgical Tools and Medical Devices*, pages 475–517. Springer, 2016.
- [81] Valérie Vince, M-A Thil, Claude Veraart, IM Colin, and Jean Delbeke. Biocompatibility of platinum-metallized silicone rubber: in vivo and in vitro evaluation. *Journal of Biomaterials Science, Polymer Edition*, 15(2):173–188, 2004.
- [82] Ankur S Kulshrestha and Anil Mahapatro. *Polymers for biomedical applications*. American Chemical Society Washington, DC, 2008.
- [83] Scott J Woltman, Gregory D Jay, and Gregory P Crawford. Liquid-crystal materials find a new order in biomedical applications. *Nature materials*, 6(12):929, 2007.

- [84] Abitha Vayyaprontavida Kaliyathan, Anitha Mathew, Ajay Vasudeo Rane, Krishnan Kanny, and Sabu Thomas. Natural rubber and silicone rubber-based biomaterials. In *Fundamental Biomaterials: Polymers*, pages 71–84. Elsevier, 2018.
- [85] D Mihov and B Katerska. Some biocompatible materials used in medical practice. *Trakia Journal of Sciences*, 8(2):119–125, 2010.
- [86] Gottfried Schmalz and Dorte Arenholt-Bindslev. *Biocompatibility of dental materials*, volume 1. Springer, 2009.
- [87] Hee C Lim, Brian Schulkin, MJ Pulickal, Sheng Liu, R Petrova, G Thomas, S Wagner, K Sidhu, and John F Federici. Flexible membrane pressure sensor. *Sensors and Actuators A: Physical*, 119(2):332–335, 2005.
- [88] Usamah Kawoos, Richard McCarron, Charles Auken, and Mikulas Chavko. Advances in intracranial pressure monitoring and its significance in managing traumatic brain injury. *International journal of molecular sciences*, 16(12):28979–28997, 2015.
- [89] Buddy D Ratner, Allan S Hoffman, Frederick J Schoen, and Jack E Lemons. Biomaterials science: an introduction to materials in medicine. *MRS Bull*, 31:59, 2006.
- [90] Mitsuo Niinomi. Metallic biomaterials. *Journal of Artificial Organs*, 11(3):105, 2008.
- [91] Sung-Pil Chang and Mark G Allen. Capacitive pressure sensors with stainless steel diaphragm and substrate. *Journal of Micromechanics and Microengineering*, 14(4):612, 2004.
- [92] Xing Chen, Daniel Brox, Babak Assadsangabi, Mohamed Sultan Mohamed Ali, and Kenichi Takahata. A stainless-steel-based capacitive pressure sensor chip and its microwelding integration. In *Solid-State Sensors, Actuators and Microsystems (TRANSDUCERS), 2015 Transducers-2015 18th International Conference on*, pages 1081–1084. IEEE, 2015.
- [93] Monika Saini, Yashpal Singh, Pooja Arora, Vipin Arora, and Krati Jain. Implant biomaterials: A comprehensive review. *World Journal of Clinical Cases: WJCC*, 3(1):52, 2015.
- [94] Luther M Gammon, Robert D Briggs, John M Packard, Kurt W Batson, Rodney Boyer, Charles W Dombay, et al. Metallography and microstructures of titanium and its alloys. *ASM Handbook*, 9:899–917, 2004.
- [95] D Eylon, A Vassel, Y Combres, RR Boyer, PJ Bania, and RW Schutz. Issues in the development of beta titanium alloys. *JOM Journal of the Minerals, Metals and Materials Society*, 46(7):14–15, 1994.
- [96] Werner Karl Schomburg. Introduction. In *Introduction to Microsystem Design*, pages 1–2. Springer, 2015.
- [97] Stephen P Timoshenko and Sergius Woinowsky-Krieger. *Theory of plates and shells*. McGraw-hill, 1959.

- [98] William P Eaton, Fernando Bitsie, James H Smith, and David W Plummer. A new analytical solution for diaphragm deflection and its application to a surface-micromachined pressure sensor. In *International Conference on Modeling and Simulation, MSM*, 1999.
- [99] YB Tian, L Zhou, ZW Zhong, H Sato, and J Shimizu. Finite element analysis of deflection and residual stress on machined ultra-thin silicon wafers. *Semiconductor Science and Technology*, 26(10):105002, 2011.
- [100] CE Imrak and İ Gerdemeli. An exact solution for the deflection of a clamped rectangular plate under uniform load. *Applied mathematical sciences*, 1(43):2129–2137, 2007.
- [101] BCL Vanam, M Rajyalakshmi, and R Inala. Static analysis of an isotropic rectangular plate using finite element analysis (fea). *Journal of Mechanical Engineering Research*, 4(4):148–162, 2012.
- [102] Wang Yun, Xu Rongqiao, and Ding Haojiang. Three-dimensional solution of axisymmetric bending of functionally graded circular plates. *Composite Structures*, 92(7):1683–1693, 2010.
- [103] PS Gujar and KB Ladhane. Bending analysis of simply supported and clamped circular plate. *International Journal of Civil Engineering*, 2(5):69–75, 2015.
- [104] Denis Benasciutti, Frank Sherratt, and Alessandro Cristofori. Basic principles of spectral multi-axial fatigue analysis. *Procedia Engineering*, 101:34–42, 2015.
- [105] MW Brown and KJ Miller. A theory for fatigue failure under multiaxial stress-strain conditions. *Proceedings of the Institution of Mechanical Engineers*, 187(1):745–755, 1973.
- [106] Xavier Pitoiset and André Preumont. Spectral methods for multiaxial random fatigue analysis of metallic structures. *International Journal of Fatigue*, 22(7):541–550, 2000.
- [107] C-C Chu. Multiaxial fatigue life prediction method in the ground vehicle industry. *International Journal of Fatigue*, 19(93):325–330, 1997.
- [108] L Del Llano-Vizcaya, C Rubio-González, Gérard Mesmacque, and T Cervantes-Hernández. Multiaxial fatigue and failure analysis of helical compression springs. *Engineering failure analysis*, 13(8):1303–1313, 2006.
- [109] Nima Shamsaei, Maksym Gladskyi, Kostyantyn Panasovskyi, Sergiy Shukaev, and Ali Fatemi. Multiaxial fatigue of titanium including step loading and load path alteration and sequence effects. *International Journal of Fatigue*, 32(11):1862–1874, 2010.
- [110] DL McDiarmid. A general criterion for high cycle multiaxial fatigue failure. *Fatigue & Fracture of Engineering Materials & Structures*, 14(4):429–453, 1991.
- [111] Luca Susmel. A simple and efficient numerical algorithm to determine the orientation of the critical plane in multiaxial fatigue problems. *International Journal of Fatigue*, 32(11):1875–1883, 2010.

- [112] Jing Li, Zhong-ping Zhang, Qiang Sun, and Chun-wang Li. Multiaxial fatigue life prediction for various metallic materials based on the critical plane approach. *International Journal of Fatigue*, 33(2):90–101, 2011.
- [113] Andrea Carpinteri, Andrea Spagnoli, and Sabrina Vantadori. Multiaxial fatigue assessment using a simplified critical plane-based criterion. *International Journal of Fatigue*, 33(8):969–976, 2011.
- [114] MH Maitournam, Cécile Krebs, and André Galtier. A multiscale fatigue life model for complex cyclic multiaxial loading. *International Journal of Fatigue*, 33(2):232–240, 2011.
- [115] Andrea Carpinteri, Giovanni Fortese, Camilla Ronchei, Daniela Scorza, Andrea Spagnoli, and Sabrina Vantadori. Fatigue life evaluation of metallic structures under multiaxial random loading. *International Journal of Fatigue*, 90:191–199, 2016.
- [116] Nima Shamsaei and Sean A McKelvey. Multiaxial life predictions in absence of any fatigue properties. *International Journal of Fatigue*, 67:62–72, 2014.
- [117] Ying-Yu Wang and Wei-Xing Yao. Evaluation and comparison of several multiaxial fatigue criteria. *International Journal of Fatigue*, 26(1):17–25, 2004.
- [118] Stefanie Stanzl-Tschegg. Very high cycle fatigue measuring techniques. *International Journal of Fatigue*, 60:2–17, 2014.
- [119] Jill M Morgan and Walter W Milligan. A 1 khz servohydraulic fatigue testing system. *High cycle fatigue of structural materials*, TMS, Warrendale, PA, pages 305–12, 1997.
- [120] Patrick S Cottler, Whitney R Karpen, Duane A Morrow, and Kenton R Kaufman. Performance characteristics of a new generation pressure microsensor for physiologic applications. *Annals of biomedical engineering*, 37(8):1638–1645, 2009.
- [121] D Wagner, FJ Cavalieri, Claude Bathias, and Nicolas Ranc. Ultrasonic fatigue tests at high temperature on an austenitic steel. *Propulsion and Power Research*, 1(1):29–35, 2012.
- [122] RG White. Developments in the acoustic fatigue design process for composite aircraft structures. *Composite Structures*, 16(1-3):171–192, 1990.
- [123] LC CHOW and RJ CUMMINS. Sonic fatigue study of an aircraft flap like structure. 1997.
- [124] FF Rudder Jr and HE Plumblee Jr. Sonic fatigue design guide for military aircraft. Technical report, ACOUSTICS AND VIBRATION ASSOCIATES SMYRNA GA, 1975.
- [125] Charles Francis Griffin and EG Dunning. Development of an advanced composite aileron for the l-1011 transport aircraft. 1982.
- [126] Richard P Vinci and Joost J Vlassak. Mechanical behavior of thin films. *Annual Review of Materials Science*, 26(1):431–462, 1996.

- [127] Hans J Griesser. *Thin Film Coatings for Biomaterials and Biomedical Applications*. Woodhead Publishing, 2016.
- [128] RC Chang, FY Chen, CT Chuang, and YC Tung. Residual stresses of sputtering titanium thin films at various substrate temperatures. *Journal of nanoscience and nanotechnology*, 10(7):4562–4567, 2010.
- [129] Alireza Moridi, Haihui Ruan, LC Zhang, and Mei Liu. Residual stresses in thin film systems: Effects of lattice mismatch, thermal mismatch and interface dislocations. *International Journal of Solids and Structures*, 50(22-23):3562–3569, 2013.
- [130] E Mastropaolo, A Bunting, C Dunare, R Cheung, et al. Fabrication and characterisation of suspended microstructures of tantalum. *Journal of Micromechanics and Microengineering*, 27(1):015020, 2016.
- [131] Roger W Pryor. *Multiphysics modeling using COMSOL: a first principles approach*. Jones & Bartlett Publishers, 2009.
- [132] PA Withey. Fatigue failure of the de havilland comet i. *Engineering failure analysis*, 4(2):147–154, 1997.
- [133] Jaap Schijve. Fatigue as a phenomenon in the material. *Fatigue of Structures and Materials*, pages 7–44, 2001.
- [134] Pietro Paolo Milella. Morphological aspects of fatigue crack formation and growth. In *Fatigue and Corrosion in Metals*, pages 73–108. Springer, 2013.
- [135] Yung-Li Lee, Jwo Pan, Richard Hathaway, and Mark Barkey. *Fatigue testing and analysis: theory and practice*, volume 13. Butterworth-Heinemann, 2005.
- [136] Y Uematsu, T Kakiuchi, K Hattori, N Uesugi, and F Nakao. Non-destructive evaluation of fatigue damage and fatigue crack initiation in type 316 stainless steel by positron annihilation line-shape and lifetime analyses. *Fatigue & Fracture of Engineering Materials & Structures*, 40(7):1143–1153, 2017.
- [137] Ralph A Bianchi, Ronald T Bradshaw, James H Farrell, and FE Reed. Survey and evaluation of sonic fatigue testing facilities. Technical report, CONESCO INC CAMBRIDGE MA, 1962.
- [138] David Shires. On the time compression (test acceleration) of broadband random vibration tests. *Packaging Technology and Science*, 24(2):75–87, 2011.
- [139] G Petrucci and B Zuccarello. Fatigue life prediction under wide band random loading. *Fatigue & Fracture of Engineering Materials & Structures*, 27(12):1183–1195, 2004.
- [140] Liang Yan and JunKai Fan. In-situ sem study of fatigue crack initiation and propagation behavior in 2524 aluminum alloy. *Materials & Design*, 110:592–601, 2016.
- [141] IV Singh, BK Mishra, S Bhattacharya, and RU Patil. The numerical simulation of fatigue crack growth using extended finite element method. *International Journal of Fatigue*, 36(1):109–119, 2012.

- [142] J. Korvink et al. *MEMS: A practical guide of design, analysis, and applications*. Springer Science and Business Media, 2010.
- [143] T.M. Adams et al. *Introductory MEMS: fabrication and applications*, volume 70. Springer Science and Business Media, 2009.
- [144] T.M. Adams et al. *Introductory Mems*. Springer, 2014.
- [145] Nadim Maluf. *An introduction to microelectromechanical systems engineering*, 2002.
- [146] Jan-Otto Carlsson and Peter M Martin. Chemical vapor deposition. In *Handbook of Deposition Technologies for Films and Coatings (Third Edition)*, pages 314–363. Elsevier, 2010.
- [147] Mattox et al. *Handbook of physical vapor deposition (PVD) processing*. William Andrew, 2010.
- [148] V. Bhatt et al. Silicon dioxide films by rf sputtering for microelectronic and mems applications. *Journal of micromechanics and microengineering*, 17(5):1066, 2007.
- [149] George et al. Atomic layer deposition: an overview. *Chemical reviews*, 110(1):111–131, 2009.
- [150] J. Bachmann et al. A practical, self-catalytic, atomic layer deposition of silicon dioxide. *Angewandte chemie international edition*, 47(33):6177–6179, 2008.
- [151] E. Kobeda et al. Intrinsic  $\text{SiO}_2$  film stress measurements on thermally oxidized Si. *Journal of Vacuum Science and Technology B: Microelectronics Processing and Phenomena*, 5(1):15–19, 1987.
- [152] Rajendra K Aithal, S Yenamandra, RA Gunasekaran, P Coane, and K Varahramyan. Electroless copper deposition on silicon with titanium seed layer. *Materials chemistry and physics*, 98(1):95–102, 2006.
- [153] Yong-hua Zhang et al. Electroplating of low stress permalloy for mems. *Materials characterization*, 57(2):121–126, 2006.
- [154] Berthold Schuderer et al. Metallization for chip scale packages in wafer level packaging, 2012. US Patent 8,163,629.
- [155] V. Guarnieri et al. Platinum metallization for mems application: Focus on coating adhesion for biomedical applications. *Biomatter*, 4(1):e28822, 2014.
- [156] W. Hasenkamp et al. Polyimide/su-8 catheter-tip mems gauge pressure sensor. *Biomedical microdevices*, 14(5):819–828, 2012.
- [157] L. Jiang et al. A review of silicon carbide development in mems applications. *International Journal of Computational Materials Science and Surface Engineering*, 2(3-4):227–242, 2009.
- [158] P.M. Sarro. Silicon carbide as a new mems technology. *Sensors and Actuators A: Physical*, 82(1-3):210–218, 2000.

- [159] R.S. Sussmann. *CVD diamond for electronic devices and sensors*, volume 26. John Wiley and Sons, 2009.
- [160] J. Miao. *Silicon Micromachining*, pages 1840–1846. Springer US, Boston, MA, 2008.
- [161] HAC Tilmans et al. Mems packaging and reliability: An undividable couple. *Microelectronics Reliability*, 52(9-10):2228–2234, 2012.
- [162] Lapadat et al. Anodic bonding. In *Handbook of Silicon Based MEMS Materials and Technologies (Second Edition)*, pages 599–610. Elsevier, 2015.
- [163] Torunbalci et al. Wafer level hermetic sealing of mems devices with vertical feedthroughs using anodic bonding. *Sensors and Actuators A: Physical*, 224:169–176, 2015.
- [164] ChingHung Hsu et al. Anodic bonding using gorilla glasses. In *Nano/Micro Engineered and Molecular Systems (NEMS), 2017 IEEE 12th International Conference on*, pages 566–569. IEEE, 2017.
- [165] Alexe et al. *Wafer bonding: applications and technology*, volume 75. Springer Science & Business Media, 2013.
- [166] H Moriceau et al. Low temperature direct bonding: An attractive technique for heterostructures build-up. *Microelectronics Reliability*, 52(2):331–341, 2012.
- [167] SL Chua et al. Direct copper-copper wafer bonding with ar/n 2 plasma activation. In *Electron Devices and Solid-State Circuits (EDSSC), 2015 IEEE International Conference on*, pages 134–137. IEEE, 2015.
- [168] Liang et al. The au/si eutectic bonding compatibility with koh etching for 3d devices fabrication. *Journal of Micromechanics and Microengineering*, 28(1):015005, 2017.
- [169] R Knechtel, M Wiemer, and J Frömel. Wafer level encapsulation of microsystems using glass frit bonding. *Microsystem Technologies*, 12(5):468–472, 2006.
- [170] Walter D Wood and Wendell L Wood. Hermetic sealing with epoxy. *Mechanical Engineering*, 112(3):46, 1990.
- [171] Tilmans et al. Mems packaging and reliability: An undividable couple. *Microelectronics Reliability*, 52(9-10):2228–2234, 2012.
- [172] MEMSCAP. Multi-user mems process or mumps.
- [173] V.R. Yarberr. Meeting the mems “design-to-analysis” challenge: The summit@v design tool environment. In *ASME 2002 International Mechanical Engineering Congress and Exposition*, pages 547–553. American Society of Mechanical Engineers.
- [174] Ann Witvrouw. Cmos–mems integration today and tomorrow. *scripta materialia*, 59(9):945–949, 2008.
- [175] Fischer et al. Integrating mems and ics. *Microsystems & Nanoengineering*, 1:15005, 2015.

- [176] Chen et al. A generalized cmos-mems platform for micromechanical resonators monolithically integrated with circuits. *Journal of Micromechanics and Microengineering*, 21(6):065012, 2011.
- [177] Sedky et al. *Post-processing techniques for integrated MEMS*. Artech House, 2005.
- [178] Narducci et al. Cmos mems capacitive absolute pressure sensor. *Journal of Micromechanics and Microengineering*, 23(5):055007, 2013.
- [179] Sundararajan Ananiah Durai and othersl. Elliptic diaphragm capacitive pressure sensor and signal conditioning circuit fabricated in sige cmos integrated mems. *IEEE Sensors Journal*, 15(3):1825–1837, 2015.
- [180] Md Shamsul Arefin et al. Integration of low-power asic and mems sensors for monitoring gastrointestinal tract using a wireless capsule system. *IEEE journal of biomedical and health informatics*, 22(1):87–97, 2018.
- [181] Mita et al. Opportunities of cmos-mems integration through lsi foundry and open facility. *Japanese Journal of Applied Physics*, 56(6S1):06GA03, 2017.
- [182] Jiang et al. Monolithic ultrasound fingerprint sensor. *Microsystems and Nanoengineering*, 3, 2017.
- [183] Cheng et al. 12 inch mems process for sensors implementation and integration. In *Solid-State Sensors, Actuators and Microsystems (TRANSDUCERS), 2017 19th International Conference on*, pages 402–405. IEEE, 2017.
- [184] Choudhary et al. *Mems: fundamental technology and applications*. CRC Press, 2017.
- [185] K. Reinhardt et al. *Handbook of silicon wafer cleaning technology*. William Andrew, 2008.
- [186] B. Zheng et al. Deposition of low stress silicon nitride thin film and its application in surface micromachining device structures. *Advances in Materials Science and Engineering*, 2013, 2013.
- [187] Donald M Mattox. *Handbook of physical vapor deposition (PVD) processing*. William Andrew, 2010.
- [188] L. Pasternak et al. Low-temperature direct bonding of silicon nitride to glass. *RSC Advances*, 8(4):2161–2172, 2018.
- [189] D. Briand et al. Bonding properties of metals anodically bonded to glass. *Sensors and Actuators A: Physical*, 114(2-3):543–549, 2004.
- [190] S Sathyanarayanan and A Vimala Juliet. Design and simulation of touch mode mems capacitive pressure sensor. In *Mechanical and Electrical Technology (ICMET), 2010 2nd International Conference on*, pages 180–183. IEEE, 2010.
- [191] Kirankumar B Balavalad and BG Sheeparamatti. A critical review of mems capacitive pressure sensors. *Sensors & Transducers*, 187(4):120, 2015.



# Appendix A

## A.1 Thin Film Shape: FEA

The deflection of a circular and square thin film membrane can be deduced from the equations A.1 and A.2 respectively. Neglecting the bending moments and residual stresses, the deflection due to straining in a circular thin film membrane can be described as

$$\Delta P \approx \frac{256}{3} \frac{t_m w_0^3}{r_m^4} \frac{E_m}{1 - \nu_m^2} \implies w_0 \approx \sqrt[3]{\frac{3r_m^4(1 - \nu_m^2)\Delta P}{256t_mE_m}} \quad (\text{A.1})$$

Where,  $\Delta P$  is the pressure difference,  $t_m$  is the thickness of the thin film membrane,  $w_0$  is the deflection of thin film at the centre,  $r_m$  is the radius of the thin circular membrane,  $E_m$  is the young's modulus of the thin film material,  $\nu_m$  is the Poisson's ratio of thin material,

Similarly, the deflection due to straining in a square thin film membrane can be described as

$$\Delta P \approx 36.9 \frac{t_m w_0^3}{s_m^4} \frac{E_m}{1 - \nu_m^2} \implies w_0 \approx \sqrt[3]{\frac{s_m^4(1 - \nu_m^2)\Delta P}{36.9t_mE_m}} \quad (\text{A.2})$$

Where,  $\Delta P$  is the pressure difference,  $t_m$  is the thickness of the thin film membrane,  $w_0$  is the deflection of thin film at the centre,  $s_m$  is the side length of the thin square membrane,  $E_m$  is the young's modulus of the thin film material,  $\nu_m$  is the Poisson's ratio of thin material,

The thin deflection of a circular, square, rectangle, elliptical thin film membrane is shown in the Figure A.1 The dimensions of each plot are shown in Table A.1

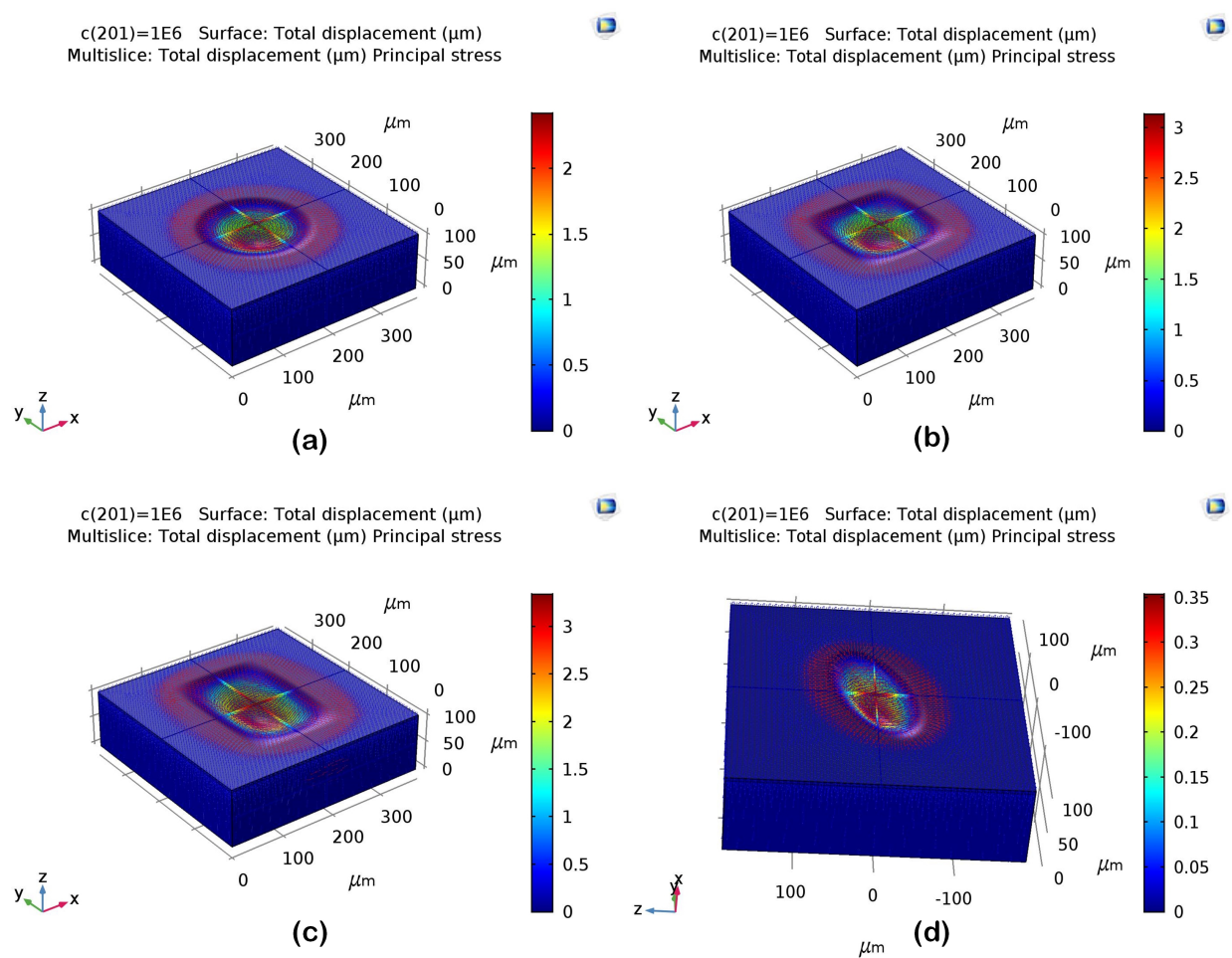


Figure A.1 The thin film deflection of various shapes (a) Circular membrane, (b) Square membrane, (c) Rectangular membrane, (d) Elliptical membrane

From the FEA plots shown in Figure A.1, it can be inferred that thin film square membrane produces more displacement than the circular or elliptical membranes. This corroborates with the theoretical equations A.1 and A.2 describing the thin film deflections due to straining (neglecting bending moments and residual stresses).

Table A.1 The model geometry for thin film shape optimization

<b>Figure A.1a</b>		
<b>Substrate</b>	<b>Cavity</b>	<b>Thin Film Membrane</b>
(1) Shape: Square (2) Side Length (a): 374 $\mu\text{m}$ (3) Thickness: 100 $\mu\text{m}$	(1) Shape: Circular (2) Radius: 100 $\mu\text{m}$ (3) Thickness: 55 $\mu\text{m}$	(1) Shape: Square (2) Side Length (a): 374 $\mu\text{m}$ (3) Thickness: 4 $\mu\text{m}$
<b>Figure A.1b</b>		
<b>Substrate</b>	<b>Cavity</b>	<b>Thin Film Membrane</b>
(1) Shape: Square Side Length (a): 374 $\mu\text{m}$ (3) Thickness: 100 $\mu\text{m}$	(1) Shape: Square (2) Side Length (a): 200 $\mu\text{m}$ (3) Thickness: 55 $\mu\text{m}$	(1) Shape: Square Side Length (a): 374 $\mu\text{m}$ (3) Thickness: 4 $\mu\text{m}$
<b>Figure A.1c</b>		
<b>Substrate</b>	<b>Cavity</b>	<b>Thin Film Membrane</b>
(1) Shape: Square (2) Side Length (a): 374 $\mu\text{m}$ (3) Thickness: 100 $\mu\text{m}$	(1) Shape: Rectangle (2) Side Length (a): 200 $\mu\text{m}$ (3) Side Length (b): 250 $\mu\text{m}$ (4) Thickness: 55 $\mu\text{m}$	(1) Shape: Square (2) Side Length (a): 374 $\mu\text{m}$ (3) Thickness: 4 $\mu\text{m}$
<b>Figure A.1d</b>		
<b>Substrate</b>	<b>Cavity</b>	<b>Thin Film Membrane</b>
(1) Shape: Square (2) Side Length (a): 374 $\mu\text{m}$ (3) Thickness: 100 $\mu\text{m}$	(1) Shape: Ellipse (2) Radius (Minor): 100 $\mu\text{m}$ (3) Radius (Major): 50 $\mu\text{m}$ (4) Thickness: 55 $\mu\text{m}$	(1) Shape: Square (2) Side Length (a): 374 $\mu\text{m}$ (3) Thickness: 4 $\mu\text{m}$



# Appendix B

## FEM of MEMS Capacitive Sensor

### B.1 Introduction

As discussed earlier, the purpose of modelling, simulation, and testing was to build a fully implantable MEMS capacitive pressure sensor. A fully implantable MEMS pressure sensor relies on a thin flexible membrane, a sealed cavity and thick substrate for sensing physical quantities from the surrounding medium. The thin flexible membrane acts as a top electrode and the thick substrate acts as a bottom electrode with a sealed cavity separating them. When the thin flexible membrane is subjected to cyclic pressure load, the membrane displaces inducing a change in the original capacitance. This capacitance between the electrodes is expressed as  $C = \frac{\epsilon_r \epsilon_0 K A}{d}$ , where  $\epsilon_r$  is the relative permittivity,  $\epsilon_0$  is the permittivity of free space, K is dielectric constant of the material used for sealing the cavity, and d is the distance between the electrodes [190, 191].

### B.1.1 Capacitance Modelling

Figure B.1 shows a 2D model of the capacitive pressure sensor (with 4  $\mu\text{m}$  thin film Ti membrane) drawn using COMSOL Multiphysics. The model comprises of a silicon substrate as the bottom electrode, a cavity sealed with borosilicate glass and a thin film membrane as the flexible top electrode. Unlike piezoresistive pressure sensors, the capacitance change in capacitive pressure sensors is not linear with the displacement of the flexible membrane. An electromechanics physics interface module has been integrated to study the electromechanical interactions that produce the capacitance changes with respect to the thin film displacements. The physics interface solves Gauss law of electric field using scalar potential as the dependent variable. The dependent variable is electric potential  $V$ , and the study is controlled by a set of governing equations in differential form as shown in equation B.1

$$\nabla \cdot D = \rho_v \quad (\text{B.1})$$

Where,  $\nabla \cdot$  is divergence operator (SI Unit: 1 per meter),  $D$  is electric displacement field,  $\rho$  is the free electric charge density. The integral form of the equation B.1 is  $\oint_A D \cdot dA = Q_{enclosed}$ ; Where  $dA$  is the area of a differential square on the enclosed surface  $A$ . The surface normal pointing out is the direction, and  $Q_{enclosed}$  is the charge inside the surface.

In a linear isotropic material, electric displacement field ( $D$ ) is directly proportional to the electric field ( $E$ ) and is described by equation B.2

$$D \propto E; D = \epsilon E \quad (\text{B.2})$$

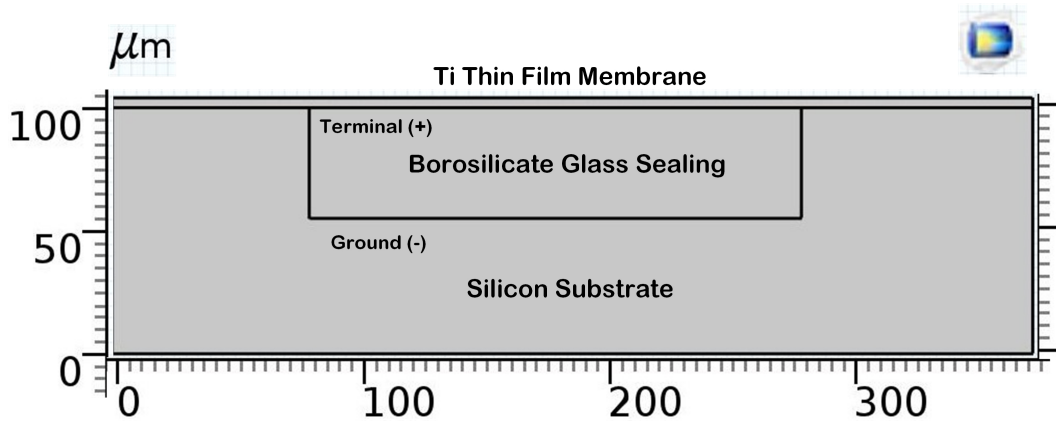


Figure B.1 The CAD model of MEMS capacitive pressure sensor with borosilicate sealed cavity

The divergence of the electric field ( $E$ ) is inversely proportional to the permittivity of free space ( $\epsilon_0$ ) and is described by the equation B.3.

$$\nabla \cdot E = \frac{\rho t}{\epsilon_0} \quad (\text{B.3})$$

Where,  $\epsilon_0 = 8.854 \text{ pF m}^{-1}$

The electric field is directly dependent on the negative divergence of electric potential ( $V$ ) and is described by the equation B.4.

$$E = -\nabla V \quad (\text{B.4})$$

A potential of 1.2 V has been applied at the intersection of the thin flexible membrane and cavity with respect to the ground potential at the bottom electrode. Figure B.2 shows the

electric potential concentration plot of MEMS capacitive pressure sensor at the positive plate (Red) and ground (Blue). The electrical displacement field form plot is shown in Figure B.3.

The Maxwell stress tensor is normally used in the calculation of electric and magnetic fields of an electromechanical device. It signifies the relationship between the electromagnetic forces and mechanical momentum. A set of stationary equations that govern the electromechanical interactions of MEMS capacitive pressure sensors are described in equation B.5

$$S = S_{ad} + J_i F_{inel}^{-T} (C : \epsilon_{el}) F_{inel}^{-1}, \epsilon_{el} = \frac{1}{2} (F_{el}^T F_{el} - 1) \quad (B.5)$$

Where, S is the second Picola-Kirchoff stress in MPa,  $S_{ad}$  is the sum of the second Picola-Kirchoff stresses, J is the total current density,  $F_{inel}$  is the inelastic force,  $\epsilon_{inel}$  is the inelastic strain. The Maxwell stress tensor plot is shown in Figure B.4

The parameters including sensitivity, long-term stability determine the performance characteristic of a MEMS capacitive pressure sensor. The sensitivity of a MEMS capacitive pressure sensor is described in the equation B.6

$$Sensitivity = \frac{\delta(\frac{\Delta C}{C_0})}{\delta p} \quad (B.6)$$

Where,  $C_0$  is the initial capacitance, and C is the change in the capacitance due to the pressure load. The relative changes in capacitance is expressed as  $\frac{\Delta C}{C_0} = \frac{(C-C_0)}{C_0}$ . The term on the left-hand side represents the slope of the sensitivity. Thus, from the plot B.5 the sensitivity of the MEMS capacitive pressure sensor model is  $1.003 \text{ Pa}^{-1}$

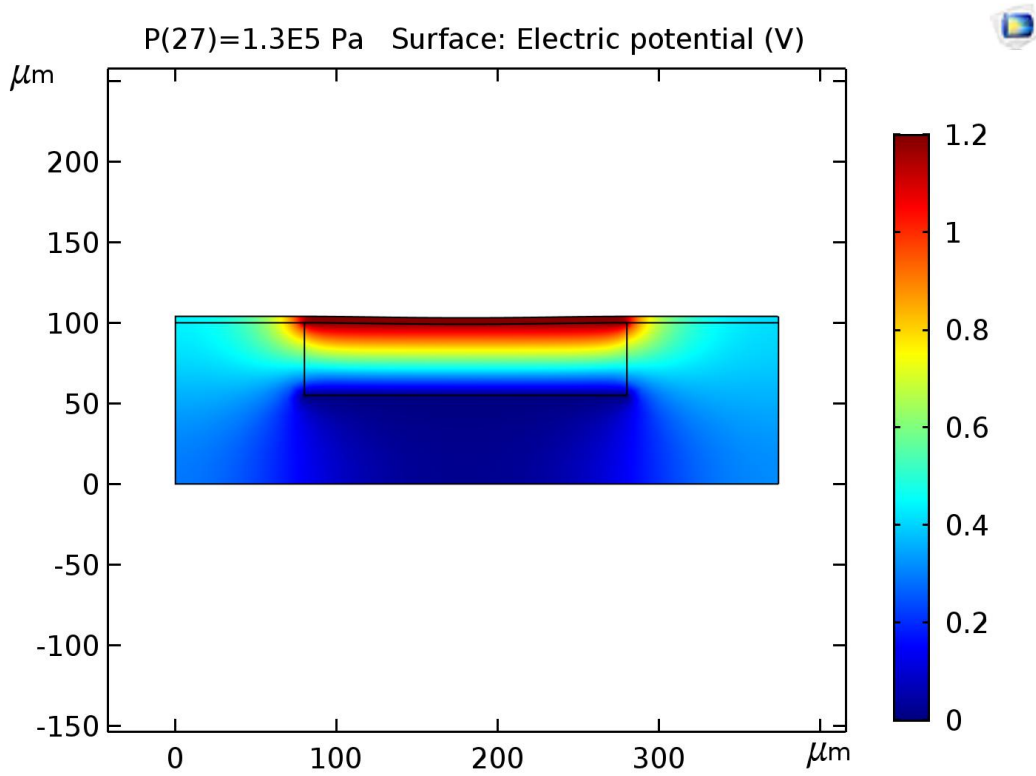


Figure B.2 The electric potential plot of MEMS capacitive pressure sensor with  $4\ \mu\text{m}$  thin film membrane

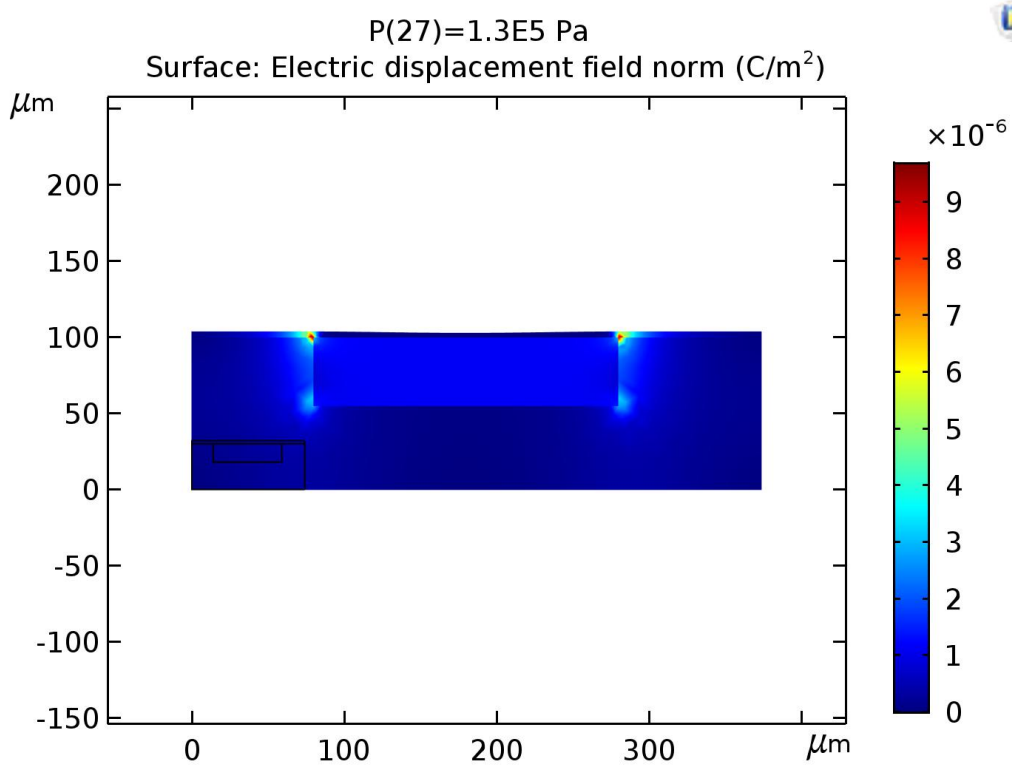


Figure B.3 The electric displacement field norm of MEMS capacitive pressure sensor with  $4\ \mu\text{m}$  thin film membrane

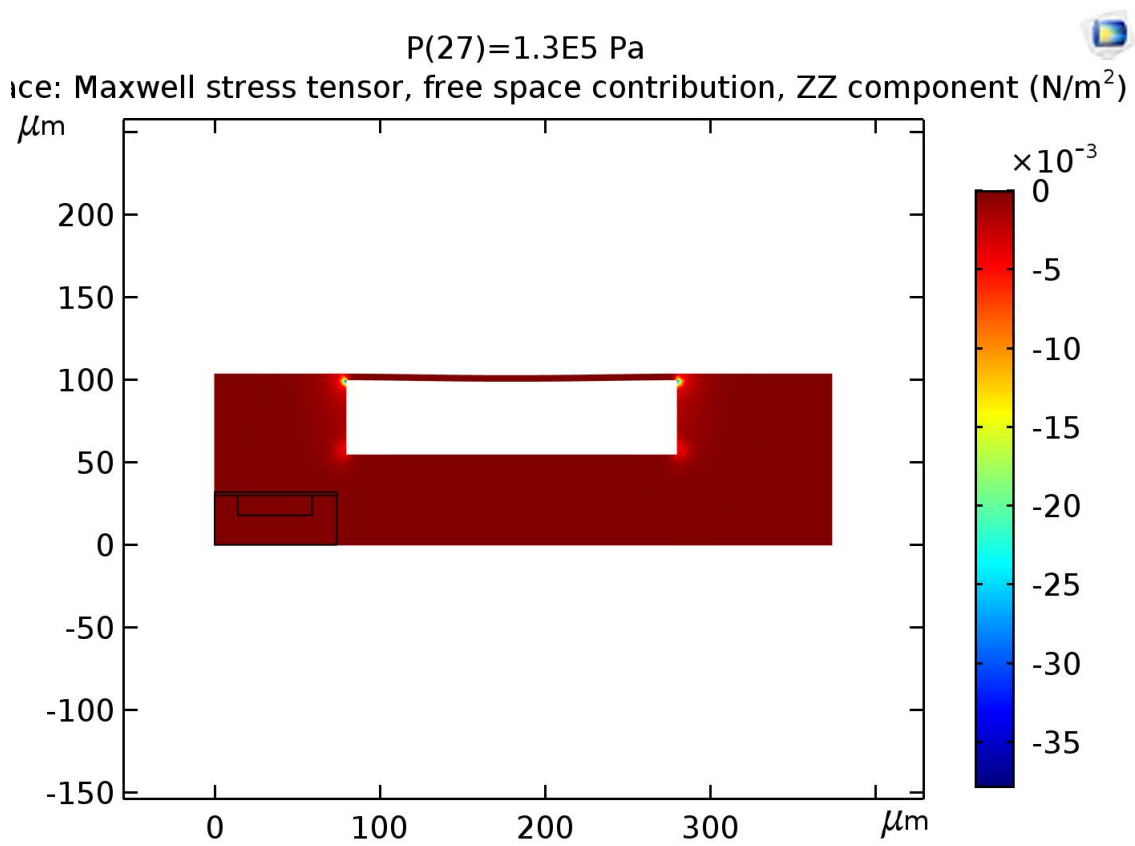


Figure B.4 The Maxwell stress tensor plot of MEMS capacitive pressure sensor with 4  $\mu\text{m}$  thin film membrane

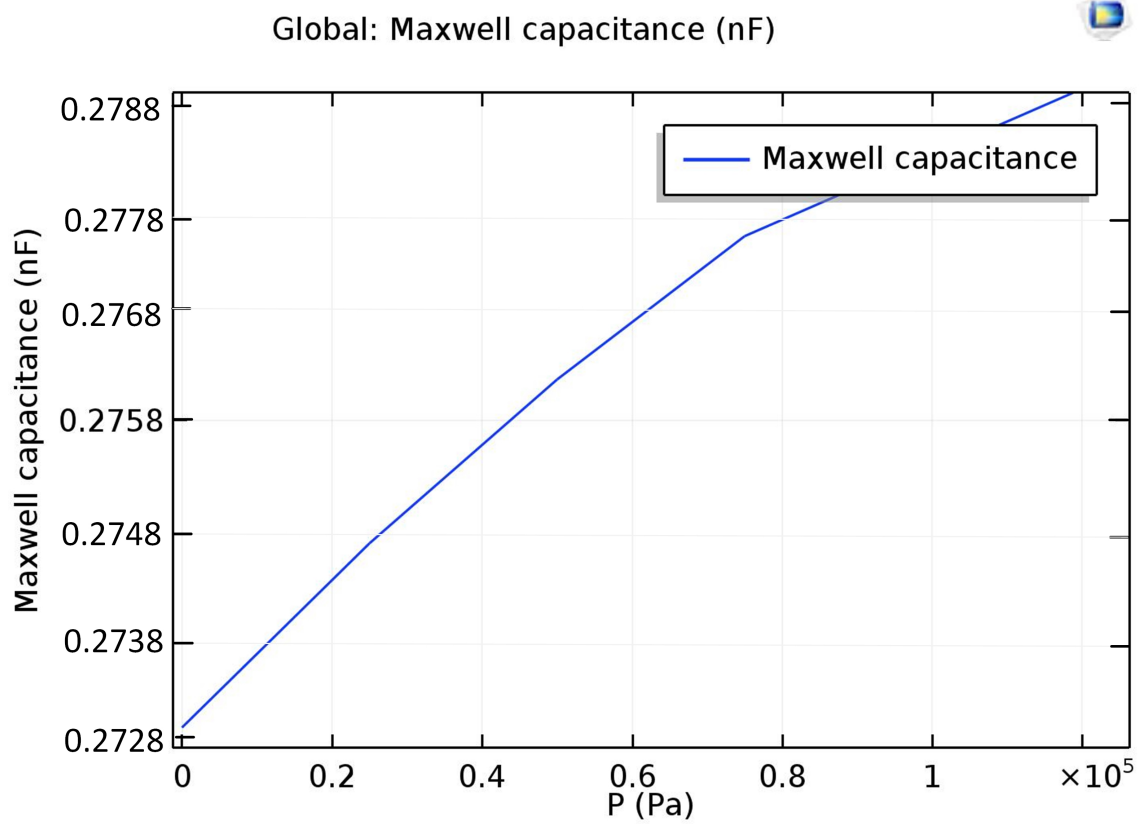


Figure B.5 The graph showing the change in capacitance with the change in pressure



# **Appendix C**

## **List of Publications**

Microsystem Technologies manuscript No.  
(will be inserted by the editor)

## Modeling, Simulation and Experimental Validation of Fatigue Behavior of Thin-Film Titanium Membranes

*For Chronic Intracranial Pressure Monitoring*

Nireekshan Kumar Sodavaram<sup>1</sup> · Fakhurul Alam<sup>1</sup> · Johan Potgieter<sup>2</sup> · David M. Budgett<sup>3</sup> · Khalid Mahmood Arif<sup>1</sup>

Received: 11/10/2018 / Accepted: date

**Abstract** The next generation fully implantable pressure sensors are valuable for intracranial pressure (ICP) monitoring, particularly in the chronic conditions of hydrocephalus. However, the accuracy, particularly in terms of the sensor drift over long duration, is a key concern. An implantable pressure monitoring system will rely on a flexible thin-film membrane as part of the pressure sensor and will interfere with a corrosive fluid (saline/blood) at a temperature of approximately 37 °C. The physics of the underlying thin film (material aging, mechanical fatigue), independent of the surrounding medium, triggers drift in the long-term monitoring of ICP. Therefore, finite element modeling (FEM) of thin-film deflection and fatigue life are essential. Although the FEM provides a theoretical view of the underlying issue, it is also necessary to validate the accuracy of the model. In this paper, we present both the numerical modeling and experimental validation of thin-film deflection and fatigue life of thin film titanium foils. The salient feature of this work is the approach of the thin-film deflection and fatigue testing (as part of the entire sensor) in contrast to the standard dog-bone based fatigue testing.

**Keywords** Drift · Multiaxial fatigue · Thin-film membrane · Implantable pressure sensor

<sup>1</sup> School of Engineering and Advanced Technology, Massey University, Auckland 0632, New Zealand. Tel.: +64 (09) 414 0800 E-mail: k.arif@massey.ac.nz

<sup>2</sup> Massey Agritech Partnership, Massey University, Palmerston North 4442, New Zealand.

<sup>3</sup> Auckland Bioengineering Institute, University of Auckland, Auckland 1010, New Zealand.

### 1 Introduction

ICP elevation associated with traumatic brain injury (TBI), hydrocephalus, and other neurological conditions is a serious concern. If left untreated, the increased fluid pressure inside the brain can shrink the cerebral blood flow (CBF) leading to brain damage or premature death. The prevalence of TBI is increasing globally, and the World Health Organization predicts TBI as the third highest cause of early deaths in all age groups by 2020 [1]. The current ICP monitoring is via invasive techniques involving catheters insertion through the skull inside the brain. However, catheters can increase the risk of infection as the brain is potentially exposed to the outside environment. In principle, the risk of infection would be overcome by a fully implantable pressure sensor. However, the accuracy, particularly in terms of the sensor drift over long durations, is a key concern [2]. An implantable pressure monitoring system will rely on a flexible membrane as part of the pressure sensor and will interfere with a corrosive fluid (saline/blood) at a temperature of approximately 37 °C (Fig. 1)

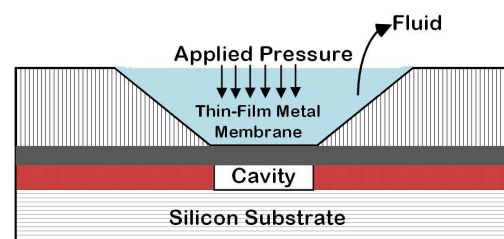


Fig. 1: Conceptual diagram of a sealed cavity thin-film membrane-based MEMS pressure sensor.

# Size Optimization and Fatigue Study of Ti-6Al-4V Membranes for Long-term ICP Measurement

Nireekshan K. Sodavaram<sup>1</sup>, Khalid M. Arif<sup>1</sup>

<sup>1</sup>School of Engineering and Advanced Technology  
Massey University  
Auckland 0632, New Zealand.  
k.arif@massey.ac.nz

David M. Budgett<sup>2,3</sup>, Daniel McCormick<sup>2,3</sup>

<sup>2</sup>Auckland Bioengineering Institute  
University of Auckland  
Auckland 1010, New Zealand.

<sup>3</sup>Millar Ltd., Auckland 1010, New Zealand.

**Abstract**—Drift in capacitive membrane pressure sensors is a serious concern in the long-term intracranial pressure (ICP) measurements. The major cause of drift is attributed to mechanical fatigue of the flexible membrane, which deflects in response to the applied pressure. Optimization of the membrane parameters, particularly size, could help in improving the fatigue life and overall performance of the membrane pressure sensors. In this paper, Ti-6Al-4V, grade 5, solution treated and annealed, biocompatible membrane has been numerically modeled for obtaining the overall desired size. In addition, multiaxial critical plane high cycle fatigue model was incorporated into the design to compute fatigue usage factors and cycles to failure of the membrane. With a diameter of 100  $\mu\text{m}$ , thickness of 4  $\mu\text{m}$ , the optimized membrane exhibited a life of about 100 million cycles to failure.

**Keywords**—diaphragm; Ti-6Al-4V; SN-curve; fatigue life; cycles to failure; long-term intracranial pressure monitoring

## I. INTRODUCTION

Membrane based capacitive pressure sensors are built with a parallel plate system with one electrode fixed to a substrate and other left flexible with the support of a sealed cavity (Fig. 1). This arrangement aids in the generation of electrical signal as membrane deflects under the influence of applied pressure. The capacitance of the parallel plate is given by  $c = \epsilon \frac{A}{d}$  [1]. However, design of implantable pressure sensors presents a host of engineering issues such as long term drift, accuracy, creep and biocompatibility. Factors that contribute to the sensor drift include inelastic deformations of the thin film membrane, nonlinear material properties, fatigue failure and residual and packaging stress induced on the membrane [2]. Catheters can easily be recalibrated to minimize the drift [3], but recalibrating a fully implantable sensor is challenging [4].

Recently, alternative transduction schemes such as localized gas bubble [5], electrochemical based micro bubbles [2], microfabricated spiral bourdon tube [6] based implantable sensors are being considered, which help in relieving some of the issues inherent with membrane based implantable sensors. However, before they become viable platform more work need to be done. Capacitive pressure sensors still can be used by resolving some of the critical issues like choosing a mechanically stable and biocompatible material, optimizing the overall size of membrane and simultaneously controlling the stresses, integrating fatigue study models in early design

stages, processing the membrane with new configurations to withstand the higher stress levels. Here in this work, numerical model for optimizing size, elastic deflections and fatigue failure of Ti-6Al-4V medical grade-5 titanium alloy is performed.

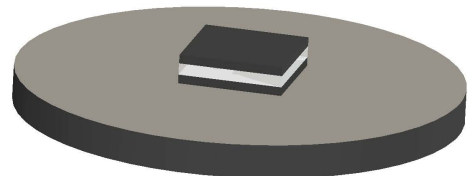


Fig. 1. Capacitive pressure sensor model with a steel base at the bottom, two electrodes in gray colour with a sealed cavity between them.

## II. MECHANICAL STABILITY OF TITANIUM ALLOY

The first objective in the design of implantable pressure sensor is to choose a mechanically stable and biocompatible membrane. While biocompatibility is the ability of the membrane to perform without adverse reaction or chronic inflammatory response to the host environment, mechanical stability is the virtue of the membrane to withstand fatigue and fracture over its intended life of operation. Mechanical stability is particularly critical in surgical implants where failure can result in discomfort to the patient and becomes deleterious in certain situations. Metallic alloys such as stainless steel, gold, cobalt-chromium and nickel-titanium alloys are most preferred in biomedical industry [7]. Their high tensile strength and resistance to corrosion and fracture and stability aid in the long-term dynamic ICP measurements [8].

Titanium is a corrosion resistant alloy with exceptional mechanical properties suitable for implantable sensors [9]. In neutral state it exists in two allotropic phases: 1) hcp- $\alpha$  phase at a temperature  $\leq 881.85^\circ\text{C}$ , and 2) bcc  $\beta$ -phase at a temperature  $\geq 881.85^\circ\text{C}$  [10]. The crystallographic transformation between two phases determines the mechanical and electrical properties of various titanium microstructures [11]. The hcp unit cell of  $\alpha$  phase at room temperatures is shown in Fig. 2. In comparison to  $\alpha$  phase alloys,  $\beta$  alloys account for only one percent of the total market in the United States and other parts of the world in spite of their advantages

Funded by a grant awarded jointly to Millar Ltd. Auckland and Massey University from Callaghan Innovation, New Zealand.

Manuscript

[Click here to access/download;Manuscript;Thinfilm-JMST\\_Rev1.docx](#)

Journal of Mechanical Science and Technology 00 (2010) 0000-0000

www.springerlink.com/content/1738-494x  
submitted manuscript under review

## Fatigue Testing of Integrated Thin Film Metal Membranes for Implantable Biomedical Pressure Sensors <sup>†</sup>

Nireekshan Kumar Sodavaram<sup>1</sup> and Khalid Mahmood Arif<sup>1</sup><sup>1</sup> School of Engineering and Advanced Technology, Massey University, Auckland, 0632, New Zealand

(Manuscript Received 000 0, 2018; Revised 000 0, 2019; Accepted 000 0, 2019) -please leave blank

### Abstract

The longevity of thin film membranes is vital for the lifetime monitoring of fluid pressure inside the human body. However, aging and mechanical fatigue of the thin film material hinders the long-term reliability of implantable pressure sensors. Despite, designers tend to neglect the fatigue life analysis of thin films in the design and fabrication of MEMS pressure sensors. Here, we present a low-cost fatigue testing system, which is custom designed from a modern multimedia speaker and subwoofer system. The subwoofer acts as an acoustic booster to amplify the sound vibrations into large stress amplitudes required for displacing the thin film membranes. A Keyence laser displacement sensor records the displacements of the thin films triggered in response to the sound-based stress amplitudes. Scanning electron microscope (SEM) is used in observing the surfaces of the thin films. An FEA parametric study and the fatigue testing results show significant correlations, except for the displacements values as the input Gaussian random vibrations are exaggerated in the experiments to visualize the bursting nature of the thin film membranes.

*Keywords:* Thin film membrane, MEMS pressure sensors, Deflections, Multiaxial fatigue, Acoustics

### 1. Introduction

Absolute pressure measurements are significant in biomedical applications as they can help separate physiological pressures from gravitational forces and atmospheric pressure oscillations [1]. In this regard, a sealed cavity MEMS capacitive membrane-based pressure sensor is suitable, which can be fabricated and packaged along with signal conditioning circuits as depicted in Fig. 1 [2]. These sensors offer high-pressure sensitivity and low temperature drift compared to piezoresistive counterparts. However, signal or sensor drift is one of the major issues that hampers the long-term function of a sealed cavity MEMS capacitive pressure sensor [3]. Each time the sensor drifts from the actual response, surgery may be required to open the patient's scalp for recalibration or replacement of the sensor. The surgery can cause discomfort to the patient and lead to severe infections. In situ recalibration could help [4] but it is not yet possible for the fully

implantable sensor that is part of an in-vivo biological medium entirely sealed from the outside environment. Hence, an implantable pressure sensor that can function for longer durations without the signal drift is essential in chronic biomedical pressure monitoring.

It is widely believed that aging and mechanical fatigue of thin film metal membranes is one of the major sources of the sensor drift in the long-term monitoring membrane-based pressure sensors [5]. Therefore, it is essential to include fatigue failure testing in the design and fabrication of such sensors.

In general, a fatigue study involves the loading of a dog-bone model into a fatigue testing machine to verify or validate the life of the concerned material specimen [6]. ASTM E466 describes the method of validating the strength of metallic materials by applying direct stress over many cycles [7]. The acceptable type and the design of the specimen are given in the standard practice ASTM manual designated as E 466 – 96 [8]. However, the standard fatigue testing cannot be employed in predicting the life of MEMS capacitive pressure sensors due to the following reasons: 1) The size limitations in preparing the dog-bone test specimens, 2) The random and semi-random loading nature of many applications [9].

<sup>†</sup> This paper was recommended for publication in revised form by Associate Editor 000 000 -please leave blank.

\*Corresponding author. Tel.: +64-9-414-0800, Fax.: +64-9-350-5618  
E-mail address: k.arif@massey.ac.nz

© KSME & Springer 2019

# A Compact Stepper Motor Actuated Disposable Microgripper

Nireekshan Kumar Sodavaram<sup>1</sup> and Khalid Mahmood Arif<sup>1,2</sup>

<sup>1</sup> School of Engineering and Advanced Technology, Massey University, 229 Dairy Flat Highway, Auckland 0632, New Zealand  
<sup>2</sup> Corresponding Author / E-mail: k.arif@massey.ac.nz, TEL: +64-9-414-0800, FAX: +64-9-350-5616

KEYWORDS: Microgripper, Cam actuation, Motorized actuation, Micromachining, Laser cutting

*This paper describes the design, modeling and experimental testing of a disposable microgripper for manipulation of micro particles and objects. We utilize a CO<sub>2</sub> laser cutter to fabricate acrylic microgripper capable of handling objects less than 300 μm in size. The microgripper forms a flexure-based compliant mechanism which is actuated with a radial cam driven by a miniature stepper motor. Finite element analysis is used to optimize the selected design for optimal stress distribution and tip displacement in response to the applied force on the legs of the mechanism. The gripper fits on an ergonomically designed holder that contains the stepper motor and a microstepping driver to control the motor. A push of a button on the holder opens and closes the microgripper, thus, making it very easy to operate. We demonstrate the utility of the microgripper through various pick and place experiments. The experimental results exhibit a high level of integrity in the design of the microgripper to manipulate a variety of microparticles.*

Manuscript received: February 29, 2016 / Revised: June 9, 2016 / Accepted: June 12, 2016

## 1. Introduction

Grasping and manipulation of micro particles/objects has various applications in research and industry. For example, a precision microgripper could be used to place a cell or particle on a micro-cantilever or nano-mechanical resonator for weighing<sup>1,2</sup> or for on-demand particle-by-particle microfabrication.<sup>3</sup> Microgrippers can also aid in micromanipulation and assembly,<sup>4,5</sup> or bio-printing.<sup>6</sup> The primary purpose of a microgripper is accurate and controlled grasping of objects of varying shapes and textures in a micromanipulation system.<sup>7</sup>

In recent years, a large variety of microgrippers, mostly differing in materials (e.g., silicon,<sup>8</sup> polymers,<sup>9</sup> hydrogels<sup>10</sup>), and actuation methods (e.g., electrothermal,<sup>11</sup> electrostatic,<sup>12</sup> piezo,<sup>13</sup> pneumatic<sup>14</sup>) has been developed. The proliferation of micro components and advancement in micromachining are two main driving forces prompting research and development in micromanipulation grippers. The choice of material and actuation method determines the utility and cost of microgripper.<sup>15</sup> Silicon is by far the most widely used material for the manufacture of microgrippers however it can only be handled in cleanrooms or similar facilities. It is a sad reality that, despite extraordinary advances in microfabrication technology, most devices on a typical wafer do not survive the entire fabrication process and yield is small even for simple microfabrication processes.

Polymers, on the other hand, are flexible, low-cost and can be processed in normal lab or workshop facilities. Moreover, many polymers exhibit excellent flexural properties which can be utilized to design microgrippers for highly accurate and precise gripping and manipulation.<sup>16</sup> The flexure-based compliant mechanisms move solely by deformation<sup>17</sup> and by using their flexural hinges instead of conventional joints, gears, and bearings. This produces clean and lubricant or other contaminant free devices, which can be used in clean environments.

Flexure-based microgrippers can also be easily actuated by pulling or pushing forces,<sup>1,18</sup> thus, making them suitable for rapid installation or release from handles. This feature is important for disposable microgrippers that can be replaced even after a single use in biological or chemical handling applications just like pipette tips.

In this paper, we describe the design, fabrication and tests of a flexure-based compact disposable microgripper (Fig. 1). This gripper is fabricated from 1 mm thick acrylic sheet in a laser cutting machine. The overall aim of the work is to show a family of low-cost, polymer based micro grippers that can be actuated by a motor driven cam mechanism.

The next section describes design details of the microgripper, which is followed by fabrication process and discussion on the developed devices. Micromanipulation results of various types of microparticles



Review

## Opportunities and Challenges of Membrane-Based MEMS Pressure Sensors in Lifetime ICP Monitoring

Nireekshan Kumar Sodavaram <sup>1</sup> 0000-0003-1542-9275, Daniel McCormick <sup>2</sup> 0000-0002-3568-0339, David M. Budgett <sup>2</sup> 0000-0002-7900-165X and Khalid M. Arif <sup>1\*</sup> 0000-0001-9042-4509

<sup>1</sup> School of Engineering and Advanced Technology, Massey University, Auckland 0632, New Zealand

<sup>2</sup> Auckland Bioengineering Institute, University of Auckland, Auckland 1010, New Zealand

\* Correspondence: k.arif@massey.ac.nz; Tel.: +64 (09) 414 0800 ext. 43580

Version February 23, 2019 submitted to *Sensors*

**Abstract:** Hydrocephalus is commonly treated by surgically inserting a ventriculoperitoneal (VP) shunt along with an invasive catheter for simultaneously draining the cerebrospinal fluid (CSF) and monitoring intracranial pressure (ICP). However, the insertion of a shunt and ICP catheter is an invasive procedure, which introduces vulnerability to infection. Besides, shunts have a reputation for frequent failures within the first two years of insertion. So how do we decide whether there is an actual rise in the ICP? Has the shunt failed, or an infection introduced by an ICP catheter has altered the value? In principle, the risk of infection and shunt failure can be overcome by using a fully implantable pressure monitoring system along with programmable shunts. However, the accuracy in terms of sensor drift over long durations is a serious concern. In this review, we state the underlying issue of the shunt failure and discuss the opportunities and challenges in the design and fabrication of a membrane-based MEMS pressure sensors. We also present our perspective on the data collection, simulation, modeling and testing of thin film membranes for building next-generation implantable pressure sensors.

**Keywords:** VP shunt, Invasive Catheters, CSF, ICP, Thin film Membrane, MEMS Pressure Sensors

### 1. Introduction

Hydrocephalus is a neurological condition that occurs due to the build-up of cerebrospinal fluid (CSF) inside the brain [1–4]. One in every thousand is born with hydrocephalus, making it very common like down syndrome, spina bifida, and brain tumors. National Institutes of Health (NIH) estimates around 700,000 children and adults are fighting with hydrocephalus in the United States (US) alone [5]. New Zealand birth defects registry records all live births (approximately 60,000 per year) suggests the total rate of hydrocephalus varied from 1.95 to 5.63 out of 10,000 births between 1980 and 2014 [6,7]. External ventricular drainage (EVD) of CSF is the most common neurosurgical interventions performed worldwide (Figure 1). For instance, the annual incidence of VP shunt placement in the US is 5.5 per 100,000 with approximately 30,000 procedures performed each year amounting to 95 million dollars [8]. Even though there is no record on the number of VP shunts interventions in New Zealand, data from two trauma centers in Hamilton and Waikato of New Zealand show an annual incidence rate of 790 cases per 100,000 of brain injuries [9]. Post-traumatic hydrocephalus may develop after brain surgery and may require VP shunts or CSF catheters for long-term monitoring and treatment. However, they frequently fail or clog (e.g., In children they are blocked about 50 % of the time within the first two years of installation), requiring multiple shunt revisions [10–12]. In general, a shunt comprises of three main components [13], which includes the following.

1. **Ventricular catheter:** A tube entering the brain through the skull for assisting CSF drainage.



**Fatigue Testing of Thin-Film Metals for Implantable Biomedical Applications**

Nireekshan K. Sodavaram<sup>1</sup>, Khalid M. Arif<sup>1</sup>, Johan Potgieter<sup>1</sup>, Fakhrul Alam<sup>1</sup>,  
David M. Budgett, PhD<sup>2,3</sup>

<sup>1</sup>SEAT, Massey University, Auckland, <sup>2</sup>Millar Ltd., <sup>3</sup>ABI, University of Auckland



### Introduction

- Pressure sensors are valuable in lifetime monitoring of bodily physical parameters, but the accuracy in terms of the sensor drift over long durations is a key concern.
- An implantable pressure sensor will rely on a flexible thin-film membrane as part of the pressure sensor and will interfere to a corrosive fluid (saline/blood) at a temperature of approximately 37°C.
- The underlying causes of drift are attributed to changes in the sensor performance independent of the environment, which may include material aging and fatigue.
- Fatigue analysis and experimental validations must be included in the initial design process of the implantable pressure sensor, particularly the thin-film membranes.

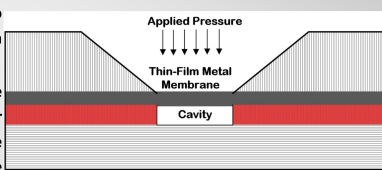


Figure 1: Pictorial Representation of a fully implantable pressure sensor

### Fatigue Testing: Titanium Alloys (4 μm and 25 μm)

Low-Cost Multimedia Acoustic based Fatigue Testing system (150 Hz to 4 kHz) for investigating the longevity of Titanium alloy: a biomaterial used as a thin membrane in pressure sensors.

Figure 2: Block Diagram of Low-Cost acoustic system: 1—Oscilloscope; 2—Gaussian Function Generator; 3—Sine wave sweep; 4—Spectrum Analyzer; 5—LK-G5001 Laser Displacement Sensor.

### Results: SEM Visualization

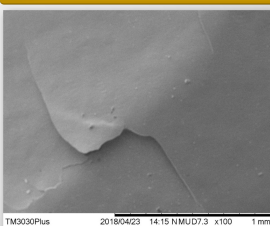


Figure 6: BSE compositional distribution of 4 μm thin-film Ti membrane after 160 million cycles

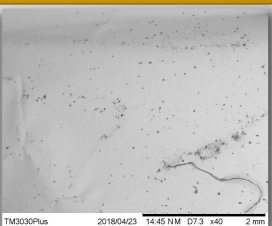


Figure 7: SE topographical distribution of 4 μm thin-film Ti membrane

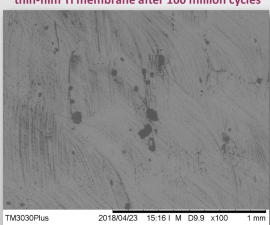


Figure 8: BSE compositional distribution of 25 μm thin-film Ti membrane after 160 million cycles



Figure 9: SE topographical distribution of 25 μm thin-film Ti membrane after 160 million cycles

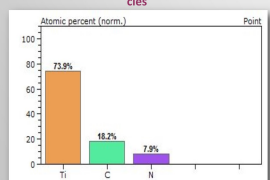


Figure 10: EDX Material compositional analysis of 4 μm thick Ti thin-films

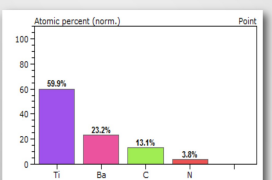


Figure 10: EDX Material Compositional analysis of 25 μm thick Ti thin-films

### Experimental Setup

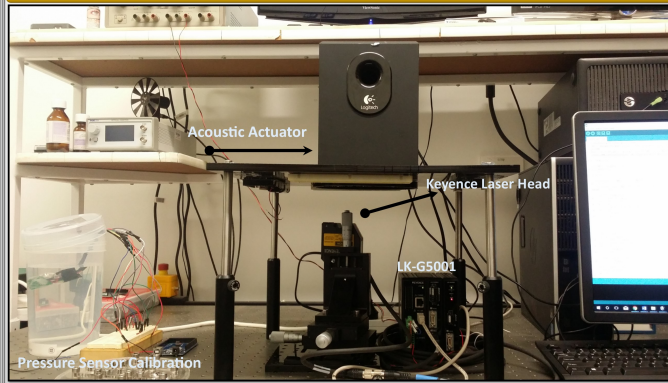


Figure 3: The Fatigue Experimental Setup: Apparatus mounted on vibration isolation bench top.

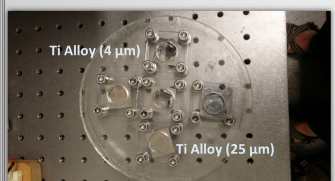


Figure 4: Ti Thin-Films Clamped to the acrylic disc which in turn is glued underneath the acoustic system

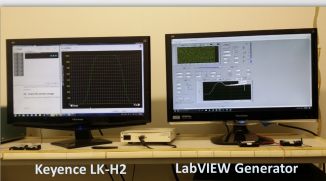


Figure 5: LabVIEW and LK-H2 Keyence displacement outputs

MaD2018: A Collaborative Future for NZ Manufacturing and Design, 21–22 May 2018, Auckland, New Zealand

### Results: Plots

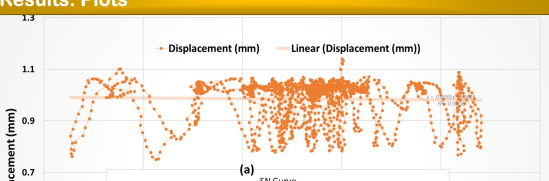
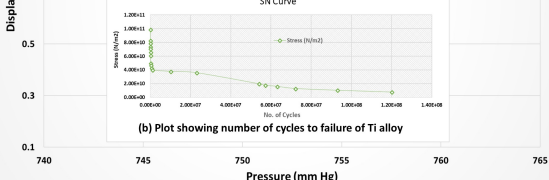


Figure 11 (a) Plot showing the displacement captured by Keyence LK-G5001 laser displacement sensor



(b) Plot showing number of cycles to failure of Ti alloy

### Experimental Setup

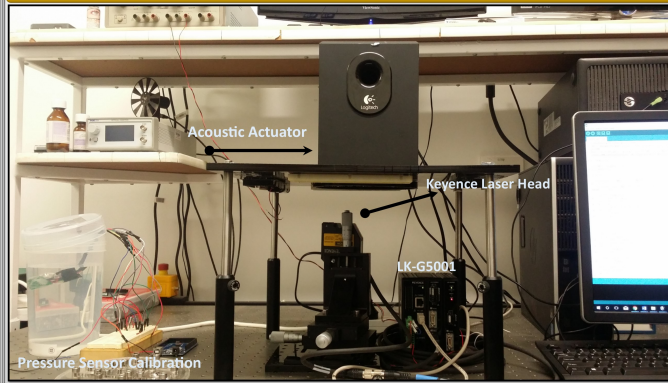


Figure 3: The Fatigue Experimental Setup: Apparatus mounted on vibration isolation bench top.

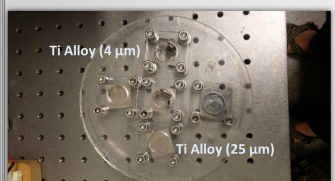


Figure 4: Ti Thin-Films Clamped to the acrylic disc which in turn is glued underneath the acoustic system

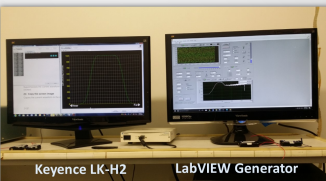


Figure 5: LabVIEW and LK-H2 Keyence displacement outputs

MaD2018: A Collaborative Future for NZ Manufacturing and Design, 21–22 May 2018, Auckland, New Zealand

### Results: Plots

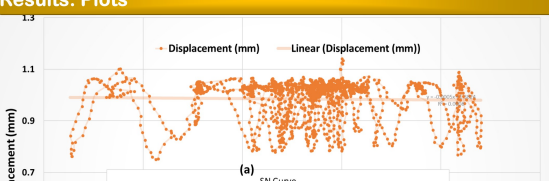
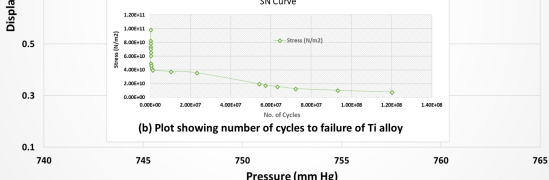


Figure 11 (a) Plot showing the displacement captured by Keyence LK-G5001 laser displacement sensor



(b) Plot showing number of cycles to failure of Ti alloy

### Experimental Setup

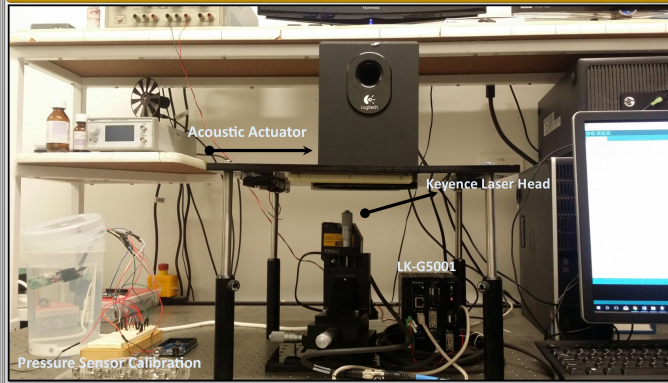


Figure 3: The Fatigue Experimental Setup: Apparatus mounted on vibration isolation bench top.

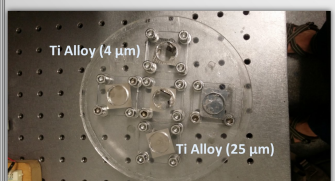


Figure 4: Ti Thin-Films Clamped to the acrylic disc which in turn is glued underneath the acoustic system

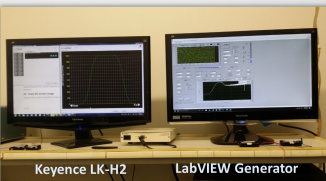


Figure 5: LabVIEW and LK-H2 Keyence displacement outputs

MaD2018: A Collaborative Future for NZ Manufacturing and Design, 21–22 May 2018, Auckland, New Zealand

### Results: Plots

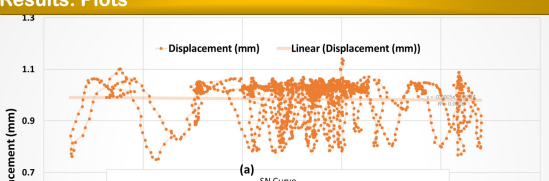
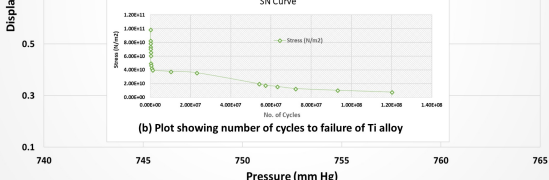


Figure 11 (a) Plot showing the displacement captured by Keyence LK-G5001 laser displacement sensor



(b) Plot showing number of cycles to failure of Ti alloy

### Experimental Setup

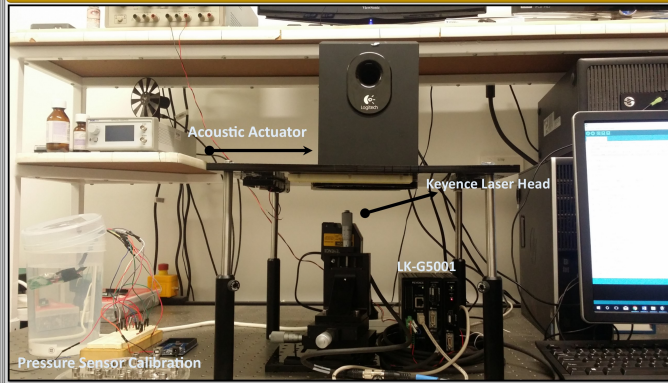


Figure 3: The Fatigue Experimental Setup: Apparatus mounted on vibration isolation bench top.

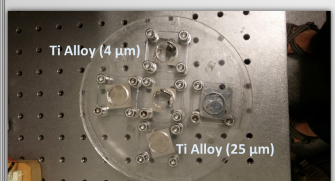


Figure 4: Ti Thin-Films Clamped to the acrylic disc which in turn is glued underneath the acoustic system

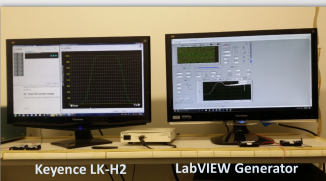


Figure 5: LabVIEW and LK-H2 Keyence displacement outputs

MaD2018: A Collaborative Future for NZ Manufacturing and Design, 21–22 May 2018, Auckland, New Zealand

### Results: Plots

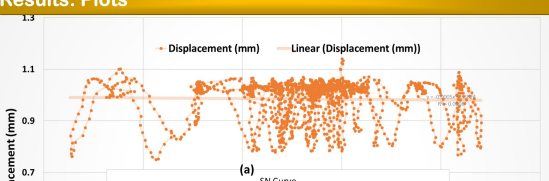
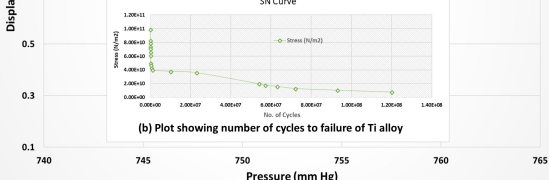


Figure 11 (a) Plot showing the displacement captured by Keyence LK-G5001 laser displacement sensor



(b) Plot showing number of cycles to failure of Ti alloy

### Experimental Setup

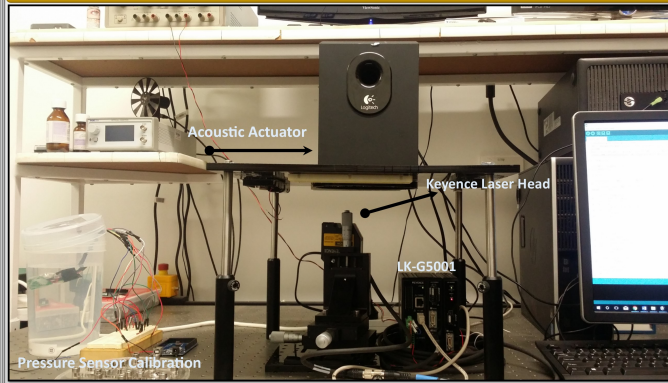


Figure 3: The Fatigue Experimental Setup: Apparatus mounted on vibration isolation bench top.

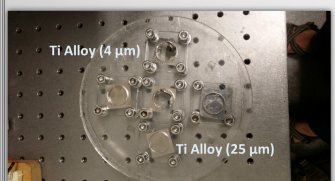


Figure 4: Ti Thin-Films Clamped to the acrylic disc which in turn is glued underneath the acoustic system

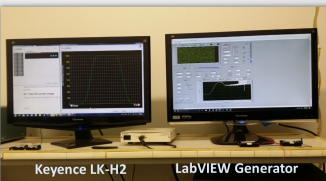


Figure 5: LabVIEW and LK-H2 Keyence displacement outputs

MaD2018: A Collaborative Future for NZ Manufacturing and Design, 21–22 May 2018, Auckland, New Zealand

### Results: Plots

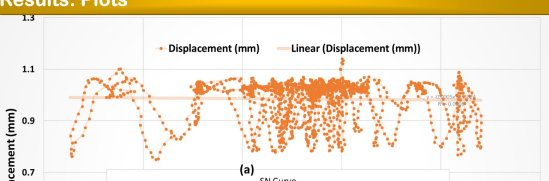
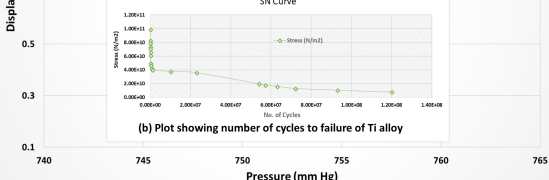


Figure 11 (a) Plot showing the displacement captured by Keyence LK-G5001 laser displacement sensor



(b) Plot showing number of cycles to failure of Ti alloy

### Experimental Setup

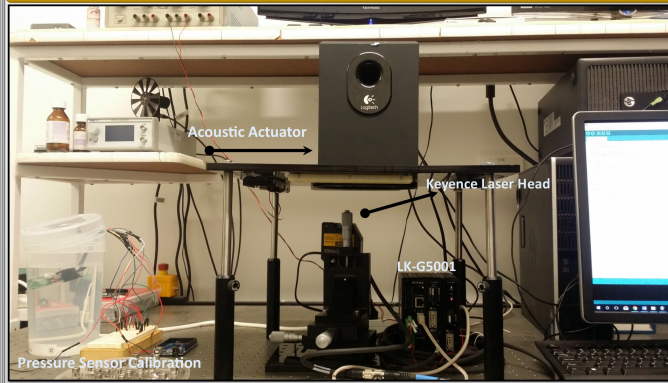


Figure 3: The Fatigue Experimental Setup: Apparatus mounted on vibration isolation bench top.

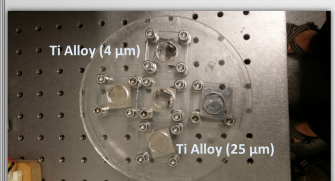


Figure 4: Ti Thin-Films Clamped to the acrylic disc which in turn is glued underneath the acoustic system

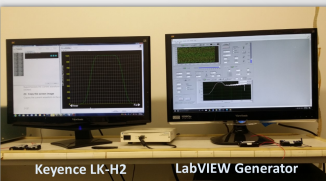


Figure 5: LabVIEW and LK-H2 Keyence displacement outputs

MaD2018: A Collaborative Future for NZ Manufacturing and Design, 21–22 May 2018, Auckland, New Zealand

### Results: Plots

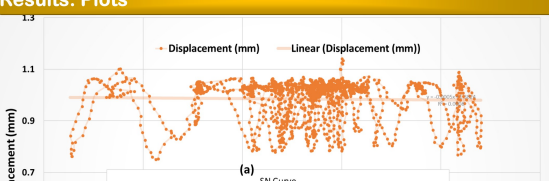
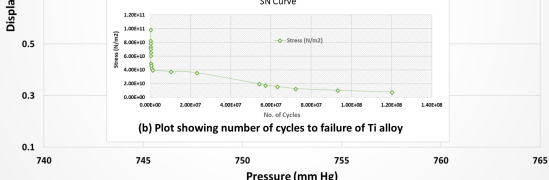


Figure 11 (a) Plot showing the displacement captured by Keyence LK-G5001 laser displacement sensor



(b) Plot showing number of cycles to failure of Ti alloy

### Experimental Setup

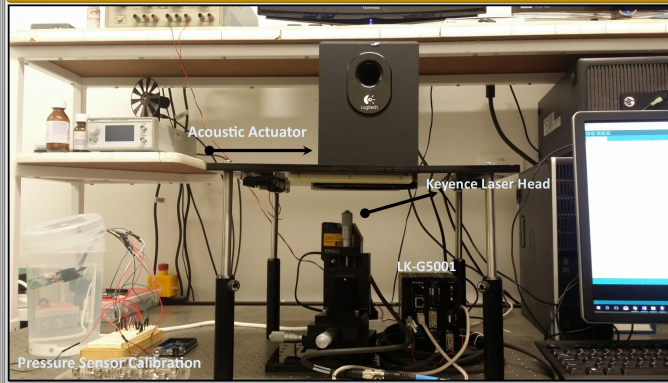


Figure 3: The Fatigue Experimental Setup: Apparatus mounted on vibration isolation bench top.

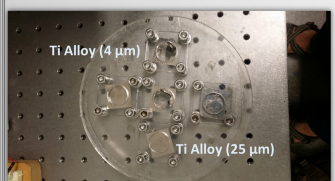


Figure 4: Ti Thin-Films Clamped to the acrylic disc which in turn is glued underneath the acoustic system

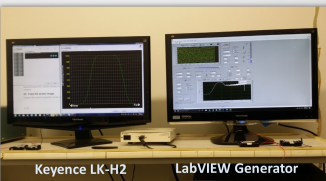


Figure 5: LabVIEW and LK-H2 Keyence displacement outputs

MaD2018: A Collaborative Future for NZ Manufacturing and Design, 21–22 May 2018, Auckland, New Zealand

### Results: Plots

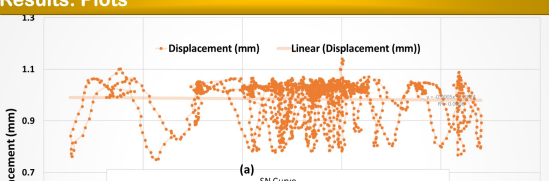
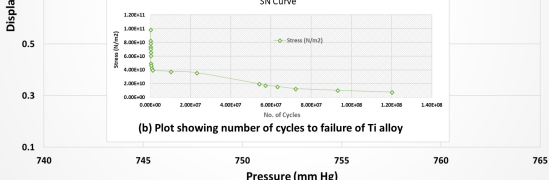


Figure 11 (a) Plot showing the displacement captured by Keyence LK-G5001 laser displacement sensor



(b) Plot showing number of cycles to failure of Ti alloy

### Experimental Setup

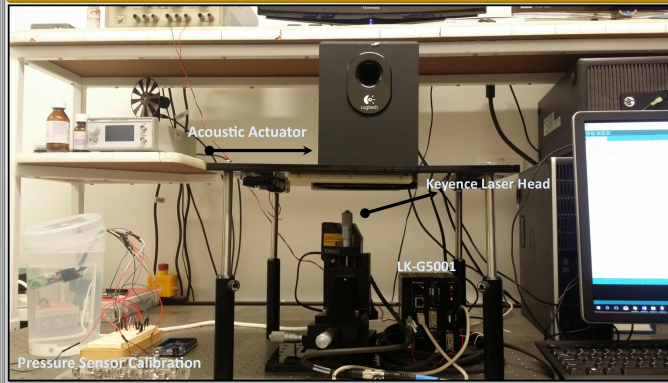


Figure 3: The Fatigue Experimental Setup: Apparatus mounted on vibration isolation bench top.

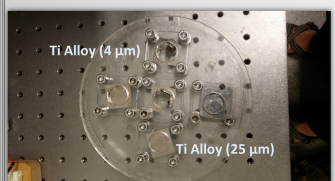


Figure 4: Ti Thin-Films Clamped to the acrylic disc which in turn is glued underneath the acoustic system

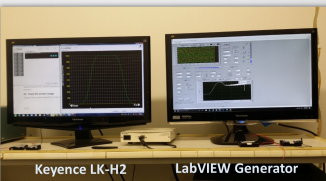


Figure 5: LabVIEW and LK-H2 Keyence displacement outputs

MaD2018: A Collaborative Future for NZ Manufacturing and Design, 21–22 May 2018, Auckland, New Zealand

### Results: Plots

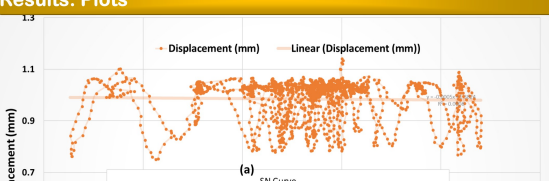
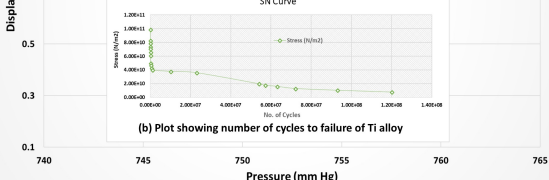


Figure 11 (a) Plot showing the displacement captured by Keyence LK-G5001 laser displacement sensor



(b) Plot showing number of cycles to failure of Ti alloy

### Experimental Setup

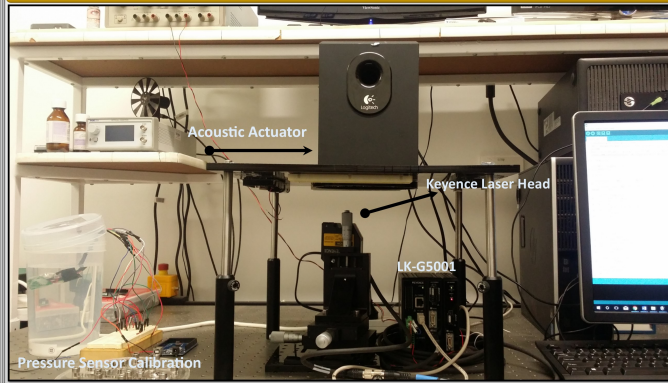


Figure 3: The Fatigue Experimental Setup: Apparatus mounted on vibration isolation bench top.

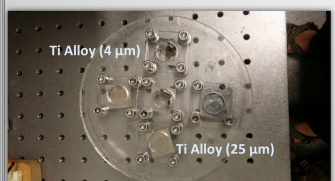


Figure 4: Ti Thin-Films Clamped to the acrylic disc which in turn is glued underneath the acoustic system

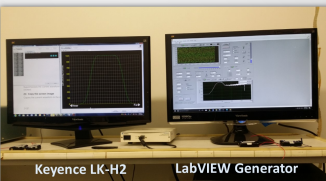


Figure 5: LabVIEW and LK-H2 Keyence displacement outputs

MaD2018: A Collaborative Future for NZ Manufacturing and Design, 21–22 May 2018, Auckland, New Zealand

### Results: Plots

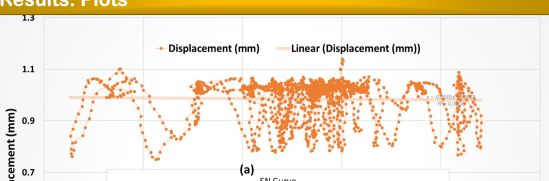
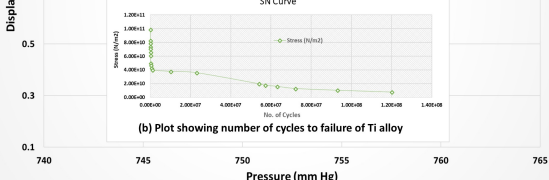


Figure 11 (a) Plot showing the displacement captured by Keyence LK-G5001 laser displacement sensor



(b) Plot showing number of cycles to failure of Ti alloy

### Experimental Setup

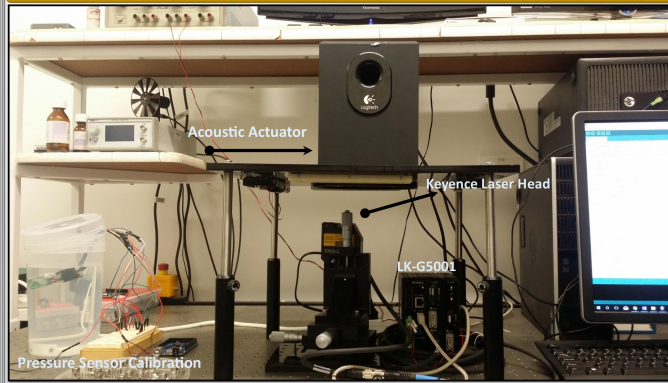


Figure 3: The Fatigue Experimental Setup: Apparatus mounted on vibration isolation bench top.

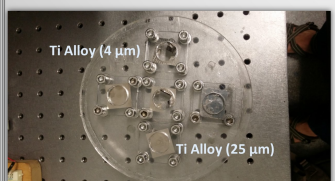


Figure 4: Ti Thin-Films Clamped to the acrylic disc which in turn is glued underneath the acoustic system

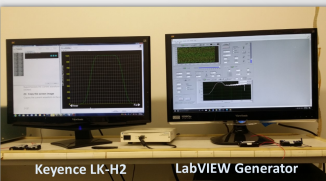


Figure 5: LabVIEW and LK-H2 Keyence displacement outputs

MaD2018: A Collaborative Future for NZ Manufacturing and Design, 21–22 May 2018, Auckland, New Zealand

### Results: Plots

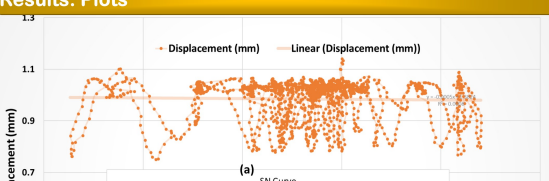
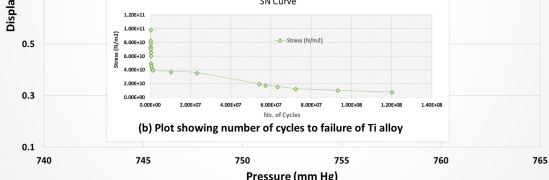


Figure 11 (a) Plot showing the displacement captured by Keyence LK-G5001 laser displacement sensor



(b) Plot showing number of cycles to failure of Ti alloy

### Experimental Setup

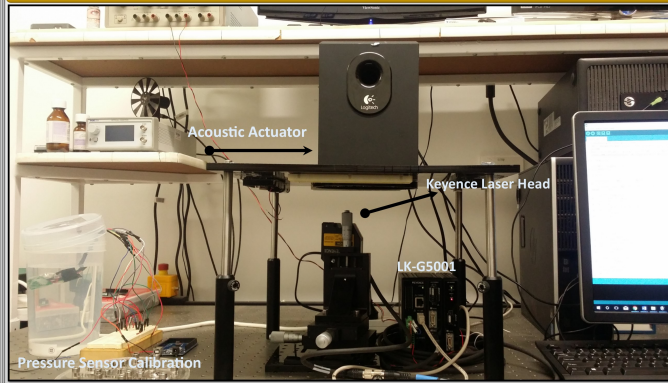


Figure 3: The Fatigue Experimental Setup: Apparatus mounted on vibration isolation bench top.

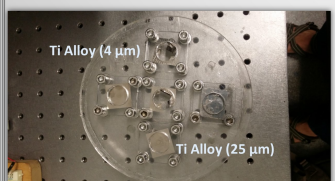


Figure 4: Ti Thin-Films Clamped to the acrylic disc which in turn is glued underneath the acoustic system

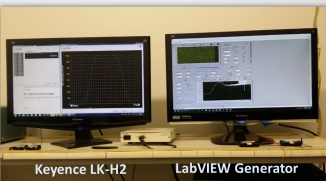


Figure 5: LabVIEW and LK-H2 Keyence displacement outputs

MaD2018: A Collaborative Future for NZ Manufacturing and Design, 21–22 May 2018, Auckland, New Zealand

### Results: Plots

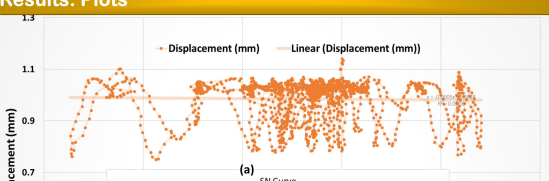
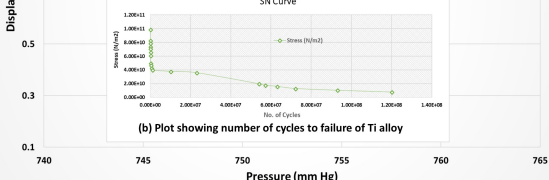


Figure 11 (a) Plot showing the displacement captured by Keyence LK-G5001 laser displacement sensor



(b) Plot showing number of cycles to failure of Ti alloy

### Experimental Setup

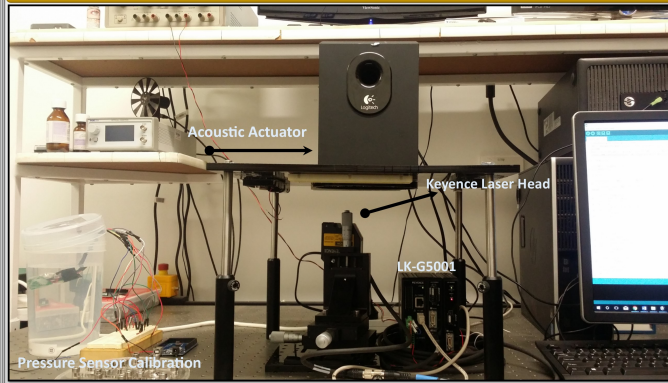


Figure 3: The Fatigue Experimental Setup: Apparatus mounted on vibration isolation bench top.

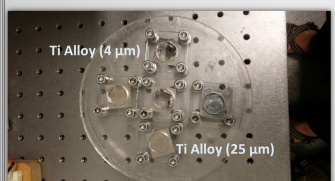


Figure 4: Ti Thin-Films Clamped to the acrylic disc which in turn is glued underneath the acoustic system

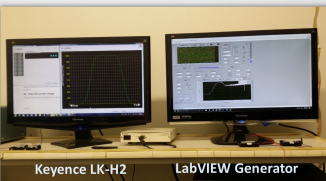


Figure 5: LabVIEW and LK-H2 Keyence displacement outputs

MaD2018: A Collaborative Future for NZ Manufacturing and Design, 21–22 May 2018, Auckland, New Zealand

### Results: Plots

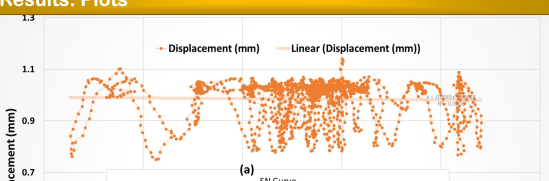
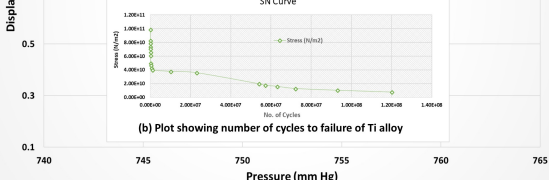


Figure 11 (a) Plot showing the displacement captured by Keyence LK-G5001 laser displacement sensor



(b) Plot showing number of cycles to failure of Ti alloy

### Experimental Setup

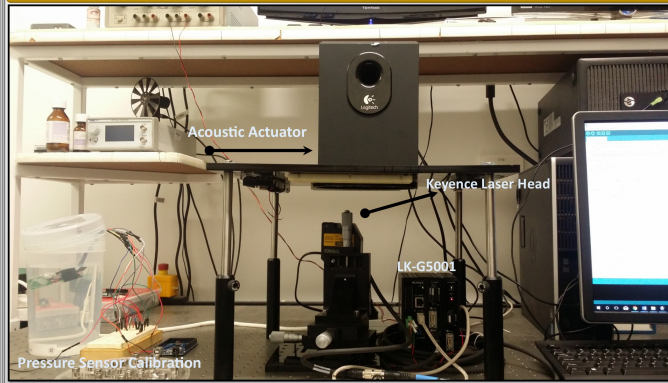


Figure 3: The Fatigue Experimental Setup: Apparatus mounted on vibration isolation bench top.

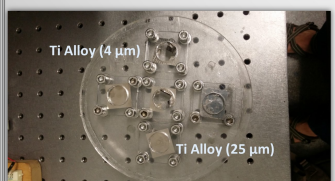


Figure 4: Ti Thin-Films Clamped to the acrylic disc which in turn is glued underneath the acoustic system

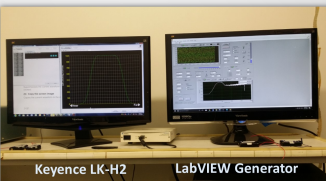


Figure 5: LabVIEW and LK-H2 Keyence displacement outputs

MaD2018: A Collaborative Future for NZ Manufacturing and Design, 21–22 May 2018, Auckland, New Zealand

### Results: Plots

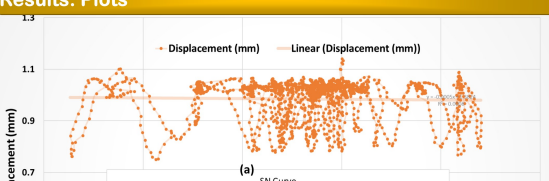
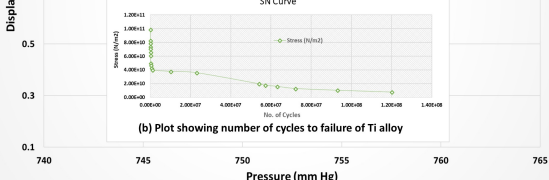


Figure 11 (a) Plot showing the displacement captured by Keyence LK-G5001 laser displacement sensor



(b) Plot showing number of cycles to failure of Ti alloy

### Experimental Setup

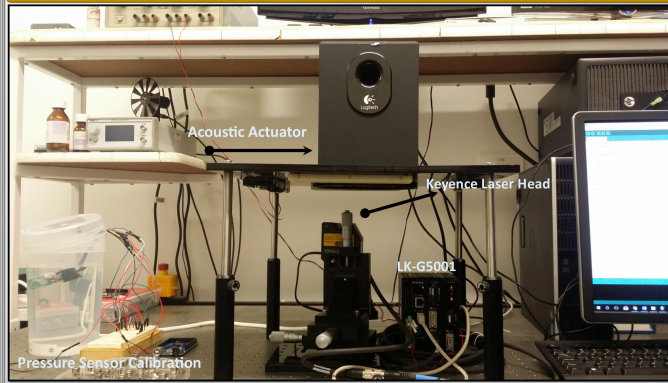


Figure 3: The Fatigue Experimental Setup: Apparatus mounted on vibration isolation bench top.

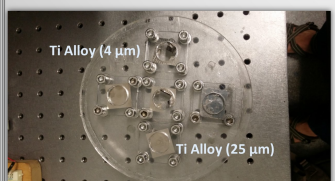


Figure 4: Ti Thin-Films Clamped to the acrylic disc which in turn is glued underneath the acoustic system

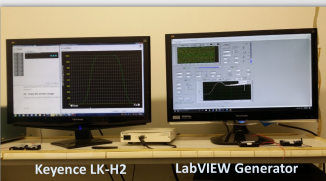


Figure 5: LabVIEW and LK-H2 Keyence displacement outputs

MaD2018: A Collaborative Future for NZ Manufacturing and Design, 21–22 May 2018, Auckland, New Zealand

### Results: Plots

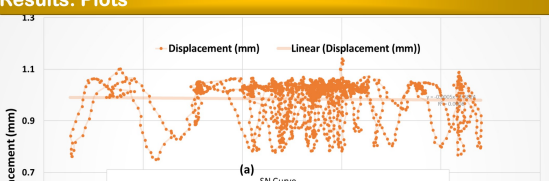
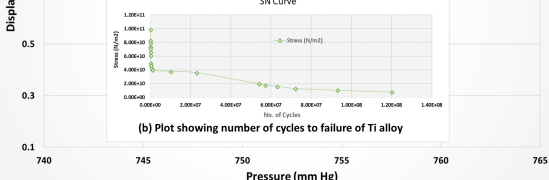


Figure 11 (a) Plot showing the displacement captured by Keyence LK-G5001 laser displacement sensor



(b) Plot showing number of cycles to failure of Ti alloy

### Experimental Setup

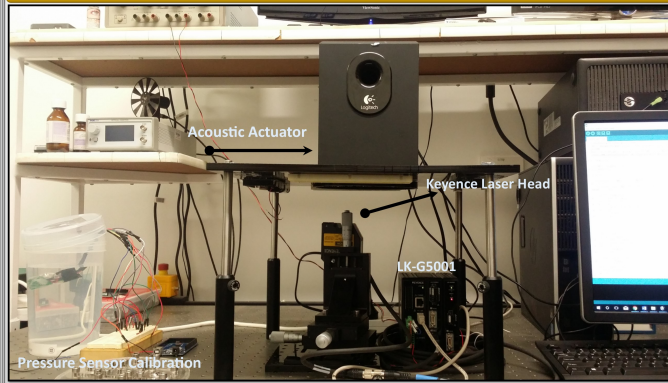


Figure 3: The Fatigue Experimental Setup: Apparatus mounted on vibration isolation bench top.

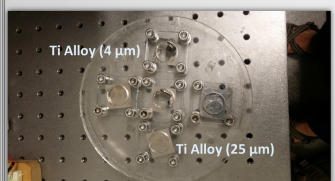


Figure 4: Ti Thin-Films Clamped to the acrylic disc which in turn is glued underneath the acoustic system

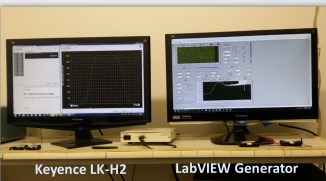


Figure 5: LabVIEW and LK-H2 Keyence displacement outputs

MaD2018: A Collaborative Future for NZ Manufacturing and Design, 21–22 May 2018, Auckland, New Zealand

### Results: Plots

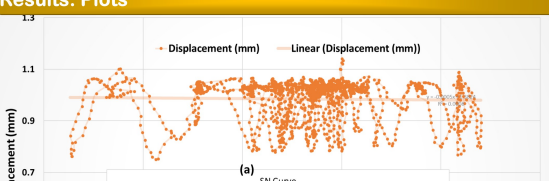
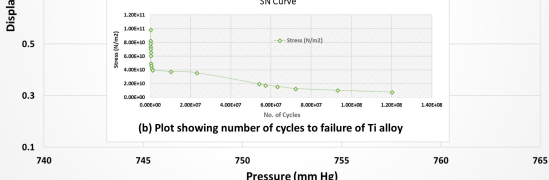


Figure 11 (a) Plot showing the displacement captured by Keyence LK-G5001 laser displacement sensor



(b) Plot showing number of cycles to failure of Ti alloy

### Experimental Setup

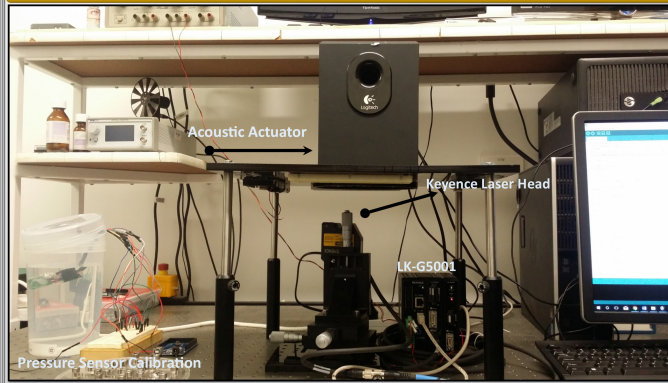


Figure 3: The Fatigue Experimental Setup: Apparatus mounted on vibration isolation bench top.

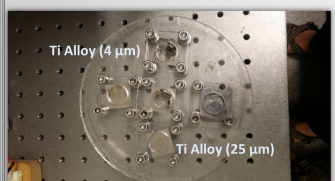


Figure 4: Ti Thin-Films Clamped to the acrylic disc which in turn is glued underneath the acoustic system

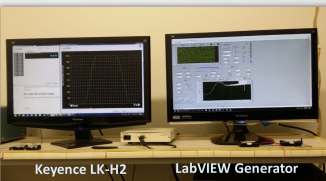


Figure 5: LabVIEW and LK-H2 Keyence displacement outputs

MaD2018: A Collaborative Future for NZ Manufacturing and Design, 21–22 May 2018, Auckland, New Zealand

### Results: Plots

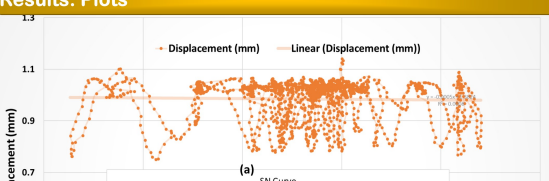
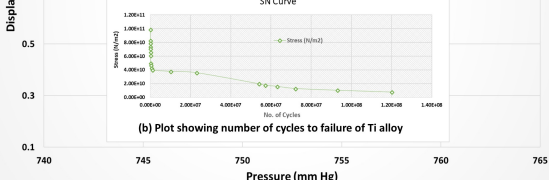


Figure 11 (a) Plot showing the displacement captured by Keyence LK-G5001 laser displacement sensor



(b) Plot showing number of cycles to failure of Ti alloy

### Experimental Setup

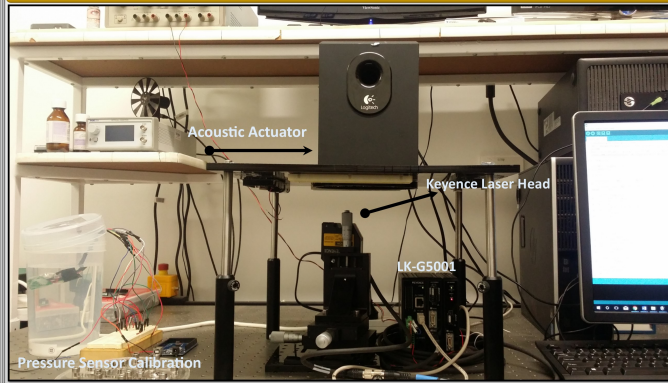


Figure 3: The Fatigue Experimental Setup: Apparatus mounted on vibration isolation bench top.

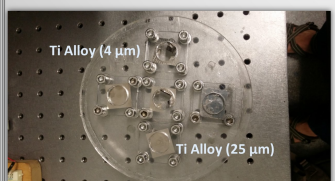


Figure 4: Ti Thin-Films Clamped to the acrylic disc which in turn is glued underneath the acoustic system

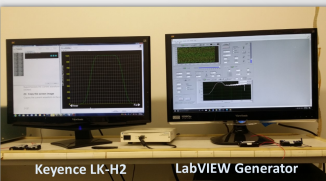


Figure 5: LabVIEW and LK-H2 Keyence displacement outputs

MaD2018: A Collaborative Future for NZ Manufacturing and Design, 21–22 May 2018, Auckland, New Zealand

### Results: Plots

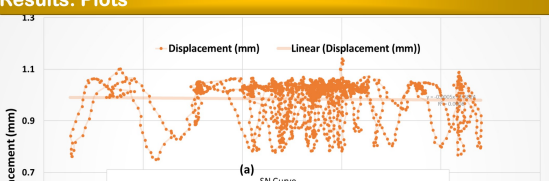
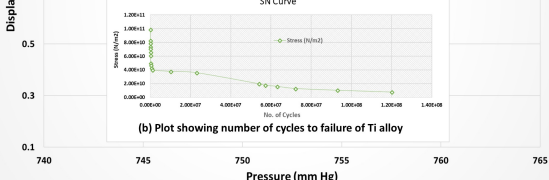


Figure 11 (a) Plot showing the displacement captured by Keyence LK-G5001 laser displacement sensor



(b) Plot showing number of cycles to failure of Ti alloy

### Experimental Setup

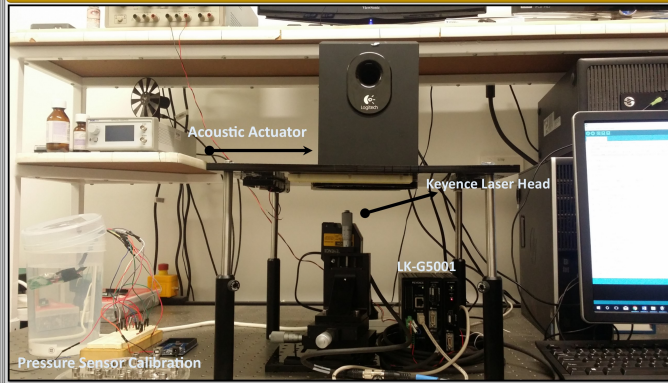


Figure 3: The Fatigue Experimental Setup: Apparatus mounted on vibration isolation bench top.




---

**MaD 2018: A Collaborative Future  
for NZ Manufacturing and Design**

---

*This is to certify that*

*Nireekshan Kumar Sodavaram*

*has been awarded*

**BEST POSTER PRESENTATION  
2<sup>ND</sup> PLACE**

*2018*

*Dr. Andy Shenk  
CEO UniServices*

*Prof. Simon Bickerton  
Chair, MaD Network*

*Dr. Mark Battley  
Co-Chair, MaD Conference  
Committee*

*Prof. Jim Johnston  
Co-Chair, Mad Conference  
Committee*

Award Sponsored by

**uniservices**<sup>+</sup>  
**IDEAS TO LIFE**

Figure C.7 Best poster award at MaD conference 2018



## The Effect of Residual Stress and Hygroscopic Swelling on MEMS ICP Sensor Drift

Nireekshan K. Sodavaram<sup>1</sup>, David M. Budgett<sup>2,3</sup>, Daniel McCormick<sup>2,3</sup>, Khalid M. Arif<sup>1</sup>,

<sup>1</sup>SEAT, Massey University, Auckland, <sup>2</sup>Millar Ltd., <sup>3</sup>ABI, University of Auckland





<sup>1</sup>SEAT, Massey University, Auckland, <sup>2</sup>Millar Ltd., <sup>3</sup>ABI, University of Auckland

### Introduction

1. CMOS integrated MEMS pressure sensors are required in several applications including industrial, biomedical devices, etc.
2. The Sensors are packaged in mechanically stable and biocompatible materials.
3. The Major issues are (1) The Effect of residual stress, (2) Hygroscopic swelling of Epoxy molds used in the fabrication
4. The main sources of residual stresses and Hygroscopic swelling are the thermal mismatches of fabrication process defects and moisture absorption of mold compounds.

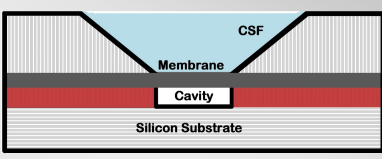


Figure 1: Pictorial Representation of a fully implantable pressure sensor

### The Effect of the Residual Stress

Almost all the surface-micromachined thin films experience residual stress as a result of fabrication process defects. The most common source is thermal stress, which is caused by differences in coefficient of thermal expansion between thin film and substrate.

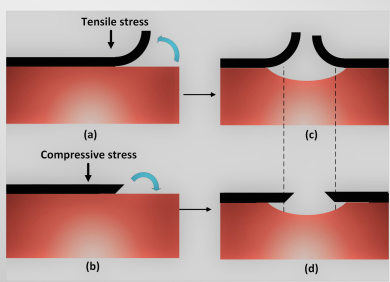
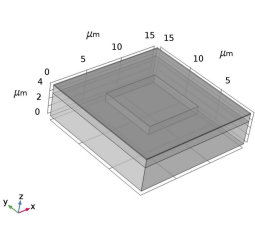
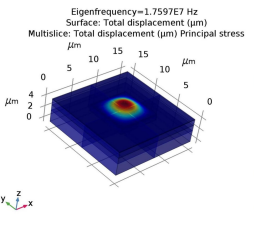


Figure 2. A Conceptual Diagram of the effect of residual stress on thin film membrane

### Finite Element Analysis (FEA) of Residual Stress

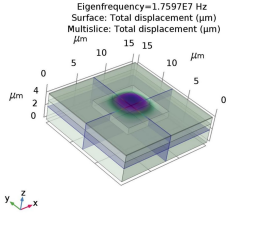
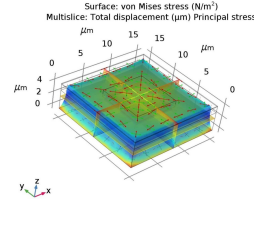



Figure 3. A Conceptual Diagram of the effect of residual stress on thin film membrane

AMN9 — Advanced Materials and Nanotechnology, A Conference supported by The McDiarmid Institute, University of Otago, University of Canterbury, and The University of Auckland.

### The Effect of Hygroscopic Swelling

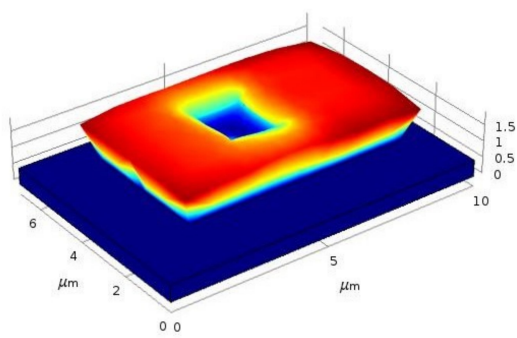
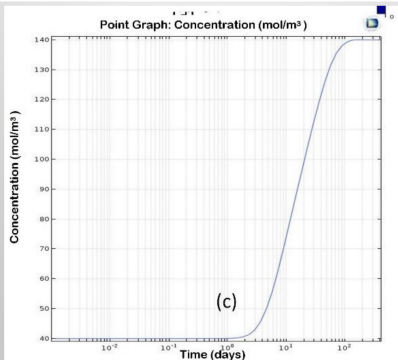



Figure 4. Top —The Displacement plot of mold compound and Sensor after 6 days; Bottom—The moisture content in the mold compound after 6 days

### Future Work— MEMS Fabrication

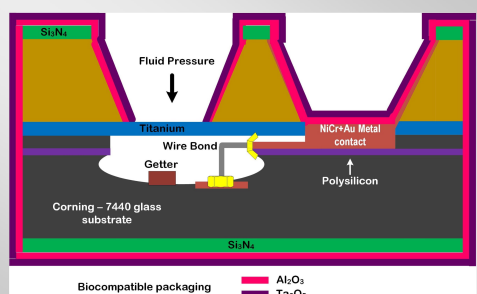


Figure 5. The final packaging, and Metallization MEMS Pressure Sensor for Biomedical pressure monitoring

### Acknowledgements

1. Sponsors of this Research: Callaghan Innovation.
2. Poster Presentation Sponsor: Massey University.
3. Support: Millar Ltd.,

### Contact Information

Web: <http://seat.massey.ac.nz/personal/k.arif/>  
 Email: [k.arif@massey.ac.nz](mailto:k.arif@massey.ac.nz); [n.kumar@massey.ac.nz](mailto:n.kumar@massey.ac.nz)

Figure C.8 A poster presented at the 9th international conference on Advanced materials and nanotechnology (AMN9)

